THE FUTURE OF MOLECULAR MR

Cellular and Molecular Imaging Workshop

ORLEANS, France

17-20 June 2024

ABSTRACTS

INVITED TALKS

IN ORDER OF PROGRAM

Stereoselective Parahydrogen Induced Polarization

Mai T. Huynh[1], Emily Buchanan[1], Sara Chirayil[1], Adeniyi M. Adebesin[2], and Zoltan Kovacs[1]
[1]Advanced Imaging Research Center, UT Southwestern Medical Center, 5323 Harry Hines Blvd., Dallas, TX 75390 USA
[2]Department of Biochemistry, UT Southwestern Medical Center, 5323 Harry Hines Blvd., Dallas, TX 75390 USA

Introduction: Hyperpolarized (HP) ^{13}C magnetic resonance spectroscopy is a powerful NMR/MR imaging modality for monitoring enzymatic fluxes in vivo because it can detect and quantify tissue metabolites in real-time independently from each other based on their characteristic NMR spectra. Currently, two HP-techniques are emerging as capable of providing sufficiently high ^{13}C signal enhancement (polarization) for in vivo studies: dissolution dynamic nuclear polarization (DNP) and parahydrogen induced polarization (PHIP). Hydrogenative PHIP involves the addition of a para-H_2 molecule to an unsaturated precursor followed by the conversion of the parahydrogen singlet spin order to heteronuclear spin polarization.[1] Inspired by asymmetric hydrogenation, here we report the stereoselective parahydrogenation of a prochiral unsaturated substrate (an enol pyruvate ester) with chiral catalysts followed by polarization transfer to ^{13}C to produce ^{13}C-hyperpolarized lactate derivatives.

Methods: Natural abundance and ^{13}C labeled O-acetyl ethyl enolpyruvate was synthesized starting from pyruvic acid and acetic anhydride. PHIP was performed with parahydrogen (>92.5%) in the presence of rhodium-bisphosphine homogenous catalysts (achiral Rh-DBBB, (S,S)- and Rh-DIPAMP in $CDCl_3$-acetone-d_6 mixture in the Earth's magnetic field (ALTADENA conditions). Spin order transfer to ^{13}C was achieved via magnetic field cycling (MFC).[2] This was accomplished by rapidly inserting the NMR sample into a zero Gauss chamber (diabatic passage) followed by slowly removing it to Earth's field (adiabatic remagnetization) and then acquiring the ^{13}C NMR spectra using a 1 Tesla Magritek Spinsolve spectrometer. The enantiomeric purity of the PHIP products was measured by chiral HPLC chromatography.[3]

Results and **Discussion:** Under ALTADENA conditions, the two protons originating from the parahydrogen remain strongly coupled during the reaction. The ^{1}H signal decay patterns of the PHIP product differed significantly depending on the catalyst used. After MCF, strongly enhanced ^{13}C-signals (^{13}C polarization up to 22%) of the carbonyls were observed in the ^{13}C NMR spectra. As expected and seen in Figure 1, the achiral catalyst yielded the racemate, the (R,R) catalyst afforded the L-lactate, while the (S,S) enantiomer produced the D-lactate derivative with excellent stereoselectivity.[3]

Conclusion: This work demonstrates that addition of parahydrogen to prochiral substrates in the presence of a chiral rhodium catalyst followed by polarization transfer to ^{13}C can generate highly ^{13}C polarized metabolic substrates with excellent stereoselectivity. Specifically, we showed that O-acetyl ethyl enolpyruvate can produce ^{13}C-polarized O-acetyl L- and D-lactic acid esters with high stereoselectivity. This method, termed stereoPHIP, is not limited to lactate. It will significantly expand the scope of PHIP to will significantly expand the scope of conventional PHIP via the rapid production of hyperpolarized chiral metabolites (hydroxy-carboxylic acids, amino acids, carbohydrates), pharmaceuticals and natural products in their biologically relevant or desired enantiomeric form.

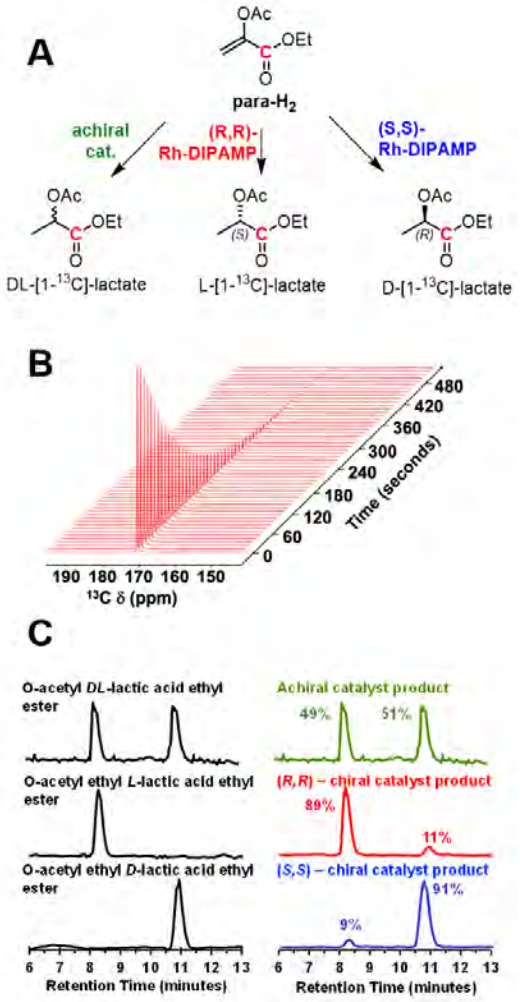

Figure 1. A) Catalytic addition of para-H_2 to O-acetyl ethyl enolpyruvate yields hypeprolarized racemic, L, or D lactate ester depending on the catalyst used. **B**) A series of ^{13}C NMR spectra acquired at 1 T using 5 ° flip angle and 10 s delay between successive scans of the hyperpolarized L-enantiomer showing the T_1 decay of the HP-^{13}C magnetization. **C**) Chiral HPLC traces of authentic samples (black) and PHIP products obtained with achiral catalyst (green), (S,S)-enantiomer (blue) and (R,R)-enantiomer (red) of the chiral catalyst Rh-DIPAMP.

References:

1 J. B. Hövener, A. N. Pravdivtsev, B. Kidd, C. R. Bowers, S. Glöggler, K. V. Kovtunov, M. Plaumann, R. Katz-Brull, K. Buckenmaier, A. Jerschow, F. Reineri, T. Theis, R. V Shchepin, S. Wagner, P. Bhattacharya, N M Zacharias, E. Y. Chekmenev, *Angew. Chem. Int. Ed.* **2018**, *57*, 11140-11162.
2 F. Reineri, T. Boi, S. Aime, Nat. Comm. **2015**, *6*, 5858.
3 M. T. Huynh, E. Buchanan, S. Chirayil, A. M. Adebesin, Z. Kovacs, *Angew. Chem. Int. Ed*. **2023**, *62*, e202311669.

Deuterium Metabolic Imaging - Rediscovery of a Powerful Imaging Tool for Precise In Vivo Monitoring of Glucose Metabolism: From Bench to Bedside

Laura Kuebler[1,2,3], Praveen Valsala[4], Nikolai Avdievitch[4], Jörn Engelmann[4], Klaus Scheffler[4,5], André F. Martins[1,2], Rolf Pohmann[4]

[1]Werner Siemens Imaging Center, Department for Preclinical Imaging and Radiopharmacy, Eberhard Karls University Tübingen. [2]Cluster of Excellence iFIT (EXC 2180) «Image-Guided and Functionally Instructed Tumor Therapies», University of Tübingen. [3]German Cancer Consortium (DKTK), DKFZ, core center Heidelberg, Germany. [4]High-Field Magnetic Resonance Center, Max-Planck-Institute for Biological Cybernetics, Tübingen. [5]Department for Biomedical Magnetic Resonance, University of Tübingen

Introduction: Deuterium metabolic imaging (DMI) is a non-invasive tool that offers quantitative measurements of metabolic processes, particularly glucose metabolism, for precise monitoring of disease progression. It provides a deeper understanding of the downstream metabolism of deuterated substrates like [6,6′-$^2H_2$]glucose or [$^2H_3$]acetate in vivo [1,2]. We optimized DMI technology at preclinical and clinical levels and effectively monitored in vivo metabolism using DMI in neuro-oncology models, bridging the gap from bench to bedside. Additionally, we have implemented ultra-fast methods to enhance DMI detection in human subjects including pioneering clinical detection in Europe using safe orally administered [6,6′-$^2H_2$]glucose. **Methods**: Preclinical: A custom-built ^2H surface coil operating at 7 T was used to acquire chemical shift imaging (CSI) in phantoms, in healthy rat brains as well as brain-implanted glioma rat models before and after injecting a bolus of 1M [6,6′-$^2H_2$]glucose (90 min p.i., 0.5 mL/min for 2 minutes (180 mg of [6,6′-$^2H_2$]glucose). CSI acquisition parameters were: imaging matrix size: 128x16x8x8, nominal resolution: 4mm^3, and an acquisition time: 30 minutes Clinical: A custom-built double-tuned radiofrequency coil with 10 transceiver (TxRx) channels for proton and 8 TxRx/2 for deuterium was used [3]. Three healthy subjects took part in the study, fasted overnight, and then [6,6′–$^2H_2$]glucose (0.75 g/kg of body weight) was orally administered. Whole brain multi-echo bSSFP 10-minute acquisitions with a resolution of 6.75 mL were conducted for DMI at different time intervals. A 2 mm^3 spatial field map with protons (^1H) was obtained for B0 correction. 10-minute 3D CSI with a resolution of 1.1 mL was performed at three-time points for the reference values of metabolites. **Results/Discussion:** Using our unique DMI setup, it is possible to facilitate accurate and precise quantitative metabolic imaging. We quantified [6,6'-$^2H_2$]glucose using CSI phantoms containing different [6,6'-$^2H_2$]glucose concentrations. Furthermore, we performed in vivo rat brain imaging using CSI - obtained prior and until 90 minutes after the bolus of 1 M [6,6'-$^2H_2$]glucose. CSIs exhibited a distinct ^2H-labeled water, [6,6'-$^2H_2$]glucose, followed by a glutamate/glutamine (Glx) peaks observed 60 minutes post-injection. In addition, glioma rats revealed increased lactate levels at the tumor regions, indicating enhanced glycolysis (Fig. 1 A). Clinical studies employing the novel bSSFP technique at 9.4T showed enhanced dynamic DMI detection at ultra-high field compared to conventional spectroscopy methods (CSI). The bSSFP imaging technique improved spatial resolution due to its exceptional signal-to-noise detection capabilities. Data showed a strong uptake of [6,6'-$^2H_2$]glucose and efficient incorporation into downstream metabolites, including ^2H-labeled water, glucose, and Glx (Fig. 1 C). Glx increases over time whereas glucose decreases. Low Glx levels are observed in the areas corresponding to the ventricles. **Conclusions**: We have successfully designed, built, and evaluated DMI technology at 7 T preclinical and 9.4 T clinical settings. In addition, we a new MR sequence that enhances time and spatial resolution for DMI was developed. In preclinical investigations, DMI has shown promising insights for future in vivo translation in oncology, improving understanding of tumor metabolism from bench to bedside. In the next steps, we will perform more DMI imaging on healthy subjects and patients with glioblastoma.

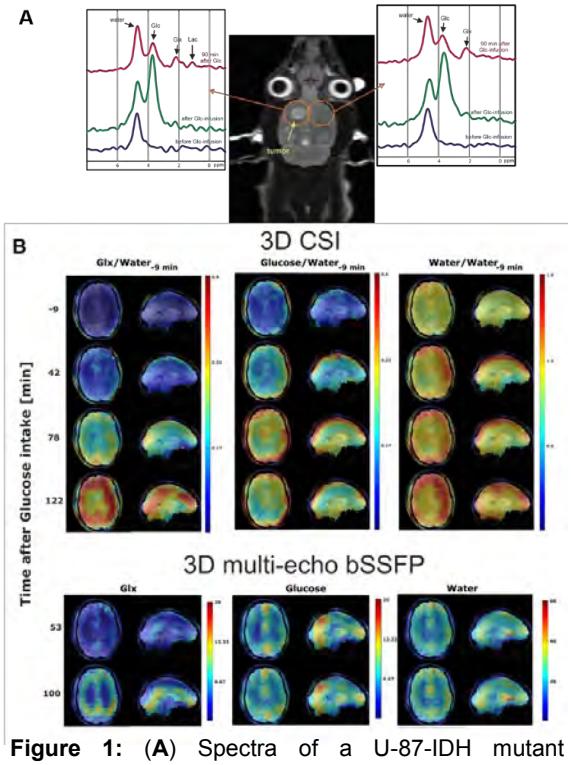

Figure 1: (**A**) Spectra of a U-87-IDH mutant gliblastoma bearing rat brain in vivo at 7 T before the [6,6-$^2H_2$]glucose injection (purple spectra), 30 minutes (green spectra) and 90 minutes (red spectra) after bolus injection of 1 M [6,6-$^2H_2$]glucose. (**B**) DMI maps of three ^2H metabolites (Glx (glutamate+glutamine), Glucose, and water) measured using the 1.1 mL and 6.75 mL bSSFP protocol at different time points after the glucose intake are overlaid over an anatomical reference. The 3D CSI data is normalized with the

References: [1] Kreis et al. Measuring Tumor Glycolytic Flux in Vivo by Using Fast Deuterium MRI. Radiology. 2019;294(2):289-296. [2]. De Feyter et al. Deuterium metabolic imaging (DMI) for MRI-based 3D mapping of metabolism in vivo. Sci Adv. 2018;4(8):eaat7314. [3] Avdievich NI et al. Double-tuned 31P/1H human head array with high performance at both frequencies for spectroscopic imaging at 9.4T. Magn Res Med. January 2020.

Metabolic neuroimaging of ApoE and APP mutational status in mouse models of Alzheimer's disease

Xiao Gao[1,2,3*], Marina Radoul[1,2*], Caroline Guglielmetti[1,2*], Lydia M. Le Page[1,2*], Huihui Li[4], Yoshitaka J Sei[4] , Ken Nakamura[4,5*], and Myriam M. Chaumeil[1,2,3*]

[1] Department of Physical Therapy, UCSF [2] Department of Radiology, UCSF [3] UCSF/UCB Graduate Program in Bioengineering, USA [4] Gladstone Institutes, USA [5] Department of Neurology, UCSF, USA. *equal contributions

INTRODUCTION: As metabolic impairment is a key player in Alzheimer's disease,[1,2,3] metabolic imaging could potentially improve diagnosis and monitoring of AD. ^{18}F-FDG Positron Emission Tomography (PET) is the imaging gold standard in AD, but radiation exposure limits its use. ^{1}H Magnetic Resonance Spectroscopy (MRS) has been applied to AD, but conclusive outcomes are lacking. Hyperpolarized ^{13}C MRS Imaging (HP ^{13}C MRSI) has been preclinically applied to brain disease models and is expanding clinically, but has yet to be applied to AD. Here, we combined these 3 methods to study the impact of 3 AD-related risk factors, namely ApoE mutation, APP mutation, and sex in genetically engineered AD mice.

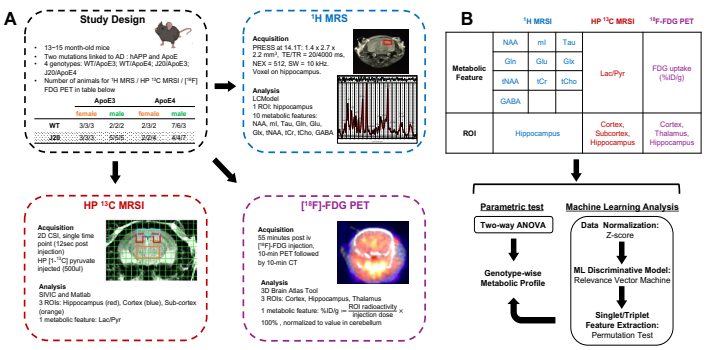

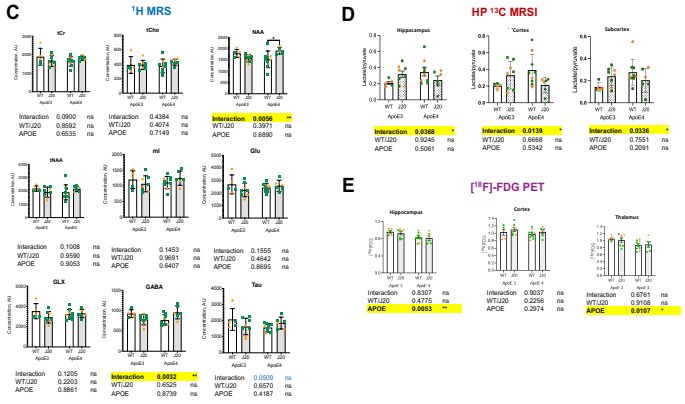

F

Combined Female & Male ♀♂

Genotype	Triplet Features	P-value	N
WT *vs.* Others	Glx + Lac/Pyr (Subcortex) + FDG (Cortex)	0.081	5
ApoE4 *vs.* Others	NAA + tCho + Lac/Pyr (Cortex)	0.158	8
J20 *vs.* Others	mI + FDG (Thalamus) + Lac/Pyr (Cortex)	0.275	8
Interaction *vs.* Others	NAA + tCho + GABA	*0.047	6

Female ♀

Genotype	Triplet Features	P-value	N
WT *vs.* Others	mI + Lac/Pyr (Subcortex) + Lac/Pyr (Cortex)	*0.031	3
ApoE4 *vs.* Others	FDG (Thalamus) + FDG (Hippocampus) + Lac/Pyr (Cortex)	0.116	2
J20 *vs.* Others	Glx + FDG (Thalamus) + FDG (Hippocampus)	0.135	3
Interaction *vs.* Others	tCho + Glu + Lac/Pyr (Cortex)	*0.009	2

Male ♂

Genotype	Triplet Features	P-value	N
WT *vs.* Others	Glu + Gln + Glx	*0.000	2
ApoE4 *vs.* Others	Gln + Glx + Lac/Pyr (Subcortex)	0.087	6
J20 *vs.* Others	mI + Glu + Gln	0.275	5
Interaction *vs.* Others	tCr + NAA + Gln	*0.040	4

METHODS: *Animals:* 27 animals (13~15 mo, **Fig.1A**) were divided in 4 groups WT (ApoE3w/o hAPP-KI), ApoE4-Only (ApoE4 w/o hAPP-KI), J20-Only (ApoE3 with hAPP-KI), and Interaction (ApoE4 with hAPP-KI). Animals were imaged on a 14.1Tesla Agilent® system (MR) or a PET/CT scanner (Siemens, USA) with 3 techniques: ^{1}H MRS, HP ^{13}C MRSI and [^{18}F]-FDG PET (see **Fig.1.A** for parameters). Statistics: All metabolic imaging metrics were first analyzed using 2-way ANOVA in Prism. Machine Learning: 16 metrics were used as input after standardization via Z-score (**Fig.1B**). Relevance Vector Machine (RVM) was implemented using sklearn-rvm toolbox. 4 RVM models were trained to assign each animal to 1 of the 4 groups with a confidence score. To estimate the impact of each metabolic feature/triplet, permutation tests (iN= 1000) were operated in a feature- and model-wise way and p-value of each feature calculated. To evaluate sex effect, RVM was operated separately for female and male.

RESULTS: Two-way ANOVA results showed a significant effect of ApoE×APP Interaction on GABA and NAA hippocampal levels (^{1}H MRS), and on lactate/pyruvate ratio across all ROIs (HP ^{13}C MR) (**Fig.1C,D**). Significantly reduced FDG uptake in hippocampus and thalamus was also found in all ApoE4 mice (**Fig.1E**). RVM algorithm was robust in handling classification of the four genotypes, with total accuracy of 92.6% for combined sex, 80% for female, and 88.2% for male. Particularly in the WT-*vs*-Others task, the RVM models showed 100% specificity and 100% sensitivity. The permutation tests identified the singlet (not shown) and triplet (**Fig.1F**) metabolic features that are pivotal for genotype classification, where a lower p-value stands for a higher impact. All 3 imaging modalities contributed pivotal features to setting boundaries between WT and AD mice, where FDG uptake (cortex), tCho level, and Lac/Pyr ratio (Cortex+Subcorex) are among the most impactful. In Interaction-*vs*-Others, most pivotal features were derived from ^{1}H MRS (**Fig.1F**), including tCr, NAA, and Gln. When looking at sex effect, ^{1}H MRS features were pivotal in male mice, whereas metabolic features from all three modalities were necessary for female mice classification.

CONCLUSIONS: Altogether, our results suggest that combining multimodal metabolic neuroimaging (^{1}H MRS, HP ^{13}C MRSI, and ^{18}F-FDG PET) and machine learning could help discriminate between AD-related mutational status, facilitate biomarker searching, and provide information of AD-related sexual dimorphism. Such knowledge would improve patient-centric clinical care and potentially create new avenues for assessment of new metabolism-targeting therapies.

REFERENCES: 1. Martins, R. N. et al. Alzheimer's disease: a journey from amyloid peptides and oxidative stress, to biomarker technologies and disease prevention strategies. *J. Alzheimers Dis.* **62**, 965–992 (2018). 2. Zhang S, et al. Glucose metabolic crosstalk and regulation in brain function and diseases. Prog Neurobiol. 2021;204:102089. 3. Butterfield, D.A., et al. Oxidative stress, dysfunctional glucose metabolism and Alzheimer disease. *Nat Rev Neurosci* **20**, 148–160 (2019). 4. Guglielmetti, C. et al Imaging immunomodulatory treatment responses in a multiple sclerosis mouse model using HP^{13}C metabolic MRI. *Commun Med* **3**, 71 (2023).

Clinical parahydrogen-based polarization - solving the outstanding technical challenges

S. Knecht, M. Gierse, S. Lukas, B.A. Rodin, Z. Ahmadova, Dagys, F. Josten, S. Mamone, A.J. Parker, J. Scheuer, C. Mueller, C. Vassiliou, M. Keim, **I. Schwartz**

NVision Imaging Technologies GmbH, 89081 Ulm, Germany;

Metabolic MRI with hyperpolarized 13C-labeled probes is crucial for studying metabolic processes in oncology, cardiology, and neurology [1,2]. Despite its potential, the clinical translation of ParaHydrogen Induced Polarization (PHIP) faces challenges. We have previously demonstrated [3] PHIP's preclinical viability. Here we focus on the three key technical aspects for clinical use: (1) Scaling the process to over 40 ml volume, maintaining >10% polarization at injection, (2) Ensuring impurity levels align with ICH guidelines, and (3) Maintaining sterility per regulatory requirements.

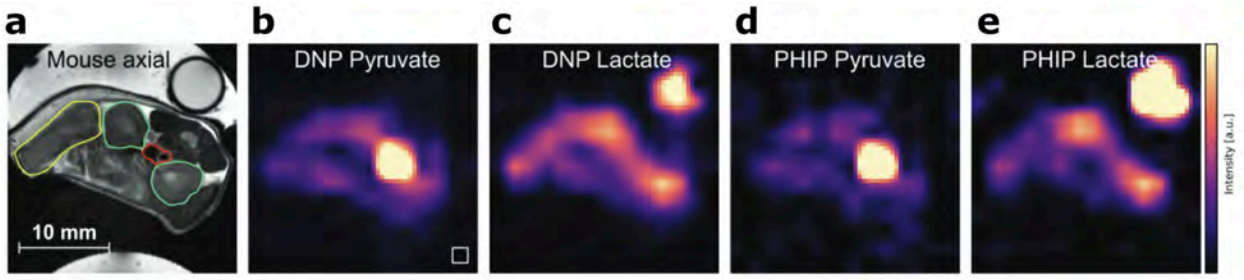

Figure 1: Comparison of metabolic MRI results of d-DNP and PHIP produced hyperpolarized 1-13C pyruvate. Pyruvate (h,d) and lactate (c,e) distributions in a tumor-bearing mouse are shown, with the corresponding anatomical reference in (a). Tumor (yellow),kidneys (green), and the blood vessel (red) ROIs are depicted. A [1-13C]lactate enriched phantom for RF power calibration is visible in the top right in the panels (a,c,e).

To tackle polarization challenges, we tailored the pyruvate precursor molecule and employed robust adiabatic RF sequences [4], achieving over 40% 13-C polarization. High-volume magnetic shields demonstrated that this high polarization is achievable in volumes exceeding dozens of ml and concentrations above 500mM pyruvate precursor.

Addressing purity challenges involved designing an automated multi-step purification process optimized for removing specific impurities. This ensures that all impurities meet defined thresholds according to ICH guidelines.For sterility challenges, we implemented polarization and purification within a sterile, disposable cassette, minimizing user interaction during dose preparation, reducing variability, and potential errors.

In conclusion, we have developed a comprehensive process for the clinical translation of PHIP-based polarization. By overcoming key technical challenges, we pave the way for a clinical PHIP polarizer, offering scalable, efficient, and widely accessible hyperpolarized pyruvate for metabolic imaging across various pathologies.

References

1. Gallagher, F. A. *Proc. Natl. Acad. Sci.* **117**, 2092–2098 (2020).
2. Apps A, *et al*. *Heart*. **104(18)**, 1484-1491 (2018).
3. Nagel, Luca, *et al. Advanced Science* **10.30** (2023): 2370208.
4. Marshall, Alastair, *et al.The Journal of Physical Chemistry Letters* **14.8** (2023): 2125-2132.

Metallocages as pH-responsive drug carriers and MRI probes

Priya Sahoo,[a] Joseph A. Spernyak[b] and Janet R. Morrow[a]

a. Department of Chemistry, the State University of New York, Amherst, NY 14260
b. Department of Cell Stress biology, Roswell Park Comprehensive Cancer Center, Buffalo, NY 14263
email: jmorrow@buffalo.edu

Introduction: Metallocages have multiple metal centers that are rigidly connected through organic linkers to give molecules of approximately 1 nm radius and cavities for encapsulation of guest molecules. Tetrahedral cages with high-spin iron(III) centers are effective T_1 MRI contrast agents with r_1 values of 8.7 $mM^{-1}s^{-1}$ in buffered solutions or 21 $mM^{-1}s^{-1}$ with serum albumin at 4.7 T, 37 ºC.1[1] These tetrahedral cages accumulate over several hours in CT26 tumors in BALB/c mice. Our interest in the design of activatable theranostic agents led us to study the encapsulation of metallodrugs inside of the cage for better delivery to tumors. Previous research has shown that the cages act as hosts for cationic organometallic complexes including platinum, ruthenium and gold complexes.[2] We have shown that Au(I) drugs, including auranofin-related compounds, are encapsulated in Fe(III) cages or their diamagnetic Ga(III) analogs. Such Au(I) phosphine based metallodrugs are among the most potent antitumor agents known to date.[3] In this study we show that the cages function as pH-activated carriers for anticancer gold drugs.

Methods: The tetrahedral Fe(III) (1) or Ga(III) (2) cages were prepared as reported,[1] and $[(PEt_3)Au(OH_2)]^+$ was encapsulated as shown by isolation of the host-guest complexes followed by ICP-MS analysis of metal, by NMR spectroscopy (for 2) or relaxivity (for 1). The host-guest complexes were studied for ease of release of the gold drug as a function of pH, temperature, and serum albumin. The iron cage with encapsulated gold (**$(PEt_3)Au@1$**) was injected via tail vein into BALB/c mice containing subcutaneous CT26 tumors and the assembly was tracked by MRI (7 T Bruker scanner) and by ex-vivo ICP-MS analysis for gold.

Discussion: NMR spectroscopy studies on **$(PEt_3)Au@2$** showed that the gold drug remains inside of the cage for 4-6 h in cages bound to serum albumin at pH 7.4 and 37 ºC. However, at pH < 6.4, the gold complex is released from the cage within minutes. Encapsulation of the gold drug in the iron cage produces a probe with increased proton relaxivity and enhances delivery to CT26 tumors in mice models as shown by MRI and by ex-vivo analysis of tumor and healthy tissue (Figure 1).

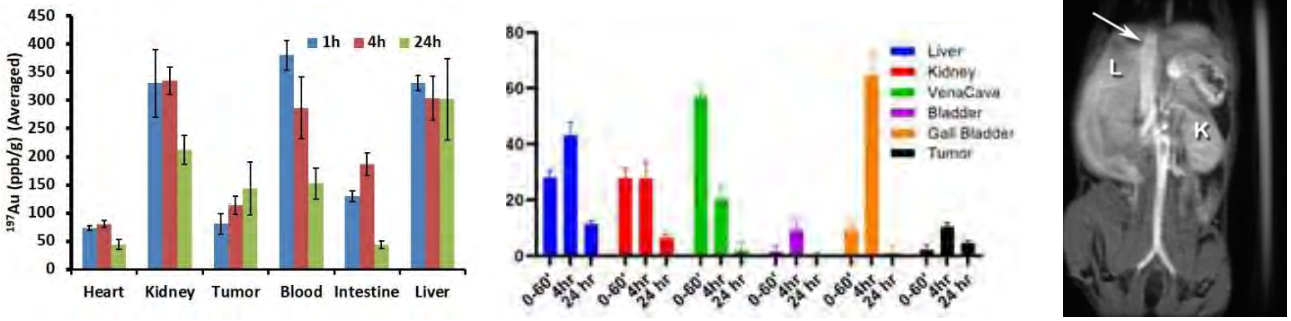

Figure 1. Left: *Ex-vivo* ICP-MS measurement of ^{197}Au in mouse organs after 1h, 4h and 24h of injection of **$Au(PEt_3)X@1$** in ppb/g tissue ±SD (n = 3). Middle: Pharmacokinetic clearance of **$(PEt_3)Au@1$** from different organs. Right: T_1 weighted MRI of BALB/c mice (12 μM/kg) showing signal enhancement by **$(PEt_3)Au@1$**.

Conclusions: Self-assembled cages with four iron centers show promise as effective T_1 MRI probes that may also deliver water-insoluble drugs to tumors. Functionalization of the cages to modulate biodistribution and tumor accumulation will be discussed.

References

(1) Sokolow, G. E.; Crawley, M. R.; Morphet, D. R.; Asik, D.; Spernyak, J. A.; McGray, A. J. R.; Cook, T. R.; Morrow, J. R. Metal-Organic Polyhedron with Four Fe(III) Centers Producing Enhanced T1 Magnetic Resonance Imaging Contrast in Tumors. *Inorg Chem* **2022**, *61* (5), 2603-2611.
(2) Hong, C. M.; Bergman, R. G.; Raymond, K. N.; Toste, F. D. Self-Assembled Tetrahedral Hosts as Supramolecular Catalysts. *Acc Chem Res* **2018**, *51* (10), 2447-2455.
(3) Massai, L.; Cirri, D.; Marzo, T.; Messori, L. Auranofin and its analogs as prospective agents for the treatment of colorectal cancer. *Cancer Drug Resist* **2022**, *5* (1), 1-14.

Fluorine containing Mn(II) complex as ^{1}H and ^{19}F MRI contrast agent candidate

Zoltán Garda[1,2], Frédéric Szeremeta[1], Océane Quin[1], Balázs Váradi[2], Enikő Molnár[2], Chantal Pichon[1], Gyula Tircsó[2] and Éva Tóth[1]

[1]Centre de Biophysique Moléculaire, CNRS, Rue Charles-Sadron, 45071 Orleans Cedex 2, France; [2]Department of Physical Chemistry, University of Debrecen, H-4032, Debrecen, Egyetem tér 1, Hungary

Introduction: ^{19}F MRI has several advantages, like high sensitivity, a broad chemical shift range and the lack of background signal, however, ^{19}F relaxation is slow and implies long repetition times, thus long MRI experiments. Our objective is to explore highly water-soluble, stable and kinetically inert Mn(II) complexes of small molar weight (< 1000 Da) ^{19}F containing ligands. Paramagnetic metal ions can largely shorten ^{19}F relaxation time, thereby increasing the ^{19}F MRI signal to noise ratio achievable in a given timeframe. We synthesized a CDTA-bisamide type ligand with two CF_3 moieties and we show here the detailed characterization of its Mn(II) complex including equilibrium and kinetic studies, ^{1}H and ^{19}F relaxation measurements, Mn(II)-F distance determination, cytotoxicity data, ^{19}F phantom as well as *ex vivo* MRI studies.

Methods: Synthesis of the ligand was based on a previous protocol[3]. Equilibrium model of the ligand and the Mn(II) complex was established at 0.15 M NaCl, 25 °C. Three different isomers (Isomer 1, 2 and 3) of the Mn(II) complex were identified and separated by reverse phase HPLC. Kinetic inertness of the complex was investigated through metal exchange reactions under slightly acidic conditions and 25 °C. ^{1}H r_{1p} and r_{2p} relaxivities were measured between 0.01and 80 MHz. ^{19}F relaxivities were determined at 188 MHz (4.7 T), 376 MHz (9.4 T) and 564 MHz (14.1 T) at 5 mM MnL concentration. ^{17}O NMR measurements were performed on an aqueous solution of the Mn(II) complexes (Isomers 1 and 3; 9.4 T, 54.2 MHz). ^{1}H and ^{19}F phantom MRI studies were conducted at 7 T, using a home-made loop-gap coil and FLASH or UTE pulse sequences (c_{MnL}= 0.41 -13.7 mM, pH = 7.4). Cytotoxicity of the MnL complex were tested on HeLa and K-562 (human lymphoblast) cell lines.

Results and Discussion: The MnL complex has high stability ($\log K_{MnL}$= 12.51(1), pMn = 8.17 at pH= 7.4 and c_{Lig} = c_{Mn2+} = 10 μM). During the HPLC investigation of the complex, we found three peaks, which were attributed to different coordination isomers of the same complex. The interconversion of the different isomers is slow (approximately 10 % in 5 days), therefore, their individual investigation was possible. The kinetic inertness of the complex (isomer mixture) is two order of magnitude higher than that of Mn(CDTA) ($t_{1/2}$= 1285 and 12[4] h, respectively, based on Cu(II) transmetallation. Zn(II) exchange reaction at pH= 6.0 showed a slight difference in the dissociation rate of Isomers 1 and 3 ($t_{1/2}$= 27 and 47 h, respectively). ^{19}F relaxation times (T_1 and T_2) were greatly reduced after complexation of the ligand with the paramagnetic Mn(II) (T_1: from 350/355 to ~ 2.5 ms; T_2: from 27/89 to ~ 1.8 ms at 9.4T), however remained similar for the different isomers. An average Mn-F distance (8.3±0.3 Å) was estimated from the ^{19}F relaxation times measured at three different field strengths. Phantom MR imaging studies show promising SNR values. Due to the short relaxation times of the complex, the best result was achieved with the UTE sequence at a low complex concentration c_{MnL}= 0.41 mM and with a relatively high matrix size in 11 minutes (SNR= 5.1, Matrix: 128 × 128, FOV: 32×32 mm, ST: 2 mm, voxel volume= 0.125 μl). MnL possesses low cytotoxicity up to 4 mM concentration in HeLa and K-562 cell lines. Furthermore, this complex is also effective in ^{1}H MR imaging, due to the presence of one water molecule in the inner coordination sphere (evidenced by ^{17}O NMR data) and its relatively high relaxivity ($r_{1p}^{20\ MHz}$ = 5.36 and 5.26 mM^{-1} s^{-1} for Isomer 1 and Isomer 3, respectively, 20 MHz, 25 °C).

Conclusion: This is the first detailed investigation of a Mn(II) complex in the context of ^{19}F MRI. Our results show that MnL is a promising candidate for ^{19}F and ^{1}H MRI endowed with fast paramagnetic relaxation and excellent SNR in phantom images.

References: 1) M. Srinivas et al., (19)F MRI for quantitative in vivo cell tracking, *Trends. Biotechnol.*, **2010**, *28*(7), 363; **2)** A. H. Schmieder et al., Recent Advances in ^{19}Fluorine Magnetic Resonance Imaging with Perfluorocarbon Emulsions, *Engineering*, **2015**, *1*(4): 475; **3)** Gy. Tircso, et al., Ethylenediaminetetraacetic acid bis(amide) derivatives and their respective complexes with Mn(II) ion for use as MRI contrast agent, International Publication Number: WO2016135234A1, **2016; 4)** Kálmán, F. K. et al., Kinetic inertness of the Mn^{2+} complexes formed with AAZTA and some open-chain EDTA derivatives *Inorg. Chem.*, **2012**, *51*(19), 10065

Molecular MR imaging of intestinal inflammation in a mouse model of colitis using a redox-active iron complex.

Irene Fernandez-Barahona,[1] Nick Rotile,[1] Negin Jalali Motlagh,[2] Iris Y. Zhou,[1] Eric Gale,[1] Peter Caravan[1], and Mariane Le Fur[1]

[1] Martinos Center for Biomedical Imaging, Institute for Innovation in Imaging, Massachusetts General Hospital and Harvard Medical School, Charlestown, MA. [2]Center for Systems Biology, Institute for Innovation in Imaging, Massachusetts General Hospital and Harvard Medical School, Boston, MA

Introduction. Inflammatory Bowel Diseases (IBD), including Crohn's disease and ulcerative colitis, are characterized by relapsing and remitting inflammation of the gastrointestinal tract and are associated with debilitating symptoms.[1] Although anti-inflammatory therapies are available, some patients do not respond to therapy and experience relapses and continuous inflammation. Non-invasive diagnostic tools are needed to inform on relapse and disease severity, guide treatment decisions, monitor treatment response and facilitate the development of novel therapeutics.[2] Neutrophils are the first immune cells recruited to the site of inflammation and play a critical role in the resolution of inflammation. However, their excessive recruitment and accumulation in IBD results in significant tissue damage through the production of reactive oxygen species (ROS) and contribute to chronic intestinal inflammation.[3] Because of the overproduction of ROS in IBD, we hypothesize that Fe-PyC3A, an MR probe that produces a signal enhancement upon activation by ROS,[4] can be used to detect inflammation and monitor disease progression in IBD.

Methods. To induce colitis, seven-week-old male C57BL/6 mice (n = 11) received 2.0% dextran sulfate sodium (DSS) in the drinking water for 5 days followed by 2 to 4 days of normal water. Age-matched mice receiving normal drinking water were used as controls (n = 7). MR imaging was conducted on day 7, 8 or 9 using Fe-PyC3A. Mice were fed a manganese deficient diet (Envigo, TD140857) for 2 days and were fasted for 12 hours prior to imaging. To minimize bowel peristalsis during scanning, mice were administered an anti-peristaltic agent (N-Butylscopolamine, 5 mg/kg) via i.p. injection. MR imaging was performed on a 4.7T (Bruker Biospec) scanner. Coronal abdominal 3D T1-weighted FLASH, axial 2D T1-weighted FLASH and coronal abdominal 3D T2-weighted TurboRARE sequences were acquired before and repeatedly after intravenous injection of Fe-PyC3A (0.2 mmol/kg). After imaging, mice were euthanized, and the colon and spleen were collected. Colon weight to length ratio and spleen weight to body weight ratio were used as markers of colitis. For MR image analysis, signal intensity (SI) of the bowel wall was measured pre and post probe injection and the % increase calculated (%SI).

Results and Discussion. Administration of DSS resulted in typical signs of colitis, including weight loss, diarrhea and fecal blood. The development of colitis was also supported by ex vivo pathological analysis where a significantly higher colon weight to length ratio was observed in DSS-injured mice compared to controls (3.2 ± 0.3 and 1.5 ± 0.2, respectively, $P < 0.001$) as well as a significantly higher spleen weight to body weight ratio (5.8 ± 2.4 and 2.5 ± 0.3, respectively, $P = 0.005$). A marked signal enhancement was observed in the DSS-treated group after injection of FePyC3A but not in the control group (Figure 1). In DSS mice, signal enhancement was observed in the distal colon (Fig 1C, yellow arrows) which is the area where inflammation predominantly develops in this mouse model of acute colitis. %SI in the distal colon at 6 minutes post FePyC3A injection was significantly higher in the DSS group compared to the control group (30.0 ± 17.3 and 5.0 ± 2.1, respectively, $P = 0.0017$), thus confirming that Fe-PyC3A can detect intestinal inflammation in vivo.

Conclusion. Our findings indicate that molecular imaging with Fe-PyC3A can report on inflammation in the DSS mouse model of colitis.

References. 1) Le Fur M, et al. Inflamm Bowel Dis. 2020;26(10):1470–1484. 2) Atreya R, Neurath MF. Curr Opin Gastroenterol. 2016;32(4):245–250. 3) Fournier BM, Parkos CA. Mucosal Immunol. 2012;5(4):354–366. 4) Wang H, et al. J Am Chem Soc. 2019;141(14):5916–5925.

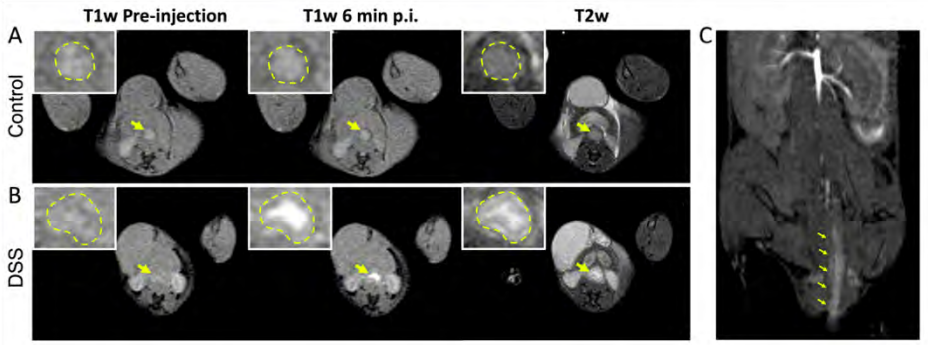

Figure 1: Molecular imaging of intestinal inflammation in the DSS mouse model of inflammatory bowel disease with Fe-PyC3A. Axial T1-weighted MR images of the distal colon of A) a control mouse and B) a DSS-treated mouse prior to and 6 minutes post injection of FePyC3A. Axial T2-weighted images are shown to delineate anatomy. Arrows point to the bowel wall. Marked signal enhancement is observed in the DSS-treated group after injection of FePyC3A but not in the control group. C) Coronal T1-weighted MR image of the corresponding DSS-treated mouse shown in B, 6 minutes post injection of FePyC3A, showing specific enhancement in the distal colon (yellow arrows).

Silvio Aime

A Magnetic Resonance Imaging-Chemical Exchange Saturation Transfer (MRI-CEST) Method for the Detection of Water Cycling across Cellular Membranes

Water flows into or out of the cells, i.e. causing the cells to expand or to shrink, basically as a consequence of the changes in the local osmotic pressure associated to the ongoing metabolic processes. Osmotic water flow follows the formation of gradients of impermeable solutes and accompanies the corresponding homeostasis processes following the solute movements across the transmembrane proteins that act as transporters for any ions/molecules. Water cycling across the membrane transporters is considered a hallmark of cellular metabolism and it could be of high diagnostic relevance in the characterization of tumors and other diseases. Although the extent of the water cycling across cellular affects the readout in MR medical images, its specific contribution is difficult to assess at the magnetic field strengths employed in clinical or animal scanners because the difference in the relaxation rates between the intra- and extra-cellular compartments is of the same order of the water exchange rate across the compartments. Many efforts have been devoted to get more insight into this issue either exploiting the intrinsic difference in the T1 beaviour of intra- and extra-cellular water at low magnetic fields or to artificially generate a difference between the two compartments by adding large amounts of paramagnetic agents in the extracellular space. Whereas the approach works well in the case of homogeneous cell suspensions with GBCA' concentrations in the mM range obvious limitations are encountered in vivo where the GBCA's concentration in the tumor region is in the range of tens of micromoles/L.

The herein reported approach relies on the response of the endogenous, intracellular CEST (Chemical Exchange Saturation Transfer) to the presence of extracellular Gd-based contrast agents (GBCAs). Paramagnetic GBCAs enhance the relaxation rate of water molecules in the extracellular compartment and, through membrane exchange, the relaxation enhancement is transferred to intracellular molecules. The effect is detected at the MRI-CEST signal of intracellular proton exchanging molecules. The magnitude of the change in the CEST response reports on water cycling across the membrane. The induced effect is quite substantial as it may cause the marked decrease (up to about 50%) of the endogenous CEST signal. We show that the voxels corresponding to the "minimum" ST% values, i.e. a condition that is reached at very short times after the GBCA i. v. injection, can be suitably mapped to represent the distribution of tumor cells characterized by high, medium and low permeability. Actually, the voxels' distribution may be conveniently clustered under histograms that yield immediate quantitation of the occurred permeability changes over the entire tumor region. The method has been first tested on Red Blood Cells and Liposome's encapsulating CEST agents. Next it has been applied on orthotopic murine models of breast cancer with different degree of malignancy (4T1, TS/A and 168FARN). The distribution of voxels reporting on membrane permeability fits well with the cells' aggressiveness and acts as an early reporter to monitor therapeutic treatments. The "membrane permeability maps" were compared with the MRI DCE (Dynamic Contrast Enhancement) images reporting on the vascular leakage of the neo-formed vessels. The information brought by the CEST response on the changes in the cell membrane permeability represents a useful contribution to an in-deoth characterizationn of the tumour phenotype. Furthermore we showed that the method could be useful also for an early monitoring of the effects of the undertaken therapeutic treatment. The disappearance of the ST% drop for the Doxorubicin treated mice clearly indicates that the water cycling across the cellular membrane is a highly responsive marker of the metabolic changes induced by Doxorubicin well before than the effect could be visualized by the changes in size and in vascular permeability.

A genetically engineered reporter system designed for ^{2}H-MRI allows quantifiable maps of reporter gene expression *in vivo*

Allouche-Arnon H., Montrazi E. T., Subramani B.[1], Harris T., Frydman L[2]. Bar-Shir A.
Weizmann institute of science, Rehovot, Israel

Introduction: Deuterium metabolic imaging became a powerful tool for spatial mapping metabolic profiles of introduced deuterated probes using ^{2}H-MRI.[1, 2] Inspired by the lack of background, quantifiable readouts, and the frequency encodability of ^{2}H-MRI data,[3] we present here, for the first time the design and implementation of a genetically engineered reporter system for mapping the expression of a reporter gene with ^{2}H-MRI. Specifically, a ^{2}H-labeled thymidine (d_3-thy) was used as a deuterated reporter probe for imaging the expression of human thymidine kinase-1 (hTK1) as the reporter gene *in vivo*.

Methods: Deuterated thymidine (d_3-thy) was synthesized, purified, and characterized (Fig. 1a). Cell-based assays: Thymidine analogs (^{3}H-thy and d_3-thy) were incubated with HEK cells expressing the hTK1 transgene or non-transfected cells (N.T.), and the intracellular content of the exogenously added thymidine was analyzed by beta-counter (^{3}H-thy), LC-MS (d_3-thy), and ^{2}H-NMR (d_3-thy). *In vivo* ^{2}H-MRI (15.2T): HEK$^{N.T}$ or HEK^{hTK1} cells were intracranially injected into the brain of immunodeficient mice. Three weeks later, mice were examined with ^{2}H-MRI following intravenous injection of d_3-thy (150 mg/kg body weight). A spectroscopic steady-state free precession (ssFP) sequence (33-points FIDs, 32×32 matrix, 7 min signal average) was used for ^{2}H-MRI, and a localized spectroscopy approach was used to collect ^{2}H-NMR data from 2mm^3 isotropic voxel.

Results/ discussion: The cellular accumulation of thymidine following its phosphorylation in cells expressing the hTK1 reporter gene was examined *in vitro* (Fig. 1b). Both the radioactive analog, ^{3}H-thy, and the deuterated one (d_3-thy) showed high accumulation in cells expressing hTK1, compared to non-transfected cells (Fig. 1c). Phantom experiments were performed to reveal that d_3-thy is detectable at sub mM concentration at ^{2}H-MRI maps when using spectroscopic ssFP (Fig. 2a). Then, d_3-thy was administrated intravenously to mice bearing HEK$^{N.T}$ or HEK^{hTK1} tumors and the accumulation of the introduced deuterated probe was clearly detected in ^{2}H-MRI maps and only in tumor cells expressing the hTK1 transgene (HEK^{hTK1}, Fig. 2b-c). *In vivo*, localized ^{2}H-NMR spectroscopy (Fig. 2e) confirmed (a peak at 1.7 ppm) the accumulation of d_3-thy in the HEK^{hTK1} tumor. Quantitative analysis of the ^{2}H-MRI signal of administrated d_3-thy (N=4) depicts a concentration of 0.4 mM of d_3-thy in the HEK^{hTK1} tumor (Fig. 2f).

Conclusion: Here, we demonstrated, for the first time, the ability to quantitatively map, with no background, a reporter gene expression with ^{2}H-MRI. Our approach capitalizes on the accumulation of deuterated reporter probe, i.e., d_3-thy, introduced systemically, solely in cells expressing high levels of the reporter gene hTK1, to provide an increased and specific (1.7 ppm) ^{2}H-MRI signal of genetically engineered tumor cells. We introduced the d_3-thy as a novel molecular tracer, demonstrating the ability to use ^{2}H-MRI in a scenario beyond metabolic imaging, and enriches the MRI toolbox used nowadays for mapping reporter gene expression.

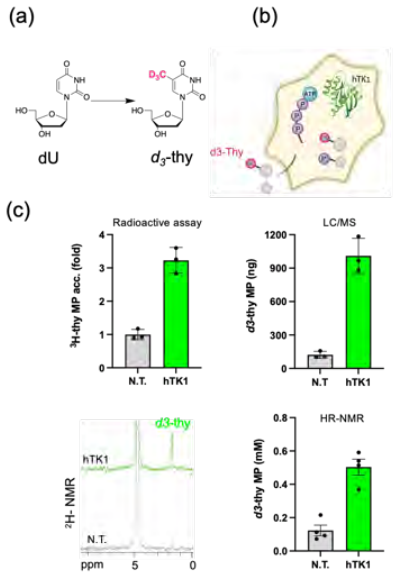

Figure 1. Cellular accumulation of thymidine in cells expressing hTK1. (a) Chemical synthesis of *d*3-thy. (b) Schematic illustration of d_3-thy cellular accumulation upon its phosphorylation by hTK1 enzyme. (c) Analysis of the intracellular content of cells (hTK1 or non-transfected, N.T). Radioactive assay (for ^{3}H-thy accumulation determination), LC/MS (for d_3-thy monophosphate, d_3-thy-MP, accumulation determination), and ^{2}H-

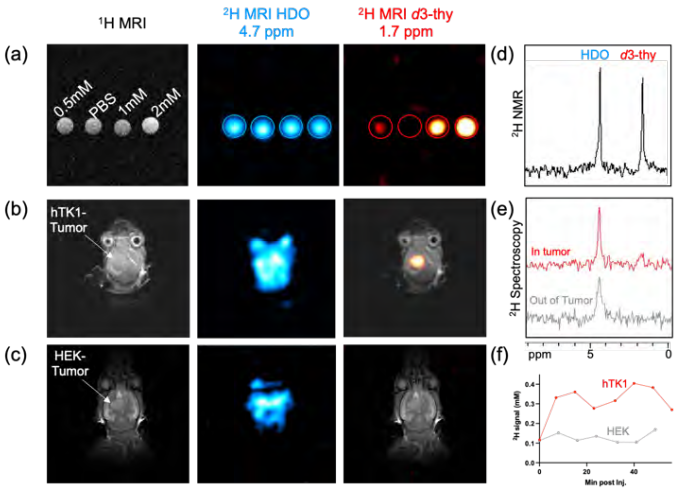

Figure 2. *In vitro* and *In vivo* imaging of d_3-thy. (a) ^{1}H-MRI and ^{2}H-MRI maps at ω=4.7 and ω=1.7 ppm of PBS and *d*3-thy solutions (0.5, 1, and 2 mM). ^{1}H MRI anatomical images (left) of an immunodeficient mouse, inoculated with HEK^{hTK1} (b) and HEK$^{N.T.}$ (c) tumors. ^{2}H-MRI maps of HDO at ω=4.7 ppm of mice brain (center), and ^{2}H-MRI maps (at ω=1.7 ppm overlaid on ^{1}H-MRI) 40 min following intravenous injection of d_3-thy (right). (d) ^{2}H-NMR spectrum of 2mM *d3*-thy solution. (e) Localized ^{2}H-MR spectrum inside (red) and outside (grey) of the hTK1 expressing tumor region. (f) Longitudinal analysis and quantification of *d*3-thy signal depicted from HEK ^{hTK1} (red) and HEK$^{N.T.}$ (grey) tumors.

References: **1**. Lu, M.; Zhu, X. H.; Zhang, Y.; Mateescu, G.; Chen, W., Quantitative assessment of brain glucose metabolic rates using in vivo deuterium magnetic resonance spectroscopy. *J Cereb Blood Flow Metab* **2017**. **2**. De Feyter, H. M.; Behar, K. L.; Corbin, Z. A.; Fulbright, R. K.; Brown, P. B.; McIntyre, S.; Nixon, T. W.; Rothman, D. L.; de Graaf, R. A., Deuterium metabolic imaging (DMI) for MRI-based 3D mapping of metabolism in vivo. *Science Advances* **2018. 3**. Montrazi, E. T.; Sasson, K.; Agemy, L.; Peters, D. C.; Brenner, O.; Scherz, A.; Frydman, L., High-sensitivity deuterium metabolic MRI differentiates acute pancreatitis from pancreatic cancers in murine models. *Sci Rep* **2023.**

Treatment response classification using oxygen enhanced (OE-), dynamic contrast enhancement (DCE-) MRI and [^{18}F]FAZA PET prediction

Marta Vuozzo[1,2], Max Zimmermann[1], Manfred Kneilling[1,2,3], Gerald Reischl[1,2],Birgit Fehrenbacher[3], Bernd J. Pichler[1,2] and Andreas M. Schmid[1,2]

[1]Werner Siemens Imaging Center, Department of Preclinical Imaging and Radiopharmacy, Eberhard Karls University Tübingen, Tübingen 72076, Germany [2]Cluster of Excellence iFIT (EXC 2180) "Image-Guided and Functionally Instructed Tumor Therapies", University of Tübingen, Tübingen 72076, Germany [3]Department of Dermatology, Eberhard Karls University Tübingen, Tübingen, Germany

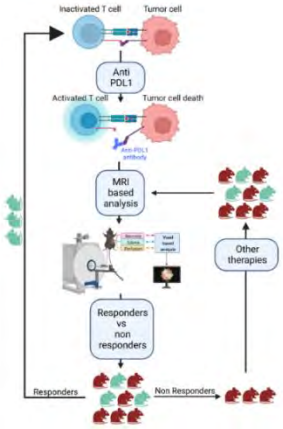

Figure 1 Graphical abstract

Introduction: Hypoxia is a common feature of malignant tumors and a potential prognostic biomarker for therapy-response. As a heterogeneous intratumoral landscape is often associated with therapy resistance and reduced efficacy[1], its precise non-invasive characterization may play a critical role for personalized medicine as well as in understanding the mechanisms of pathogenesis. Previous reports show a direct correlation between oxygen sensitive MRI and hypoxia PET rat models of prostate tumors[2]. **Methods:** We use multiparametric MRI including T1 and T2* mapping, DCE-MRI, and dynamic oxygen-level dependent contrast to characterize tumor tissue. Furthermore, the expression of inhibitory immune checkpoints (ICP, e.g. PD-L1) by tumor cells and immune cells inhibit tumor antigen (TA)-specific T-cells. Consequently, ICP-blockade is applicable to restore TA-specific T-cell functions. The aim of our study is to establish an efficient MR protocol and a complementary data analysis during an ICP inhibitor-based immunotherapy in a colon cancer mouse model and to monitor the therapy response using voxel-based computational approaches. C57BL/6 mice were subcutaneously injected with 5x10^5 MC38 tumor cells. 200 µg of antiPD-L1 (clone: 10F.9G2) were intraperitoneally injected 3 times a week for 2 weeks. 11 ± 1 MBq of [^{18}F]FAZA were i.v. injected and a 10 min static scan performed after 2 hours of awake uptake. After T2-weighted (T2W) anatomical images, a blood oxygen level dependent (BOLD) and tissue oxygen level dependent (TOLD) MRI while applying a 100% oxygen gas breathing challenge, followed by a Gd-based DCE assessment of perfusion were performed. T1 and T2* maps, and an alternation of T1w and T2*w images were acquired pre, post, and during the challenge to generate contrast dynamics multiparametric maps. PET images were aligned and up-sampled to the voxel-size of the MRI images. Supervised and unsupervised clustering methods were applied using Matlab. Gaussian-mixture models (GMM) cluster maps, PET, and predicted PET maps were compared with immunofluorescence staining (CA-IX, Collagen IV, HIF1a). **Results and Discussion:** Tumor size was measured over time and varied strongly between responders (14.5 ± 23.3 mm^3) and non-responders (548.2 ± 217.8 mm^3) at the endpoint of the study. The applicability of GMM clustering to the heterogeneous pool of parameters obtained from all generated maps was tested using the voxels of all tumors. When applying a Neural Network (NN) for clustering, good separations of voxels were observed compared to the manually assigned responders vs non-responders. The predicted maps of the PET data show a very good correlation with the original PET data and confirmed by immunofluorescence staining. Within this project, a novel analysis pipeline was established to assess, voxel-based, the intratumoral heterogeneity using MRI and validated with PET and immunofluorescence data. Furthermore, we plan its clinical translation by applying a similar protocol to humans. **Conclusion:** To the best of our knowledge, this study is the first to use the synergistic value of multiple MRI parameters to correlate and predict PET determining the intratumoral heterogeneity in preclinical models.

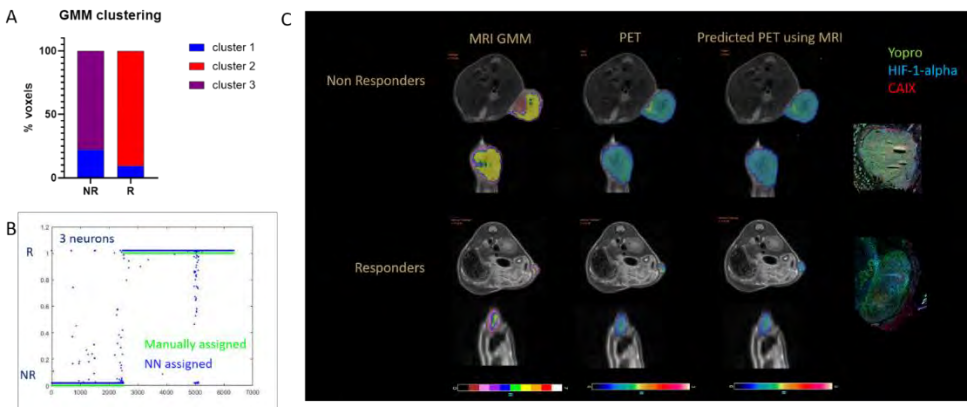

Figure 2. Supervised and unsupervised voxel-based analysis and PET and MRI images comparison with immunofluorescence. A) Using the voxels from all the tumors, we tested the applicability of Gaussian Mixture Models (GMM) clustering to the heterogeneous pool of parameters obtained from all generated maps. We obtained a good separation between responders vs non-responders voxels. B) When applying a Neural Network (NN) for clustering it was observed a really good separations of voxel compared to the manually assigned responders vs non-responders. C) The prediction PET maps show a really promising correlation with the original PET data and immunofluorescence staining.

REFERENCES: [1] Junttila, M. R. & de Sauvage, F. J. Influence of tumour micro-environment heterogeneity on therapeutic response. Nature 501, 346–354 (2013). [2] Zhou H, Chiguru S, Hallac RR, Yang D, Hao G, Peschke P, Mason RP. Examining correlations of oxygen sensitive MRI (BOLD/TOLD) with [18F]FMISO PET in rat prostate tumors. Am J Nucl Med Mol Imaging. 2019 Apr 15;9(2):156-167. PMID: 31139498; PMCID: PMC6526364

Metabolic Activity Diffusion Imaging [MADI]:

Non-Invasive, High-Resolution Mapping of Sodium Pump Flux and Cell Metrics *In Vivo*

Charles S. Springer, Jr.,[a] Martin M. Pike,[a] Xin Li[a]

[a]Advanced Imaging Research Center, Oregon Health & Science University

MADI employs water diffusion-encoding of the strong tissue ^1H_2O NMR signal.[1-3] It describes the diffusion-weighted transverse ^1H_2O decay in terms of fundamental tissue properties: **a)** the voxel cell [number] density **ρ** (10^5 cells/μL(tissue)), **b)** the voxel-mean cell volume **V** (pL/cell), and **c)** the voxel-mean *homeostatic* cellular water efflux *rate constant* $\mathbf{k_{io}}$ (s^{-1}). The $k_{io}V$ product (the cellular, homeostatic active trans-membrane water cycling [AWC] metabolic *rate*, $^cMR_{AWC}$ (pL(H_2O)cycled/s/cell), is particularly interesting: it is proportional to the ubiquitous cell membrane Na^+,K^+-ATPase (NKA; "Sodium Pump") homeostatic flux, $^cMR_{NKA}$. NKA may be biology's most crucial enzyme, and MR_{NKA} has not before been measurable *in vivo*.

Brain ρ, V, k_{io}, and $k_{io}V$ parametric maps are very informative.[2] In the healthy human brain, the $k_{io}V$ map correlates well, qualitatively (**Fig. 1**) and quantitatively (**Fig. 2**), with the tissue glucose consumption metabolic rate ($^tMR_{glc}$) map, determined by invasive ^{18}FDG-PET. In comparison, MADI requires no cyclotron, hot lab, or pharmacodynamic modeling (there is no injection), and has ^1H_2O MRI resolution. The nominal Fig. 1 voxel in-plane dimensions/volumes are: **1a** $(2.5\ mm)^2/16$ μL, **1b** $(1.6\ mm)^2/8.2$ μL.

Fig. 1. $^tMR_{glc}$ from ^{18}FDG-PET | $^cMR_{AWC}$ from MADI

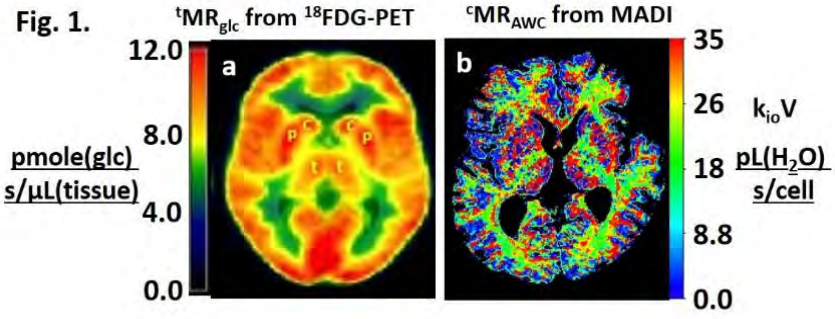

The neural cell ATP concentration, $[ATP_i]$, is homeostatic: it arises from a balance between ATP production ($^cMR_{ATP}$), mainly by glucose metabolism, and ATP consumption, mainly by $^cMR_{NKA}$. The $^cMR_{NKA}$ flux is sensitive to many factors, but highly important is $[ATP_i]$, which (in turn) makes $^cMR_{NKA}$ sensitive to $^cMR_{ATP}$. But glucose ATP production can be varied: when it is oxidative, $^cMR_{ATP}/MR_{glc}$ is larger; when is it glycolytic, $^cMR_{ATP}/MR_{glc}$ is smaller. In Fig. 2, the $^cMR_{AWC}/^tMR_{glc}$ ratios are consistent with cortical and internal GM (*thalamus*, *putamen*, *caudate*) metabolism being more glycolytic, while WM metabolism is more oxidative. With poorer resolution, this has long been suggested by human brain ^{31}PMRSI and ^{23}NaMRSI.

Fig. 2. $^cMR_{AWC}/^tMR_{glc}$

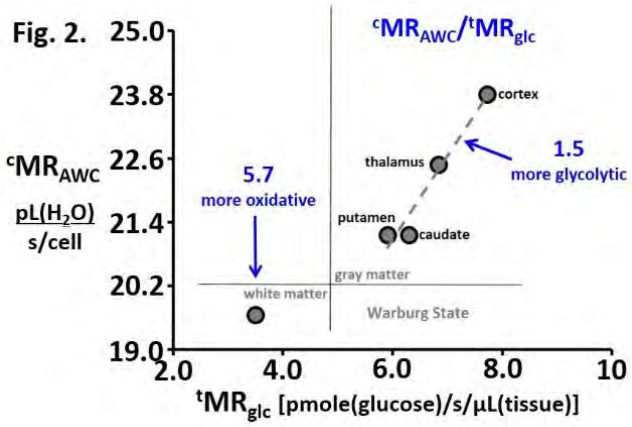

Within brain glioblastoma (and other malignant tumors), however, the $^cMR_{ATP}/MR_{glc}$ ratio can become very small: while $^tMR_{glu}$ actually increases, we find $k_{io}V$ ($^cMR_{AWC}$) decreases substantially.[4] In the cancer cell, the Warburg state represents a metabolic switch significantly diverting mitochondria from ATP production. The Warburg switch is invisible to ^{18}FDG-PET since it occurs after the latter's rate-limiting step (glucose phosphorylation). Furthermore, PET and MRSI approaches generally lack intra-tumor resolution capability. MADI, however, resolves Warburg state regions from other tumor regions.[4]

In summary, MADI ties together years of ^{13}C, ^{23}Na, and ^{31}P *in vivo* spectroscopy, with significantly greater spatial resolution. Furthermore, it may be capable of brain function measurements.[5]

References:

1. Springer, Baker, Li, Moloney, Wilson, Pike, Barbara, Rooney, Maki, "Metabolic activity diffusion imaging (MADI): I. Metabolic, cytometric modeling and simulations." *NMR Biomed*. **36:** e4781 (2023).

2. Springer, Baker, Li, Moloney, Pike, Wilson, Anderson, Sammi, Garzotto, Kopp, Coakley, Rooney, Maki, "Metabolic activity diffusion imaging (MADI): II. Noninvasive, high-resolution human brain mapping of sodium pump flux and cell metrics." *NMR Biomed*. **36:** e4782 (2023).

3. Neil, Ackerman, "Metabolic activity diffusion imaging (MADI): A new paradigm." *NMR Biomed.* **36:** e4841 (2023).

4. Schlegel, Baker, Holland, Stoller, Packwood, Li, Barajas, Springer, Pike, "Metabolic Activity Diffusion Imaging [MADI] of Rat Brain Glioma," *Proc. Int. Soc. Magn. Reson. Med.* **31,** 3924 (2023).

5. Pike, Li, Baetscher, Barbara, Sammi, Stevens, Springer, "Does MADI Detect Temporal Brain Metabolic Activity Changes?," *Proc. Int. Soc. Magn. Reson. Med.* **31,** 5177 (2023).

Exploring the efficacy of paramagnetic chelates embedded in nanogels as MRI probes

Marco Ricci[1], Fabio Carniato[1], Lorenzo Tei[1], Francesca Garello[2], Enzo Terreno[2], Giacomo Parigi[3], Enrico Ravera[3], Claudio Luchinat[3], Mauro Botta[1]

[1]*Department of Science and Technological Innovation, University of Piemonte Orientale, Alessandria, Italy;*
[2]*Molecular Imaging Centre, Department of Molecular Biotechnology and Health Sciences, University of Turin, Italy;*
[3]*Magnetic Resonance Center (CERM) and Department of Chemistry "Ugo Schiff", University of Florence, Italy.*

Introduction: In recent years, nanogels (NGs) have garnered increasing interest among the wide array of nanoparticles. These soft and hydrophilic nanoparticles boast a 3D crosslinked network capable of retaining a large volume of water, thereby mimicking biological fluids[1]. NGs can be loaded with paramagnetic metal complexes, which are likely to exhibit a notable increase in relaxivity (r_1).[2] However, despite their appealing properties, little is known about the relaxometric properties and in vivo behavior of paramagnetic NGs. We have explored the properties of nanogels (NGs) using multinuclear and multifrequency NMR relaxometric techniques. Specifically, we investigated: a) NGs incorporating Gd^{3+} complexes with varying coordination geometries and hydration states (q = 2, 1, 0);[3,4] b) stabilized NGs where Mn^{2+}/Gd^{3+}/Dy^{3+} chelates serve as both contrast agents and cross-linking agents[5].

Methods: Two types of nanogels (NGs) were synthesized and examined in this study: **A**) NGs formed through the non-covalent aggregation of biocompatible polymers such as chitosan, hyaluronate, and tripolyphosphate. These NGs encapsulated four complexes via ionotropic gelation: $[GdDOTA]^-$ (q = 1), $[GdAAZTA]^-$ (q = 2), GdTACN-Pic_3 (q = 0), and $[GdDOTP]^{5-}$ (q = 0). Additionally, NGs containing $[GdDOTP]^{5-}$ were PEGylated for an in vivo study conducted on healthy BALB/c mice at 1 T. **B**) NGs synthesized by covalently crosslinking chitosan with chelating agents capable of coordinating paramagnetic metal ions. Specifically, NGs were stabilized using a bisamide derivative of Mn-t-CDTA and bifunctional Gd- and Dy-1,7-$DOTAGA_2$ chelates. The biocompatibility of Mn-NGs was evaluated using the macrophage cell line RAW 264.7. Subsequently, Mn-NGs were tested in mice with subcutaneous breast cancer tumors (1 T; Aspect M2 MRI System). The relaxivity was measured as a function of temperature and B_0, and the data were fully analysed using a model that considers the effects of a static zero-field splitting and the occurrence of localized fast local motions associated with the slow tumbling of the NGs. The characterization of the complexes was completed through the measurement of ^{1}H NMRD profiles (0.01 – 120 MHz) and ^{17}O NMR data (11.7 T).

Results and Discussion: Type-**A** NGs: At clinical magnetic fields (1.5–3.0 T), these NGs demonstrated superior r_1 values compared to clinically available contrast agents (CAs). This enhanced r_1 stemmed from a notable constraint on the rotational mobility of the confined chelates. Particularly noteworthy, NGs based on $[GdDOTP]^{5-}$ exhibited a substantial increase in r_1 (ca 80 mM^{-1} s^{-1} at 298 K and 0.5 T), attributed to a significant contribution from the second sphere water network. Despite their excellent relaxometric properties, ionic nanogels encounter challenges related to chemical stability in biological environments, as studies have revealed their tendency to degrade and rapidly release paramagnetic complexes when dispersed in biological fluids. Type-**B** NGs: these novel NGs show: i) r_1 values seven times higher than that of clinical CAs at 1.5 T; ii) high stability over time under physiological conditions, thus excluding metal leaking or particles aggregation; iii) good extravasation and accumulation, with a maximum contrast achieved at 24 h post-injection in mice bearing subcutaneous breast cancer tumor; iv) high T_1 contrast (1 T) in the tumor 24 h post-injection. We consider these findings to offer valuable insights for the development of highly efficient MRI probes utilizing matrices that exhibit proven biocompatibility and stability in biological fluids.

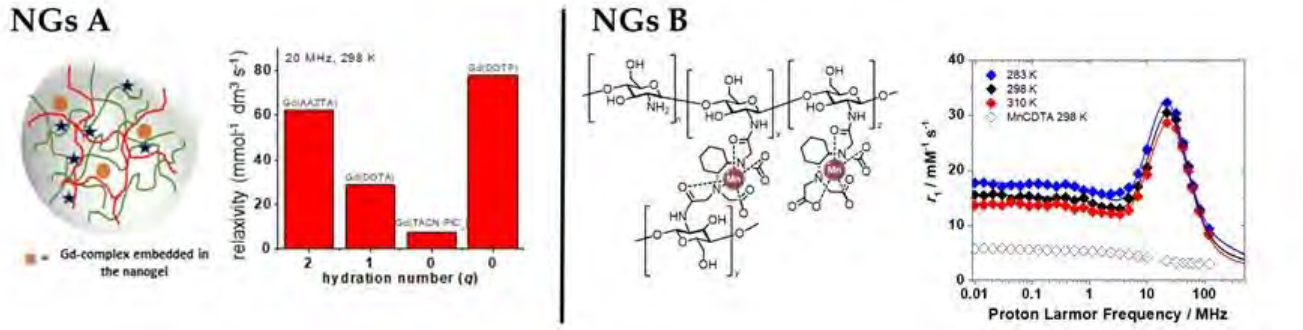

Figure 1: *(left) Schematic representation of Type-**A** NGs incorporating Gd-chelates; (right) ^{1}H NMRD profiles of Type-**B** NGs cross-linked with Mn-complexes.*

References: **1**. Wang, H *et al. J. Mater. Chem. B* 5, 6986-7007 (2017); **2**. Courant, T. *et al. Angew. Chem., Int. Ed*. 51, 9119-9122 (2012); **3**. Carniato, F. *et al. ACS Appl. Bio. Mater. 3*, 9065-9072 (2020); **4**. Carniato, F. *et al. Inorg. Chem. 61*, 5380-5387 (2022); **5**. Carniato, F. *et al. Small 19*, 2302868-2302882 (2023).

Complexes of Eu^{II} as contrast agents for MRI

S. A. Amali S. Subasinghe,[a] Md Mamunur Rashid,[a] Md. Abul Hassan Samee,[b] Jason T. Yustein,[c] Robia G. Pautler,[b] and Matthew J. Allen[a]

[a] *Department of Chemistry, Wayne State University, Detroit, MI, United States of America*
[b] *Aflac Cancer and Blood Disorders Center, Children's Healthcare of Atlanta, Emory University School of Medicine, Adlanta, GA, United States of America*
[c] *Department of Integrative Physiology, Baylor College of Medicine, Houston, TX 77030*

Introduction: This study explores the properties of europium-based contrast agents relevant to their use as responsive probes to image hypoxia. There is a need to study both the *in vitro* and *in vivo* properties of europium-based agents in assessing the viability of these molecules to serve as contrast agents.

Methods: Ligands and metal complexes were prepared using standard chemical synthetic techniques. Air-sensitive manipulations were performed in a wet glovebox under an atmosphere of nitrogen gas. Samples were sealed using paraffin wax prior to removal from the glovebox. Concentrations of europium were measured using inductively coupled plasma mass spectrometry or energy-dispersive X-ray fluorescence spectroscopy. Cyclic voltammetry was performed using a glassy carbon working electrode, platinum wire auxiliary electrode and Ag/AgCl reference electrode. All animal studies were done in accordance with protocols preapproved by the Institutional Animal Care and Use Committee of Baylor College of Medicine. T_1-weighted and ^{19}F-MRI scans were performed with a Bruker BioSpec 9.4 T horizontal bore MRI scanner.

Results and Discussion: We have studied the physicochemical properties of several europium-containing complexes and performed imaging experiments *in vivo*. We have demonstrated that Eu-containing complexes can be made ratiometric,[1] and further, we show that the probes can be made to persist in oxygenated solutions (including *in vivo*).[2] Ratiometric probes were prepared using fluorinated ligands, in which contrast is enhanced in ^{1}H-MRI when Eu is in the divalent oxidation state and ^{19}F-MRI signal is detected when Eu is in the trivalent oxidation state. Persistence in oxygenated solution was achieved using phosphonate-containing ligands to hinder the approach of oxygen to Eu as a function of pH.

Conclusion: The results demonstrate that europium-based contrast agents are a promising set of molecules for imaging hypoxic regions of tumors. Future research is being focused on extending the persistence time of the probes *in vivo* to enable delivery to sites of interest and application of the probes to study cancer and immunotherapy.

References:

1. Subasinghe, S. A. A. S.; Ortiz, C. J.; Romero, J.; Ward, C. L.; Sertage, A. G.; Kurenbekova, L.; Yustein, J. T.; Pautler, R. G.; Allen, M. J. Toward quantification of hypoxia using fluorinated Eu(II/III)-containing ratiometric probes. *Proc. Natl. Acad. Sci. U.S.A.* **2023**, *120*, e2220891120.
2. Rashid, M. M.; Corbin, B. A.; Jella, P.; Ortiz, C. J.; Samee, M. A. H.; Pautler, R. G.; Allen, M. J. Systemic delivery of divalent europium from ligand screening with implications to direct imaging of hypoxia. *J. Am. Chem. Soc.* **2022**, *144*, 23053–23060.

Probing Cholinergic Brain Function Using Multimodal Molecular Imaging

Sajal Sen, Miranda Dawson, Gregory Thiabaud, Sayani Das, Alan Jasanoff
Department of Biological Engineering, MIT

Introduction: Acetylcholine plays critical roles as a neurochemical signaling molecule in the brain and periphery.[1] Developing molecular imaging strategies to monitor cholinergic function in living tissue is of outstanding interest in both basic and applied neuroscience. A tractable approach for assessing cholinergic function is to measure activity of cholinesterase enzymes (ChEs), which lyse choline esters at synapses and serve as important biomarkers in neurodegenerative diseases.[2–6] Here we present the design and validation of a new family of contrast agents for investigating cholinesterase enzyme activity *in vivo*. Importantly, these ChE-responsive Texaphyrin (**ChERT**) probes provide strong contrast in magnetic resonance imaging (MRI), photoacoustic imaging, and fluorescence microscopy, thus offering a means for comparing measurements across a range of spatial and temporal scales.[7] **ChERT** compounds undergo hydrophilic-to-hydrophobic transition and charge reversal upon hydrolysis in the presence of ChEs. This changes their contrast properties and promotes transient accumulation at sites of ChE-catalyzed turnover, thereby permitting amplified detection and measurement of ChE activity at cholinergic synapses via a "solubility switch" mechanism (Fig 1A). [8]

Results and Discussion: The candidate sensor molecule (**ChERT**) and analogous non-hydrolyzable compound (**Control**) were synthesized, characterized, and selected from a library of compounds for future studies (Fig 1B). Next, the cholinesterase sensitivity of these contrast agents was tested *in vitro*, using acetylcholinesterase and its close analog enzyme butyrylcholinesterase. Monitoring HPLC retention time and DLS data confirm a change in solubility profile upon hydrolysis of **ChERT**, but not **Control**, in the presence of ChEs (Fig 1C). *In vitro* studies demonstrated a change in MRI relaxivity, photoacoustic, and fluorescence signal intensity due to this enzymatic reaction (Fig 1D). Interestingly, in the presence of a ChE inhibitor tacrine or for **Control**, no such change was observed. Once validated by *in vitro* experiments, **ChERT** was administered using intracerebroventricular injections. This resulted in achieving a wide-field distribution of the contrast agent in rodent brains which was further confirmed by MRI and photoacoustic imaging (Fig 1E). A longitudinal study with MRI indicated that there is a time-dependent increase in T_1-weighted MRI signal for rats treated with **ChERT** in ChE enzyme enriched region, such as dorsal thalamus, in the brain (Fig 1F). In comparison, rats co-injected with **ChERT** and tacrine exhibited significantly lower change under analogous condition. These results provide initial indication that ester cleavage affects the pharmacokinetics of **ChERT**, which can be inhibited by tacrine, providing a means for assessing cholinergic activity *in vivo* using longitudinal MRI measurements. In concert, **ChERT** should thus provide a means for preclinical assessment of phenotypes and treatments that interact with ChE, in the long term possibly including cholinergic activity monitoring and ChE-related disease diagnosis in humans.

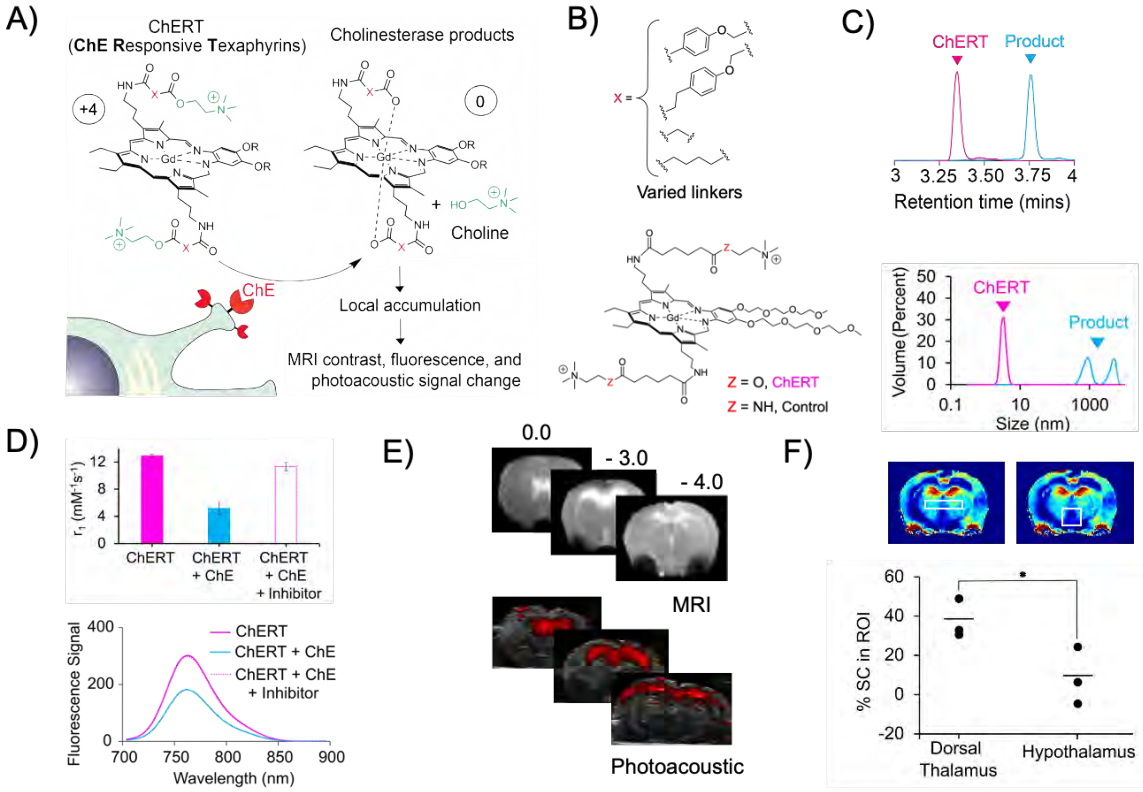

References: 1) Picciotto, M. R. *et* al. *Neuron*. October 4, 2012, pp 116–129. 2) Soreq, H. *et* al. *Nat Rev Neurosci* **2001**, *2* (4), 294–302. 3) Darvesh, S. *et* al. *Nat Rev Neurosci* **2003**, *4* (2), 131–138. 4) Chatonnet, A. *et* al. *Biochemical Journal* **1989**, *260* (3), 625–634. 5) Greig, N. H. *et* al. *Proceedings of the National Academy of Sciences* **2005**, *102* (47), 17213–17218. 6) Dong, M. X. *et* al. *Biomed Res Int* **2017**, *2017*. 7) Sessler, J. L. *et* al. *J Am Chem Soc* **1993**, *115* (22), 10368–10369. 8) Westmeyer, G. G. *et* al. *Chem Biol* **2014**, *21* (3), 422–429.

Deciphering the Efficacy of Iron(III) Complexes as MRI Contrast Agents

Rocío Uzal-Varela[1], Fátima Lucio-Martínez[1], Mauro Botta[2], David Esteban-Gómez[1], Carlos Platas-Iglesias[1], Aurora Rodríguez-Rodríguez[1]

[1]*Centro Interdisciplinar de Química e Bioloxía (CICA) and Departamento de Química, Facultade de Ciencias, Universidade da Coruña, A Coruña 15071, Galicia, Spain;* [2]*Dipartimento di Scienze e Innovazione Tecnologica, Università del Piemonte Orientale, Viale T. Michel 11, 15121 Alessandria, Italy.*

Introduction: The pivotal role of gadolinium-based contrast agents (GBCAs) in enhancing magnetic resonance imaging (MRI) has been undisputed since their clinical approval in the late 1980s. However, the emergent concerns regarding free gadolinium's toxicity have led the exploration of alternative contrast agents.[1] Transition metal complexes, and more specifically, the ones derived from the endogeneous cation Iron(III), are shown to be a promising alternative to GBCAs, underscoring the importance of developing non-toxic, efficient molecular MRI contrast agents.

Methods: We delved into the design, synthesis, structural and physico-chemical characterization of a series of Iron(III) complexes to reach a better understanding of the mechanisms that govern the water proton relaxation enhancement in the presence of the paramagnetic ion.

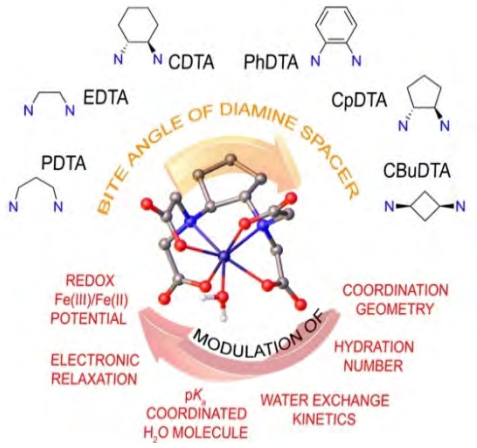

Figure 1*. Summary of structural and dynamic parameters that affect the efficiency of Fe(III) complexes as MRI contrast agents.*

Results and Discussion: The modulation of the steric hindrance around the water molecule directly bound to the metallic center, as well as the bite angle of the donor atoms, regulates the ^{1}H relaxivities of the Fe(III) family of complexes (*Figure 1*). These changes affect the number of coordinated water molecules and their exchange rates. Cyclic voltammetry experiments in aqueous solution allow us to estimate the redox potential for the Fe(III)/Fe(II) pair. This value should be shifted out of the biological window to avoid complex dissociation upon reduction. The redox stability in the presence of ascorbic acid (a possible reducing agent present in human blood plasma) provides a hint about the ability of the Fe(III) complexes to trigger Fenton reactions. Modulating the pK_a values characterizing the hydrolysis of the coordinated water molecule is key to avoiding hydrolisis and the formation of hydroxo- and oxo-complexes at high pH values, as well as transchelation by transferrins.

Conclusion: Fe(III) complexes have great potential as MRI contrast agents. However, to achieve high stability and provide high enhancement, they need to overcome several challenges, such as: (1) to improve their redox stability to prevent their *in vivo* reduction to Fe(II) analogues; (2) to coordinate water molecules to the Fe(III) ion to attain relaxivities similar to those of the conventional Gd(III) MRI contrast agents used in clinical settings; (3) to ensure the thermodynamic stability and kinetic inertness of the complex, so that they do not decompose or react before being eliminated from the body. But, these Fe(III) probes have an advantage as high-field MRI contrast agents, as their Nuclear Magnetic Relaxation Dispersion (NMRD) profiles exhibit a maximum around 7 T, where the inner-sphere relaxivity depends on both rotation and electronic relaxation.[2]

References: **1.** Mariane Le Fur, Peter Caravan, *The biological fate of gadolinium-based MRI contrast agents: a call to action for bioinorganic chemists*, Metallomics, Volume 11, Issue 2, February 2019, Pages 240–254, https://doi.org/10.1039/c8mt00302e. **2.** Zsolt Baranyai, Fabio Carniato, Alessandro Nucera, Dávid Horváth, Lorenzo Tei, Carlos Platas-Iglesias, Mauro Botta, *Defining the conditions for the development of the emerging class of Fe^{III}-based MRI contrast agents*, Chemical Science, Volume 12, Issue 33, 2021, Pages 11138-11145, https://doi.org/10.1039/D1SC02200H

Manganese-enhanced MRI (MEMRI) and its expansion using nanoparticles

Ichio Aoki[1]

[1]National Institutes for Quantum Science and Technology (QST), Japan

MRI contrast agents in clinical practice have long been dominated by compounds based on Gadolinium (Gd). Gd^{3+} has seven unpaired electrons, a high positive capability in T1-weighted imaging, high stability, and nonionic properties. Although iron oxide nanoparticles and Mn-DPDP have been temporarily used in the clinical field, Gd complexes have become virtually fixed.

When designing MRI contrast agents with a higher tissue accumulation capability or multifunctional theranostic properties, prolonged retention in the bloodstream provides a higher concentration in the targeted tissue, higher sensitivity, and higher therapeutic efficacy than short excretion. For example, antibody-drug-conjugates (ADC) have a long half-life of several days to several weeks in the blood because they can utilize the recycling mechanism *via* the neonatal Fc receptor (FcRn), which is involved in inhibiting IgG degradation *in vivo*[1]. In addition, when contrast agents are polymerized/nanoparticulated to add functionality, many are excreted into the gastrointestinal tract *via* the liver bile rather than kidneys. In these polymeric contrast agents, their blood retention is prolonged by adding a "stealth effect" to the contrast agent that avoids capture by the liver.

In the design of contrast agents with long blood retention for preclinical studies[2], there have been no problems associated with Gd. However, certain risks associated with the clinical application of Gd exists. Nephrogenic systemic fibrosis (NSF), including fatal cases, has been reported in patients with renal dysfunction, and the risk of prolonged Gd excretion is high. A prerequisite for using a Gd-chelate is that it should be excreted from the body in a short time. In other words, it is difficult to propose a clinically oriented development plan for a "contrast agent with long blood retention" using Gd.

In addition, concerns have been raised regarding the environmental effects of Gd. The Gd contrast agent used in MRI scans is quickly released into drains within a few hours, often into rivers and oceans. Japan has the most MRI machines per population in the world. In Japan, 1.27 million contrast exams are performed annually (Medical Facilities, Static and Dynamic Survey in Japan 2018), and 4.5 tons of Gd is released annually into rivers through sewage (estimated dose per adult male at 3870 mg). A San Francisco Bay soil survey in 2016 reported a more than seven-fold increase in gadolinium concentrations from 23.2 pmol/kg in 1993 to 171.4 pmol/kg in 2013[3]. Furthermore, the Tama River in Tokyo has a concentration of 140 pmol/kg [Gd][4] and the Havel River in Germany has a concentration of approximately 500 pmol/kg [Gd][5]. Gd emissions in amounts that are not permitted to be excreted in the laboratory are tacitly approved for patient benefit in medicine because no alternative methods exist.

Manganese (Mn) has properties similar to those of Gd in terms of relaxivity. Manganese is a bioessential element and is found in many foods, with a median intake of 1.6–2.3 mg/day and an absorption rate of 5–10%, and homeostasis is maintained unless excessive intake is continued. Although it is difficult for Mn to exceed Gd in relaxivity because of its five unpaired electrons, several Mn contrast agents with equivalent performance have been developed by designing chelates[6]. It is expected that Mn will be utilized as a "long half-life" metal complex contrast agent with higher safety and functionality in the future.

Experimentally, the use of Mn^{2+} as a Ca^{2+} analog, has been active since around 2000 under the term MEMRI[7], and has been utilized as a neural depolarization marker[8], a neuroaxonal tracer [9], or a method of "staining" neural microstructures[10] *in vivo*. Although the use of Mn as an ion produces some toxicity or physiological alterations depending on its dosage, it is an important contrast agent for basic biological studies that reflects cellular function. In this presentation, I will focus on Mn contrast agents and their properties, including (1) Mn for neuroscience research (MEMRI), (2) Mn as a reactive contrast agent[11], and (3) theranostic Mn contrast agents, which are both reactive and therapeutic[12].

REFERENCES:

[1] D. C. Roopenian and S. Akilesh, *Nat Rev Immunol* **2007**, *7*, 715-725. [2] K. M. Bennett, et al., *Adv Drug Deliv Rev* **2014**, *74*, 75-94. [3] V. Hatje, et al., *Environ Sci Technol* **2016**, *50*, 4159-4168. [4] A. Yaida, et al., *BUNSEKI KAGAKU* **2020**, *69*, 341-350. [5] S. Kulaksız and M. Bau, *Applied Geochemistry* **2011**, *26*, 1877-1885. [6] C. T. Farrar, et al., *Radiology* **2018**, *287*, 581-589. [7] A. C. Silva, et al., *NMR Biomed* **2004**, *17*, 532-543; G. Saar and A. P. Koretsky, *Front Neural Circuits* **2018**, *12*, 114. [8] Y. J. Lin and A. P. Koretsky, *Magn Reson Med* **1997**, *38*, 378-388. [9] R. G. Pautler, et al., *Magn Reson Med* **1998**, *40*, 740-748; K. S. Saleem, et al., *Neuron* **2002**, *34*, 685-700. [10] T. Watanabe, et al., *NMR Biomed* **2004**, *17*, 554-568; I. Aoki, et al., *Neuroimage* **2004**, *22*, 1046-1059; X. Yu, et al., *Nat Neurosci* **2005**, *8*, 961-968. [11] P. Mi, et al., *Nat Nanotechnol* **2016**, *11*, 724-730; J. Liu, et al., *ACS Nano* **2021**, *15*, 13526-13538. [12] I. Aoki, et al., *Transl Res* **2015**; D. Kokuryo, et al., *Nanomedicine* **2015**, *11*, 229-238; E. Yuba, et al., *Mol Pharm* **2021**, *18*, 3342-3351.

Targeting vascular cell adhesion molecule 1 (VCAM-1) for an improved diagnosis and management of myocarditis using cardiac immuno-MRI.

Swannie Pédron[1], Sara Martinez de Lizarrondo[1], Mikaël Naveau[2], Eloïse Lemarchand[1], Albane Lemire[1], Romaric Saulnier[2], Charlène Jacqmarcq[1], Paul U. Milliez[1,3], Denis Vivien[1,3], Maxime Gauberti[1,4], Thomas Bonnard[1]
[1]Normandie Université, UNICAEN, INSERM UMRS-U1237, PhIND, Institut BB@C, Cyceron, Caen, France
[2]Normandie Université, UNICAEN, CNRS INSERM, UAR 3408, Cyceron, Caen, France
[3]CHU Caen, Clinical Research Department, CHU de Caen Côte de Nacre, Caen, France
[4]CHU Caen, Radiology Department, CHU de Caen Côte de Nacre, Caen, France

Introduction: Cardiovascular Magnetic Resonance imaging is crucial for diagnosing and monitoring myocarditis. However, its effectiveness depends on the disease stage and cannot always assess therapeutic responses. Using a more specific and sensitive contrast agent for myocarditis diagnosis would greatly improve its clinical management. We investigated the potential of cardiac immuno-MRI of VCAM-1 expression, an endothelial adhesion molecule over-expressed during inflammation, to assess early diagnosis and therapeutic response in myocarditis.

Methods: Experimental autoimmune myocarditis (EAM) was induced in rats with porcine myosin on day 0. ELISA dosage of VCAM-1 protein was performed on harvested hearts to confirm its over-expression between myosin and control rats. CMR was performed in a small animal 7T MRI (Bruker, BioSpec 70/18) at days 0, 7, 14 and 21. Cardiac immuno-MRI was revealed on T_2*-weighted sequences after the injection of micro-sized particles of iron oxide targeting VCAM-1 (MPIO@αVCAM-1, 2mg/kg). The specificity of the signal for the target was verified with MPIO functionalized with control isotype (MPIO@IgG). The inflammation signal detected was compared to late gadolinium enhancement (LGE) using T_1-weighted sequences, the current gold standard for myocarditis diagnosis. Some rats were treated using a corticosteroid treatment (dexamethasone, i.p., 1 mg/kg) 3 times a week starting from day 0 of EAM.

Results: ELISA dosage on harvested hearts confirmed the over-expression of the VCAM-1 protein in EAM condition. After the injection of MPIO@αVCAM-1, multiple foci of hypointensities were detected on the myocardial wall in rats that received myosin, indicating particles binding to VCAM-1 molecules (**a**). This signal uptake is significantly higher than in SHAM rats (n=5, *p<0,05) (**b**). No significantly hyposignal was found in myosin rats that received non-targeted particles, MPIO@IgG, confirming the specificity of the signal (n=4,5, *p<0,05) (**c**,**d**). Hyposignal correlated with the Late Gadolinium Enhancement (LGE) (**e**,**f**). The MPIO@αVCAM-1 signal enables early visualization of inflammation (at 14 days) and discrimination of treated rats.

Discussion: These results suggest that molecular imaging using VCAM-1 targeted MPIOs can provide a new tool to efficiently diagnose myocarditis on MRI at an earlier stage and evaluate the therapeutic response. Cardiac immuno-MRI could enhance the specificity of the myocarditis diagnosis, especially in cases where LGE is transmural, posing a challenge in distinguishing between ischemic and inflammatory diseases. The ongoing development of biocompatible and biodegradeable MPIOs highlights the potential for introducing cardiac immuno-MRI into clinical practice.

Conclusion: Cardiac immuno-MRI of VCAM-1 provides highly sensitive and precise tracking of inflammation activity in autoimmune myocarditis. This method could significantly enhance the specificity of diagnosis and prognosis compared to the current practice based on LGE MRI.

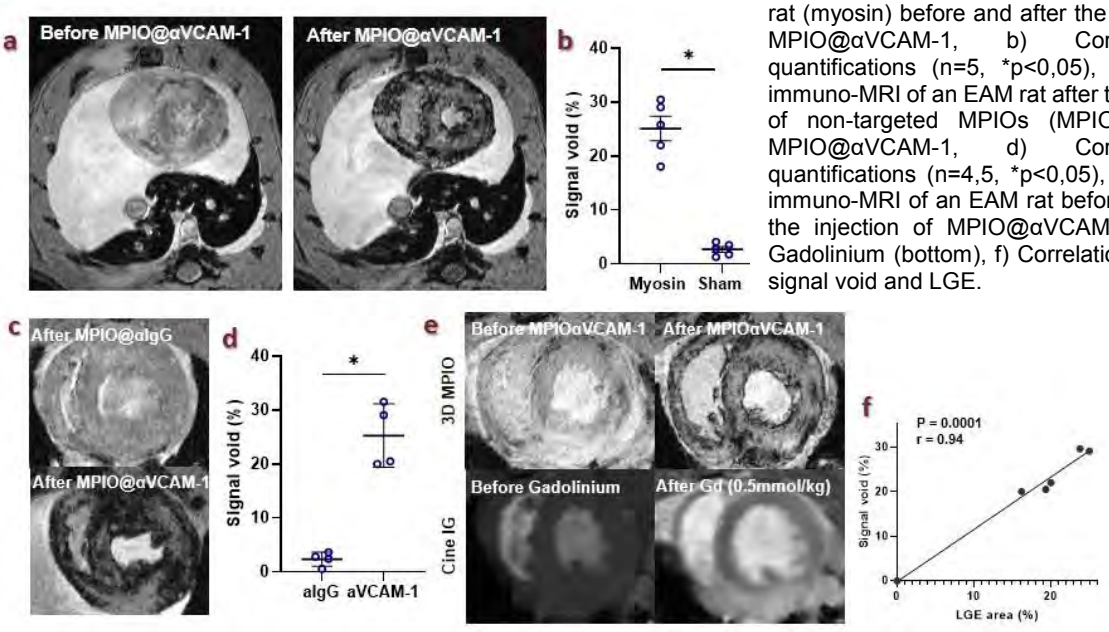

Figure 1: a) Cardiac immuno-MRI of an EAM rat (myosin) before and after the injection of MPIO@αVCAM-1, b) Corresponding quantifications (n=5, *p<0,05), c) Cardiac immuno-MRI of an EAM rat after the injection of non-targeted MPIOs (MPIO@IgG) vs MPIO@αVCAM-1, d) Corresponding quantifications (n=4,5, *p<0,05), e) Cardiac immuno-MRI of an EAM rat before and after the injection of MPIO@αVCAM-1 (top) or Gadolinium (bottom), f) Correlation between signal void and LGE.

^{19}F NMR in Theranostic Engineered Protein Fibers: Unveiling Protein Structure and Temperature

Dustin Britton[†], Jakub Legocki[†], Orlando Aristizabal[§,¶], Orin Mishkit[§,¶], Chengliang Liu[†], Sihan Jia[†], Paul Douglas Renfrew[‖], Richard Bonneau[‖,⊥,#], Jin Kim Montclare[†,¶,▽,£,°], and Youssef Z. Wadghiri[§,¶,°]

† Dept of Chemical and Biomolecular Engineering, NYU Tandon School of Engineering, §. Center for Advanced Imaging Innovation and Research (CAI^{2}R) & ¶. Bernard and Irene Schwartz Center for Biomedical Imaging, Dep. of Radiology, NYU Grossman School of Medicine, , ‖. Center for Computational Biology, Flatiron Institute, Simons Foundation, ⊥. Center for Genomics and Systems Biology, NYU. #. Courant Institute of Mathematical Sciences, Computer Science Dept, £ Department of Biomedical Engineering, New York University, New York, NY, 11201, USA ▽Dept of Chemistry,NYU, °Department of Biomaterials, NYU College of Dentistry.

Introduction. Theranostic agents represent a growing field in biomedicine that help to overcome limitations in biomaterials providing therapy and diagnosis of diseases[1]. These materials help to monitor the development of disease after therapeutic treatment as well as provide a simultaneous diagnosis and treatment of a disease[1]. To create an ideal theranostic biomaterial, without compromising drug encapsulation, diagnostic imaging must be optimized for improved detection[2]. One such method to improve this specificity is by strategically integrating exogenous fluorine, which is not found naturally in the human body, into biomaterials[3, 4] We developed a protein-based fluorinated self-assembling fiber, $Q2_{TFL}$ as a theranostic agent capable of ^{19}F NMR using noncanonical amino acid incorporation of trifluoroleucine (TFL). We demonstrate that $Q2_{TFL}$ has increased sensitivity for ^{19}F NMR and can encapsulate the hydrophobic small molecule, curcumin (CCM). Furthermore, we show that $Q2_{TFL}$ may be used *in vivo* as a visible fiber assembly via ^{1}H magnetic resonance imaging (MRI) and high-frequency ultrasound as well as a sensitive biomaterial using ^{19}F NMR. Interestingly, we show that $Q2_{TFL}$ possesses a ratiometric ^{19}F NMR signal proportional to its protein structure and environmental temperature indicating its potential as a multifunctional *in vivo* probe.

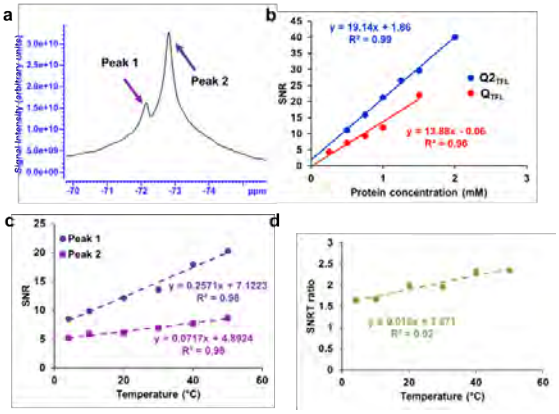

Figure 1 a. NMR spectrum at 500 MHz of $Q2_{TFL}$ at 1.5 mM showing two peaks **b.** SNR of $Q2_{TFL}$ and Q_{TFL} as a function of protein concentration **c.** Temperature dependence of SNR from independent peaks. **d.** Linear correlation of temperature with SNRT ratio showing ability to predict temperature.

Methods. *Protein biosynthesis and characterization:* $Q2_{TFL}$ and Q_{TFL} were expressed as described previously[5] *via* NCAA incorporation in *E. coli* cells[6]. Affinity chromatography facilitated protein purification, followed by assessment of secondary structure *via* circular dichroism and attenuated total reflectance-Fourier transform infrared spectroscopy. TEM confirmed the formation of nanofiber assemblies, while MALDI-TOF MS quantified TFL incorporation. Fluorescence and confocal microscopy evaluated CCM binding by $Q2_{TFL}$. *^{19}F NMR:* ^{19}F detection was studied using a Bruker AVIII-500 (11.7 T) NMR with a broadband BB(F)O CryoProbe. The ^{19}F signal was acquired with a one-pulse sequence. *Phantom and In Vivo MRI:* MRI and NMR were performed on a Bruker Biospec 70/30 micro-MRI system (Billerica, MA, USA) equipped with a BGA-12S-HP gradient coil insert powered by IECO high-performance gradient amplifier (Helsinki, Finland).

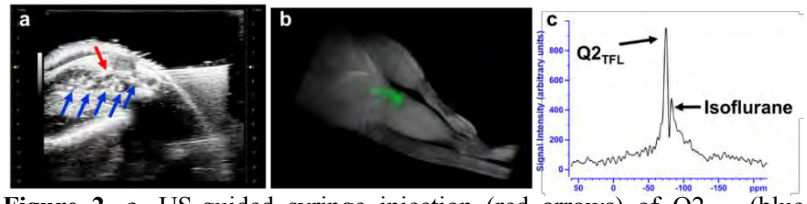

Figure 2. **a.** US-guided syringe injection (red arrows) of $Q2_{TFL}$ (blue arrows) into left hind leg. **b.** 3D rendering showcasing $Q2_{TFL}$ fibers distribution **c.** $Q2_{TFL}$ *in vivo* ^{19}F NMR performed after injection.

Results. $Q2_{TFL}$ achieved 95% incorporation of TFL and exhibited strong α-helical character and nanofiber assembly. This assembly was further strengthened by its ability to bind small hydrophobic molecule, CCM. The signal-to-noise ratios of the triplet peaks in ^{19}F NMR demonstrated a proportional relationship to the protein's TFL content (**Figure 1b**). To assess temperature dependence, the environmental temperature was altered during NMR data acquisition. (**Figure 1c**). This revealed a linear relationship between the ratios of NMR peak SNRs and temperature (SNRT) (**Figure 1d**). Finally, $Q2_{TFL}$ was evaluated *in vivo* using ultrasound (US)-guided intra-articular injection in C57Bl6 mice (**Figure 2a**). High frequency US visualization demonstrated the echogenicity of $Q2_{TFL}$, while T_2-darkening MRI contrast allowed differentiation from the surround tissue (**Figure 2b**). Additionally, $Q2_{TFL}$remained traceable *in vivo using* ^{19}F NMR (**Figure c**).

Discussion. $Q2_{TFL}$, a revolutionary fluorinated protein fiber, combines effective drug delivery with unique multimodal imaging capabilities. This versatile platform acts as dual-function probe, monitoring both temperature and protein structure, paving the way for next-generation theranostic biomaterials. Its thermoresponsiveness and potential for protein conformation offer exciting possibilities for personalized medicine. By merging therapeutic and diagnostic modalities into a compact and efficient platform, $Q2_{TFL}$ emerges as a promising candidate for the development of highly versatile and effective theranostic agents.

Conclusion. $Q2_{TFL}$ forms nano- to mesoscale fibers that encapsulate CCM and offer multimodal imaging capabilities. It provides contrast in both ^{1}H MRI and high-frequency ultrasound, while remaining readily detectable *in vivo* through sensitive ^{19}F NMR. Notably, analyzing the distinct triplet pattern of processing of TFL within $Q2_{TFL}$ paves the way for its potential use as a temperature probe and for monitoring relative changes in the protein structure.

References

(1) Jeyamogan *et al. Archives of Medical Research* **2021**, *52*, 131-142.
(2) Eggeling, C., *Journal of Physics D: Applied Physics* **2018**, *51*, 040201.
(3) Monkovic *et al.* Montclare, J. K. Fluorinated Protein and Peptide Materials for Biomedica Applications. In *Pharmaceuticals*, 2022; Vol. 15.
(4) Marsh *et al. ACS Chemical Biology* **2014**, *9*, 1242-1250.
(5) More *et al.* Montclare, J. K., *Biomacromolecules* **2015**, *16*, 1210-1217.
(6) Montclare, J. K. *et al. ChemBioChem* **2009**, *10*, 84-86.

MRI-Assisted Delivery of Radiopharmaceuticals to Tumors Using SPIONs-Anchors

Sara Lacerda[1], Retna P. Fauzia[2], Antonia G. Denkova[3], Sandra Même[1], Julien Sobilo[4], Eva Tóth[1], Kristina Djanashvili[2]

[1]CNRS, Centre de Biophysique Moléculaire, Orléans, France; [2]Delft University of Technology, Biotechnology, Delft, The Netherlands; [3]Delft University of Technology, Radiation Science and Technology, Delft, The Netherland; [4]CNRS, TAAM-In vivo Imaging Centre, MO2VING, Orléans, France

Introduction: Delivery of radiopharmaceuticals solely to tumor sites is especially important in alpha-radiotherapy.[1] When administered as small complexes, the high-energy alpha-radioisotopes are excreted before achieving sufficient tumor accumulation, while their long-circulating nano-analogues inadvertently damage healthy organs during this process. This study explores the efficacy and therapeutic potential of a biorthogonal two-step delivery of DOTA-based radiopharmaceuticals to breast tumors pre-targeted with functionalized MRI-detectable superparamagnetic iron oxide nanoparticles (SPIONs; Fig.1a).

Methods: Surface of SPIONs, prepared by thermal decomposition,[2] was functionalized with polyethylene glycol (PEG5000), folic acid (FA), fluorescein isothiocyanate (FITC) and azide (N_3) groups, pre-conjugated with (3-aminopropyl)trimethoxysilane (APTMS) linkers. Specific accumulation of SPIONs in HeLa cells was checked by confocal microscopy. The click-reaction was studied using Eu-DOTA-cyclooctyne (BCN) with APTMS-N_3 and SPIONs-N_3 by ^{1}H NMR, relaxivity and UV-measurements. In vivo imaging was done after injection of SPIONs (10mg/kg; MRI), followed by ^{111}In-DOTA-BCN (20MBq; SPECT) into 4T1-bearing mice. The therapeutic effects were tested with an alpha-emitter ^{225}Ac-DOTA-BCN (1-10kBq) applied to 3D spheroids, monitoring their shape/size and viability.

Results/Discussion: SPIONs were synthesized, morphologically and magnetically characterized (Fig.1b,c) and after functionalization with PEG-FA-FITC, the targeting ability was demonstrated in vitro by incubation with FA overexpressing HeLa 3D spheroids (Fig.1d). In vivo MRI showed highest signal 24h post administration of SPIONs-PEG-FA-N_3 to 4T1-mice (Step 1, Fig.1e). Solution ^{1}H NMR studies of the dynamics of click-reaction revealed the first adduct within 5 min (Fig.1f). To demonstrate this in vivo, ^{111}In-DOTA-BCN was administered in mice after 24h pre-targeting with SPIONs-PEG-FA-N_3 (Step 2). A higher uptake of ^{111}In-DOTA-BCN was detected by SPECT compared to control mice without pre-injected nanoparticles (Fig.1g,h). This approach was successfully translated to the treatment of 3D spheroids using ^{225}Ac-DOTA-BCN, demonstrating a much greater impact on the spheroids size and viability in the presence of N_3-functionalized SPIONs compared to those exposed to the same radiation dose without pre-targeting.

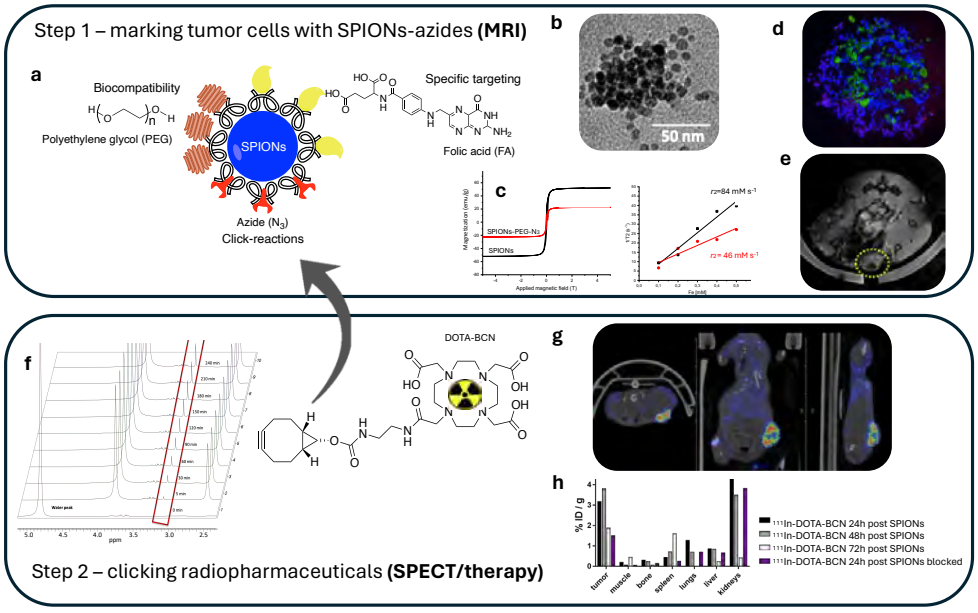

Figure 1: Concept, chemistry and results: a) design of functionalized SPIONs; b) TEM images; c) Magnetization (left) and r_2-relaxivity (right) of SPIONs before/after functionalization; d) Confocal images of SPIONs-FITC (green) at the surface of 3D spheroids (nuclei marked with blue DAPI; e) MRI images of 4T1-bearing mouse after injection of SPIONs; f) click-dynamics studied by ^{1}H NMR; g) SPECT images post injection with ^{111}In-DOTA-BCN 24h after pre-targeting with SPIONs; h) ex-vivo biodistribution.

Conclusion: Efficient breast tumor targeting with FA-functionalized SPIONs-N_3 was demonstrated by in vivo MRI, while click-reaction between the surface-exposed azides and ^{111}In-DOTA-cyclooctyne was visualized by SPECT. The in vitro results with ^{225}Ac-analogue suggest that this strategy holds great potential for advancing internal radionuclide therapy in the clinic, thanks to its ability to protect the organs from the circulating high-energy radionuclides.

Acknowledgements: This work was supported by LPDP (Indonesia Endowment Fund for Education) and Swim to Fight Cancer Foundation (2022).

References: 1. de Kruijff, R.M., Wolterbeek H.T. and Denkova, A.G. 'A Critical Review of Alpha Radionuclide Therapy-How to Deal with Recoiling Daughters?', *Pharmaceuticals*, **2015**, 8, 321-336. **2.** Park,J., An, K., Y. Hwang, J. G. Park, H. J. Noh, J. Y. Kim, J. H. Park, N. M. Hwang and T. Hyeon, 'Ultra-large-scale syntheses of monodisperse nanocrystals', *Nat Mater*, **2004**, 3, 891-895.

Polymer Microparticles as Multivalent Xenon Hosts for HyperCEST NMR

Samuel Lehr[1,3], Jabadurai Jayapaul[1,2], Leif Schröder[1,2,3]

[1] Division of Translational Molecular Imaging, German Cancer Research Center (DKFZ), Heidelberg, Germany
[2] German Cancer Consortium (DKTK), Partner Site Heidelberg, Germany
[3] Department of Physics and Astronomy, Ruprecht-Karls-University, Heidelberg, Germany

Introduction: The use of hyperpolarized Xenon-129 in conjunction with chemical exchange saturation transfer (HyperCEST) enables molecular imaging applications with MR detection of a highly diluted ^{129}Xe spin pool that exhibits reversible binding to a specific molecular host environment [1]. The search for suitable host structures that allow optimal depolarization conditions based on efficient ^{129}Xe exchange kinetics is a necessity to translate this method into *in vivo*. Since the sorption of ^{129}Xe in polymer microparticles (MP) has been reported elsewhere [2,3], this study investigates the potential of polymer MPs as novel multivalent contrast agents in a HyperCEST setting.

Methods and Material: We investigated two types of commercially available polymer MPs (~90 µm size): TentaGel PAP (TGPAP, Rapp Polymere, Germany) with cleavable polyethylene glycol (PEG) grafted onto a polystyrene (PS) matrix, and TentaGel RAP (TG RAP), a structurally closely related version with uncleavable PEG. Additionally, we studied acetylated and PEG-cleaved variants of TGPAP. For each of the samples 50 mg MPs (dry weight) were dispersed in a mixture of water and antifoaming agent (0.4% v/v) resulting in MP concentrations of approx. 0.2 fM. ^{129}Xe was hyperpolarized in a custom SEOP polarizer and measurements were conducted on a 9.4 T NMR spectrometer (Bruker Biospin, Ettlingen, Germany). We recorded multiple z-spectra for each of the four substances using a 15 s cw-saturation with 1 mW to evaluate their HyperCEST responses (see *Figure 1*).

Results: TGPAP MPs, whether unmodified or acetylated, displayed a pronounced HyperCEST response at approximately 26 ppm, indicating reversible binding of ^{129}Xe within the polymer matrix's micropores with favorable exchange kinetics matching the chosen saturation parameters. Conversely, TGRAP MPs exhibited a weaker signal due to less optimal exchange conditions. Cleavage of PEG from TGPAP led to complete signal disappearance upon measurement of the resulting MPs, indicating structural changes in the polymer matrix during the harsh cleavage process.

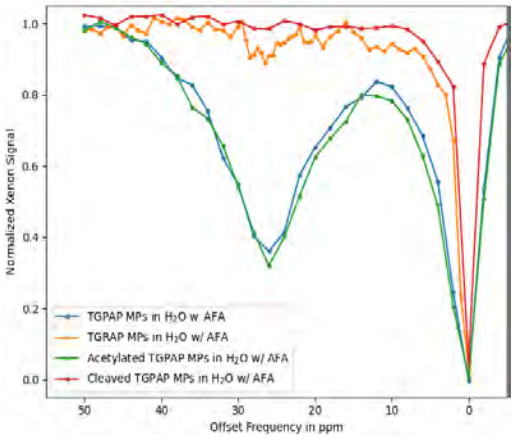

Figure 1: Z-spectra resulting from reversible ^{129}Xe binding into different types of polymer MPs in HyperCEST measurements using four different samples: unmodified TGPAP MPs (blue), unmodified TGRAP MPs (orange), acetylated TGPAP (green) and PEG-cleaved TGPAP (red) MPs in aqueous dispersion.

Discussion: Our study shows that robust HyperCEST responses can be obtained from polymer MPs making them a promising ^{129}Xe host system. The results emphasize the crucial influence of the physicochemical structure of polymer MPs on their HyperCEST responses. MP size, Micropore size, total surface area, PEG content and cross-linking seem to play a key role in influencing the binding and exchange kinetics, which are essential aspects for an effective performance of polymer MPs as multivalent ^{129}Xe hosts. Tailoring these properties is critical for the optimization of polymer MPs with respect to HyperCEST imaging applications. Nevertheless, polymer MPs offer a wide variety of opportunities for further customization, including exploring different polymer compositions, surface functionalization, sizes and pore sizes to improve their performance as HyperCEST agents. Furthermore, the pharmacokinetics, biocompatibility, and cell affinity of PS nanoparticles can be tailored by modifying surface properties and particle size of the MPs [4].

Conclusion and Outlook: Our findings suggest that polymer MPs can serve as tunable multivalent ^{129}Xe hosts, and initial HyperCEST measurement showed a pronounced and robust response for some of the investigated materials. Furthermore, the MPs could find an *in vivo* application as basis for functionalized HyperCEST biosensors [5] after adjustment of biocompatibility and cell interactions. Although the biocompatibility of the investigated polymer MPs has not yet been tested and might limit direct *in vivo* application, these MPs could serve as low-cost components of *in vitro* phantom models after injection into a gel or tissue sample, thus simplifying the testing and optimization of localized HyperCEST-MRI contrast by circumventing the complex and expensive administration of targeted biosensors.

Acknowledgement:
We acknowledge financial support by the Deutsche Forschungsgemeinschaft (Koselleck grant no. SCHR 995/5-1) and the Dieter Morszeck Stiftung. Samuel Lehr is funded by the German-Israeli Helmholtz International Research School “Cancer-TRAX”.

References:
[1] Saul, P., Schröder, L., Schmidt, A. B., & Hövener, J. **2023**. Nanomaterials for hyperpolarized nuclear magnetic resonance and magnetic resonance imaging. *WIREs Nanomedicine and Nanobiotechnology*, 15(4). **[2]** Simpson, J. H., Wen, W., Jones, A. A., Inglefield, P. T., & Bendler, J. T. **1996**. Diffusion coefficients of xenon in polystyrene determined by xenon-129 NMR spectroscopy. *Macromolecules*, 29(6), 2138–2142. **[3]** Locci, E., Roose, P., Bartik, K., & Luhmer, M. **2009**. Probing polymer colloids by 129Xe NMR. Journal of Colloid and Interface Science, 330(2), 344–351. **[4]** Loos, C., Syrovets, T., Musyanovych, A., Mailänder, V., Landfester, K., Nienhaus, G. U., & Simmet, T. **2014**. Functionalized polystyrene nanoparticles as a platform for studying bio–nano interactions. *Beilstein Journal of Nanotechnology*, 5, 2403–2412. **[5]** Jayapaul, J., & Schröder, L. **2020**. Molecular Sensing with Host Systems for Hyperpolarized ^{129}Xe. *Molecules*, 25(20), 4627.

Unveiling Tumor Characteristics with Low and Ultra-Low Field Magnetic Resonance Techniques

Simonetta Geninatti Crich[1], Simona Baroni[1], Sabrina Enkhanoufi[1], Sahar Rakhshan[1], Diego Alberti[1], Valeria Bitonto[1], Maria Rosaria Ruggiero[1], Alessandra Pittaro[2], Isabella Castellano[2], Silvio Aime[1]
Dep. of Molecular Biotechnology and Health Sciences University of Torino.
Pathology Unit, Department of Medical Sciences, University of Turin, 10126 Torino, Italy.

Conventional MRI excels at high-resolution in the visualization of tumor lesions, but has limitations in the assessment of key features related to metabolism. In this study, we demonstrate that novel, easy to apply strategies performed at low and ultra-low magnetic fields allow to obtain relevant information that are invisible at standard, clinically used MRI. Our work developed along two main directions. The first was to develop an innovative diagnostic approach based on the acquisition of Nuclear Magnetic Relaxation Dispersion (NMRD) profiles using Fast Field Cycling Relaxometers (FFC-NMR) to obtain quantitative information on tumour characteristics. The FFC-NMR technique measures the relaxation rate of protons at different magnetic field strengths, revealing differences between healthy and cancerous tissue. The method is based on the observation that at low magnetic fields (in contrast to what is observed at clinically used magnetic fields), the recovery of ^{1}H magnetisation depends on the rate of water exchange across the cell membrane. The extent of water cycling is related to the activity of membrane transporters, and the relaxometric readout then becomes a biomarker for the metabolic state of the tumour cells, providing important information on tumour aggressiveness and grading,[1] which is fundamental for deciding on therapeutic strategies and for monitoring treatment in real time[2]. Furthermore, due to the difference in R_1 at low field between healthy and tumour tissue, the method is also proposed for tumour margin assessment in breast conserving surgery[3] and to assess tumour grade and lymph node status in breast cancer patients. NMRD profiles also allow to assess to ^{14}N quadrupolar peaks whose characteristics can provide additional information on the investigated tumor tissues. The second approach deals with the characterisation of the tumour microenvironment by applying Overhauser Magnetic Resonance Imaging (OMRI) to monitor tumour associated enzyme activity at ultra-low magnetic fields (200 μT) close to the earth magnetic field (25-65 μT). OMRI is a double resonance imaging technique that combines the advantages of MRI with the use of stable radicals as polarizing agents to enhance the NMR proton signal. We designed and tested an "off-on" nitroxide containing probe (forming EPR silent micelles) which becomes EPR active upon release from the nanosized particles, allowing sensitive detection of esterase activity. This approach differentiates healthy and cancerous tissue based on their varying esterase levels. Both these techniques could significantly improve clinical diagnosis, treatment decisions, and therapy monitoring in oncology. While the FFC relaxometry lacks spatial resolution, the gained knowledge paves the way for developing next-generation diagnostic tools that leverage the growing number of FFC-MRI scanners worldwide.

References

1)MR Ruggiero, S. Baroni, S Pezzana, G Ferrante, S Geninatti Crich, S Aime, Evidence for the role of intracellular water lifetime as a tumour biomarker by in vivo Field-Cycling relaxometry, Angew Chem Int Ed Engl, 2018 Jun 18;57(25):7468-7472.

2) MR Ruggiero, S Baroni, V Bitonto, R Ruiu, S Rapisarda, S Aime, S Geninatti Crich Intracellular Water Lifetime as a Tumor Biomarker to Monitor Doxorubicin Treatment via FFC-Relaxometry in a Breast Cancer Model Front Oncol 2021 Dec 3;11:778823.

3)V Bitonto, MR Ruggiero, A Pittaro, I Castellano, R Bussone, L M. Broche, D J. Lurie, S Aime, Simona Baroni and Simonetta Geninatti Crich Low-Field NMR Relaxometry for Intraoperative Tumour Margin assessment in Breast-Conserving Surgery Cancers 2021, 13, 4141.

Quantitative PET/MRI of Perfusion and Excretion with a New 18F-Labeled Gadolinium-Based Probe: Preclinical Experience

Remy Chiaffarelli[1,2], Jan Kretschmer[1,2], Jonathan Cotton[1,2], Miloslav Polasek[3], and André Martins[1,2,4]

[1]Werner Siemens Imaging Center, University Hospital Tuebingen, Tuebingen, Germany. [2]Cluster of Excellence iFIT (EXC 2180) "Image-Guided and Functionally Instructed Tumor Therapies," University of Tuebingen, Tuebingen, Germany. [3]Institute of Organic Chemistry and Biochemistry of the CAS, Prague, Czech Republic. [4] German Cancer Consortium (DKTK), partner site Tübingen, German Cancer Research Center (DKFZ), Heidelberg (Germany)

Introduction: PET/MR imaging synergizes the exceptional sensitivity and signal quantification of PET with the functional and anatomical insights of MRI. Despite the potential for hybrid approaches in precision imaging, the main emphasis in combined PET/MRI applications has been on reducing scan durations, largely due to the lack of probes capable of producing both PET signal and MRI contrast.[1] We report a new hybrid PET/MRI probe, [^{18}F][Gd(FL^1)], built as analogue of already clinically approved, non-specific MRI contrast agents. This probe is readily radiolabelled, has excellent stability *in vivo* and suitable pharmacokinetics allowing for monitoring perfusion and renal filtration. **Methods:** [^{18}F][Gd(FL^1)] was synthesized by direct radiolabelling of a macrocyclic Gd(III) precursor chelate with an optimized directed $^{18}F^-$ by fluorine isotopic exchange (Fig. 1A). Dissociation half-life was determined by acid-assisted decomplexation in a relaxometer (0.1 M HCl; 37°C; 0.47T). For imaging, the radiolabelled product was doped with non-radioactive [^{19}F][Gd(FL^1)] to enhance MR contrast. Phantom and *in vivo* experiments with healthy mice (n=6) were performed on a 7T preclinical scanner (Bruker Clinscan) with an in-house built PET insert. DCE images, T_1 maps, and PET scans were acquired simultaneously for 60 minutes after a bolus injection of the probe (0.09 ± 0.03 mmol/kg of Gd; 0.91 ± 0.16 MBq). *Ex vivo* biodistribution was assessed by γ-counting and autoradiography (^{18}F), ICP-OES and LA-ICP-MS (Gd content). Glomerular filtration rates (GFRs) were estimated from the natural logarithm of the kidney's time-activity curves.[2] **Results/Discussion:** [Gd(FL^1)] showed a remarkable kinetic inertness with a dissociation half-life of $t_{1/2}$ = 45h, comparable to [Gd(DOTA)] (Fig. 1B). PET/MRI phantoms of [^{18}F][(Gd(FL^1)] at various Gd concentrations revealed a perfect linear correlation between relaxation rates (R_1) and PET signal (Fig. 1C). Concentrations determined with γ-counter and ICP-OES showed linear correlations (R^2=0.98). In healthy mice, [^{18}F][Gd(FL^1)] showed consistent signal in both modalities (Fig. 1D) with quick renal clearance and no retention in other organs, which was also confirmed *ex vivo*. A linear regression analysis between probe concentration in tissues determined via γ-counting and ICP-OES yielded R^2 = 0.96 (Fig. 1E). Radiotracer uptake in femur samples was 0.86 ± 0.12 %ID/g, indicating no significant defluorination. Unexpectedly, the right kidneys of 2 mice showed abnormal probe accumulation, resulting in T_2 effect (hypointense MR signal) from 25 minutes p.i (Fig. 1F, bottom). PET images showed higher uptake in identical regions, providing better quantification capabilities owing to the linear characteristics of PET signal (Fig. 1F, top). The estimated GFR of these kidneys was substantially different from those without probe accumulation (-0,038 vs -0,059 ± 0,005). *Ex vivo* autoradiography and LA-ICP-MS showed the same distribution patterns, and PAS staining highlighted histological abnormalities that were compatible with the imaging findings. **Conclusion:** We developed a first-of-its-kind PET/MRI probe [^{18}F][Gd(FL^1)] with excellent physico- and radiochemical properties. Preclinical PET/MR imaging in mice proved the advantages of combining two modalities in a single probe to obtain complementary quantitative and functional information of tissues. Notably, our probe has shown significant potential in the quantitative imaging of kidney excretion and represents an excellent scaffold for further development of responsive and quantitative PET/MRI probes.

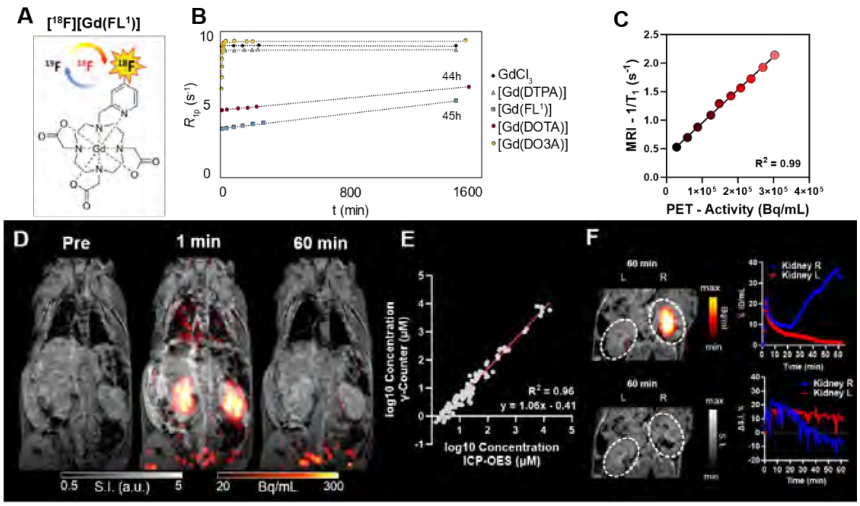

Figure 1. (**A**) [^{18}F][(Gd(FL^1)] structure. (**B**) Relaxation rate during 24h acid-assisted decomplexation for [Gd(FL^1)] and other Gd(III) chelates, to determine the dissociation half-life. $GdCl_3$ solution is used for reference. (**C**) Correlation plot between radioactivity measured with PET imaging and relaxation rates in a phantom containing 0-0.5 mM [^{18}F][(Gd(FL^1)]. (**D**) *In vivo* PET/DCE MR images before and after injection of a cocktail of [Gd(FL^1)] and the radiolabelled [^{18}F][Gd(FL^1)]. (**E**) Linear regression analysis of concentration of [^{18}F][Gd(FL^1)] in organs calculated from γ-counter activity and measured by ICP-OES, on logarithmic scale. (**F**) Mouse with unexpected probe accumulation in the right kidney: (left) PET/MR images; (right) dynamics of radiotracer uptake and MR signal in left and right kidneys showing opposite trends.

References: [1] Judenhofer, M., et al. Simultaneous PET-MRI: a new approach for functional and morphological imaging. Nat Med 14, 459–465 (2008) **[2]** Calvert, N.D., et al. Direct mapping of kidney function by DCE-MRI urography using a tetrazinanone organic radical contrast agent. Nat Commun 14, 3965 (2023)

Molecular MRI of Neuroinflammation Using Fe-PyC3A

Chunxiang Zhang,[1] Can Zhang,[2] **Iris Yuwen Zhou,[1]** and **Eric M Gale[1]**

Athinoula A. Martinos Center for Biomedical Imaging, Department of Radiology,[1] and Genetics and Aging Research Unit, Department of Neurology,[2] Massachusetts General Hospital and Harvard Medical School.

Introduction. Neuroinflammation plays an important role in the progression of neurodegenerative disease states such as Alzheimer's Disease. During neuroinflammation, microglial cells adopt a pro-inflammatory 'reactive' phenotype that release reactivity oxygen species (ROS) in the brain extracellular spaces creating in an aberrantly oxidizing neurotoxic microenvironment. Our lab invented an oxidative activated MR imaging probe called Fe-PyC3A, which upon chemical oxidation switches from an MRI silent complex of Fe^{2+} to the corresponding Fe^{3+} complex, which is strongly visible to the MRI scanner. We hypothesized that MRI using Fe-PyC3A may provide a noninvasive biomarker for neuroinflammatory activity. The experiments we will present provide proof of concept for MRI using Fe-PyC3A as a noninvasive marker of neuroinflammation, and demonstrate a mechanistic link between Fe-PyC3A brain enhancement and microglial oxidative burst activity.

Materials and Methods: *Imaging probes*. Fe-PyC3A was synthesized as per our usual methods. Gd-DOTA (manufactured by Guerbet) was used as non-oxidatively activated negative control probe. *Mouse models*. Neuroinflammation was generated through i.p. injection of lipopolysaccharide (3 mg/kg), mice receiving injection with only saline were used as control. To further examine the mechanistic link between Fe-PyC3A MRI signal enhancement and neuroinflammation, we used both wild-type (WT) C57BL/6 mice and B6.129S-Cybb^{tm1Dn}/J (gp91phox knockout) mice which cannot assemble the NADPH oxidase II complex required for microglial oxidative burst, as loss of function control. Mice were imaged 24h after receiving LPS or saline injection. *Imaging and ex vivo analysis.* MRI was performed on 4.7T scanner (Bruker Biospec). Prior to injection of either imaging probe mice received an iv injection containing 250 µL of 25% wt/wt mannitol in water to transiently disrupt the blood-brain-barrier. Mice were imaged dynamically with a series of 2D multi-slide T_{1w} gradient echo sequences prior to and 2 min after injection of either 0.3 mmol/kg or 0.1 mmol/kg Gd-DOTA. Brain tissue harvested after imaging was analyzed for microglial activation using Iba1 immunostaining. *Data analysis*. Regions of interest (ROIs) were drawn in the hippocampus and cortex, and the percentage (post-pre)injection change in signal intensity (ΔSI%) computed. For either Fe-PyC3A or Gd-DOTA, we separately compared ΔSI% in LPS and placebo treated WT and LPS-treated NOX2-deficient mice using one-way ANOVA followed by Tukey's post-test for multiple comparisons. Correlations between Iba-1 immunostaining and ΔSI% were tested by computing Pearson's product-moment correlation coefficient.

Results: Images recorded prior to an 2 mind after Fe-PyC3A in WT mice treated with saline or LPS, and in NOX2 deficient mice treated with LPS are compared in Figure 1A-C. Microglial staining is compared in Figs 1D, confirming substantial neuroinflammatory activity in both WT and NOX2-deficient (gp91phox knockout) mice treated with LPS. The ΔSI% values are compared in Fig 1E, demonstrating how Fe-PyC3A differentially enhanced brain tissue in LPS-treated WT mice and confirming a mechanistic link between Fe-PyC3A brain signal enhancement and immune cell oxidative burst activity. Furthermore, in ΔSI% correlated positively and significantly with hippocampus microglial staining ($r = 0.88$, $P < 0.001$). *Imaging with Gd-DOTA did not distinguish between any group, and did not correlate with microglial immunostaining,* further underscoring the specificity of MRI using Fe-PyC3A for detecting neuroinflammation activity.

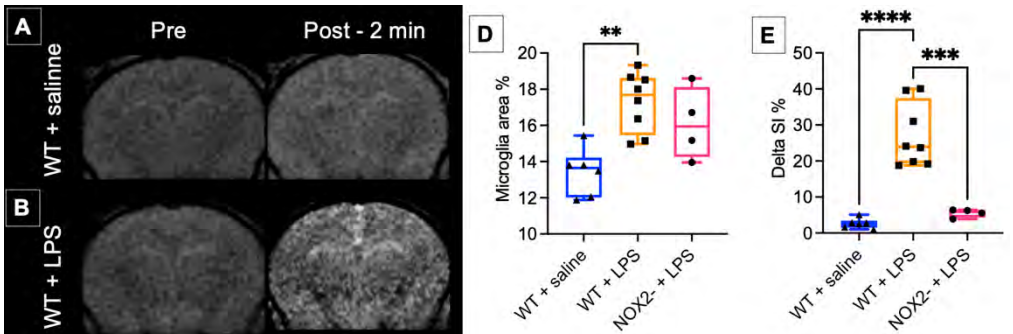

Fig 1. (A-C) Axial 2D T1-weigted brain images prior to and 2 min-post injection of Fe-PyC3A in WT mice treated with saline (A), LPS (B), and NOX-deficeint mice treated with LPS (C). (D-E) Comparison of Hippocampal area stained Iba-1 positve (D) and of hippocampal ΔSI% (E). ***P < 0.001, ****P < 0.0001.

Conclusions: MRI using Fe-PyC3A is a potentially powerful non-invasive marker for neuroinflammation.

Noninvasive Early Detection and Stage of Chronic Lung Diseases with Precision MRI (pMRI)

Dongjun Li[1], Oluwatosin Y. Ibhagui[1], Hongwei Han[2], Guangda Peng[2], Maureen L. Meister[3], Zongxiang Gui[1], Jingjuan Qiao[1,4], Sophia Bamishaye[1], Francis Akinoltan[1], Mani Salarian[1], Bin Dong[1], Yi Yuan[2], Yiting Xu[1], Hua Yang[5], Shanshan Tan[1], Ganesh Satyanarayana[2], Shenghui Xue[4], Sandi Li[7], Ravi Chakra Turaga[2], Yuguang Meng[1,7], Nedumangalam Khan Hekmatyar[1], Phillip Sun[6], Wei Zhou[7], Xiangming Ji[2], Zhi-ren Liu[3], and Jenny J. Yang*[,1,4]

[1]Department of Chemistry, Center for Diagnostics and Therapeutics, Advanced Translational Imaging Facility, Georgia State University, Atlanta, GA, 30303, USA. [2]Department of Biology, Georgia State University, Atlanta, GA, 30303. [3]Nutrition, Georgia State University, Atlanta, GA, 30303, USA. [4] InLighta Biosciences, Atlanta, GA, 30303, USA. [5] Department of Ophthalmology, Emory University, Atlanta, GA 30322, USA. [6]Emory National Primate Research Center, Emory University, Atlanta, GA, 30329, USA. [7] Winship Cancer Institute, Emory University, Atlanta, GA 30322, USA.

Abstract: Chronic lung diseases, such as idiopathic pulmonary fibrosis (IPF), chronic obstructive pulmonary disease (COPD), and lung cancer, are major leading causes of death worldwide and are generally associated with poor prognoses. The heterogeneous distribution of collagen, mainly type I collagen associated with excessive collagen deposition, plays a pivotal role in the progressive remodeling of the lung parenchyma to chronic exertional dyspnea for IPF, COPD and lung cancer. To address the pressing need for noninvasive early diagnosis and drug treatment monitoring of pulmonary fibrosis and lung cancer, we report the development of human collagen-targeted protein MRI contrast agent (hProCA32.collagen1) to specifically bind to collagen I overexpressed in multiple lung diseases.

When compared to clinically approved Gd^{3+} contrast agents, hProCA32.collagen1 exhibits significantly better r1 and r2 relaxivity values, strong metal binding affinity and selectivity, and transmetallation resistance. Here we report the robust detection of early and late-stage lung fibrosis with stage-dependent MRI signal-to-noise ratio (SNR) increase, and with good sensitivity and specificity, using a progressive bleomycin-induced IPF mouse model. Spatial heterogeneous mapping of usual interstitial pneumonia (UIP) patterns with key features closely mimicking human IPF, including cystic clustering, honeycombing, and traction bronchiectasis, were noninvasively detected by multiple MR imaging techniques and verified by histological correlation. We further report the detection of fibrosis in the lung airway of an electronic cigarette-induced COPD mouse model, using hProCA32.collagen1-enabled precision MRI (pMRI), and validated by histological analysis. We have also achieved the first detection of subclinical invasive lung nodules and adrenal gland metastasis of LKB1 with heterogenous distribution of collagen in our mouse model with a 3-fold increase of Contrast-Noise Ratio (CNR) compared with CT imaging. The developed hProCA32.collagen1 is expected to have strong translational potential for the noninvasive detection and staging of lung diseases and facilitating effective treatment to halt further chronic lung disease progression.

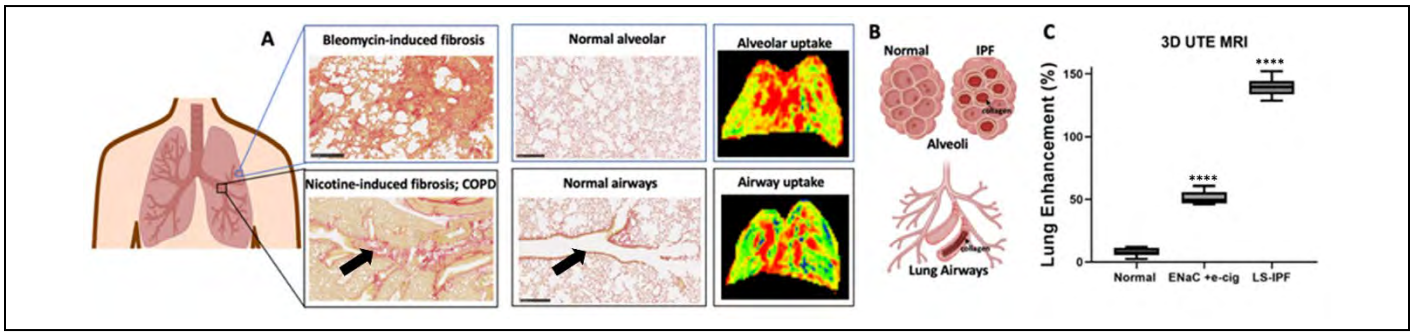

Figure. Comparison of collagen accumulation pattern and hProCA32.collagen1 pattern uptake in BM-induced IPF and E-cigarette-induced lung fibrosis in COPD mouse models. (**A-B**). Collagen accumulation and binding in IPF (top) and COPD (bottom) with overexpression of collagen 1 (red color) at alveolar and bronchial airways, respectively, compared to normal healthy mice (middle panel). Human collagen-targeted protein MRI contrast agent (hProCA32.collagen1) detected collagen overexpression in IPF and COPD at the alveolar (top) and bronchial airways (bottom) in 3D UTE MRI. (**C**) Comparison of lung signal enhancement (%) in normal mice, nicotine-induced lung fibrosis model for COPD, and bleomycin-induced mice model (LS: Late stage, ****$P < 0.001$ one-way ANOVA)

Keywords

MRI, collagen, Protein-based contrast agent, lung fibrosis, IPF, COPD, lung cancer and metastasis

A New Collagen III Targeted MRI Probe for Molecular Imaging of Cardiac Fibrosis

Authors: Nadia Chaher[1], Giuseppe Digilio[2], Sara Lacerda[3], Ling Gao[1], Begoña Lavin Plaza[1,4], Carlos Velasco[1], Gastão Cruz[1,5], Claudia Prieto[1,7], René M. Botnar[1,6,7,8], Alkystis Phinikaridou[1,6]

Affiliations: [1] School of Biomedical Engineering & Imaging Sciences, King's College London, 4th Floor, Lambeth Wing, St Thomas' Hospital, London SE1 7EH, UK, [2] Dipartimento di Scienze e Innovazione Tecnologica, Università del Piemonte Orientale, 13100 Vercelli, Italy, [3] Centre de Biophysique Moléculaire, CNRS UPR 4301, Université d'Orléans, rue Charles Sadron, 45071 Orléans, France , [4] Department of Biochemistry and Molecular Biology, School of Chemistry, Complutense University, Madrid, Spain, [5] Department of Radiology, University of Michigan, Ann Arbor, MI, [6] BHF Centre of Excellence, Cardiovascular Division, [7] Escuela de Ingeniería, Pontificia Universidad Católica de Chile, Santiago, Chile, [8] Instituto de Ingeniería Biológica y Médica, Pontificia Universidad Católica de Chile, Santiago, Chile.

Introduction: Heart failure (HF) is a major cause of morbidity and death affecting 64 million people globally[1]. Myocardial fibrosis, characterised by changes in type I (COL1) and III (COL3) collagen, drives HF[2,3]. Although, cardiac magnetic resonance (CMR) is a preferred method to detect fibrosis non-invasively, it only provides indirect measures to diagnose fibrosis. Molecular imaging can directly visualise fibrosis, but current imaging probes are limited to COL1. In this study, we present the development of the first COL3-specific imaging probe and its application for molecular CMR to directly image changes in COL3 in myocardial scar and monitoring of treatment response.

Methods: To develop a COL3-binding probe, a small peptide was conjugated to a DOTA-chelator and tagged with Europium [Eu(III)] for *in vitro* screening, gallium [^{68}Ga] for *in vivo* PET/CT distribution, and gadolinium [Gd(III)] for *in vivo* CMR. Functional and molecular CMR was carried out in mice at days 10 and 21 post-MI (n=6/group) using a 3T clinical MRI scanner. A subgroup of mice was also imaged using a negative control probe and Gadovist (n=3). Mice treated with Enalapril (20mg/kg/day) immediately after MI were imaged on days 10 and 21 (n=6/group). Cardiac function was analysed using 2D short axis cine images of the LV. T_1-weighted 3D inversion recovery (IR) late gadolinium enhancement (LGE) images were captured 60 minutes post-intravenous injection (0.2mmol/kg). For T_1 mapping a 2D Look-Locker sequence with an inversion pulse, followed by 30 inversion delay images was used.

Results: We developed a high-affinity imaging probe that specifically binds to COL3 (Kd=5.3μM) (**Fig. 1A**). The probe showed fast blood clearance and no unspecific binding (**Fig. 1B**). Molecular CMR, using the COL3 probe, showed high signal enhancement on day 10 that decreased by day 21 as COL3 gets naturally replaced by COL1 (**Fig. 1C**). No enhancement was observed within the scar using the negative probe or clinical agent Gadovist. Histology showed the co-localisation between the MRI enhancement seen with the COL3 probe and a scar rich in COL3 fibres at day 10. Enalapril-treated mice exhibited similar enhancement on day 10 but had a significantly higher COL3 signal at day 21 compared with untreated mice (**Fig. 1D**). This suggests that enalapril may alter the natural turnover of COL3 and extend its deposition. Quantitative T_1 mapping showed lower T_1 values in the infarct (~530ms) compared with the remote (~670ms) myocardium. Cardiac function was similar between the groups, suggesting that molecular changes in COL3 may precede functional changes.

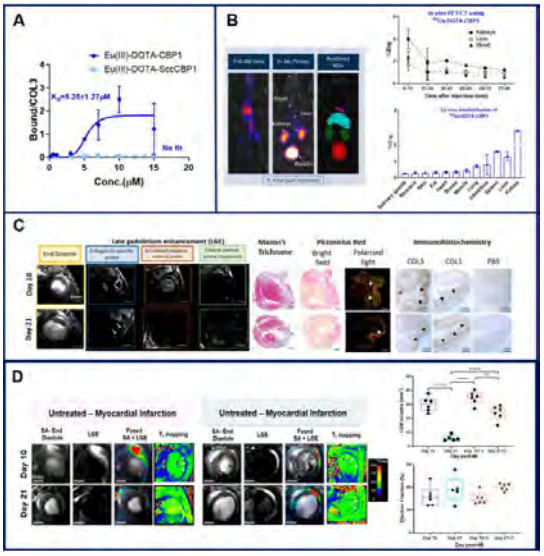

Figure 1 – Molecular imaging of COL3 in myocardial fibrosis. **A.** *In vitro* binding assays show high affinity and specificity of the probe to COL3. **B.** *In vivo* PET/CT and *ex vivo* biodistribution demonstrate favourable pharmacokinetics. **C.** First *in vivo* molecular CMR of collagen III (COL3) to image cardiac fibrosis**.** High enhancement was observed at day 10 that decreased by day 21 using the COL3 probe. Negligible enhancement was observed when using scrambled probe and Gadovist. MRI signal co-localised with COL3 rich scar by histology. **D**. *In vivo* molecular CMR of COL3 in untreated and Enalapril-treated showed similar enhancement at day 10 but significantly higher enhancement at day 21 in the treated mice. No functional changes were observed.

Discussion: We have developed the first probe suitable for molecular imaging of COL3. Combining this probe with quantitative CMR, enabled detection and quantification of, previously undetectable, COL3 following myocardial infarction and response to treatment in vivo.

Conclusion: Molecular imaging of COL3 may provide a new tool to investigate the functional role of COL3 in myocardial fibrosis non-invasively. This tool could address a considerable knowledge gap and potentially enable detection and characterisation of myocardial fibrosis earlier allowing staging of disease and monitoring of novel therapies.

References: [1] Savarese G *et al.* Cardiovasc Res. 2023 [2] Bateman, E.D. *et al*. Thorax 1981 [3] Jugdutt, B.I. Circulation 2003

Molecular brain imaging with engineered hemodynamics

Robert Ohlendorf [1,3], Nan Li [2,3], Alan Jasanoff [3]
[1]Max-Planck Institute for Biological Cybernetics, Max-Planck-Ring 11, 72076 Tuebingen, Germany; [2]Advanced Imaging Research Center and Department of Neuroscience, UT Southwestern Medical Center, 2201 Inwood Rd., Dallas, TX 75390; [3]Massachusetts Institute of Technology, 77 Massachusetts Ave., Cambridge, MA 02139

Introduction | How the mammalian brain processes information, stores memories and maintains homeostasis depends on the dynamic communication between neurons, glia cells, blood vessels and many other cell types via signaling molecules such as neurotransmitters, neuropeptides and hormones throughout the entire brain. Currently no technology can measure brain-wide molecular signaling with sufficient spatial and temporal resolution in living mammals, which poses a major roadblock for understanding molecular foundations of brain function and dysfunction in disease states.

Methods | Hemodynamic imaging using functional magnetic resonance imaging (fMRI) or functional ultrasound (fUS) represents the gold standard for imaging whole-brain function in animals and humans and the only method that can measure brain-wide function with a temporal resolution of single seconds and in-plane spatial resolution of 100 µm. Yet, hemodynamic imaging lacks critical information on molecular pathways or signaling molecules underlying the measured imaging signals. We leverage the power of hemodynamic imaging and provide it with molecular information by developing a technology that converts target molecular signal into hemodynamic imaging contrast in fMRI, ultrasound, or optical imaging. We apply this technology for molecular brain imaging in living rats using T_2*-weighted MRI.

Results/Discussion | We developed bioluminescence imaging using hemodynamics (BlusH), which utilizes vascular expression of the light-activated cyclase protein PAC to convert light signals from bioluminescent molecular reporters into hemodynamic imaging signals visible in MRI and other modalities (Panel A). We tested the BlusH principle *in vitro* by quantifying the light output of bioluminescent luciferase proteins and validating light-driven activation of hemodynamic pathways by PAC and direct stimulation of such pathways by the bioluminescent reporter GLuc. Targeting expression of PAC to the brain vasculature in rats yielded robust light-activated signal changes in T2*-weighted MRI that colocalized with PAC expression and light stimulation patterns. Finally, wide-field expression of PAC allowed us to accurately map GLuc expression in deep brain regions and three dimensions using MRI (B-D).

Conclusion | Bioluminescence imaging usually suffers from poor tissue penetration of light signals, leading to low-resolution and largely superficial signal detection. BlusH leverages the rich toolbox of bioluminescent reporters to visualize intra- and extracellular molecular processes throughout the brain using noninvasive fMRI providing a bridging technology between brain-wide functional imaging with fMRI and molecular nuclear imaging.

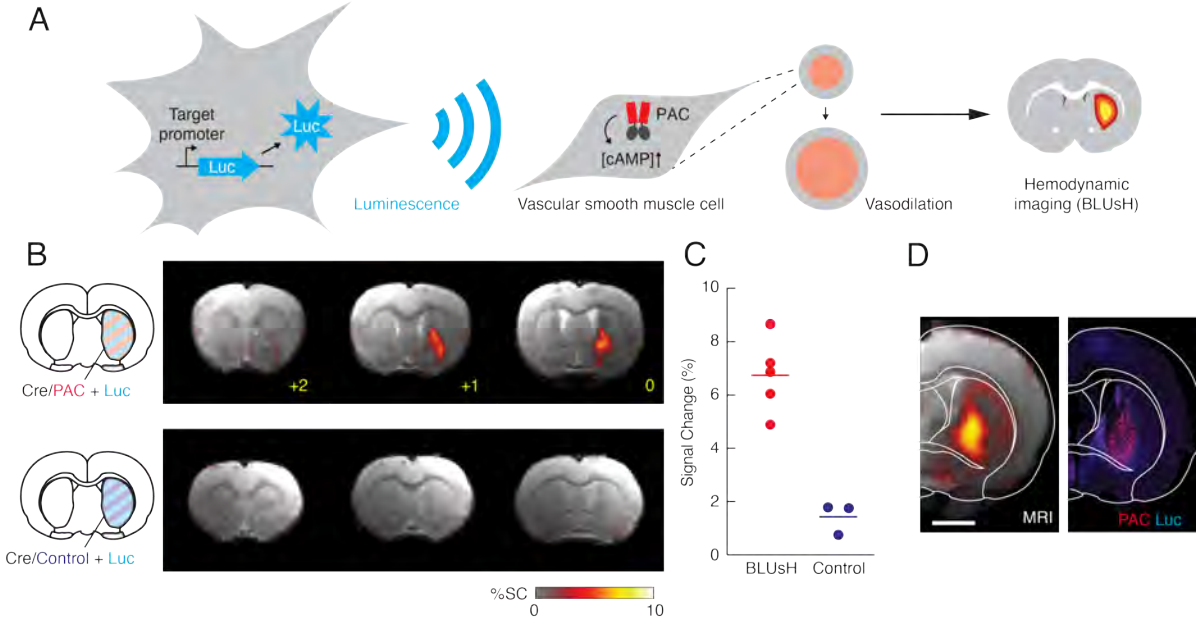

Figure: (A) In the BlusH mechanism, vascular cells are photosensitized by expression of the light-activated adenylate cyclase PAC. Light emission by cells expressing luciferase reporters (Luc) triggers PAC-mediated vasodilation and subsequent hemodynamic imaging signals. (B) BlusH imaging of endogenous luciferase expression. BlusH (top) or control (bottom) imaging of brain regions from representative animals transduced with viruses as schematized at left. Bregma coordinates in yellow. (C) Peak signal changes observed in BlusH and control experiments. (D) Comparison of signal change profiles detected by BlusH MRI vs. postmortem histology of Luc and PAC expression in representative animal, showing correspondence of profiles at an individual animal level. Scale bar = 2 mm.

Endogenous ^{31}P CEST: A tool for monitoring Glycolysis without contrast agents .

Giulia Vassallo, Cecilia Fiorucci, Francesca Garello, Silvio Aime and Daniela Delli Castelli
Department of Molecular Biotechnology and Health Science, via Nizza 52 Turin, Italy, E-mail: daniela.dellicastelli@unito.it

Introduction: The dysregulation of glycolysis stands as a metabolic anomaly observed across various pathologies. Among these dysregulations, foremost is the well-documented phenomenon occurring in numerous solid tumors, recognized as the Warburg effect. Beyond the field of oncology, glycolysis is involved to generate anomalies within peripheral cells in prominent neurodegenerative diseases, namely Alzheimer's and Parkinson's disease, and amyotrophic lateral sclerosis. Furthermore, the alteration of glycolysis is intertwined with the pathogenesis of prevalent liver pathologies, including steatosis and liver cirrhosis. In clinical and pre-clinical settings, numerous imaging techniques have been successfully used to detect aberrant glycolysis such us ^{18}FDG-PET, HP ^{13}C MRI, DMI (Deuterium Metabolic Imaging) and ^{1}H-CEST-MRI [1]. All these techniques share the limitation of relying on exogenous contrast agents to observe the *in vivo* fate of injected metabolites. Indeed, the MRI approach owns a detection limit that does not permit visualization of metabolites from the glycolytic pathway at their endogenous concentrations, even when the detection deals with a magnetically active species such as P-31 whose nat. abundance is 100%. On this basis we deemed of interest to design a novel method for detecting relevant glycolysis involved molecules *in viv*o. In principle Heteronuclear CEST-MRI owns the property of increasing the detectability threshold of the target molecule. This is the consequence of the reduction of the concentration of the "bulk" species that acts as reporter of the CEST effect (in the case of ^{1}H-CEST, this must be the water signal, with a concentration in vivo of 55.6 M). In the case of ^{31}P-CEST one may use the endogenous ^{31}P signal of γ-ATP while saturating the signals of the phosphate groups belonging to the phosphorylated molecules of the glycolytic cascade. ^{31}P MRS saturation transfer has been widely employed to measure Pi ↔ ATP and PCr ↔ ATP exchange fluxes by saturating the γ-ATP spin pool and detecting differences in the signal of either PCr or Pi to estimate Creatine Kinase activity. The same principle is applied here to investgate the glycolysis activity, with the difference that the saturated signals are below the S/N ratio and hence undetectable by MRS. Thanks to the amplification effect of the CEST contrast modality, it becomes possible to indirectly detect signals from phosphorylated metabolites *via* the most abundant signal of γ-ATP.

Methods: ^{31}P-CEST experiment were performed on mice liver by using a Bruker Pharmascan at 7T equipped with a ^{1}H/^{31}P dual tuned volume coil. Z-spectra, centered on the ^{31}P signal of γ–ATP, were acquired over a frequency range of 30 ppm, with steps of 1 ppm. The acquisition of the Z spectrum was carried out by applying an Image-Selected In vivo Spectroscopy (ISIS) pulse sequence that takes 1 minute and 20 seconds per point (TR = 5s TE=5ms, ns=2, voxel size 1.6 cc) for a total scan time of about 40 minutes. The saturation scheme was performed by applying a selective block pulse for 2 sec at 2uT. ^{31}P-Z-spectra were acquired on two groups of five mice each, namely i) 5 healthy mice, ii) 5 healthy mice treated with a glycolysis inhibitor (NaF, 0.36mmol/Kg))

Results and discussion:

The figure below displays a liver localized ^{31}P Z spectrum acquired on the γ-ATP signal. It shows different exchanging peaks some of which might be assigned to the phosphorylated molecules belonging to the glycolytic pathway. The Z spectra acquired on healthy mice (red squares) displays ST (up to about 20%) to γ-ATP from molecules belonging to the glycolytic pathway. Treating mice with NaF, a glycolysis inhibitor, results in a noticeable decrease in the ST (black squares) for all exchanging peaks, particularly pronounced in the glycolytic region. Based on these findings, we believe that this method can offer insights into glycolysis activity, relying solely on endogenous species. Notably, the approach enables the detection of molecules at sub-millimolar concentrations, which would otherwise be challenging to detect by MRS. Significant effort is still required to improve the sensitivity and resolution of the method and to extract quantitative information regarding enzymatic activity.

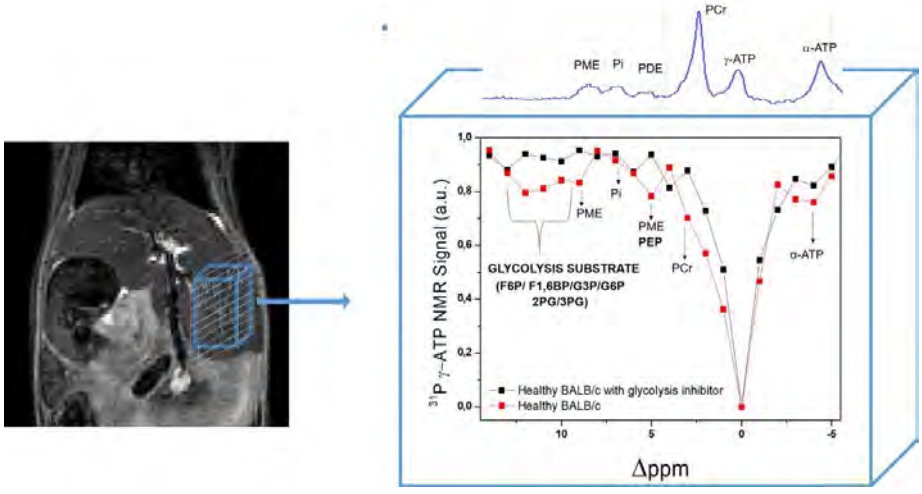

References

[1] Von Morze et al. *Magn Reson Med. 2021;85:1795–1804.*
[2] R. S. Balaban and A. P. Koretsky *AJP-Cell Physiol 2011:301*

Advancing Precision Imaging: Novel Nanotechnology-Based Contrast Agents for MRI and Multimodal Diagnosis

Imaging approaches are indispensable in diagnosing and monitoring a range of illnesses, such as cardiovascular diseases, cancer, and fibrotic disorders. The advent of precision imaging, enabled by innovative nanoparticles, has transformed theranostic imaging by significantly enhancing specificity and sensitivity. This abstract presents recent advancements made by our research group in developing and applying nanoparticles, including lipid particles, pure or doped iron oxides, and calcium carbonates, to improve their diagnostic and therapeutic capabilities. These biocompatible nanoparticles have unique, tunable physicochemical properties that facilitate targeted delivery for advanced molecular imaging and controlled release of therapeutic agents.

Iron oxide nanoparticles are particularly noteworthy due to their superparamagnetic characteristics, making them exceptional MRI contrast agents. Our research has expanded their potential beyond this traditional role, opening up new possibilities for single modality and hybrid imaging applications, including MRI and PET, particularly in the context of 'hot spot' molecular imaging. By incorporating various metals into the core of extremely small iron oxide nanoparticles, we have examined their impact on relaxometry. Furthermore, functionalization with specific ligands, such as peptides, antibodies, or small molecules, enables targeted homing to atheroma plaques. This capability allows for detailed mappings of plaque morphology and composition, facilitating early diagnosis and aiding in cardiovascular disease risk stratification.

Calcium carbonate nanoparticles offer versatility for both imaging and therapy due to their biocompatibility and potential for surface functionalization. By conjugating these inorganic nanoparticles with targeting moieties, they can accumulate in specific tissues, enabling non-invasive visualization and tracking of disease progression, while simultaneously monitoring therapeutic responses with high resolution. They are scalable and reproducible in synthesis, making them suitable for releasing encapsulated drugs and acting as an effective theranostic tool for various applications. Our research group has also investigated the effects of incorporating different atoms, such as Mn, on their relaxometric properties with different applications.

The utilization of lipid-based nanoparticles has led us to the development of MRI-visible formulations designed to treat several diseases. These nanoparticles serve as a sophisticated platform, integrating therapeutic delivery with diagnostic imaging to provide cellular and molecular insights into treatment efficacy. Recent studies have demonstrated the potential of these nanoparticles in enhancing early-stage detection capabilities and broadening applications in areas such as immunotherapy, gene therapy, and diagnostics. This information is critical for assessing disease prognosis and evaluating the effectiveness of, for instance, anti-fibrotic treatments.

The application of precise imaging techniques with novel, functionalized nanoparticles holds great promise in various medical fields as a theranostic tool. These cutting-edge tools are poised to revolutionize both diagnostic imaging and therapeutic delivery by enabling earlier disease detection, personalized treatment planning, and real-time monitoring of disease progression. These advancements are critical for improving patient outcomes. Our presentation will also highlight specific theranostic applications in different fields.

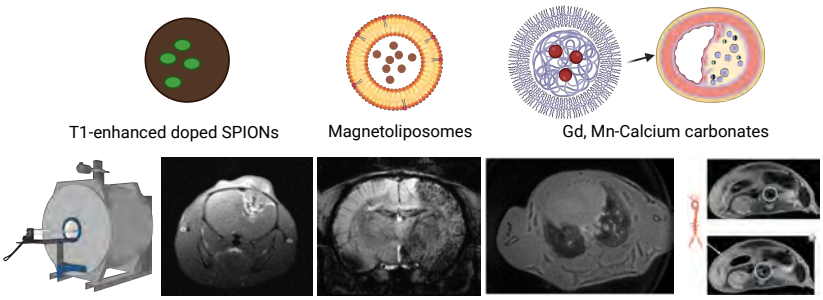

MRI using redox-active iron complex for in vivo assessment of neuroinflammation in a mouse model of multiple sclerosis

Chunxiang Zhang,[1,2] **Eric Gale**,[1] and **Iris Zhou**[1]

[1]Athinoula A. Martinos Center for Biomedical Imaging, Department of Radiology, Massachusetts General Hospital/Harvard Medical School; [2]Department of Radiology, The Third Affiliated Hospital of Zhengzhou University, Zhengzhou, China.

Introduction

Experimental autoimmune encephalomyelitis (EAE) is a common mouse model that mimics the clinical symptoms of multiple sclerosis patients for evaluating neuroinflammation [1]. During active neuroinflammation, inflammatory immune cells in the brain, astrocytes and microglia, are significantly activated, generating a neurotoxic microenvironment in part due to the secretion of reactive oxygen species [2,3]. We hypothesize that extracellular ROS released by reactive microglia and astrocytes during neuroinflammation will mediate the oxidation of Fe-PyC3A from the low-relaxivity Fe^{2+} state to the high-relaxivity Fe^{3+} state [4], generating strong MR signal enhancement. Here, we performed brain imaging with the oxidatively activated ROS-sensing MRI contrast agent, Fe-PyC3A, in a mouse model of EAE-induced neuroinflammation for non-invasive detection of astrocytes and microglia changes.

Methods

A total of 12 C57BL/6 male mice (10-11 weeks old). EAE is induced in C57BL/6 mice by immunization with an emulsion of MOG35-55 in complete Freund's adjuvant, followed by administration of pertussis toxin in PBS, first on the day of immunization and again on the following day (N = 8). Mice were monitored daily, and clinical disease severity was measured using the standard EAE grading scale. Control mice received i.p. injection of saline (3 mg/kg) (N = 4). On day 20 post-immunization, animals were anesthetized with isoflurane (1.5%) and imaged with a 4.7 Tesla Bruker MRI scanner equipped with a custom-built volume coil. Prior to i.v. injection of 0.3 mmol/kg Fe-PyC3A or 0.1 mmol/kg Gd-DOTA, the blood-brain barrier was transiently disrupted via i.v. injection of 25% wt/wt mannitol in the control mice. 2D multi-slice T1-weighted gradient echo images were acquired dynamically before and up to 20 minutes post-injection of Fe-PyC3A or Gd-DOTA. We selected hippocampus as regions of interest (ROIs) and analyzed the (post-pre) injection percentage change in signal intensity (SI%) from these ROIs and (post-pre) injection change in brain ROIs vs. muscle contrast to noise ratio (ΔCNR) from 2 -10 min after Fe-PyC3A or Gd-DOTA injection. Mice were euthanized 1h post-injection, and brain tissue was harvested for immunohistochemical evaluation of microglial activation (Iba1) and astrocytes activation (glial fibrillary acidic protein (GFAP)). The proportional area of Iba-1 and GFAP expression (area %) in the hippocampus was measured in ImageJ.

Results

T1w images recorded prior to and after Gd-DOTA or Fe-PyC3A injection into control and EAE mice demonstrate differential hippocampal signal enhancement in the EAE mice as shown in **Figure 1A**. We found that significantly higher SI% in the hippocampus of EAE mice than in the controls (P=0.13) at 2 min post-Fe-PyC3A (**Figure 1B**) with no significant difference in the SI% between the two groups (P<0.0001) using Gd-DOTA as a non-oxidatively activated negative control probe. In the EAE mice, the ΔCNR in the hippocampus induced by Fe-PyC3A was significantly higher than that using Gd-DOTA (P<0.0001). Iba-1 immunostaining demonstrates significantly greater microglial activation in EAE mice vs. controls (P = 0.027) in the hippocampus, while GFAP immunostaining shows greater astrocyte activation (P = 0.004) (**Figure 1C**). The proportional area of Iba-1 and GFAP expression significantly and positively correlated with SI% (r = 0.792, P < 0.001 and r = 0.872, P < 0.0001; respectively), and ΔCNR (r = 0.702, P < 0.001, and r = 0.743, P < 0.001; respectively), for mice imaged with Fe-PyC3A. In contrast, no significant correlations between SI% or ΔCNR and Iba-1 or GFAP positive area were observed in the hippocampus and cortex for mice imaged with Gd-DOTA.

Conclusion

Molecular MRI using Fe-PyC3A provided robust and selective contrast enhancement in the hippocampus of EAE mice as compared to controls. MR imaging using oxidatively activated MR imaging probes such as Fe-PyC3A merits further evaluation as a marker to quantify neuroinflammation in neurological disorders.

References

[1] Rivers TM, et al. J Exp Med. 1933;58(1):39-53. [2] Sheng WS, et al. Neurochem Res. 2013;38(10):2148-2159. [3] Simpson DSA, et al. Antioxidants (Basel). 2020;9(8):743. [4] Wang H, et al. J Am Chem Soc. 2019;141(14):5916-5925.

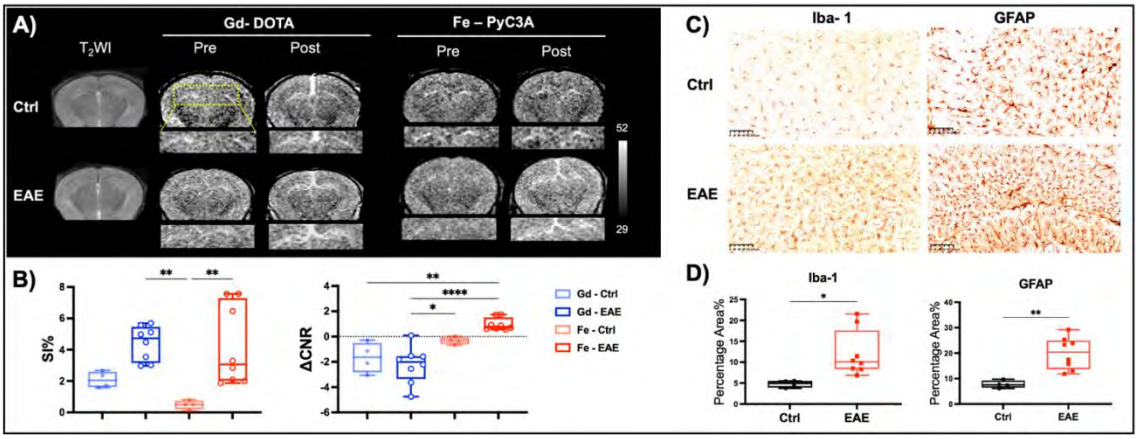

Figure 1 *A) T_1-weighted images acquired before and after injection of 0.1 mmol/kg Gd-DOTA or 0.3 mmol/kg Fe-PyC3A in control and EAE groups (C57BL/6 mice). B) Comparison of SI% and ΔCNR of hippocampus after mice injected with Fe-PyC3A or Gd-DOTA. C) Representative Iba-1 and GFAP immunohistochemistry images for control and EAE mice taken at 20×. D) Proportional area of Iba-1 and GFAP expression (microglia and astrocytes area %) in the hippocampus.*

Any-nucleus Distributed Active Programmable Transmit (ADAPT) Coil

Victor Han[1], Chunlei Liu[1,2]

[1]*Department of Electrical Engineering and Computer Sciences, University of California, Berkeley, CA, USA*

[2]*Helen Wills Neuroscience Institute, University of California, Berkeley, CA, USA*

Introduction: There are 118 known elements. Nearly all of them have NMR active isotopes and at least 39 different nuclei from 33 different elements have been used in biological and biomedical NMR studies[1]. Despite the availability of dozens of NMR active isotopes, most of today's MRI is based on only one nucleus – ^{1}H. Although various technological advances have made the imaging of nuclei other than ^{1}H, or X-nuclei, more clinically feasible, the proliferation of these studies is still held back by the low availability of the tools able to perform them. Whenever an X-nucleus is to be studied, a heavy investment is needed to obtain additional expensive MRI hardware (e.g. RF amplifier, coils and receiver chains) to enable imaging of the specific nucleus of interest. Here, we present the Any-nucleus Distributed Active Programmable Transmit Coil (ADAPT Coil), an inexpensive and untuned, yet scalable, coil capable of efficiently transmitting at arbitrary frequencies using a unique architecture composed of many high-frequency semiconductor power switches integrated directly into the coil structure. By doing so, the coil and RF amplifier are merged into a single device that directly converts DC power into RF fields at any relevant frequency. On the receive side, we use several single-tuned receiver coils to demonstrate the capabilities of our transmit coil. A corresponding arbitrary frequency receiver coil is under development. A paper corresponding to this work has been accepted to *Magnetic Resonance in Medicine*.

Theory and Methods: Resonant coils are severely limited in their bandwidth. So, to make an arbitrary nucleus transmit coil, our approach applies high voltage directly to an untuned coil. This approach mirrors that taken by Mandal et al. and Hopper et al.[2–4] in their low-frequency NMR system covering up to 3 MHz. Their approach, however, is limited by the voltage and speed capabilities of the semiconductors used to apply the voltage, thus confining it to small sizes and low frequencies. Our approach overcomes semiconductor limitations by drawing inspiration from the distributed active transformer[5] in the integrated circuits literature, which addresses a similar problem of generating higher output voltages from low-voltage CMOS transistors by placing several transistors in a loop. Figure 1a-c shows the most basic case of our approach where high-power switches alternating at the RF frequency change the current path of a DC voltage source between two coil halves, thus generating RF currents. Instead of breaking the coil into two halves, we can continue to break it up into smaller pieces, each with a pair of out-of-phase switches connected to the negative terminal of the DC voltage source (Figure 1d-f). Now the same voltage source drives several smaller inductances (coil segments) in parallel and thus can produce larger RF currents. These RF currents together then produce larger magnetic fields than what one set of switches could produce alone.

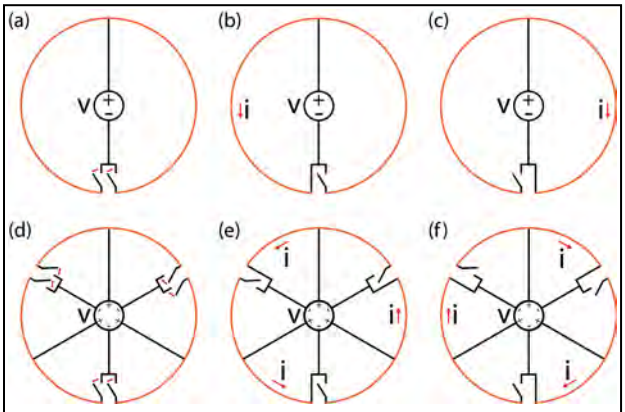

Figure 1: (a-c) Using two switches to connect a DC voltage source across each half of a coil in an alternating manner produces AC current. (d-f) More switches and connections to the DC voltage source enable practical scaling by further segmenting the coil.

The coil architecture was implemented using commercial parts assembled on a four-layer FR4 printed circuit board (PCB). Both phantom and ex vivo (not shown) X-nuclei images were taken using the same ADAPT Coil at 3T by simply changing the control signals for transmit. Multiple single-tuned receive coils were used. The fabricated 9 cm diameter ADAPT Coil has arbitrary frequency capabilities up to 127.7 MHz (^{1}H 3T Larmor frequency).

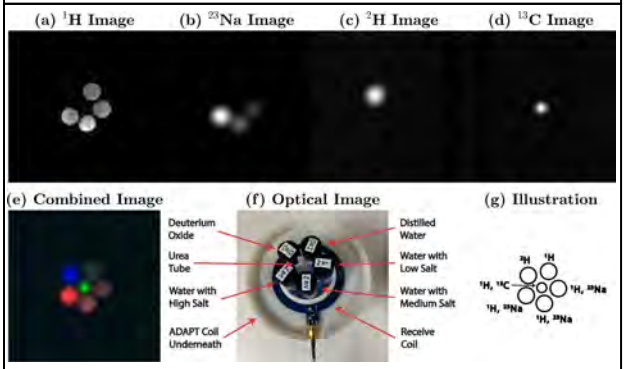

Figure 2: Magnetic resonance images of the bottle and tube phantom.

Results: Figure 2 shows GRE images of a bottle and tube phantom with ^{1}H (Figure 2a), ^{23}Na (Figure 2b), ^{2}H (Figure 2c), and ^{13}C (Figure 2d). The images are overlaid in Figure 2e, a labeled photograph of the phantom is shown in Figure 2f, and an illustration of the phantom is shown in Figure 2g.

Discussion and Conclusion: We present the ADAPT Coil, a scalable and inexpensive method of building arbitrary nucleus transmit coils for high-field, human-scale MRI. The parts on this coil prototype cost less than $116 and a birdcage coil can be similarly built following this strategy. Even without an arbitrary nucleus receive coil, the ADAPT Coil provides many benefits by itself, such as being reusable between scanners of different field strengths and enabling polarization transfer between X-nuclei and ^{1}H. Heteronuclear CEST and hyperpolarized MRI with ^{1}H readout have been shown and would be enabled by this coil. With at least 39 biologically-relevant nuclei[1], we believe the capability to obtain signal from arbitrary X-nuclei can revolutionize the use of magnetic resonance in medicine.

References: 1. Patching SG. NMR-active nuclei for biological and biomedical applications. *Journal of Diagnostic Imaging in Therapy*. 2016; **2.** Mandal S et al. An ultra-broadband low-frequency magnetic resonance system. *Journal of Magnetic Resonance*. 2014; **3.** Hopper T et al. Low-frequency NMR with a non-resonant circuit. *Journal of Magnetic Resonance*. 2011; **4.** Mandal S et al. An extremely broadband low-frequency MR system. *Microporous and Mesoporous Materials*. 2013; **5.** Aoki I et al. Distributed active transformer-a new power-combining and impedance-transformation technique. *IEEE Transactions on Microwave Theory and Techniques*. 2002;

Magnetic resonance imaging of macrophage response to radiation therapy

Fanny Chapelin, PhD[1]; Harrison Yang[2]; Brock Howerton, MS[1]

[1] Shu Chien-Gene Lay Department of Bioengineering, University of California San Diego, La Jolla, CA, USA

[2] F. Joseph Halcomb III, M.D. Department of Biomedical Engineering, University of Kentucky, Lexington, KY

Introduction: Surgery, chemotherapy, and radiotherapy (RT) are all mainstay modalities for treating cancer. The body responds to these therapies through immune responses and distinguishing between antitumor and tumor promoting immune responses can be difficult. Standard practice of macrophage quantification currently involves immunostaining of a biopsied tumor. However, this technique is invasive and fraught with numerous limitations. An imaging biomarker capable of non-invasively depicting and quantifying tumor associated macrophages and *de novo* macrophages infiltrating the tumor *in vivo* could obviate the need for such invasive means.

Methods: In this study, a fluorine nanoemulsion was intravenously delivered to mice bearing breast or colorectal tumors to label and subsequently track macrophage dynamics in response to radiation therapy [1-3]. Murine colon cancer cell line MC38 and murine breast cancer cell line 4T1 were selected due to their high worldwide incidence and frequent treatment with radiation therapy (RT). Ten Balb/c mice received unilateral mammary fat pad injection of 5×10^5 4T1 cells in 100 µL PBS. Ten C57BL/6J mice received unilateral mammary fat pad injection of 5×10^5 MC38 cells in 100 µL PBS. Tumors we allowed to grow for 4-5 days prior to radiation therapy start. Two days prior to radiation (D-2), all mice received intravenous injection of fluorine nanoemulsion (200 µL, C = 150 mg/ml). After baseline MR imaging, five mice in each tumor model were irradiated with a single 8 Gy dose. Mice were monitored for two weeks for tumor growth and ^{19}F signal using a 7T Bruker MR Scanner with a dual-tune ^{1}H/^{19}F volume coil. To gauge the power of our imaging method, we ran correlation tests between the fluorine signal detected and tumor burden irrespective of the timepoint.

Results: Colon tumors displayed significant tumor growth reduction following high dose radiation therapy as early as 7 days post-RT (p=0.01, Fig. 1A&B). Normalized fluorine signal measurements in tumors increased significantly in the RT treated group as early as day 4 post-treatment (p=0.01, Fig. 1C) and continued to remain significantly higher than the untreated group at days 7 and 15 (p = 0.05 and p=0.02, respectively). This indicates significant macrophage influx in the treated tumors, which concurs with previous literature[4, 5]. In the breast cancer model, baseline (day 0) fluorine signal was higher for all mice compared to the colon cancer model. In the treated group, signal intensity appeared to persist or increase with respect to tumor growth, whereas signal decreased in the control group. Conversely to the colon cancer model, all mice bearing 4T1 tumors displayed slower growth but persistent growth, even after therapy. Quantitatively, tumor growth reduction in the RT-treated mice was significant as early as day 4 post-therapy (p=0.009) and remained significantly different throughout the experiment. In 4T1 tumors, macrophage influx seemed slower compared to the MC38 model, as significant signal change only occurred 15 days post-RT (p=0.0005). Spearman's correlation coefficients were significant for all treatment groups (p<0.03).

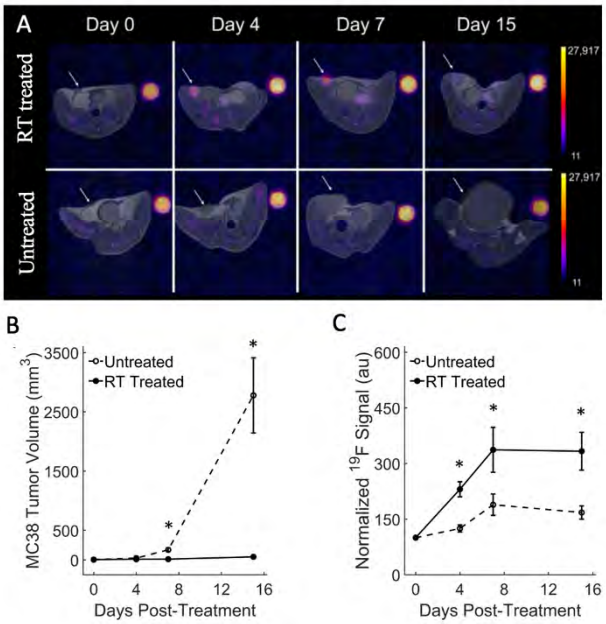

Figure 1. Longitudinal *in vivo* imaging and quantitative analysis of ^{19}F-labeled macrophages in colon tumors**:** Representative ^{1}H/^{19}F MRI overlays of RT treated and untreated (**A**) control mouse bearing MC38 tumors at day 0, 4, 7 and 15 after RT. (**B**) Longitudinal tumor volume measurements show significant tumor growth reduction in RT treated MC38 tumors at day 7 post treatment (*p=0.01). By day 15, the gap between groups widens (*p=0.003). (**C**) Normalized fluorine signal in tumors increases significantly in the RT treated group by day 4 post-treatment (*p=0.01) and continues at days 7 and 15 respectively). Data are presented as mean ± standard error.

Discussion: This study is the first to correlate macrophage signal change to tumor volume and a first step towards accurate non-invasive assessment of RT efficacy. A significant change in ^{19}F signal was found between radiotherapy treated and untreated groups for both the breast and colon cancer models two weeks after irradiation. Treated groups in both cohorts also displayed significant tumor regression. Fluorine signal change correlated to tumor volumes, indicating that MR imaging of macrophage recruitment in tumors may be a valid biomarker of RT efficacy. Additionally, tumors possess apparent mechanistic differences depending on their origin and have varied responses to RT. Therefore, it was imperative to analyze more than one tumor model.

Conclusion: Our findings support the potential therapeutic benefit of incorporating MRI of macrophage dynamics in RT workflow. Non-invasive imaging tools are becoming increasingly necessary to provide safe and accurate tumor prognosis. Finding ways to increase probe specificity to distinguish macrophage phenotypes will be the next challenge but ultimately can dramatically better patient outcomes.

References: (1) Yang, R. *Magn Reson Insights* 2018. (2) Daldrup-Link, H. E. *Clin Cancer Res* 2011, (3) Khurana, A.; *Magn Reson Med* 2017. (4) Croci, D. *Sci Transl Med* 2022. (5) Beach, *Front Oncol* 2022.

Water-Resonant Spin-Locking with MR Fingerprinting for Rapidly Exchanging Proton Quantification

David E. Korenchan[†], Nikita Vladimirov[‡], Or Perlman[‡], and Christian T. Farrar[†]

[†]Athinoula A. Martinos Center for Biomedical Imaging, Massachusetts General Hospital, Charlestown, MA
[‡]Department of Bio-Medical Engineering, Tel Aviv University, Tel Aviv, Israel

Introduction: Chemical exchange saturation transfer (**CEST**) is useful for characterizing diseases and monitoring treatment, such as for brain cancers. Currently, most clinical CEST involves amide proton contrast, which is sensitive to changes in protein content and/or pH within cells. There is a great need to expand CEST to detect and quantify fast-exchanging amine protons to monitor changes in small molecules such as glutamate (**Glu**), which enhances glioma cell motility and growth[1]. While CEST magnetic resonance fingerprinting (**CEST-MRF**) can generate quantitative maps of amide proton exchange rate and concentration in animals and humans[2–4], the faster proton exchange of Glu poses challenges for generating sufficient contrast. In theory, water-resonant chemical exchange spin-locking (**CESL**) generates more contrast from intermediate-exchange protons than by direct saturation *via* CEST[5,6]. Therefore, we hypothesized that introducing CESL elements into an MRF schedule would improve the accuracy of exchange parameter maps.

Methods: Solutions of glutamate were prepared at 10-80 mM concentrations and titrated to pH 7.0 at room temperature. Samples were placed in tubes, arranged within a four-tube imaging phantom, and imaged on a horizontal-bore 9.4 T preclinical scanner at room temperature. Imaging scans included a QUantification of Exchange rate using varying Saturation Power (**QUESP**)[7,8] and T_1 and T_2 mapping sequences, along with the MRF imaging schedules (n = 30 iterations), each using an echo-planar imaging (**EPI**) readout. MRF dictionary generation and dot-product matching were performed with custom Python scripts, and image ROI data were processed in MATLAB. Error maps were generated between MRF-derived parameter maps and the nominal Glu concentration or the average exchange rate across all four tubes, as determined using QUESP.

Results: Using CESL rather than CEST increased the signal contrast ratio between 10 and 80 mM by a factor of about 3.5, even with less than half the duration (**Fig. 1A-B**). By substituting half of the MRF schedule iterations with water-resonant CESL, the mean MRF error in the concentrations was reduced for the 10- and 80-mM tubes and the standard deviation decreased for all tubes (**Fig. 1C-D**). The mean exchange rate was also improved for all tubes except the 80 mM tube, which is likely due to the spin-lock times being too long to effectively capture exchange-dependent signal decay. Initial results on the same phantom at 4.7 T also show substantial improvements in concentration and exchange rate quantification (data not shown).

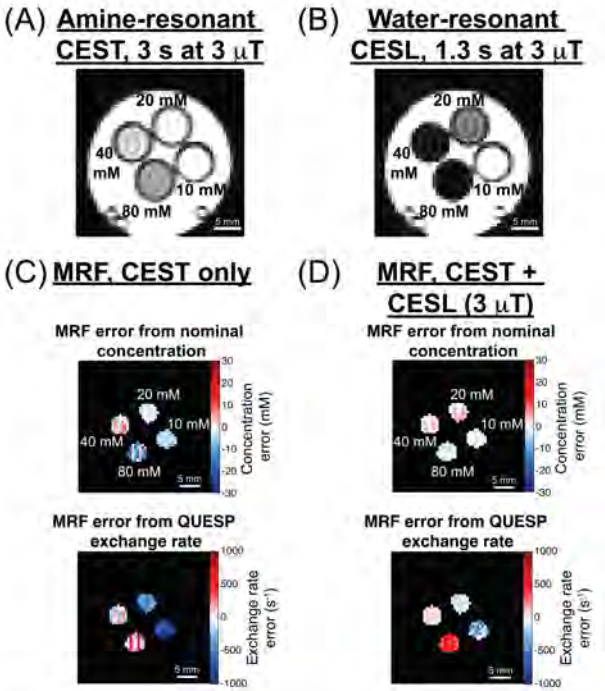

Figure 1. CESL on water improves exchange contrast for quantifying rapidly exchanging protons at 9.4 T. (A-B) Comparison of CEST *vs.* CESL contrast in a four-tube Glu phantom, pH 7. The mean color intensities of the 10 mM tube are equal. (C-D) Error maps of MRF-quantified Glu concentration and exchange rate show lower error by including CESL elements in the MRF schedule.

Discussion: GluCEST requires a 7 T or higher field strength to keep Glu amine proton exchange in the slow-exchange regime for sufficient contrast. By enhancing the detectability of intermediate-exchange solute protons, CESL may enable GluCEST for widely available MRI 3 T scanners since the water-proton chemical shift dispersion nearly matches the reported *in vivo* Glu amine exchange rate at 3 T[9]. Combining CEST and CESL in a single MRF schedule leverages the chemical shift specificity of CEST and the sensitivity of CESL to rapidly exchanging protons.

Conclusion: CESL is highly promising for accurate quantification of concentrations and exchange rates for rapidly exchanging protons, such as those from Glu. Future investigation will involve optimization of the combined CEST-CESL schedule and image reconstruction with AutoCEST, a machine learning framework[3], and *in vivo* neuroimaging.

References:

[1]de Groot, J. & Sontheimer, H. *Glia* **59**, 1181–1189 (2011). [2]Cohen, O., Huang, S., McMahon, M. T., Rosen, M. S. & Farrar, C. T. *Magn Reson Med* **80**, 2449–2463 (2018). [3]Perlman, O., Zhu, B., Zaiss, M., Rosen, M. S. & Farrar, C. T. *Magn Reson Med* **87**, 2792–2810 (2022). [4]Weigand-Whittier, J. *et al. Magn Reson Med* **89**, 1901–1914 (2023). [5]Jin, T., Autio, J., Obata, T. & Kim, S.-G. *Magn Reson Med* **65**, 1448–1460 (2011). [6]Zaiss, M. & Bachert, P. *Phys Med Biol* **58**, R221–R269 (2013). [7]McMahon, M. T. *et al. Magn Reson Med* **55**, 836–847 (2006). [8]Zaiss, M. *et al. Magn Reson Med* **79**, 1708–1721 (2018). [9]Cai, K. *et al. Nature med* vol. 18 302–6 (2012).

Redox double-switch cancer theranostics through Pt(IV) functionalised manganese dioxide nanostructures

Beatriz Brito[1,2,3], Maria R. Ruggiero[1],Thomas W. Price,[1] Manuel Bañobre-López[2], Juan Gallo[2] , Graeme Stasiuk[1]

[1]*Department of Imaging Chemistry and Biology, School of Biomedical Engineering and Imaging Sciences, King's College London, SE1 7EH, London, UK* graeme.stasiuk@kcl.ac.uk

[2]*Advanced (Magnetic) Theranostics Nanostructures Lab, International Iberian Nanotechnology Laboratory, Avenida Mestre José Veiga, 4715-330 Braga, Portugal*

[3]*Department of Biomedical Sciences, University of Hull, HU6 7RX, Hull, UK*

Introduction: Smart theranostics refer to dynamic platforms that integrate multiple functions, including at least imaging, therapy and responsiveness, in a single agent.[1,2] Different smart theranostic systems have been devised in the search for improved diagnostic and therapy efficiency, particularly in oncology, where these agents can respond to changes in the pH, redox environment, or enzymes.[1,2] This work describes the synthesis of MnO_2-Pt nanoparticles (NPs) as redox responsive theranostics for MRI-guided delivery of Pt-based cancer therapy.

Methods: ***Synthesis:*** Using facile ultrasonication chemistry,[3] a series of Mn_xO_y-Pt(IV) NPs were synthesised. These NPs were thoroughly characterised by DLS, TEM, ICP, UV-vis, XPS, FTIR and XRD. **MR *Imaging:*** Relaxometry studies were performed at 1.5 T and MR phantom images were acquired at clinical fields of 3.0 T. ***In vitro imaging and therapeutic evaluation***: The *in vitro* MR efficiency and off-ON switchable properties of the NPs were assessed by imaging 2D and 3D cell cultures of a human lung carcinoma cell line (A549). The cytotoxicity of the NPs was assessed in 2D and 3D cell cultures of the A549 cell line. ***In vivo imaging*** T_1-weighted MR images of tumour-bearing Balb/c nude mice before (pre) and 20 min, 1 h, 3 h, 6 h and 24 h after intratumoral injection of MnO_2-Pt(IV) NPs, using a 9.4 T MR scanner. MnO_2-Pt(IV) NPs (n=5), $MnCl_2$ (n=6) and saline (n=1).[4]

Results and discussion: The synthesis of MnO_2-Pt NPs was optimised to ensure optimal switch off/ON MR properties. Relaxometry studies revealed T_1 signal enhancements as high as 136-fold for NPs with lower Pt/Mn ratios after treatment with a reducing agent, in agreement with the contrast enhancement observed in MR phantoms (3 T). Similarly, *in vitro* MRI studies on 2D and 3D cell cultures of A549 cells treated with the MnO_2-Pt NPs showed a significant enhancement of the T_1 signal over 12 h, which indicates the MnO_2-Pt NPs can be efficiently reduced to free Mn(II) by the cells. Results from cell viability studies show that the toxicity of the nanosystem (IC_{50} = 100.0 µM) is considerably higher than that of the precursor Pt(IV) prodrug (IC_{50} = 420.5 µM). A significant tumour signal enhancement was observed immediately after the injection of MnO_2-Pt(IV) NPs, suggesting that the nanoparticles were readily reduced in the tumour. Importantly, the T_1 signal enhancement in the tumour could still be detected 24 h post-injection of the NP, but not of $MnCl_2$, which was cleared much faster (3 h) from the tumour tissue.

Conclusions: These MnO_2-Pt NPs are equipped with redox responsive imaging and therapeutic modalities. They can be reduced *in vivo* by cancer cells, leading to a significant increase of the T_1 signal. This reduction also leads to cancer cell death by Pt-induced apoptosis. MnO_2-Pt nanosystems can induce a T_1 switch as the drug is released in cancer cells. Importantly, these nanostructures led to a strong and long-lasting T_1 signal enhancement *in vivo*, with a 240% T_1 enhancement observed at 3 h post-injection (*vs* 110% for $MnCl_2$) following intra-tumoural injection. These results indicate that MnO_2-Pt(IV) nanostructures present great potential as redox responsive dual switch MR theranostics for cancer therapy.

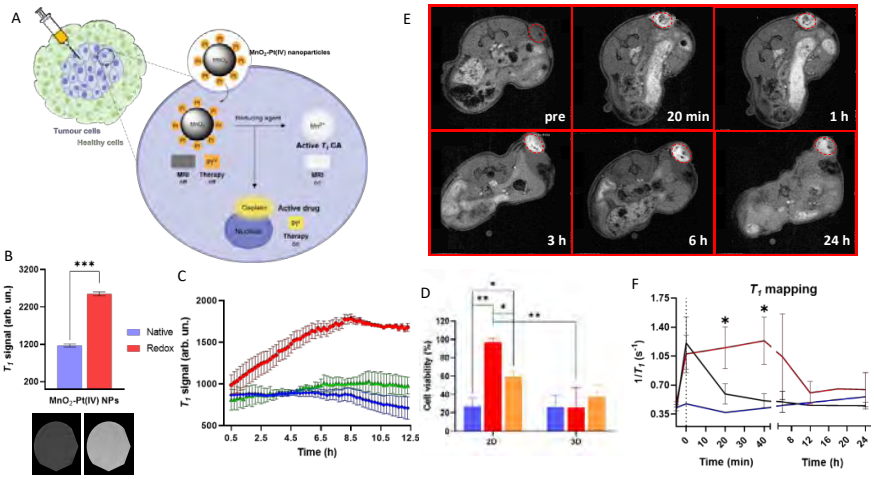

Figure 1. A) Proposed redox responsive mechanism of MnO_2-Pt(IV) NPs. **B)** T_1-weighted MRI phantoms of MnO_2-Pt(IV) NPs and corresponding signal before (blue) and after (red) redox treatment, [Mn] = 0.7 mM, ***p<0.0001. **C)** MR T_1 signal evolution of 2D model of A549 cells treated with MnO_2-Pt NPs (0.6 mM of Mn) over time, at 3 T. Blue: cells; purple: NPs in media, red: cells treated with NPs and representative T_1 images acquired. **D)** Comparison of cell viability in 2D and 3D A549 cell cultures after 48 h of treatment Pt concentrations of 100 µM (blue cisplatin, red, Pt(IV), orange MnO_2-Pt(IV), (n=3), *p<0.04 and **p<0.005.E) T_1-weighted MR images of tumour-bearing Balb/c nude mice before (pre) and 20 min, 1 h, 3 h, 6 h and 24 h after intratumoral injection of MnO_2-Pt(IV) NPs, using a 9.4 T MR scanner **F)** Local T_1 values of tumour and muscle tissues of mice treated with MnO2-Pt(IV) NPs (n=5), $MnCl_2$ (n=6) and saline (n=1), obtained using a T_1 mapping sequence on the 9.4 T MR scanner, showing mean and errors (SEM), *p<0.045

References: 1) Parodi, et al. Smart nanotheranostics responsive to pathological stimuli. *Front Bioeng Biotechnol*, **2020**, 8, 503. **2)** Brito, et al. Smart magnetic resonance imaging-based theranostics for cancer. *Theranostics* **2021**, 11 (18), 8706. **3)** Bañobre-López, et al. Tunable performance of manganese oxide nanostructures as MRI contrast agents. *Chem Eur J*, **2018**, 24 (6), 1295-1303.**4)** B. Brito, et. al. Redox double-switch cancer theranostics through Pt(iv) functionalised manganese dioxide nanostructures, *Nanoscale*, **2023**, 15, 10763-10775

Imaging oxidative stress markers in experimental neuroinflammation using a highly efficient myeloperoxidase-activatable MRI probe

Cuihua Wang[1,2], Enrico G. Kuellenberg[1,2], Negin Jalali Motlagh[1,2], Gregory R. Wojtkiewicz[2], John W. Chen[1,2]

[1]Institute for Innovation in Imaging, Department of Radiology, Massachusetts General Hospital, Charlestown, MA 02129; [2]Center for Systems Biology, Massachusetts General Hospital and Harvard Medical School, Boston, MA 02114.

Introduction: Myeloperoxidase (MPO) is a pro-inflammatory and highly oxidative enzyme expressed by neutrophils, macrophages and microglia, and is found in active demyelinating lesions in multiple sclerosis (MS) patients and in experimental autoimmune encephalomyelitis (EAE) model of MS. Acrolein-protein adducts derived from highly reactive acrolein generated from MPO oxidation are found around macrophages and microglia in active MS lesions and EAE infiltrates.[1] We have developed a new generation of MPO activatable MRI probe (heMAMP) (**Fig. 1A**), which is not only thermodynamically more stable, but also possesses high efficacy in detecting MPO activity *in vivo* in inflammation and tracking treatment effect of MPO inhibition in a mouse model of unstable atherosclerosis.[2] In this study, we hypothesize that heMAMP MRI can report the changes of MPO activity and correlate with acrolein levels at different stages of EAE.

Methods: *Synthesis*. heMAMP was synthesized following an established procedure we have published previously.[2] *EAE induction*. All animal experiments were approved by and in compliance with the Institutional Animal Care and Use Committee at Massachusetts General Hospital. 8-10 weeks old C57BL/6 mice were used to induce EAE with myelin oligodendrocyte glycoprotein (MOG_{35-55}) injected subcutaneously at four sites (axillary and inguinal of the mice), and mice injected with vehicle as control. N = 8-10 mice for each group. *In vivo imaging*. We performed MR imaging with serial T1-weighted sequence before injection and after administration of heMAMP (0.1 mmol/kg) intravenously on a 4.7-T small animal MR scanner (Bruker, MA). *MPO activity assay*. MPO was captured by anti-MPO antibody, and its activity was measured using 10-acety-3,7-dihydroxyphenoxazine (ADAH) assay. $P < 0.05$ was considered as significant difference. Data were expressed as means ± SEM.

Results: We observed much higher signal enhancement in the lesions in the spinal cord (**Fig. 1B**) at the acute stage of the EAE mice (1-2 days after symptom onset) compared to those in the chronic stage 60 min post-injection (7.64 ± 2.96 vs. 0.25 ± 1.54, p = 0.028) (**Fig. 1B** and **1C**). Similarly, total lesion volume and MPO activity in the chronic stage were markedly decreased compared to that in the acute stage (1.24 ± 0.54 μm^3 vs. 0.41 ± 0.28 μm^3, p = 0.0062; 37.69 ± 6.29 RFU/s vs. 13.35 ± 4.61 RFU/s, p=0.001, respectively), which correlated well with the imaging data. Acrolein adduct assay showed that acrolein level in the acute stage was much higher than that in the chronic stage (1070 ± 65.30 vs. 365.6 ± 49.29, p<0.0001), and no significant difference between the chronic stage and sham (**Fig. 1F**).

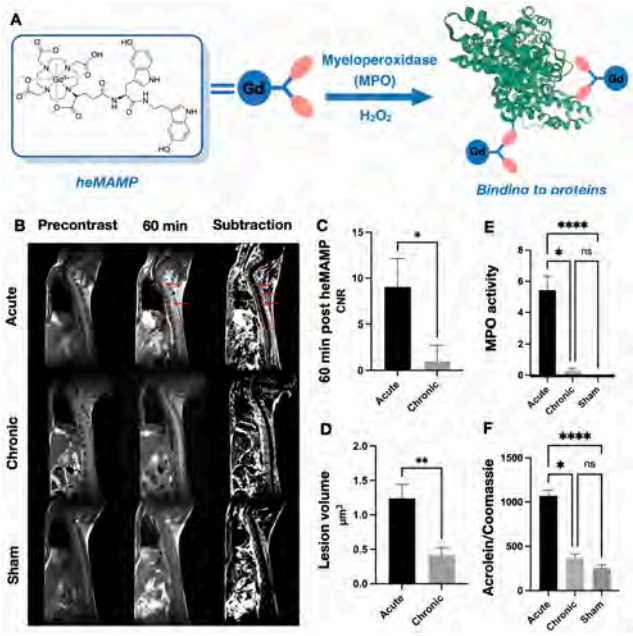

Figure 1. **A)** Graphic illustration of the activation mechanism of heMAMP by MPO. **B)** MR images of heMAMP at different stages of EAE for the precontrast and at 60 min. **C)**, **D)**, and **E)** Total lesion volumes, contrast-to-noise ratios (CNRs), and MPO activity at the acute and chronic stages of MOG_{35-55} induced EAE mice and sham mice. **F)** Acrolein adduct assay at acute and chronic stages of EAE and sham mice.

Discussion and Conclusion: Both MPO activity and acrolein levels were markedly increased during the acute stage of EAE. heMAMP MRI correlated well with *ex vivo* MPO activity and acrolein adduct assays in both acute and chronic stages in MOG_{35-55}-induced EAE model. In conclusion, MR imaging of heMAMP could provide a noninvasive imaging tool to detect MPO activity and acrolein levels in active lesions in MS.

References: 1. Spaas, J. *et al*. Carnosine quenches the reactive carbonyl acrolein in the central nervous system and attenuates autoimmune neuroinflammation. *J Neuroinflammation* **2021,** *18*, 255.
2. Wang, C. *et al*. Highly Efficient Activatable MRI Probe to Sense Myeloperoxidase Activity. *J Med Chem* **2021,** *64*, 5874-5885.

Improving the relaxivity response of potential Mn(II)-based pH-responsive probes

Enikő Madarasi,[a] Balázs Váradi,[a] András Zubor,[a] Zoltán Garda,[a] Enikő Molnár,[a] Fairodzliana Zaharia,[a] István Kapus,[a] Ferenc Krisztián Kálmán,[a] György Trencsényi,[b] János Kiss,[c] Gergő Veres,[c] Imre Tóth[a] and Gyula Tircsó[a]

[a]University of Debrecen, Department of Physical Chemistry, Faculty of Science and Technology, [b]Division of Nuclear Medicine, Department of Medical Imaging, Faculty of Medicine, and [c]Clinical Center, Medical Imaging Clinic, Radiology, Debrecen, Hungary

Introduction: Molecular probes capable of detecting variations in environmental pH can be of particular interest for the non-invasive detection of diseases, metabolic disorders etc. Tissues with lowered pH indicate the presence of hypoxia, tumor growth and metastases (malignant tumors present with pH ranging from 6.6–7.2). [1] Myocardial ischemia and low tissue pH is often go together and can indicate heart disease.[2] Therefore pH responsive probes can provide relevant information which in turn may impact directly the treatment or monitoring their efficacy. Couple of years ago we have reported the first Mn(II)-based pH-responsive probe, PC2A-EA.[3] The given probe responds to the changes in pH near to physiological pH (pK=6.88), but its response is modest in terms of relaxivity. Therefore, in the present work, we investigated the possibility of improving the relaxivity response of Mn(II)-based pH-responsive probes by designing ligands possessing amide (3,9-PC2AM^{Pip}-EA) or bidentate picolinate (3-PCPA-EA) pendant arms into the ligand structure.

Methods: Ligands were synthesized using standard chemical synthetic techniques, while the metal complexes were isolated and characterized by high-pressure liquid chromatography (HPLC), mass spectrometry (MS), and ^{1}H relaxometry. The thermodynamic stability of the Mn(II) complexes were determined by the combination of pH-potentiometric and ^{1}H relaxometric techniques, while solvent exchange kinetics was studied via variable temperature ^{17}O NMR method. Dissociation kinetics of the complexes were accessed by studying metal exchange reactions with essential (Cu(II) and Zn(II)) metal ions; and their serum stability was also evaluated by using commercially available human blood serum. T_1 and T_2-weighted images of the phantoms were acquired at 25 °C by using clinical (Siemens Magnetom Essenza 1.5 T and Philips Achivea 3T) MRI scanners.

Results: The 3,9-PC2AM^{Pip}-EA ligand forms a thermodynamically less stable Mn(II) complex (logK_{MnL}=14.73, pMn=7.79) than that observed for the acetate derivative (logK_{MnL}=15.92, pMn=9.27). However, the replacement of the two acetate groups in the parent 3,9-PC2A-EA ligand by a bidentate picolinate group resulted in a significant increase in the stability constant of (logK_{MnL}=18.96, pMn=9.53) while the protonation constants of the complexes were found to be acceptable for the use in both cases (6.55 and 6.18, respectively). Kinetic studies showed that the inertness of the [Mn(PCPA-EA)] complex did not improve significantly ($t_{1/2}$=6.92 h at pH=6.0, 25 eq. Zn(II) ion at 37 °C) and this was also true for the relaxivity data corresponding to the "turned on" (q=1) and "turned off" (q=0) forms (r_{1p}/r_{2p}=3.21/4.58 (q=1) vs. 1.02/1.10 (q=0)). However, the inertness of the [Mn(PC2AMPip-EA)] complex ($t_{1/2}$=119.6 h at pH=6.0 with 25 eq. Zn(II) ion at 37 °C) and relaxivity data (r_{1p}/r_{2p}=4.49/8.57 (q=1) vs. 1.87/2.50 (q=0)) were significantly improved as compared to the values observed for the parent [Mn(3,9-PC2A-EA)] chelate.

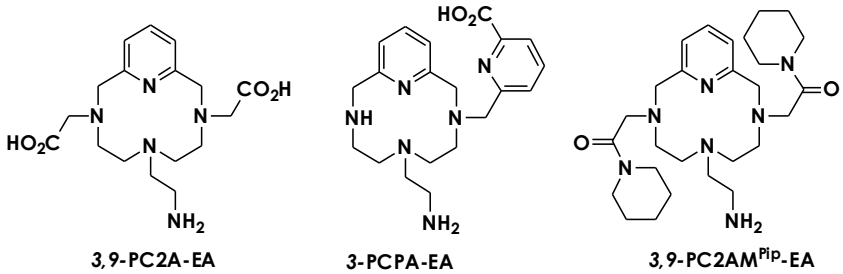

Figure 1. Formulae of the *3,9*-PC2A-EA, 3-PCPA-EA and *3,9*-PC2AM^{Pip}-EA ligands.

Discussion: The use of a picolinate side chain attached to the pyclen macrocycle (3-PCPA-EA) improves the stability of the Mn(II)-based pH-responsive probe, but does not affect its relaxation and dissociation kinetics parameters notably. In contrast, the Mn(II) complex of the PC2A-bis(amide) (3,9-PC2AM^{Pip}-EA) derivative has significantly better relaxation and kinetic parameters than the parent compound (3,9-PC2A-EA).

Conclusion: The relaxivity response of the Mn(II)-based pH-responsive probes can be tuned by the proper selection of the metal binding pendant arms.

References: [1] R. A. Gatenby, E. T. Gawlinski, A.F. Gmitro, B. Kaylor, R. J. Gillies, *Cancer Res.* **2006,** *66,* 5216–5223; [2] G.-X. Yan, A. G. Kleber, *Circulation Res.,* **1992** *71(2),* 460-470; [3] R. Botár, E. Molnár, Gy. Trencsényi, J. Kiss, F. K. Kálmán, Gy. Tircsó, *J. Am. Chem. Soc.* **2020,** *142(4),* 1662–1666.

Acknowledgement: The research was funded by the Hungarian National Research, Development and Innovation Office (NKFIH K-134694, FK-134551 and PD-138064 projects). The scientific research was supported by the Gedeon Richter's Talentum Foundation established by Gedeon Richter Plc (Gedeon Richter Ph.D. Fellowship). The research was prepared with the professional support of the Doctoral Student Scholarship Program of the Cooperative Doctoral Program of the Ministry of Innovation and Technology financed from the NKFIH.

Texaphyrin-Based Calcium Sensor for Multimodal Imaging

Grégory D. Thiabaud,[1] Miriam Schwalm,[1] Sajal Sen,[1] Ali Barandov,[1] Jacob Simon,[1] Peter Harvey,[1] Virginia Spanoudaki,[2] Peter Müller,[3] Jonathan L. Sessler,[4] and Alan Jasanoff*[1]

[1]Department of Biological Engineering, Massachusetts Institute of Technology, Cambridge, Massachusetts 02139, United States; [2]Preclinical Imaging & Testing Facility, Koch Institute at MIT, Cambridge, Massachusetts 02139, United States; [3]Department of Chemistry, X-ray Diffraction Facility, Cambridge, Massachusetts 02139, United States; [4]Department of Chemistry, The University of Texas at Austin, Austin, Texas 78712-1224, United States.

Introduction: The ability to monitor intracellular calcium concentrations using fluorescent probes has led to important insights into biological signaling processes at the cellular level. An important challenge is to relate such measurements to broader patterns of signaling across fields of view that are inaccessible to optical techniques. A calcium sensitive small molecule displaying both optical and magnetic resonance imaging capabilities would allow researchers to overcome this challenge and would be valuable for studying brain activity at both cellular and whole brain levels.

Methods: To meet this need, we synthesized molecular probes that couple calcium-binding moieties (BAPTA) to lanthanide or transition metal texaphyrins, resulting in complexes endowed with a diverse complement of magnetic and photophysical properties.[1]

Results: Fluorescence and photoacoustic emissions, as well as longitudinal relaxivity of the new calcium-sensitive texaphyrin (CaST) probes are altered upon addition of calcium chloride. Calcium-dependent responses of the new probes are also in line with results obtained using bimolecular BAPTA/metallotexaphyrin model systems. We show that the CaST probes are cell permeable and permit intracellular calcium levels to be assessed by the above-mentioned three imaging modalities, and that they are also detectable by multimodal imaging in brain tissue.

Discussion: Results from relaxivity measurements in cells are comparable in magnitude to the previously reported intracellular calcium sensor from our lab.[2] The responses obtained upon calcium stimulation by MRI and photoacoustic are somewhat lower in complex media (such as intact cells) than in simple buffers. One explanation is that the very opened coordination sphere in lanthanide texaphyrins make them very susceptible to axial coordination with biomolecules, which in turn can restrict the dynamic range of the probes.

Conclusion: This work establishes a route for monitoring signaling processes over a range of spatial and temporal scales using three different modalities with one reporter. We are currently working on tuning access to the metal center to improve response properties and prevent interference from biological solutes.

References: [1] Thiabaud, G. D.; Schwalm, M.; Sen, S.; Barandov, A.; Simon, J.; Harvey, P.; Spanoudaki, V.; Müller, P.; Sessler, J. L.; Jasanoff, A. Texaphyrin-based calcium sensor for multimodal imaging. *ACS Sensors* **2023**, *8*, 3855-3861. [2] Barandov, A.; Bartelle, B. B.; Williamson, C. G.; Loucks, E. S.; Lippard, S. J.; Jasanoff, A. Sensing intracellular calcium ions using a manganese-based MRI contrast agent. *Nat. Commun.* **2019**, *10*, 897.

POSTER PRESENTATIONS

IN ORDER OF PROGRAM

Enhancing Assessment of Tumor Metastatic Aggressiveness through Combined Shift/AcidoCEST

Anaïs Choffart[1,2], Remy Chiaffarelli[1,2], Max Zimmermann[1,2], Laura Kuebler[1,2,3], André F. Martins[1,2,3]
[1]University Hospital of Tuebingen, Werner Siemens Imaging Center, Department of Preclinical Imaging, Tuebingen, Germany, [2]University of Tuebingen, Cluster of Excellence iFIT (EXC 2180), Tuebingen, Germany, [3]German Cancer Consortium (DKTK), partner site Tübingen, German Cancer Research Center (DKFZ), Heidelberg, Germany

Introduction: Tumor cells typically display a hyperglycolytic metabolic phenotype characterized by increased lactate production, known as the Warburg effect. This shift in oxidative metabolism frequently leads to a more acidic microenvironment[1]. This adverse microenvironment represents a metabolic hallmark in invasive cancer cells. However, to date, no effective methods are available to evaluate cancer progression and metastatic potential *in vivo*. This study marks the first instance of combining acidoCEST with shiftCEST to simultaneously map extracellular pH and lactate, enabling discrimination of tumor aggressiveness.

Methods: Two PyMT-derived murine breast cancer cell lines, a parental and a G6 metastatic, were selected for their distinct phenotypic aggressiveness and organ tropism. Cells were injected orthotopically in the 4th mammary fat pad of C57BL/6N mice. Hybrid shift/acidoCEST spectra were acquired on cells supernatant or tumor-bearing mice on a 7T preclinical MR scanner (Brucker Biospec 70/30) following the injection of the iopamidol+Shift Reagent (SR) solution. CEST acquisitions were performed using 3 or 14 µT and 6- or 5- second continuous saturation pulses for acidoCEST[2] or shiftCEST[3], respectively. The uptake of [13C]lactate was assessed following the incubation of the cell lines with medium containing 3 mM of [1-13C]lactate. Metabolites were extracted from the supernatant and analyzed using NMR.

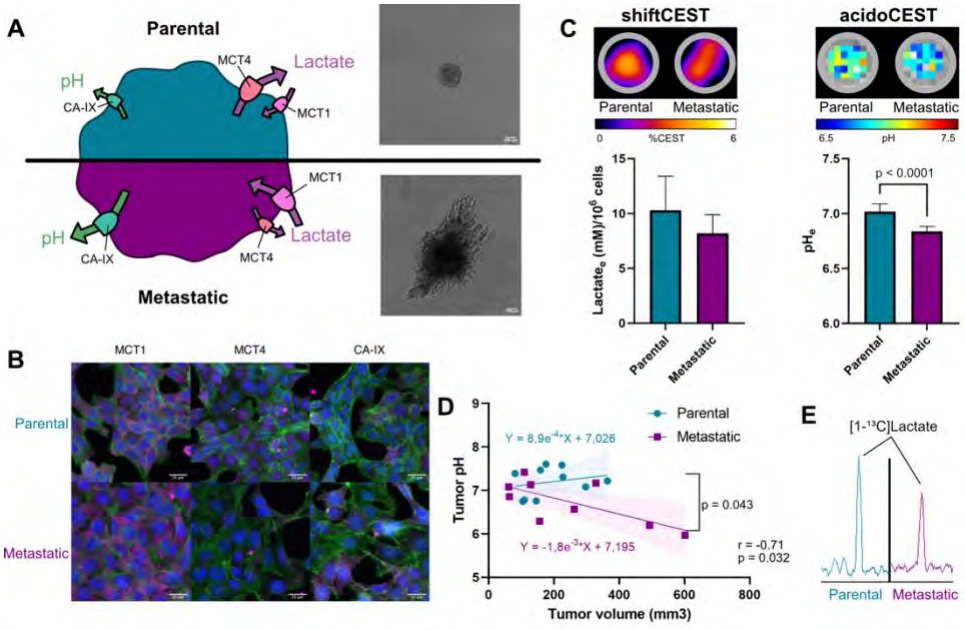

Figure 1: Hybrid CEST imaging for extracellular metabolic detection of tumor aggressiveness. *A) Left: Schematic representation of the altered metabolism in the two murine cell lines. Right: Microscopy images of the spheroid invasion assay on Day 5. B) Microscopy images of protein expression assessed by immunofluorescence. C) Left: CEST image at 47 ppm (top) and shiftCEST MRI quantification (bottom) of lactate produced by the cells over 48h. Right: Voxel representation (top) and acidoCEST MRI quantification (bottom) of the corresponding pH. D) Correlation plot comparing Tumor pHe and tumor volume. E) [13C] NMR spectra of cells' supernatant after 48h of incubation with [1-13C]lactate.*

Results and discussion: The *in vitro* characterization of the PyMT-derived cells demonstrated a pronounced invasion phenotype for the metastatic cell line that correlated with enhanced metabolic activity. We investigated whether this metabolic drift resulted in an increased extracellular lactate secretion or acidity. Simultaneous shift/acidoCEST performed on supernatants revealed an increased acidification with the metastatic cell line, despite a lower lactate secretion. The same tendency was observed in the tumor-bearing mice, where metastatic tumors exhibited a negative correlation between tumor volume and pHe. In contrast, no correlation was observed for the parental non-metastatic tumors. Moreover, metastatic tumors exhibited reduced lactate levels compared to parental tumors.

Discussion: The reduced lactate level observed in the metastatic tumors despite a higher acidity are indicator of a potential altered metabolic adaptation. Metabolomics suggested a new capability of metastasis to uptake lactate from the tumor microenvironment, matching our preclinical results.

Conclusion: In conclusion, our study underlines the efficacy of shift/acidoCEST as a reliable method for non-invasive detection of extracellular acidity and lactate production in tandem by MRI. Our research highlights the adaptability of tumor metabolism, demonstrating its ability to repurpose waste products such as lactate to thrive in hostile environments and potentially facilitating invasion of surrounding tissues.

References: [1] Corbet, Cyril, et Olivier Feron. « Tumour Acidosis: From the Passenger to the Driver's Seat ». Nature Reviews. Cancer, vol. 17, no 10, octobre 2017, p. 577-93. PubMed, https://doi.org/10.1038/nrc.2017.77. [2] Moon, Brianna F., et al. « A Comparison of Iopromide and Iopamidol, Two AcidoCEST MRI Contrast Media That Measure Tumor Extracellular PH ». Contrast Media & Molecular Imaging, vol. 10, no 6, 2015, p. 446-55. PubMed, https://doi.org/10.1002/cmmi.1647. [3] Zhang, Lei, et al. « Imaging Extracellular Lactate In Vitro and In Vivo Using CEST MRI and a Paramagnetic Shift Reagent ». Chemistry, vol. 23, no 8, février 2017, p. 1752-56. PubMed, https://doi.org/10.1002/chem.201604558.

Bioinspired microparticles for molecular imaging of microthrombi during acute ischemic stroke

Charlène Jacqmarcq[1], Audrey Picot[1], Jules Flon[1], Marina Rubio[1], Florent Lebrun[1], Sara Martinez de Lizarrondo[1], Mikaël Naveau[2], Aurélie Malzert-Fréon[3], Benoît Bernay[4], Didier Goux[5], Maxime Gauberti[1,6], Denis Vivien[1,7], Thomas Bonnard[1]

1 Normandie Univ, UNICAEN, INSERM UMR-S U1237, Physiopathology and Imaging of Neurological Disorders (PhIND), GIP Cyceron, Institute Blood and Brain @ Caen-Normandie (BB@C), Caen, France ; 2 UNICAEN, CNRS UMS 3408, Caen, France ; 3 UNICAEN, CERMN, Caen, France ; 4 UNICAEN, US EMerode, Plateforme Proteogen, Caen, France ; 5 UNICAEN, US EMerode, Centre de Microscopie Appliquée à la Biologie (CMAbio3), Caen, France ; 6 CHU Caen, Department of Neuroradiology, Caen, France ; 7 CHU Caen, Clinical Research Department, Caen, France ;

Introduction : Microthrombi can form in the context of strokes, either through the breakdown of a proximal clot or by direct formation within the cerebral microcirculation. These are challenging to detect using current imaging methods, yet they can result in long-term dementia and cognitive impairments(1). Contrast agents developed for detecting clots in MRI have the drawbacks of being either insensitive or non-biocompatible(2). In this study, we propose using polydopamine, a biomaterial, to aggregate iron oxide nanoparticles into clusters and reveal microthrombi in MRI.

Methods : We synthesized iron oxide microparticles from commercial superparamagnetic iron oxide particles (SPIO) (Vivotrax, Magnetic Insight), which were clustered using polydopamine. The microparticles (referred to as PHySIOMIC for Polydopamine Hybridized Superparamagnetic Iron Oxide Mussel-Inspired Clusters) were characterized using optical and transmission electron microscopy, dynamic light scattering, and microfluidics. Microthrombi formation was induced by injecting murine thrombin into the middle cerebral artery of the mouse, creating a proximal clot with microthrombi in the cerebral cortex. PHySIOMIC were intravenously injected 30 minutes after stroke induction. MR images were acquired using a susceptibility-weighted sequence (T_2*).

Results : The resulting particles have a diameter of 700 nm and exhibit a signal twice as strong as SPIO alone in MRI. Following intravenous injection immediately after the induction of stroke and microthrombi formation in a thromboembolic stroke model in mice, the particles are seen as a pronounced hyposignal in the ipsilateral cerebral cortex. This signal area correlates with the lesion size measured 24 hours later in the same animals using a T_2-weighted sequence. Treatment with the reference fibrinolytic, recombinant tissue-type Plasminogen Activator (rTPA), resulted in the disappearance of the hyposignal in MRI.

Discussion : In this study, we have demonstrated that clustering SPIO into microparticles leads to a heightened MRI signal, facilitating the detection of minute events like microthrombi. The regions where microthrombi are visualized using these particles correlate with the lesion size measured 24 hours later, indicating the potential to predict lesion size based on PHySIOMIC measurements. Furthermore, these particles enable the monitoring of microthrombi during thrombolysis; specifically, the administration of fibrinolytic treatment results in the observed signal loss, corresponding to the dissolution of microthrombi in the cerebral cortex.

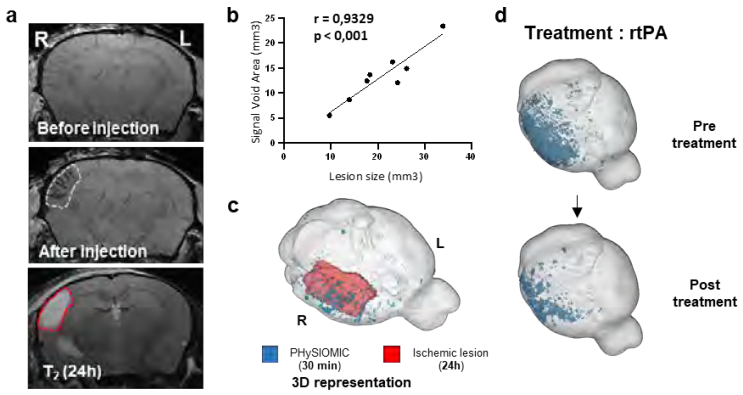

Figure 1. a, Mr images before, after injection of PHySIOMIC and stroke-induced lesion 24 hour later. **b,** Correlation between PHySIOMIC' signal void measurement and lesion size. **c,** 3D representation of PhySIOMIC signal void and lesion. **d,** representation of PHySIOMIC before and after treatment with rtPA.

Conclusion : The PHySIOMIC microparticles hold great promise for detecting microthrombi, which in the thromboembolic stroke model can predict the lesion size, as well as for monitoring the reperfusion of microvessels in stroke patients undergoing treatment. The biocompatibility of the materials ensures the contrast agent is well metabolized, paving the way for future clinical use.

References :

(1) Bhatia R. et al. (2010). Low rates of acute recanalization with intravenous recombinant tissue plasminogen activator in ischemic stroke. Stroke 41, 2254–2258.

(2) Shapiro E.M. et al (2005). Sizing it up: Cellular MRI using micron-sized iron oxide particles. Magnetic Resonance in Medicine 53, 329–338

In Vitro Phantom Solution for ^{129}Xe HyperCEST: Preclinical Sequence Optimization Under Enhanced Relaxation

Hannah Gerbeth[1,2,3], Leif Schröder[1,2,3]

[1]Division of Molecular Translational Imaging, German Cancer Research Center (DKFZ), Heidelberg, Germany
[2]German Cancer Consortium (DKTK), DKFZ, core center Heidelberg, Germany
[3]Department of Physics and Astronomy, Ruprecht-Karls University Heidelberg, Germany

Introduction: Xenon-129 HyperCEST measurements improve the sensitivity and specificity of molecular diagnostics with NMR/MRI. However, the translation from *in vitro* to *in vivo* applications requires further research. Challenges include reduced relaxation times and lower concentrations of hyperpolarized gas (hp) in the target tissue, leading to reduced signal intensity. To address this, an in vitro phantom solution that mimics the relaxation times of blood was developed to pre-evaluate the acquisition parameters and saturation optimization. This ensures an optimal experimental setup before starting *in vivo* testing, to minimize animal burden.

Methods: Measurements were performed on a Bruker Avance III HD console at 9.4 T. A gas mixture of 2% Xe, 10% N_2, and 88% He was dispersed into a 1 ml sample solution for 15 s at a flow rate of 80 ml/min and an operating pressure of 4.5 bar (abs.).

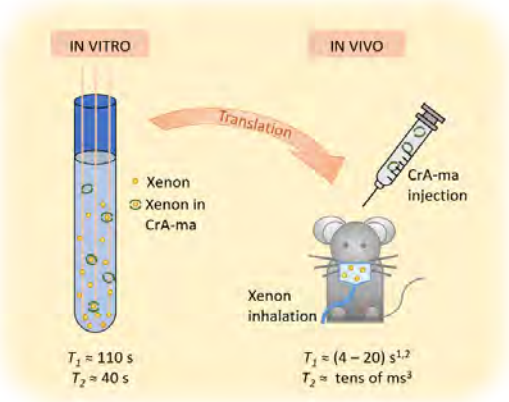

Figure 1: Comparison of longitudinal and transversal relaxation times *in vitro* and *in vivo*. *In vitro* values were measured on a Bruker Avance III HD console at 9.4 T and 20°C. The *in vivo* values found in literature can vary and depend on magnetic field strength, temperature, bloodoxygenation, and tissue type.

Different concentrations of relaxation agents BSA (Bovine Serum Albumin), antifoam A (AFA), and Dotarem® were investigated for their influence on hp ^{129}Xe relaxivities. The T_2 relaxation times were measured with a conventional CPMG sequence, while T_1 relaxation times were determined by bubbling hp ^{129}Xe into the phantom and recording signals over increasing time delays. Based on the results of the relaxometry measurements, an *in vitro* phantom solution with reduced relaxation times was developed.

To investigate, whether HyperCEST measurements under these enhanced relaxation cponditions yield sufficient CEST contrast, z-spectra were acquired using the host molecule Cryptophane-A monoacid (CrA-ma) at a constant saturation power of 2 mW and different saturation times.

Results and Discussion: The final *in vitro* phantom solution contained 5.4% BSA, 0.3% AFA and 500 µM Dotarem®. The combined influence of these relaxation agents reduced the relaxation times of hp ^{129}Xe from 110 s ($T1$) and 40 s (T_2) in pure water to physiologically relevant 11 s and 30 ms, respectively (Fig. 1).[1,2,3]

HyperCEST measurements of hp ^{129}Xe in the phantom solution reveal two distinct peaks at -133 ppm and -126 ppm. While the first one corresponds to xenon caged in CrA-ma, the origin of a second peak (possibly from CrA-ma binding to BSA or AFA-induced micelle formation) is under investigation. Although the short T_1 relaxation times of xenon in solution cause an overall signal reduction of up to 40% with increasing saturation time, a good relative HyperCEST contrast of up to 30% could be observed (Fig. 2). At saturation times close to T_1, distinct and well-separated peaks affirm promising spectral resolution.

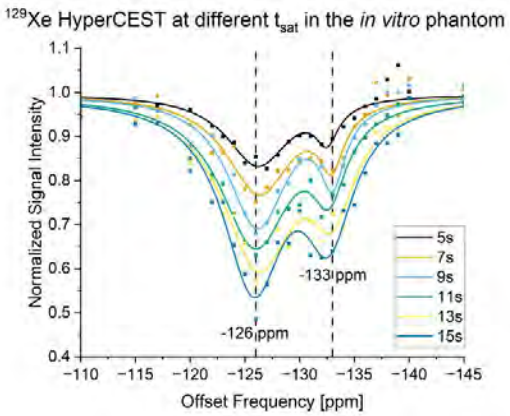

Figure 2: HyperCEST spectra of Xenon-129 in an *in vitro* phantom solution with *in vivo* like relaxation conditions. The normalized signal intensities at different offset frequencies are shown for different saturation times. CrA-ma was used as a host-system. The signal peak of Xe@CrA-ma is seen at -133 ppm. A second peak is visible at -126 ppm, whose origin remains under investigation.

Conclusion: Our study demonstrates that an *in vitro* phantom solution with reproducible relaxation times approaching those of xenon in a physiological environment is suitable for sequence testing and optimization. Future studies will address the effects of saturation power on the HyperCEST signal.

References: **1** G.J. Wilson, et al. Longitudinal relaxation times of 129Xe in rat tissue homogenates at 9.4 T. *Magn Reson Med*. 41(5):933-8, 1999 **2**. J Wolber, et al. On the oxygenation-dependent 129Xe T1 in blood. *NMR Biomed*., 13(4):234–7, 2000. **3** X. Xu, et al. Hyperpolarized 129Xe gas lung MRI-SNR and T2* comparisons at 1.5 T and 3 T. *Magn Reson Med.* 68(6):1900-4, 2012.

Novel ligand platform for Mn(II) complexation: from general CAs to liver specific probes

Gergő Zoltán Sajtos,[a,b] Balázs Váradi,[a,b] Enikő Molnár,[a] Enikő Madarasi,[a,b] Ferenc Krisztián Kálmán,[a] Norbert Lihi,[a] and Gyula Tircsó[a]
[a]*University of Debrecen, Department of Physical Chemistry, Faculty of Science and Technology*
[b]*University of Debrecen, Doctoral School of Chemistry*

Introduction: Tissue specific probes offer several advantages over conventional extracellular contrast agents. Lower dosage is required to achieve a similar enhancement in terms of image contrast, which in turn minimizes the side effects experienced by patients. Targeting molecules or proteins of known bioprocesses can also yield further information about the functionality of these biological pathways. Complications of hepatological diseases, including cirrhosis, hepatitis, liver tumor and metastasis are among the leading cause of death worldwide, therefore the need for safe and reliable liver specific agents is clear. One of the most widely used "vector" fragments for targeting hepatocytes is the 4-ethoxybenzyl (EOB) moiety due to its efficiency and established pharmacokinetics. The given moiety is used in the commercial contrast agent gadoxetane ($[Gd(EOB\text{-}DTPA)]^{2-}$) and there are several examples in the literature for Mn(II)-based probes functionalized with EOB side chain.[1] In our work we designed a rigid macrocycle (bis-pyclen) based chelator containing a picolinic acid pendant arm (BPPA, L_1). In order to achieve liver specificity, L_1 was further functionalized with EOB group resulting in the BPPA-EOB (L_2) ligand.

Methods: The parent macrocycle and the pendant arms were synthesized as previously described in the literature. These building blocks were then combined to yield target ligands. Final products were purified using preparative HPLC and the structure and purity of the ligands were confirmed with HPLC, HRMS, ^{1}H and ^{13}C NMR techniques. The stability and protonation constants of the metal complexes were determined by pH-potentiometric, ^{1}H relaxometric and UV-Vis spectrophotometric measurements. Metal exchange kinetics of the Mn(II) complexes with Cu(II) and Zn(II) ions were studied using UV-Vis spectrophotometric and ^{1}H relaxometric methods. Serum stability, relaxivity and the affinity constant of the Mn(II) complex with HSA were measured with ^{1}H relaxometric method using commercially available lyophilized human blood serum and HSA. Inner sphere water exchange was characterized via variable temperature ^{17}O NMR method.

Results: The Mn(II) complex of L_1 possesses exceptional thermodynamic stability ($\log K_{MnL1}$=16.14) with a pMn value of 10.98, evidenced only for Mn(II) chelates formed with some bispidine derivatives.[2] Dissociation half-life of MnL_1 extrapolated to pH=7.4 from Cu(II) displacement measurements is 2669 hours. This shows a significant improvement in inertness compared to the complexes of other pyclen and bis-pyclen based ligands. MnL_1 was found to have one metal-bound water molecule (q=1) and has a relaxivity of 2.05 (r_{1p}) and 5.69 (r_{2p}) at 37 °C, 1.41 T. Functionalization of L_1 with the EOB side chain lead to a decrease in complex stability ($\log K_{MnL2}$=15.22, pMn=9.07), but did not have a significant impact on dissociation kinetic properties as confirmed by metal exchange reactions involving Zn(II) ion. Relaxivities of MnL_2 in buffer solution almost doubled compared to that of parent complex MnL_1, reaching 3.49 (r_{1p}) and 10.92 (r_{2p}). This increase in relaxivity can be attributed mostly to slower rotation of the molecule and outer-sphere hydration effects. HSA affinity constants at 37 °C were measured for both MnL_1 and MnL_2 and were found to be 30 M^{-1} and 323 M^{-1} respectively. HSA binding strength of MnL_2 is comparable to other contrast agents containing the EOB substituent.

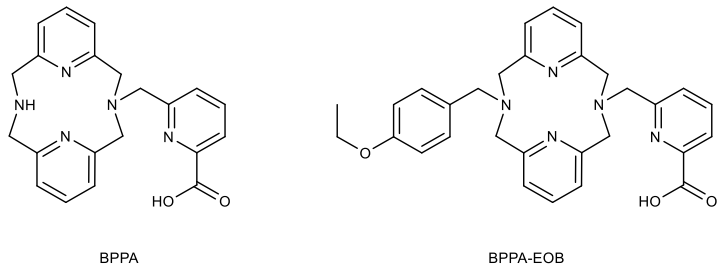

BPPA BPPA-EOB

Figure 1. Structures of BPPA (L_1) and BPPA-EOB (L_2) ligands

Discussion: The metal complexes of L_1 and L_2 have fast formation kinetics, yet high inertness as a result of the rigid pre-organized structures of the ligands. Along with the high thermodynamic stability, this makes them viable for both MRI and radiolabeling applications (e.g. ^{52}Mn/Mn bimodal PET/MRI). The macrocyclic secondary amine nitrogen in L_1 allows for further functionalization. Properties of L_2 show that the EOB pendant arm does not compromise the favorable attributes of L_1, while it increases relaxivity and HSA binding ability of the Mn(II) complex, both required for a potential liver specific MRI probe.

References: [1] R. C. Hall, J. Qin, V. Laney, N. Ayat, Z.-R. Lu, *ACS Appl. Bio Mater.,* **2022,** *5(2),* 451-458; [2] P. Cieslik, P. Comba, B. Dittmar, D. Ndiaye, É. Tóth, G. Velmurugan, H. Wadepohl, *Angew. Chem. Int. Ed.* **2022**, 61, e202115580

Acknowledgement: The research was funded by the Hungarian National Research, Development and Innovation Office (NKFIH K-134694, FK-134551 and PD-138064 projects). Supported by the ÚNKP-23-2 New National Excellence Program of the Ministry for Culture and Innovation from the source of the National Research, Development and Innovation Fund.

Pyclen-based Gd complexes for zinc sensing by MRI

Adrien Uguen, Jean-François Morfin, Célia Bonnet

Centre de Biophysique Moléculaire, UPR 4301 CNRS, rue Charles Sadron, 45071 Orléans, France.

Introduction: Zinc, the second most abundant transition metal ion in humans, plays a major role in the functioning of the body. However, its quantitative distribution and exact role are not well understood. Its concentration is highly regulated and any disturbance of its homeostasis is implicated in various pathologies such as cancers (prostate, pancreas and breast), neurodegenerative diseases, or diabetes.[1,2] Therefore, monitoring Zn^{2+} in vivo by non-invasive technique such as MRI is important in biomedical research to understand its biological role, and to provide earlier diagnosis for specific pathologies.[3]

Methods: Ditopic ligands containing a pyclen (3,6,9,15-tetraazabicyclo[9.3.1]pentadeca1(15),11,13-triene) derivative for Gd^{3+} complexation and a modified DPA unit for Zn^{2+} binding were synthetized and characterized by NMR and High Resolution Mass Spectrometry (HRMS) using an electron spray ionization (ESI) technique. Protonation constants of ligands and stability constants of Gd^{3+} complexes were determined by potentiometry in 0.15M NaCl at 25°C. NMRD profiles were measured between 0.01 and 400 MHz at 25°C, 37°C and 50°C in the absence and in the presence of Zn^{2+}. The selectivity for Zn^{2+} vs physiological cations was determined using T1 measurements at 60 MHz. The interactions of these complexes with Human Serum Albumin (HSA) were studied by relaxometry, Isothermal Titration Calorimetry (ITC) and fluorescence. The luminescence lifetime of the europium complexes were obtained by recording the decay of the emission intensity.

Results and Discussion: We had previously developed a first generation of Zn-responsive systems based on a pyridinic unit for Gd^{3+} complexation.[4] By modifying the Zn-binding unit, we could show that the systems respond to Zn^{2+} in the presence of HSA, and we could quantify Zn^{2+}.[5,6,7] In-vivo studies of one of these systems showed an accumulation of this contrast-agent in Zn-rich tissues.[8] By modifying the Gd^{3+}-complex using pyclen derivatives, we now study the influence of the charge and steric hindrance of the Gd^{3+} complex on the Zn^{2+} response. 5 pyclen derivatives with different Zn-binding units have been successfully synthesized (**Figure**). The NMRD profiles show a different behavior depending on the position of the carboxylate on the DPA, and we are currently rationalizing the origin of this difference. Finally, the interaction with HSA in the presence and in the absence of Zn^{2+} are under-going on all the other systems.

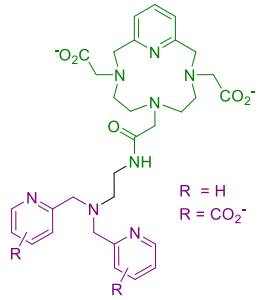

References: 1. Dick, R. et al. Am. J. Alzheimers Dis. Other Demen. **2010**, 25, 572 ; **2.** Kelleher, S.L. et al., Adv. Nutr., **2011**, 2, 101-111. **3.** Clavijo Jordan, M. V. et al., Proceedings of the National Academy of Sciences, **2016**, 113(37), E5464-E5471. **4.** C.S. Bonnet, F. Caillé et al., *Chem. Eur. J*., 2014, 20, 10959-10969. **5.** K.P. Malikidogo et al. *Chem. Commun*., **2018**, 54, 7597- 7600. **6.** Bödenler M., Malikidogo, K.P. et al. Chem. Eur. J. **2019**, 25, 8236-8239. **7.** K.P. Malikidogo, M. Isaac, A. Uguen et al., *Inorg. Chem*., **2023**, 62, 42, 17207–17218. **8.** K.P. Malikidogo, M. Isaac, A. Uguen et al., *Chem. Commun*., **2023**, 59, 12883-12886.

Development of nanoparticle-based ^{19}F MRI probe labeling β-lactamase

Hiroto Fukuda[1], Masafumi Minoshima[1,2], Kazuya Kikuchi[1,3]

[1]Graduate school of engineering, Osaka university, [2]JST PRESTO, [3]Immunology Frontier Research Center, Osaka university.

Introduction: β-lactamase is an enzyme expressed in drug-resistant bacteria. This enzyme hydrolyzes β-lactam antibiotics to survive against these drugs[1]. Hence, detection of β-lactamase leads to the diagnosis of drug-resistant bacteria. In addition, β-lactamase is used as a reporter gene in wide range of living organisms[2] because this enzyme is not expressed in mammalian cells. Therefore, there is an urgent need to develop a system for detection of β-lactamase *in vivo*. To date, fluorescent probes have been developed detecting β-lactamase by fluorescence wavelength shift or turn-on fluorescence. However, it is not suitable for in *vivo* imaging because of the lack of light penetration. In contrast, ^{19}F MRI has the advantage of the high contrast signal from probes *in vivo* because of the second highest sensitivity following the ^{1}H and the little background signals from endogenous biomolecules. Furthermore, the localization of the contrast agent is determined by overlaying with ^{1}H MRI and ^{19}F MRI images. However, low dose of ^{19}F atoms in small molecule-based probes results in low ^{19}F MRI signals intensity, especially *in vivo*. In our lab, highly sensitive ^{19}F MRI contrast agent FLAME (*FL*uorine *A*ccumulated *S*ilica Nanoparticle for *M*RI Contrast *E*nhancement) has developed[3]. The core of the nanoparticle is PFCE which has 20 equivalents of fluorine atoms, and the surface is coated with silica. The two features allow us to observe ^{19}F MRI signals from the mice and to modify the surface of the nanoparticle easily.

Methods: For visualizing β-lactamase with ^{19}F MRI nanoprobe, we focus on β-lactamase inhibitors which have diazabicyclooctane (DBO) structure. The β-lactamase inhibitors selectively react with β-lactamase by forming stable covalent adducts with DBO[4]. We designed ^{19}F MRI probe (FLAME-DBO) to detect the β-lactamase *in vivo* (Figure 1.). We introduced DBO ligands on the surface of the silica nanoparticle. We prepared FLAME by previously reported scheme and modified the surface of the nanoparticle to obtain FLAME-DBO. The labeling efficiency for β-lactamase-expressing cells was examined by ^{19}F NMR.

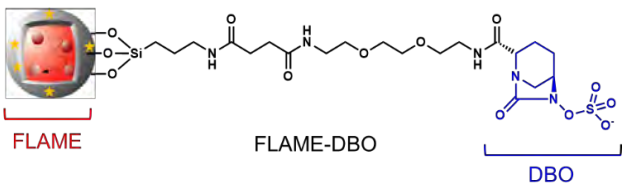

Figure 1. Design of nanoparticle-based ^{19}F MRI probe.

Results and Discussion: FLAME-DBO shows binding ability with β-lactamase and enough T_2 relaxation time after binding. Furthermore, we confirmed the binding of FLAME-DBO to β-lactamase expressed on mammalian cell membrane. This nanoparticle exhibited 3.2-fold improvement in the number of ^{19}F molecules from β-lactamase-expressing cells compared with non-expressing cells (Figure 2.). When β-lactamase on the cell is inhibited by β-lactamase inhibitor, the ^{19}F labeling efficiency by the nanoparticle from β-lactamase-expressing cell was suppressed. In summary, DBO ligand on the nanoparticle enhances the accumulation of the nanoparticle on β-lactamase-expressing cells.

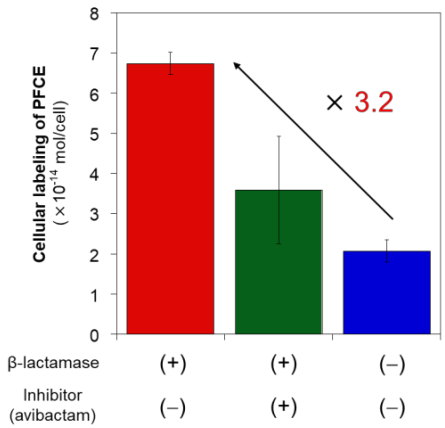

Figure 2. Labeling of FLAME-DBO to β-lactamase-expressing cells., n = 3.

Reference: 1. C. Walsh *et al.*, *Nature*, **2000**, *406*, 775; **2.** G. Zlokarnik *et al.*, *Science*, **1998**, *279*, 84; **3.** H. Matsushita *et al.*, *Angew. Chem. Int. Ed.*, **2014**, *53*, 1008; **4.** D. E. Ehmann, *et al.*, *Proc. Natl. Acad. Sci. U.S.A.*, **2012**, *109*, 11663.

MRI Thermometry using PARASHIFT Agents

Carlson Alexander,[1] Huishan Li,[1] Nicola J. Rogers,[1] David Parker[1]

[1]JC STEM ChemProbes Laboratory, Department of Chemistry, Hong Kong Baptist University, Kowloon Tong, Hong Kong, China.

Introduction

Temperature monitoring in living systems is highly sought after due to the close interrelationship between tissue temperature, cellular level processes, and physiology.[1] To date, MR Imaging has been explored using a range of techniques towards non-invasive temperature mapping *in vivo*, including the widely used 'proton resonance frequency' (PRF) method, with a 0.01 ppm K^{-1} temperature coefficient associated with H-bonding changes.[2] We present an update on our work with paramagnetically-shifted MRI molecular probes, *i.e.* PARASHIFT agents,[3] as temperature probes for *in vivo* thermometry. These systems are based on chiral 'cyclen' backbones in order to lock the ring-inversion of the macrocycle in pursuit of rigid structures with sharp proton resonances.[4] We exploit the intrinsic temperature dependence of the paramagnetic hyperfine shift (due to the changes in magnetic anisotropy that arises from a thermal population of available electronic energy levels), and demonstrate large pseudo-linear temperature coefficients (ca. 0.4 ppm K^{-1}) over physiological temperature ranges, *i.e.* forty times more sensitive to temperature change than PRF.[3,5,6] To optimise the detection sensitivity of such PARASHIFT probes, a large NMR-equivalent reporter group signal is required that is shifted about 50 ppm (at 3 Tesla) from the diamagnetic window (0-10 ppm) to allow direct detection against zero background using fast imaging sequences (which have excitation bandwidths of 10 kHz).[5]

Methods

The (*S*)-Et_4 chiral cyclen was synthesised from the appropriate chiral aziridine in a cyclotetramerisation catalysed by BF_3.[4] Alkylation or phosphinomethylation allowed formation of the C_4 symmetric chiral DOTA ligand **(L_1)**[4] and its methyl phosphinate analogue, the C_4 symmetric chiral DOTPMe ligand, **(L_2)**, from which **[Ln(L_1)]$^-$** and **[Ln(L_2)]$^-$** were prepared. Paramagnetic NMR spectra were measured at 1.4, 1.9 and 9.4 T, using fast acquisition and short delay times, and large sweep-widths of up to 400 ppm. R_1 relaxation rates (T_1^{-1}) were measured using fast inversion recovery experiments, whilst R_2 rates (T_2^{-1}) were estimated from spectral linewidths. Probe temperatures were calibrated against ethylene glycol.

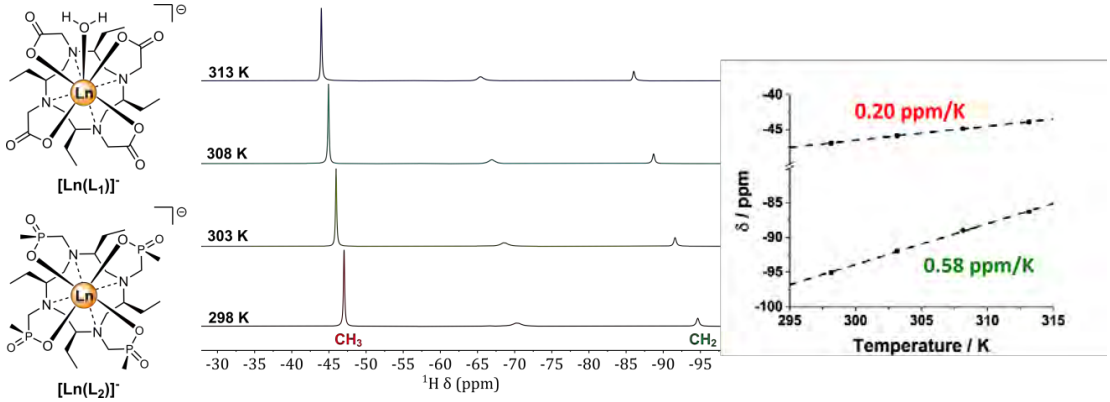

Figure 1: (*left*) Structures of complexes under study; (*middle*) ^{1}H NMR at different temperatures with **[Dy(L_1)]$^-$**; (*right*) A plot of chemical shift against temperature with **[Dy(L_1)]$^-$**.

Results and discussion

Lanthanide complexes of the chiral ethyl-appended cyclen macrocycles produce well-resolved paramagnetic NMR signals that shift with temperature. The methyl and methylene chemical shifts within **[Dy(L_1)]$^-$** are observed at -50 and -95 ppm (at room temperature) and shift with temperature coefficients of 0.20 and 0.58 ppm K^{-1} respectively. The peak difference (i.e. $\Delta\delta$ K^{-1}) can be used to calibrate probe temperature, with a temperature coefficient of $\Delta\delta$ = 0.38 ppm K^{-1}.

Conclusion

Large temperature coefficients were observed with these complexes. Shifted resonances with different coefficients within **[Dy(L^1)]$^-$** at -50 and -90 ppm, for example, generate a measurable parameter which can unequivocally determine temperature. Related work on macrocyclic transition metal complexes and other chiral complexes is underway.

References

1) A. D. Sherry *et al*., MRI Thermometry based on PARACEST agents, *J. Am. Chem. Soc*., 2005, **127**, 17572-17573; 2) J. C. Hindman, Proton Resonance Shift of Water in the Gas and Liquid States, *J. Chem. Phys*., 1966, **44**, 4582-4592; 3) D. Parker *et al*., Moving the goal posts: enhancing the sensitivity of PARASHIFT proton magnetic resonance imaging and spectroscopy, *Chem. Sci*., 2013, **4**, 4251-4258; 4) C. J. Anderson, P. Caravan, G-L. Law *et al*., Chiral DOTA chelators as an improved platform for biomedical imaging and therapy applications, *Nat. Commun.*, 2018, **9**, 857; 5) D. Parker, A. M. Blamire *et al*., A new paramagnetically shifted imaging probe for MRI, *Magn. Reson. Med*., 2017, **77**, 1307-1317; 6) D. Parker, N. J. Rogers *et al*., Employing paramagnetic shift for responsive MRI probes, *Coord. Chem. Rev.*, 2019, **383**, 30-42.

Preparation of nano-ruler MRI contrast agent

Nanami Maehara[1,2], Akira Sumiyoshi[1], Kae Sato[2], Mitsuru Naito[3], Kanjiro Miyata[3], Ichio Aoki[1], Kensuke Osada[1]
[1]National Institutes for Quantum Science and Technology, Chiba, Japan [2]Graduate school of science, Japan Women's University, Tokyo, Japan [3]Graduate School of Engineering, The University of Tokyo, Tokyo, Japan

Introduction: Earlier diagnosis and earlier medical intervention before a disease develops to a serious condition become more important to promote healthy life expectancy. To this end, detecting the signs of diseases as early as possible is a key technology. It is recently noticed that mild chronic inflammation called "inflammaging" occurs, which leads to various age-related diseases, such as atherosclerosis, diabetes, autoimmune diseases, and cancer. One of its symptoms is the disruption of vascular structures with its "pore" size ranging from a few nanometers to several tens of nanometers according to the progresses of the diseases. MRI is considered as a suitable modality for diagnosis because it allows for visualization of vascular structures with the spatial resolution close to 100 μm in three-dimension without radiation. Disruption of vascular structure may be detected by accumulation of contrast agents, which have leaked through the pore. However, conventional contrast agents clinically used, such as Gd-DOTA, may not accumulate in sufficient amount for detection because it undergoes rapid clearance from body. The properties of contrast agents demanded for detecting the disrupted vasculatures would be (i) prolonged circulation in bloodstream, (ii) the size smaller than the pore size of disrupted vasculature for leakage, and (iii) elimination from body after the imaging. For such properties, we focused on the "nano-ruler polymer" [1]. The polymer circulates in blood without being captured by reticuloendothelial system (RES), covers the size range of the pore size, and permits renal clearance by controlling its size. Thus, we modify the nano-ruler polymer for nanoprobe to detect inflammaging by MRI (**Figure 1**). Here, we show a preparation of a 3 nm-sized nanoprobe as the first prototype.

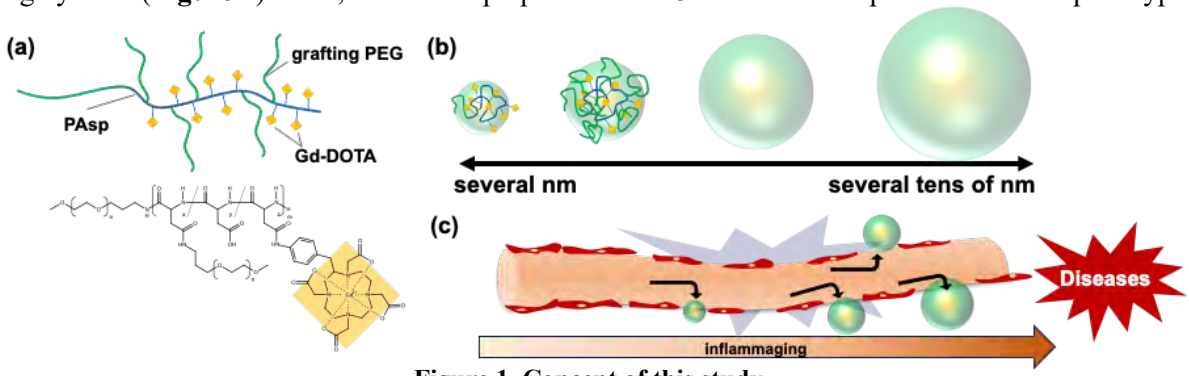

Figure 1. Concept of this study
(a)Structure of "nano-ruler MRI contrast agent" (b)The nanoprobe can control its size (c)Detecting the vasculature disruption.

Methods: The nano-ruler polymer is composed of poly(aspartic acid) (PAsp) as a backbone polymer and poly(ethylene glycol) (PEG) as graft polymers. We synthesized a polymer with single grafted PEG (2k) namely PEG-*b*-PAsp as a small-sized nanoprobe among the series, which is conjugated with Gd-DOTA. Synthesized polymer was characterized by GPC, ^{1}H-NMR, and fluorescence correlation spectroscopy (FCS). The biodistribution was evaluated by using fluorescently labeled polymer in mice. Cy5-COOH was used as a model of Gd-DOTA given the comparable molecular weight.

Results & Dissection: Degree of polymerization in PAsp segment was determined to be 99 from ^{1}H-NMR. The molecular weight distribution and the hydrodynamic diameter (D_H) of PEG_{2k}-*b*-$PAsp_{99}$ was determined as 1.3 from GPC and 3 nm from FCS, respectively. Contrasted to the model of Gd-DOTA, the polymer remained in bloodstream 1 hour after the intravenous administration. Fluorescence signal from the polymer was observed mainly in liver and kidney, while that in spleen was limited. Therefor it is considered that the liver accumulation is likely derived from liver-bile execration, instead of the RES capture. Fluorescence signal was not observed in any of organs and blood at 72 h. the *in vivo* confocal laser scanning microscopy study confirmed the clearance of the polymer from kidney and liver. These biodistribution properties agree with the request of the nanoprobe for inflammaging imaging.

Conclusion: The prototype 3 nm-sized nanoprobe was successfully prepared. We will apply the probe to the inflammaging model mice to detecting the vasculature disruption by MRI in future.

References: **[1]** M. Naito, Y. Watanuki, K. Toh, J. Yum, B. S. Kim, K. Taniwaki, S. Ogura, H. Ishida, M. Cho, H. Chaya, K. Miyajima, K. Osada, K. Minegishi, Y. Aoki, Y. Yamasaki, K. Miyata, Size-tunable PEG-grafted copolymers as a polymeric nanoruler for passive targeting muscle tissues. *Journal of Controlled Release* 347 607-614 (2022)

Activity-based ^{19}F-MRI Sensing of Zn^{2+}: A Novel Strategy for Quantitative Mapping of Cation Dynamics with Ultimate Specificity

Balamurugan Subramani, Lucia M. Lee, Nishanth D. Tirukoti, Hyla Allouch-Arnon and, Amnon Bar-Shir
Weizmann Institute of Science, Rehovot, 7610001, Israel

Introduction: Imaging sensors developed for metal ions are mostly based on specific ion recognition capabilities and non-covalent interactions between the ion of interest and the synthetic probe. Nevertheless, an alternative strategy for ion recognition, one that uses molecular reactivity, is desired to allow (i) ultimate specificity, (ii) detectability of transient changes in ion levels, and (iii) enhanced contrast-to-noise changes. Several examples have shown activity-based fluorescence sensing for Zn^{2+}.[1,2,3] Specifically for these designs, binding zinc mediates hydrolytic cleavage of acetyl groups in the probe, providing a large fluorescence response. Fluorescent imaging, however, does not apply to deep tissue imaging and is incapable of quantitative assessments. Inspired by the activity-based Zn^{2+} sensing strategy and the quantifiability of ^{19}F-MRI signals, we designed a highly reactive but very specific synthetic fluorinated probe for MRI mapping of the Zn^{2+}. Upon binding to Zn^{2+}, the synthetic probe is readily hydrolyzed, and the resonance of its ^{19}F-functional group is shifted by more than 12 ppm, allowing the display of Zn^{2+} distribution as an artificial MRI-colored map highlighting its ultimate specificity compared to other metal ions.

Methods: A fluorinated-chelate **LML-1** was synthesized using reductive amination and acetylation methods. After determining the T_1 relaxation time of purified **LML-1**, fully recovered ^{19}F-NMR experiments were performed on an 11.7 T NMR spectrometer at 25 °C and 37 °C. To this end, PBS solutions (pH = 7.2) containing 3 mM **LML-1** and 3 mM of either Zn^{2+} or Ca^{2+} were examined to determine the reactivity and half-life time ($t_{1/2}$) of **LML-1**. Then, a phantom composed of six tubes was set where each sample tube contained **LML-1** in PBS (pH = 7.2) and one of the examined cations (Ca^{2+}, Mg^{2+}, Na^{+}, K^{+}, Zn^{2+} or no cation). The phantom was placed in a 9.4 T MRI scanner, and ^{1}H-MRI and ^{19}F-MRI data were obtained. Two ^{19}F-MRI data sets were acquired with the center frequency O_1 set at -116 ppm (without Zn^{2+} activity) or at -128 ppm (following Zn^{2+} activity).

Results and discussion: The probe **LML-1** containing a Zn^{2+} binding moiety was synthesized, purified, and characterized. The ^{19}F NMR of the probe in PBS showed a single ^{19}F signal at -116 ppm (Figure 1a, top). Upon adding Zn^{2+} to the solution of **LML-1**, an additional peak of Zn^{2+}-**LML-1** complex was obtained at -128 ppm (Figure 1a, bottom). Within an hour, the probe signal fully converted to the Zn^{2+}-complex ($t_{1/2}$= 10 mins, Figure 1b). The same experiment repeated at 37 °C yielded a faster hydrolysis of the acetyl group ($t_{1/2}$= 5 mins, Figure 1c). Importantly, without the addition of Zn^{2+} and upon the addition of Ca^{2+} to the **LML-1** solution, only a trace conversion of the fluorinated chelate could be detected after 3 days, emphasizing the stability of the probe for a very long time, even in aqueous solution. ^{19}F-MRI experiments of a phantom clearly showed the ability to use the activity-based **LML-1** to map Zn^{2+} (-128 ppm, red) with no background signal and differentiate this signal from unreacted **LML-1** (-116 ppm, green) by displaying it in a multicolor ^{19}F-MRI (Figure 1d).

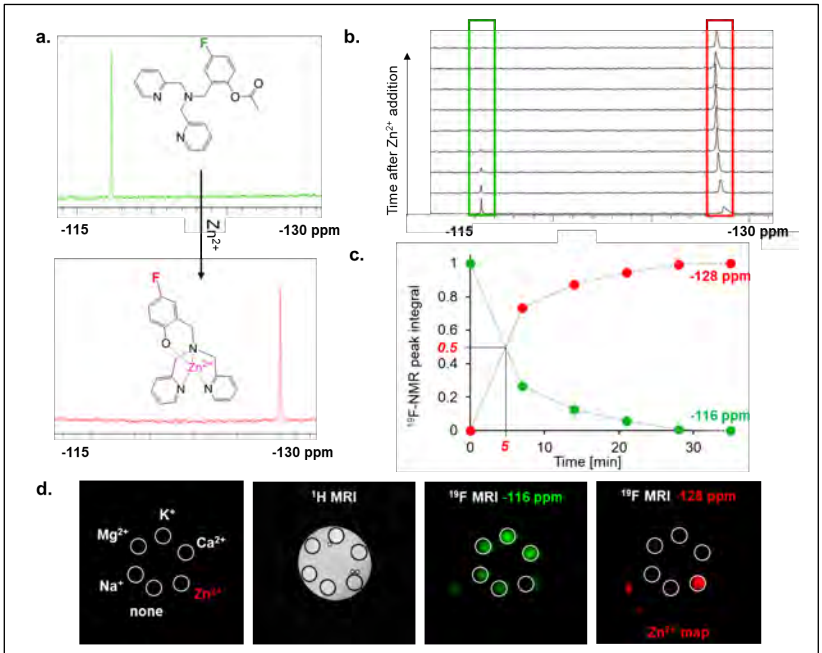

Figure 1. a) The chemical structures and corresponding ^{19}F-NMR spectra of **LML-1** (red, top) and its hydrolyzed form complexed with Zn^{2+} (green, bottom). b) Real-time^{19}F-NMR experiments showing the conversion of **LML-1** (-116 ppm) to its hydrolyzed form (-128 ppm). c) Kinetic plot showing the conversion rate and half life time ($t_{1/2}$) of **LML-1** in the presence of Zn^{2+}. d) MRI experiments; from left-to-right: phantom orientation, ^{1}H-MRI, ^{19}F-MRI at -116 ppm (colored green, no Zn^{2+}) and ^{19}F-MRI at -128 ppm (colored red, with Zn^{2+}).

Conclusion: We showed a conceptually novel approach for mapping Zn^{2+} with MRI. Our approach uses molecular reactivity to provide several advantages, especially: (i) Zn^{2+} specificity, (ii) detectability of transient changes in Zn^{2+} levels, and (iii) enhanced contrast-to-noise changes. We have demonstrated that binding Zn^{2+} induces hydrolysis of the acetyl group of the probe, forming a Zn^{2+}-**LML-1** complex with a significant change in the ^{19}F-NMR resonance. We showed the probe is specific to Zn^{2+} compared to other biologically relevant cations, suggesting its potential ability to image mobile zinc in live cells and tissues.

References: (1) *Proc. Natl. Acad. Sci. USA* **2014**, *111*(1), 143-8. (2) *ACS Sens.* **2016**, *1*(1), 32-39. (3) *J. Am. Chem. Soc.* **2020**, *143*(14), 6477-6482.

Molecular MRI of cardiac fibrosis and response to antifibrotic therapy

K. Amoiradaki[1]*, M. Tomczyk[2], X. Wang[1], G. Lima da Cruz[1,4], C. Velasco[1], L. Zentilin[5], F. Bortolotti[5], C. Prieto[1,6], R. Botnar[1,3,6,7], M.Giacca[2,3], A. Phinikaridou[1,3]

1. School of Biomedical Engineering and Imaging Sciences, King's College London, London, United Kingdom.
2. School of Cardiovascular and Metabolic Medicine & Sciences, King's College London, London, United Kingdom.
3. BHF Centre of Research Excellence, Cardiovascular Division, King's College London, London, United Kingdom.
4. Department of Radiology, University of Michigan, Michigan, United States.
5. Molecular Medicine Laboratory, International Centre for Genetic Engineering and Biotechnology, Trieste, Italy.
6. Escuela de Ingeniería, Pontificia Universidad Católica de Chile, Santiago, Chile.
7. Institute for Biological and Medical Engineering, Pontificia Universidad Católica de Chile, Santiago, Chile.

Introduction: Cardiac fibrosis drives heart failure. Currently, there is a clinical need to diagnose and treat cardiac fibrosis. Chordin-like 1 (Chrdl1) is a TGF-β1 antagonist that was recently discovered to inhibit fibrosis. Here, we used molecular MRI to longitudinally monitor the efficacy of Chrdl1 in reducing existing cardiac fibrosis.

Methods: MI was induced in CD1 mice by permanent occlusion of the coronary artery. The adeno-associated viral vectors serotype 9 (AAV9) expressing Chrdl1 (AAV9-Chrdl1) or an empty vector (AAV9-Control) were injected intravenously one week post-MI. *In vivo* MRI was carried out at 1 week post-MI, before treatment was administered, and repeated at 4 weeks. Cine imaging was used to assess left ventricular geometry and function. Late gadolinium enhancement (LGE) images were obtained 60-90 minutes after intravenous injection of collagen (EP-3533) and elastin (Gd-ESMA)-targeting probes on two consecutive days. T1 mapping was performed using a 2D Look-Locker sequence to calculate the relaxation rate (R1, s^{-1}). ΔR1 (s^{-1}) = R1(infarct) - R1(remote myocardium).

Results

In mice receiving the AAV9-Control treatment, cardiac fibrosis increased and cardiac function worsened between 1 and 4 weeks post-MI **(Fig. 1A-C)**. Conversely, AAV9-Chrdl1 treatment inhibited further collagen and elastin deposition and improved the ejection fraction at 4 weeks **(Fig. 1A-C)**. This was evident by a decrease in LGE volume (**Fig. 1C-D)** and lower R1 values in the scar **(Fig. 1E, F)** in the infarct. Importantly, treatment with AAV9-Chrdl1 reduced collagen than elastin accumulation in the infarcted myocardium shown by the decrease in ΔR1 after EP-3533 and Gd-ESMA administration **(Fig. 1E-F)**.

Conclusion

Molecular MRI of cardiac fibrosis with a clinical 3T scanner enables longitudinal monitoring of novel antifibrotic treatments. Using this imaging technique, we show that systemic administration of Chrdl1, in the presence of established fibrosis, inhibits adverse cardiac remodelling and excess extracellular matrix deposition and improves cardiac function.

Acknowledgments

This work was supported by the King's BHF Centre of Research Excellence RE/18/2/34213, PG/2019/34897 and RG/20/1/34802.

References

1. Ruozi, G. *et al*. (2022). *Science Translational Medicine*, *14*(660).
2. Helm, P. *et al*. (2008). *Radiology*, *247*(3).
3. Ramos, I. *et al*. (2018). *Circulation. Cardiovascular Imaging*, *11*(11).

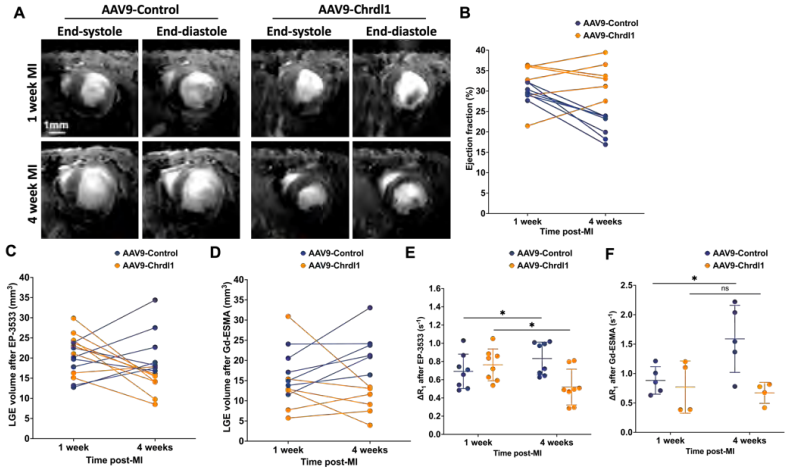

Figure 1. AAV9-Chrdl1 inhibits cardiac fibrosis when administered intravenously at 1 week post-MI.
(A) Representative 2D cine short axis images of the heart at end-systole and end-diastole phases indicating cardiac contractility. **(B)** Ejection fraction measured for the same animals at 1 week and at 4 weeks post-MI. Statistical analysis: Paired t-test. **(C- D)** LGE volume (mm^3) measured at 1 week and 4 weeks post-MI after the injection of EP-3533 and Gd-ESMA imaging probes. Statistical analysis: Unpaired t-test. **(E-F)** ΔR1 (s^{-1}) of remote and infarcted myocardium measured after injection of EP-3533 and Gd-ESMA at 1 week and 4 weeks post-MI. Statistical analysis: Paired t-test. * $p<0.05$.

Molecular imaging of early brain injury in subarachnoid hemorrhage

Sara MARTINEZ DE LIZARRONDO[1], Suzanne GOURSAUD[1], Manuel NAVARRO-OVIEDO[1], Benoit ROUSSEL[1], Peter J. LENTING[2], Mikael NAVEAU[3], Denis VIVIEN[1], Carine ALI[1], Maxime GAUBERTI[1].

1.*Normandie Université, UNICAEN, INSERM UMRS-U1237, PhIND, Institut BB@C, Cyceron, Caen, France.* ***2.****Laboratory for Hemostasis, Inflammation & Thrombosis, UMR-U1176. INSERM, Le Kremlin-Bicêtre, France.* ***3.*** *Normandie Université, UNICAEN, CNRS UMS 3408, Cyceron, Caen, France*

Background: Subarachnoid hemorrhage (SAH) is the third most common subtype of stroke, frequently leading to severe neurological deficits and high mortality rates[1]. Early brain injury (EBI), manifesting within the first 72 hours after SAH, encompasses a spectrum of pathological changes, including cerebral edema, microcirculatory dysfunction and neuroinflammation[2]. Although associated with clinical outcome, these changes are often imperceptible with conventional imaging techniques, underscoring the need for new biomarkers.

Methods: We developed a molecular imaging strategy to detect endothelial activation[3] in the mouse brain after experimental SAH, which was induced by prechiasmatic injection of blood in mice. At 24 hours, 72 hours, and 7 days after SAH, we performed molecular imaging of endothelial activation using microparticles of iron oxide (MPIO) targeted to P-Selectin and vascular cell adhesion molecule 1 (VCAM-1)[4]. Probes distribution was revealed by magnetic resonance imaging (immuno-MRI) and by a new modality called magnetic particle imaging (MPI). In parallel, we longitudinally analyzed brain and plasma levels of endothelial activation markers, including Von Willebrand factor (VWF) by ELISA, qPCR and immunofluorescence.

Results and Discussion: At 24 hours after SAH, immuno-MRI revealed a massive overexpression of VCAM-1 (but not P-Selectin) in the cerebral vasculature. This was confirmed by qPCR and immunohistology. Thereafter, VCAM-1 expression and other markers of endothelial activation progressively returned to baseline after 7 days. Interestingly, the change in VCAM-1 expression at 24 hours after SAH can be detected using magnetic particle imaging, paving the way for bedside monitoring of EBI.

Conclusions: EBI induces early and brain wide endothelial activation after experimental SAH. Multimodal molecular imaging of VCAM-1 using immuno-MRI and MPI is a new biomarker for EBI.

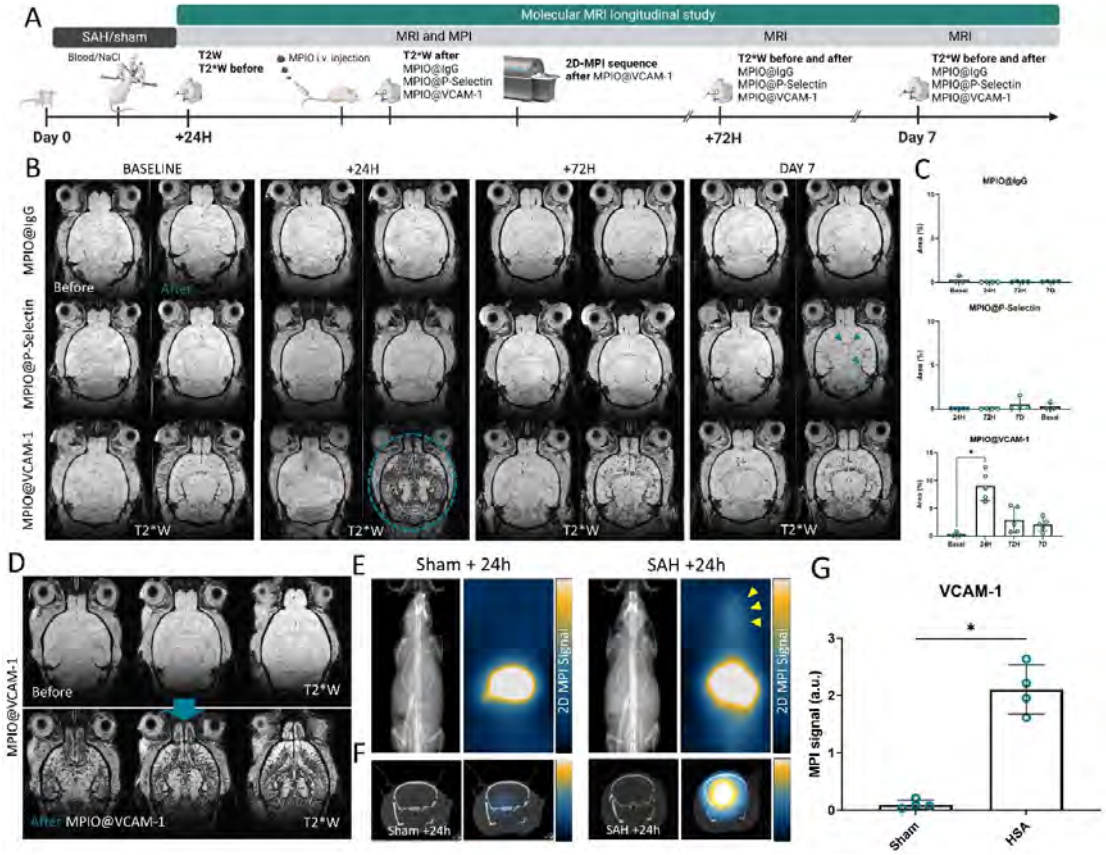

Figure 1. Immuno-MRI reveals brain wide overexpression of VCAM-1 after SAH. A. Timeline of the procedure. **B.**Representative T2*-weighted images before and after successive intravenous injection of MPIOs targeted against @IgG, @P-Selectin and @VCAM-1 (up to 4 mg/kg equivalent iron) at 24 hours, 72h and 7 days after SAH. **C.**Corresponding quantification of targeted MPIO induced signal void in the brain (n = 4-5). **D.**Representative T2*-weighted images (three slices per animal) before and after intravenous injection of MPIO@αVCAM-1 (4 mg/kg) 24 hours after SAH. **E.**Representative 2D CT-MPI images after intravenous injection of MPIO@VCAM-1 at 24 hours after SAH AS compared to controls **F.**Representative CT-MPI images of the brain of mice showing MPIO@VCAM-1 signal in SAH group at 24h **G.**Corresponding quantification of targeted MPIO induced MPI in the brain in SAH at 24h as compared to sham. *P < 0.05.

References: *1.Claassen J et al. Lancet. 2022;400:846-862; 2.Lauzier DC, et al. Stroke. 2023;54:1426-1440; 3.Frijns CJ, et al. J Neurol Neurosurg Psychiatry. 2006;77:77-83; 4.Martinez de Lizarrondo S, et al. Sci Adv. 2022;8:eabm3596.*

Hybrid PET/MRI contrast agent for *in vivo* pH quantification

Jan Kretschmer[1,2], Remy Chiaffarelli [1,2], Yasmin Al-Moufleh[1], Jonathan Cotton[1], Angelina Prytula-Kurkunova[1,2], Andre Ferreira Martins[1,2,3]

[1] Dr. J. Kretschmer, Yasmin Al-Moufleh, Remy Chiaffarelli, Angelina Prytula-Kurkunova, Dr. Jonathan Cotton, Prof. Dr. A. F. Martins, Werner Siemens Imaging Center, Department of Preclinical Imaging and Radiopharmacy, Eberhard Karls University Tübingen, Röntgenweg 13/1 ,72076 Tübingen (Germany), E-mail:, jan.kretschmer@med.uni-tuebingen.de [2] Dr. J. Kretschmer, Remy Chiaffarelli, Angelina Prytula-Kurkunova, Prof. Dr. A. F. Martins, Cluster of Excellence iFIT (EXC 2180) "Image-Guided and Functionally Instructed Tumor Therapies", Eberhard Karls University Tübingen [3] Prof. Dr. A. F. Martins German Cancer Consortium (DKTK), partner site Tübingen, German Cancer Research Center (DKFZ), Im Neuenheimer Feld 280, Heidelberg 69120 (Germany)

Introduction: Cancer cells exhibit a metabolic shift favoring increased glycolysis over mitochondrial oxidative phosphorylation, irrespective of oxygen levels. This glycolytic upregulation leads to an elevated extracellular pH acidification (pHe) in the tumor microenvironment. Despite the significance of pH and tumor acidosis, there is a lack of established tools for non-invasive and quantitative imaging of the spatial distribution of tumor pHe. To address this need, we introduce [18F]*q*-pH-1, an *in vivo* stable, low molecular weight PET/MRI hybrid contrast agent for quantitative pH determination (Figure 1A).

Methods: The determination of relaxivities and responsiveness in various media used 0.1-0.5 mM samples at pH 7.4 and pH 5-8 for responsiveness determination in a 7T MRI scanner. [18F]*q*-pH-1 was synthesized through nucleophilic substitution of the nitro precursor using [18F]TBAF in DMSO at 120°C for 15 minutes. The PET/MRI phantom included [18F]/[19F]q-pH-1 samples, each containing a cocktail with 0.5 mM of [19F]q-pH-1 and 0.5 MBq activity of [18F]q-pH-1; and a challenge with human serum. Simultaneous PET/MRI was performed on a 7T scanner with a PET insert. *In vivo* experiments on healthy mice included T1 maps and DCE sequences following a 0.1 mmol/kg [19F]/[18F]q-pH-1 bolus in PBS. Pharmacokinetics and agent stability were determined through urine analysis using HPLC.

Results and Discussion: The r_1 of agent 1.18 mM-1*s-1 in HEPES buffer increases by 42% in presence of human serum albumin (HSA) and by 34% in human serum (HS). This suggests a non-specific interaction of [19F]*q*-pH-1 with HSA or other biomolecules present in serum. The [19F]*q*-pH-1 showed impressive responsiveness to pH in HS with an r_1 increase by 198% from pH 8 to 5.0 (Figure 1B). Notably, r_1 in HS increases by 85% with a linear trend in biologically-relevant range of pH (7.5-6.7; Figure 1B). Radiolabelling yielded 250 MBq of [18F]*q*-pH-1 in less than 30 mins with a 40% RCY. Simultaneous PET/MRI of [19F]/[18F]*q*-pH-1 cocktail (Figure 1C-F) shows constant PET signal, confirming consistent concentration (Figure 1C), while MRI signal decreases with rising pH (Figure 1D,F). Simultaneous *in vivo* PET/MRI imaging allowed to distinguish areas of different pH in the kidney and demonstrated rapid renal clearance of the agent. LC-MS analysis of urine from the *in vivo* experiment confirmed the presence of the intact metal chelate.

Conclusions: We designed, developed, and characterized a novel pH-responsive PET/MRI contrast agent [18F]*q*-pH-1. *In vitro* experiments showed remarkable responsiveness to physiologically relevant pH ranges in human serum (pH 6.3 to 7.5). Moreover, this contrast agent is kinetically stable *in vivo*, increasing its potential for further preclinical applications in relevant oncology models.

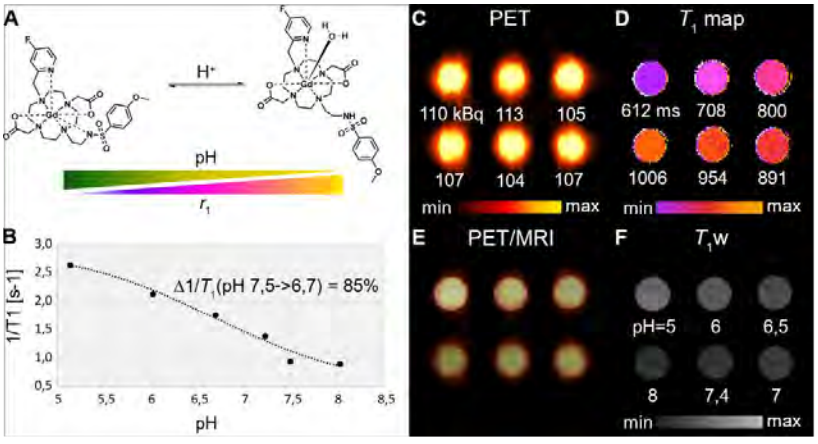

Figure 1. A Structure of [19F]*q*-pH-1 and illustration of the functional protonation mechanism. The sulphonamide pendant arm de-coordinates from the metal centre at low pH, allowing access to water molecule, leading to higher relaxivity. **B** pH-dependent change in longitudinal relaxation rates of [19F]*q*-pH-1 in MR phantoms at 7T at 37 °C acquired in human serum. **C-F** Simultaneous PET/MRI imaging of a phantom containing [18F]/[19F]*q*-pH-1. **C** The PET images show the same intensity of PET signal (shown under each sample in kBq) of the PET/MRI phantom. **D** T_1 map of a [18F]/[19F]*q*-pH-1 phantom with T_1 values of individual samples. Signal intensity depicted in colour gradient. **E** Overlay of PET and T1w MR images. **F** MRI T_1 weighted image shows decreasing signal intensity with increasing pH across the samples.

Hybrid immuno-PET-MR with Gallium-68 labelled microsized matrix-based magnetic particles (M3P)

Swannie Pédron[1], Amaury Guillou[1,2], Fabien Fillesoye[2], Charlène Jacqmarcq[1], Cécile Perrio[2], Denis Vivien[1,3], Maxime Gauberti[1], Jonathan Vigne[1,3]*, Thomas Bonnard[1]*

[1]Normandie Université, UNICAEN, INSERM, PhIND (Physiopathology and Imaging of Neurological Disorders), Institut Blood and Brain @ Caen-Normandie, Cyceron, 14000 Caen, France.

[2]Normandie Univ, UNICAEN, CEA, CNRS, UAR 3408, Cyceron, Boulevard Henri, Becquerel, 14074 Caen, France.

[3]CHU Caen, Clinical Research Department, CHU de Caen Côte de Nacre, Caen, France.

Inflammation diagnosis and monitoring is crucial for disease characterization and management. Current imaging approaches mainly consist of (i) MRI coupled with gadolinium chelates highlighting hyperemia and inflammatory edema and (ii) PET with [^{18}F]fluorodesoxyglucose that shows metabolic activity or TSPO ligands that reveal microglial activation. Despite their clear input for several indications in oncology or cardiology, the development of more specific probes, providing a more resolutive, sensitive and earlier detection of inflammatory activity is warranted.

We have developed a bimodal PET-MR tool built on our previously developed microsized polydopamine matrix-based magnetic particles (M3P).[1] Anti-VCAM-1 antibodies were grafted to the polydopamine matrix via an aza-Michael addition. Subsequent Ga-68 radiolabeling in HEPES buffer (0.3M, pH4.0) provided [^{68}Ga]Ga-M3P@anti-VCAM-1 (0.5-1.0 GBq). *In vivo* immuno-PET-MRI experiments were carried out using a preclinical PET-MR 7T system (Bruker) on a sepsis murine model (LPS i.p. 5 mg/kg) versus sham control. Whole body T_2 MRI and pre-injection kidney T_2* MRI were first performed. Dynamic PET was then carried out for 10 min after intravenous injection of [^{68}Ga]Ga-M3P@anti-VCAM-1, followed by post-injection kidney T_2* MRI.

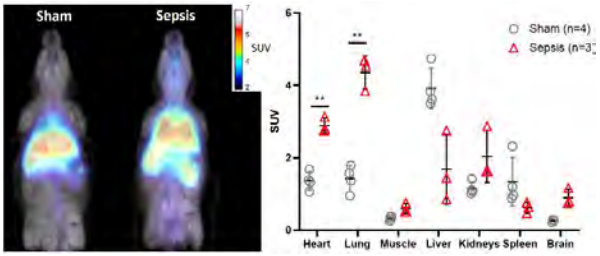

*Figure 1. PET-MR acquisition of a sham control and a sepsis mouse after the injection of [68Ga]Ga-M3P@anti-VCAM-1. Standard uptake values ware quantified on PET acquisitions in the different tissues (n=3,4, **p<0.01)*

PET-MR acquisitions (**Figure 1**) highlighted the rapid accumulation of [^{68}Ga]Ga-M3P@anti-VCAM-1 in mononuclear phagocyte system tissues of the sham animals; SUV of 3.92±0.56 in the liver and 1.33±0.67 in the spleen (n=4). In the sepsis animals, uptakes in the lung in every animals and in the kidneys in some animals were identified compare to the sham control (SUV uptake values of 4.35±0.46 VS 1.42±0.35 in the lung, ** p<0.01 and 2.03±0.73 VS 1.15±0.73 in the kidneys p=0.71, n=3,4). The sepsis animal identified with high kidney inflammation on whole body PET scan, high resolution T_2* MRI scans revealed the pattern of vascular inflammation and VCAM-1 expression in the kidneys whereas no signal uptakes were seen in the kidneys of sham animals.

In this study, we validated that the bimodal probe reveals vascular inflammation at whole body level. [^{68}Ga]Ga-M3P@anti-VCAM-1 enables both high-resolution molecular MRI mapping at local level on T_2* sequences and quantification and sensitive detection using PET imaging. This novel immune-PET-MR technology show great promises to improve the diagnosis and monitoring of inflammation, especially in the context of lung and kidney disorders.

1. Martinez de Lizarrondo S, et al. Tracking the immune response by MRI using biodegradable and ultrasensitive microprobes. Science Advances. 2022. doi/10.1126/sciadv.abm3596

Declaration of financial disclosure is required

The authors declare the following competing interests: C.J., D.V., M.G. and T.B. have filed patent application (EP N° 21 306 073.4 (30 July 2021)) for the use of M3P as contrast agent. The other authors declare that they have no competing interests.

Imaging Intravascular Macrophages Using Micro-sized superparamagnetic Decoys by MRI

Sara MARTINEZ DE LIZARRONDO[1], Manuel NAVARRO-OVIEDO[1], Denis VIVIEN[1], Maxime GAUBERTI[1].
1.Normandie Université, UNICAEN, INSERM UMRS-U1237, PhIND, Institut BB@C, Cyceron, Caen, France

Introduction: During inflammatory processes, intravascular macrophages are capable of phagocytizing circulating debris in the circulation[1].
Hypothesis: Intravenous injection of contrast-loaded decoys could be used to label intravascular macrophages *in situ* and map their distribution by non-invasive imaging.
Methods: We synthetized superparamagnetic decoys with hydrodynamic diameters from 20 nm to 4.5 µm (Fig.1A). Experimental models of neuroinflammation (intrastriatal injection of LPS or TNF) and ischemic stroke (thrombin model and ferric chloride model) were performed in mice[2]. High resolution 3D T2*-weighted MRI sequences[3] were performed after intravenous injection of the superparamagnetic decoys.
Results and Discussion: In experimental models of neuroinflammation, intravenous injection of superparamagnetic decoys with a diameter of 1 µm (but neither smaller nor larger particles) reveals intravascular phagocytic cells in the cerebral circulation, in a dose dependent manner (Fig.1B,C). In ischemic stroke, we found that intravenous injection of the decoys leads to numerous signal voids in the vessels in and around the infarct core at 48 hours (Fig.1D). Interestingly, the intravascular phagocytic activity appears much higher in permanent rather than transient models of ischemic stroke. Pre-treatment with anti-CD11a blocking antibodies significantly reduced the number of intravascular macrophages in stroke. Histological studies confirmed that injected decoys are phagocytized by intravascular cells which express typical markers of the monocyte/macrophage lineage including CX3CR1 dependent GFP expression and CD68 (Fig.1C). Lastly, we produced biodegradable and biocompatible submicrometric decoys which elicited the same characteristics in both experimental models (Fig.1E-F).
Conclusions: Intravenous injection of superparamagnetic decoys in the micrometer size range allows to image intravascular macrophages. This new method allows studying the pathophysiological roles of intravascular macrophages in experimental models and could be easily translated to humans since biodegradable decoys are available.

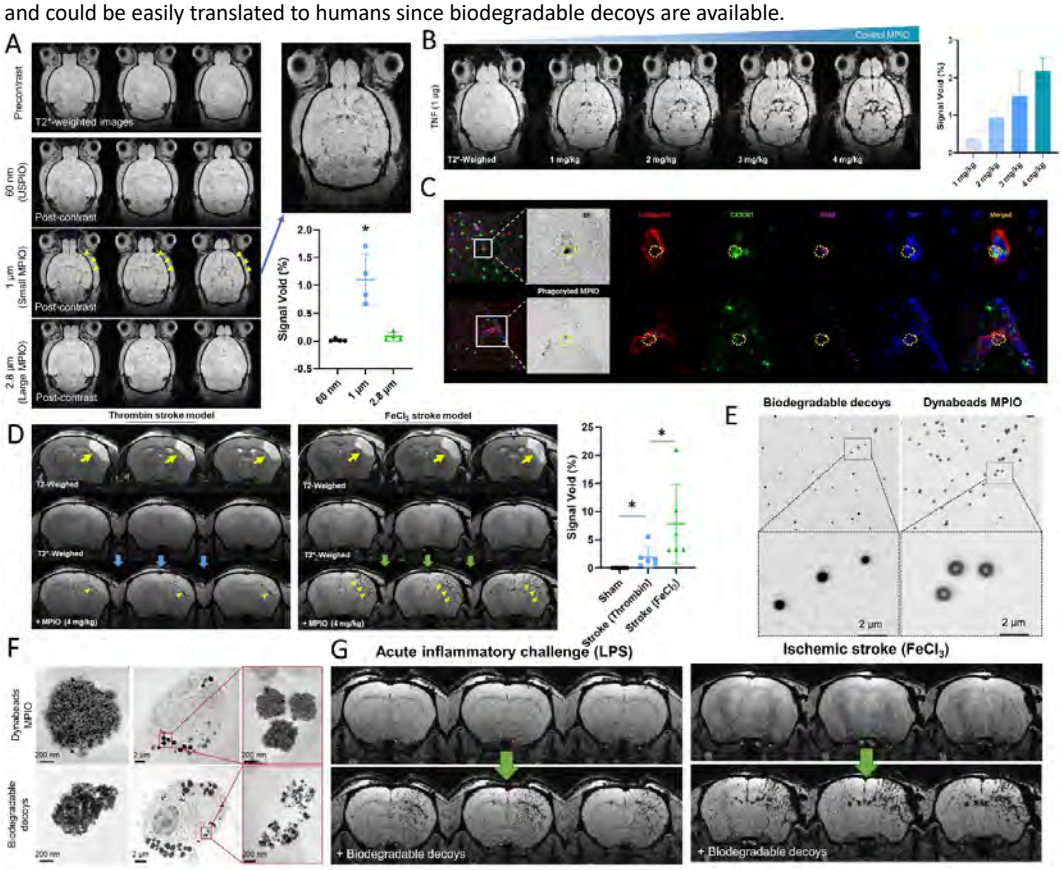

Figure 1. Submicrometric decoys allow imaging of intravascular macrophages *in situ*. A. Size comparison of nano- and micro-metric particles (up to 2.8µm) to image intravascular macrophages **B.** Representative T2*-weighted images before and after successive intravenous injection of 1µm MPIOs (up to 4 mg/kg equivalent iron) to image macrophages *in situ* in a model of neuroinflammation (TNF). **C.** Histological studies of phagocytic cells showing typical markers of the monocytic/macrophage lineage. **D.** Comparison of intravascular macrophages imaging in transient (thrombin) and permanent ($FeCl_3$) models of ischemic stroke and respective signal void quantification. **E.** Representative optical and **F.** TEM imaging showing size comparison and biodegradable capacities of commercial MPIO (non-biodegradable) versus biocompatible and biodegradable decoy after incubation with macrophages **G.** Imaging on intravascular macrophages using biodegradable decoys in experimental models of neuroinflammation and stroke. *P < 0.05.

References: 1. Nikovics K, et al. Biomedicines. 2021 Oct 4;9(10):1393. **2.** Montagne, A ,et al. Neuroimage 2012 : 63, 760–770. **3.** Martinez de Lizarrondo S, et al. Sci Adv. 2022;8:eabm3596.

Relaxivity enhancement of contrast agent for MRI by using sub-10 nm self-folding macromolecular drug carrier

Shan Gao[1], Akira Sumiyoshi[1], Nobuhiro Nishiyama[2], Ichio Aoki[1], Kensuke Osada[1], Yutaka Miura[2]
[1]Institute for Quantum Medical Science, National Institutes for Quantum Science and Technology, Chiba, Japan.
[2]Laboratory for Chemistry and Life Science, Tokyo Institute of Technology, Kanagawa, Japan.

Introduction: Nano-sized contrast agents have the potential to provide the highly specific contrast enhancement of tumors during MRI. Specifically, metal complexes used as contrast agents (CAs) can achieve the increase in rotational correlation times through conjugation with macromolecules, thereby enhancing molecular relaxivity[1]. Simultaneously, they exhibit prolonged blood circulation with selective accumulation into solid tumors through enhanced permeability and retention effects[2]. Various architectures, such as liposomes, polymeric micelles, and nanoparticles, were developed as carriers for CAs to malignant tissues[3]. However, the current molecular design of CAs is reaching its limitations in terms of relaxivity and tumor accumulation. In response to this, we propose a novel self-folding macromolecular drug carrier (SMDC) to enhance the performance of CAs. The SMDC is formed by automatic intramolecular self-folding of a single polymer chain containing hydrophilic and hydrophobic segments in water (**Fig 1a**). With this design, high tumor accumulation can be achieved, and the relaxivity value can be increased with minimal loading of gadolinium complexes, thus highly enhanced tumor imaging can be realized.

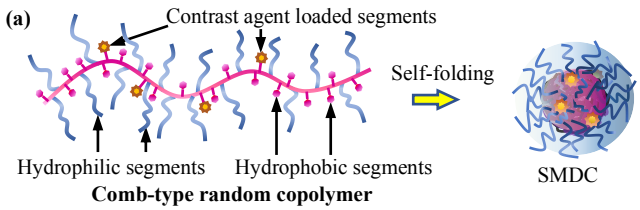

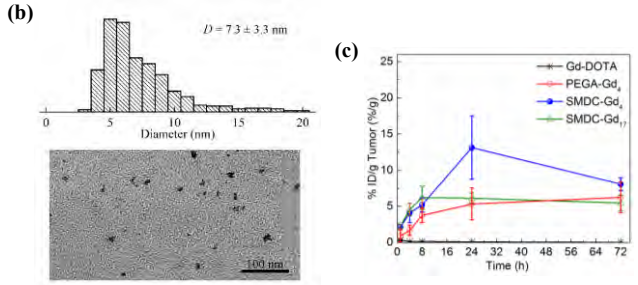

(d)

	r_1 at 0.47 T [s^{-1}mM^{-1}]	r_1 at 1.50 T [s^{-1}mM^{-1}]	r_1/r_2 at 0.47 T	r_1/r_2 at 1.50 T
Gd-DOTA	3.4	2.9	0.83	0.91
PEGA-Gd$_4$	19.6 ± 0.1	15.1 ± 0.1	0.83	0.74
PEGA-Gd$_{12}$	20.4 ± 0.1	14.7 ± 0.1	0.89	0.74
SMDC-Gd$_4$	25.9 ± 0.1	17.8 ± 0.1	0.83	0.59
SMDC-Gd$_9$	22.8 ± 0.1	17.8 ± 0.1	0.81	0.60
SMDC-Gd$_{17}$	24.7 ± 0.1	18.3 ± 0.1	0.83	0.58

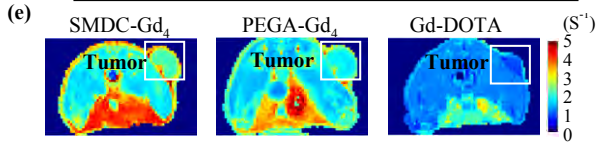

Figure 1. Design and characterization of SMDC-Gd$_4$. **(a)** Formation of SMDC structure. **(b)** Diameter distribution and TEM image of SMDC-Gd$_4$. **(c)** Tumor accumulation in biodistribution assay. **(d)** Longitudinal relaxivities and relaxometric ratios at 0.47 T and 1.50 T magnetic fields. **(e)** Quantitative R_1 maps of CT26 tumor-bearing mice at 1 T MRI.

Methods: A series of random copolymers with hydrophilic and hydrophobic segments were synthesized by RAFT polymerization to serve as the backbone of SMDC. These macromolecules were used to form the Gd chelate-loaded SMDC (SMDC-Gd) and characterized to serve as contrast agent in MRI for cancer. The properties of SMDC-Gd were indicated by relaxivity measurement and biodistribution assay. Finally, it was utilized as contrast agent in MRI on tumor bearing mice to investigate its performance.

Results and discussion: The formation of the candidate CA, SMDC-Gd$_4$, was indicated by TEM images and quantified data. The results showed that SMDC-Gd$_4$ realized a size of 5-7 nm in diameter with narrow distributions, consistent with the results of DLS, SLS, and SAXS analysis (**Fig 1b**). According to biodistribution results, SMDC-Gd$_4$ demonstrated superior performance over other groups, showcasing high tumor targeting accumulation, relatively low accumulation in organs, and rapid blood clearance (**Fig 1c**). In the relaxivity measurement results, the longitudinal relaxivity (r_1) of samples at two different magnetic fields were summarized in **Fig 1d**. Compared to the clinically approved Gd-DOTA, SMDC-Gds and PEGA-Gds exhibited higher r_1 values due to slowed down rotation resulting from conjugation of polymer and CAs. Additionally, SMDC-Gds showed higher r_1 values compared to PEGA-Gds. Here, notably, the self-folding process of SMDC-Gds created a crowded complex environment, facilitating the rise in relaxivities because of possible restrictions of internal motion around the interface of SMDC-Gds. Little effect was attributed to the increasing number of Gd-DOTA molecules within the same formulation, suggesting that SMDC-Gd could potentially induce high relaxivities with a minimal Gd payload. Moreover, regarding the influence of the magnetic field on r_1, SMDC-Gds exhibited slightly lower r_1 values at 1.5 T than that at 0.47 T as expected. These results supported the performance of SMDC-Gd as a positive macromolecule contrast agent. In tumor-targeted R_1 maps of T_1-weighted MRI, the strong contrast enhancement of SMDC-Gd$_4$ was directly observed at 24 hours post-injection, which was attributed to the high relaxivity and high tumor accumulation, affirming the viability of SMDC-Gd$_4$ in MRI (**Fig 1e**).

Conclusion: These findings demonstrated the feasibility of the developed SMDC-Gd$_4$ as a contrast agent in cancer MR imaging. Furthermore, this work indicated possibilities of SMDC to serve as drug delivery system for tumor-targeting accumulation and contrast enhancement by loading various functional groups.

References: (1) Terreno E, *et al*. *Chem. Rev*. 2010, 110, 3019-3042. (2) Caravan P, *et al*. *Contrast Media Mol. Imaging*. 2009, 4, 89-100. (3) Wang AZ, *et al*, *Annu. Rev. Med*. 2012, 63, 185-198.

Multi-nuclear MR-based profile of lithium treatment in mice hints at astrocyte activation

Tor Rasmus Memhave[1,2,3], Susann Boretius[1,2,3]
[1]German Primate Center, Leibniz Institute for Primate Research, Göttingen, Germany
[2]Georg-August Universität Göttingen, Göttingen, Germany
[3]International Max Planck Research School for Neurosciences, Göttingen, Germany

Introduction: Lithium is the frontline treatment for bipolar disorder. However, lithium treatment is challenging due to a narrow therapeutic window and only ~30% of patients are perfect responders[1]. Furthermore, the mood-regulatory mode of action is only partly understood. Disentangling lithium's direct effect on the brain from changes related to bipolar disorder in patients is challenging, complicating early detection of treatment response. We aimed to establish a magnetic resonance (MR) based profile of acute lithium treatment in mice.

Methods: We fed twenty mice either a high lithium (n=8), low lithium (n=4), or a placebo diet (n=8) for 3-4 weeks. To establish an MR-based profile of lithium treatment in mice, we acquired multi-nuclear MR imaging (^{1}H, ^{7}Li MRI) and MR spectroscopy (^{1}H, ^{7}Li, ^{31}P MRS). ^{1}H and ^{31}P were acquired at baseline and after three weeks on lithium-enriched/placebo diet. In week 4, ^{7}Li MRI/S was acquired. The modalities used are shown schematically in figure 1.

Results: ^{7}Li MRS of mice on a lithium enriched diet showed brain lithium concentrations within the therapeutic window (high lithium: 0.9±0.1 mM; low lithium: 0.4±0.1 mM). ^{7}Li MRI revealed a non-homogenous distribution of lithium with high signal in central brain regions[2]. ^{31}P MRS hinted at increased phosphocreatine in the brain of mice on a high lithium diet (confirmed by ^{1}H MRS). ^{1}H MRS showed decreased neuronal markers (N-acetylaspartate and glutamate-to-glutamine ratio) and increased myo-inositol – characteristic of glial activation. We observed no change in total brain or cerebrospinal fluid volume. Diffusion MRI showed decreased apparent diffusion coefficient and increased neurite density index in cortex, corpus callosum, and hippocampus in mice on a high lithium diet.

Discussion: The acute phase of lithium treatment may be mistaken for illness with decreased neuronal markers and apparent diffusion coefficient. However, when paired with increased neurite density index and no change in brain volume, a closer look reveals an increased glial contribution to the signal. These changes occurred across three distinct brain regions in both grey and white matter. Taken together, our findings hint at increased astrocyte activity and density. Thereby offering support for the hypothesis that astrocytes are a target of lithium treatment[3].

Conclusion: We established an MR-based profile of lithium treatment in healthy, wild-type mice that hints at an increased astrocyte activity. This profile may be a novel MR-detectable biomarker of lithium treatment.

References:

[1] Alda. *Who are excellent lithium responders and why do they matter?* World Psychiatry (2017)

[2] Memhave, Moussavi, and Boretius. *SPIRAL MRI for in vivo lithium-7 imaging: a feasibility study in mice after oral lithium treatment*. Scientific Reports (2024)

[3] Rivera and Butt. *Astrocytes are direct cellular targets of lithium treatment: novel roles for lysyl oxidase and peroxisome-proliferator activated receptor-γ as astroglial targets of lithium.* Translational Pysichiatry (2019)

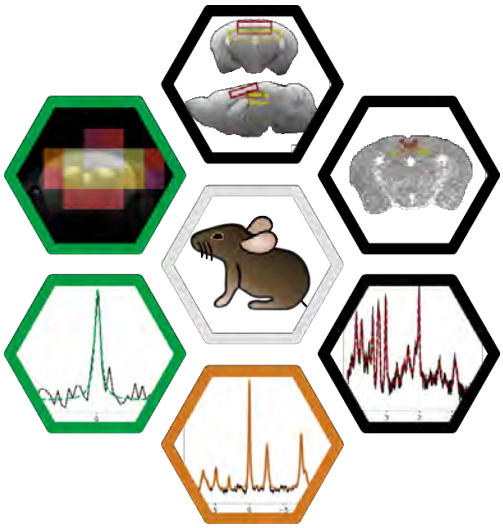

Figure 1: Schematic representation of multi-nuclear MRI in mice. Clockwise from the top: ^{1}H anatomical and diffusion MRI as well as MRS for (micro)structural changes and metabolism (in black); ^{31}P MRS (in orange) for energy metabolism; and ^{7}Li MRS and MRI for lithium uptake and distribution (green)

Hyperpolarized ^{13}C imaging of Alzheimer's Disease: impact of sex, genotype and age in the hAPP-J20 model

Marina Radoul[1,2*], Lydia M. Le Page[1,2*], Caroline Guglielmetti[1,2], Huihui Li[3,4], Yoshitaka J Sei[3,4], Ken Nakamura[3,4] and Myriam M. Chaumeil[1,2]

[1] Department of Physical Therapy and Rehabilitation Science, [2]Department of Radiology and Biomedical Imaging, UCSF, San Francisco, USA, [3]Gladstone Institute of Neurological Disease, Gladstone Institutes, San Francisco, USA, and [4]Department of Neurology, UCSF, San Francisco, USA; * authors with equal contribution

INTRODUCTION: Metabolic impairment is a major factor in most neurodegenerative diseases, including Alzheimer's disease (AD)[1]. Although [^{18}F]-FDG-PET visualizes reduced glucose uptake in AD[2], repeated use is limited by radiation and high background. Hyperpolarized (HP) ^{13}C MR has been used for investigation of brain tumors[3], multiple sclerosis[4], trauma[5], and diet model of dementia[6], but has yet to be applied to AD. In this study, we tested if HP ^{13}C metabolic imaging can provide information on sexual dimorphism and metabolic aging in the hAPP-J20 (J20) AD model.

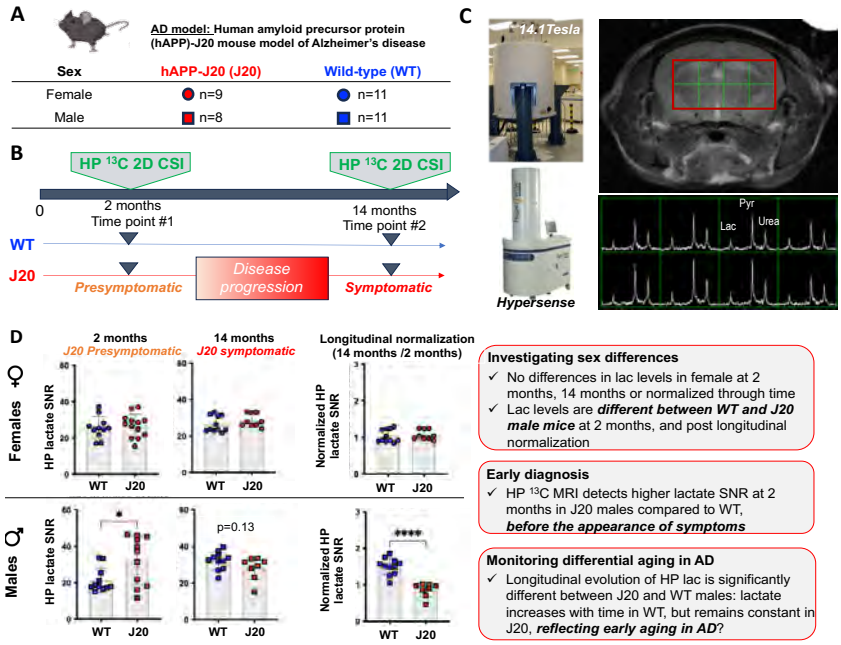

Figure 1: Animal model (A) and study design (B). T2 MRI image of a WT mouse with HP ^{13}C 2D CSI grid and spectra (C). Key findings of the study: focus on lactate **(D)**

METHODS: Animals: 1) WT females (n=11) and males (n=11); 2) hAPP-J20 female (n=9) and male mice (n=8) (**Fig.1A,B**) were imaged twice: pre-symptoms (2-months-old) and after amyloid plaques formed (14-months-old) [7,8].
MR acquisitions were conducted on a 14.1T MR system (Agilent) with 100G/cm gradients and a 40mm ^{1}H-^{13}C volume coil. 24µl [1–^{13}C]pyruvate (15mM OX63) was polarized for ~1h on a Hypersense (Oxford). 300µl of the 80 mM solution was injected via tail vein over 12s. 2D-^{13}C CSI was acquired 18s after using: TE/TR= 0.56/68ms; SW 4006Hz; 256 points; FA=10°; FOV=30×30mm²; 5mm thickness (**Fig.1C**).
Data analysis was done using MATLAB and SIVIC (http://sourceforge.net/apps/trac/sivic/). The AUC of HP[1-^{13}C]pyruvate and HP[1-^{13}C]lactate were measured for each voxel. Lac, total-^{13}C (lac+pyr), Lac/total-^{13}C and Lac/Pyr were averaged over 8 brain voxels (**Fig.1C**).
Statistical analysis: Paired data were analyzed using two-way ANOVA and unpaired data using t-test (*p<0.05; **p<0.01; ***p<0.005).

RESULTS: We investigated the impact of sex, genotype and age, and their interactions, on all derived HP metrics. As summarized in **Fig.1D**, key findings were mostly seen on HP lactate. First, whereas there are no differences in lactate levels in female at 2 months, 14 months or when normalized through time, HP^{13}C-lactate levels are different between WT and J20 male mice at 2 months, and post longitudinal normalization, indicating that HP^{13}C imaging can investigate metabolic sexual dimorphism. Second, HP ^{13}C MRI detects higher lactate SNR at 2 months in J20 males compared to WT, before the appearance of symptoms, indicating the potential of HP ^{13}C imaging for early diagnosis of AD. Finally, we show that evolution of HP ^{13}C-lactate is significantly different between J20 and WT males: lactate increases with time in WT, but remains constant in J20, which possibly reflects early aging in AD.

DISCUSSION: Our study is the first to report that age, genotype and sex, and their interactions, have significant impacts on HP ^{13}C metabolic imaging parameters, especially HP lactate, in a mouse model of AD. Specifically, hyperpolarized ^{13}C imaging provides unique metabolic information specific to sex, APP mutational status and metabolic aging in an AD model. Altogether, our results highlight the potential of HP^{13}C neuroimaging to improve understanding and monitoring of AD. Upon clinical translation, such method could improve early diagnosis and patient-centric monitoring of AD progression, and potentially assessment of therapeutic response.

REFERENCES [1]. L. Xu et al. Brain metabolism in Alzheimer's disease: biological mechanisms of exercise *Translational Neurodegeneration*. 2023, 12, 33. **[2]**. Ya-Nan Ou, et al. FDG-PET as an independent biomarker for Alzheimer's biological diagnosis *Alzheimer's Research & Therapy.* 2019 11, 57 **[3]**. A.W. Autry, et al. Characterization of serial hyperpolarized ^{13}C metabolic imaging in patients with glioma. NeuroImage: Clinical. 2020, 27, 102323 **[4]**. C. Guglielmetti, et al. Hyperpolarized ^{13}C MR metabolic imaging can detect neuroinflammation in vivo in a multiple sclerosis murine model. *Proc Natl Acad Sci U S A*. 2017 Aug 15; 114(33): E6982–E6991. **[5]**. C. Guglielmetti, et al. In vivo metabolic imaging of Traumatic Brain Injury. *Scientific Reports*. 2017: 7, 17525 **[6]**. Y.-S. Choi et al. Hyperpolarized [1-^{13}C] pyruvate MR spectroscopy detect altered glycolysis in the brain of a cognitively impaired mouse model fed high-fat diet. *Mol Brain*. 2018; 11: 74; **[7]** L. Mucke, E. et al**.** High-Level Neuronal Expression of Aβ$_{1–42}$ in Wild-Type Human Amyloid Protein Precursor Transgenic Mice: Synaptotoxicity without Plaque Formation**.** *J Neurosci*. 2000**;** 20(11): 4050–4058**; [8]**. A.L. Wright et al**,** Neuroinflammation and Neuronal Loss Precede Aβ Plaque Deposition in the hAPP-J20 Mouse Model of Alzheimer's Disease**.** *PLoS One*. 2013; 8(4): e59586

Magnetic resonance imaging monitoring of CD4+ T cells for solid organ transplantation applications

Fanny Chapelin, PhD[1]; Aman Khurana, MD[2]; Songyue Han[1], Francesc Marti, PhD[3]; Roberto Gedaly, MD[3]
[1] Shu Chien-Gene Lay Department of Bioengineering, University of California San Diego, La Jolla, CA; [2] Department of Radiology, University of California San Diego, La Jolla, CA; [3] Department of Surgery, University of Kentucky, Lexington, KY

Introduction: The field of solid organ transplantation (SOT) has made great strides in providing life-saving solutions for patients with end-stage organ failure. However, allograft rejection occurs in 25-50% of transplant recipients[1]. Effective immunosuppression management is therefore essential to improve transplant outcomes. Infusion of regulatory T cells (Tregs) alongside SOT is a promising strategy aimed at achieving immune homeostasis to prevent rejection[2]. However, the development of effective Treg-based therapies requires methods to determine their longitudinal fate and efficacy *in vivo*. With the use of contrast agents, magnetic resonance imaging (MRI) has emerged as an effective tool for noninvasive, real-time monitoring of cellular processes. Combining cell-sorting microbeads (e.g., CD25-targeting microbeads) with MRI technology has shown potential for enhanced visualization and tracking of Treg cells after transplantation[3]. In an attempt to broaden the application spectrum and potentially the signal change induced by these microbeads we decided to investigate CD4 microbeads as a labeling agent for T cells and Tregs. This approach would not only enhance our understanding of Treg cell dynamics in the context of organ transplantation, but also opens up new possibilities in the broader field of immunotherapy.

Materials and methods: CD4+ T cells were isolated from blood donors and cultured under controlled conditions to ensure viability and functional integrity. Microbead labeling conditions were optimized using different concentrations and incubation times and compared to unlabeled controls via Prussian Blue staining, phenotype stability, and electron microscopy. Cell pellets of both groups were also prepared for MR imaging of signal attenuation, with agarose gels as controls. Twenty million CD4 microbead-labeled T cells were injected intravenously into seven 8-10 week old female immunodeficient mice using the optimized labeling protocol. Seven mice received equivalent unlabeled T cells and served as control. MRI scans were performed at scheduled intervals (pre, 24 h and 72 h post-injection) to monitor the distribution and movement of these labeled cells in the mouse abdomen. MRI images were acquired on a preclinical Bruker 7T imaging system using a mouse birdcage body coil (Bruker). Axial images of mouse liver were acquired using a Turbo RARE sequence and a T2map Multi Slice Multi Echo (MSME) sequence with TR = 2000 ms and 10 TEs equally spaced from 6.4 to 64 ms, Matrix size = 128 × 128, FOV = 36 × 24 mm^2, Slice thickness = 1.2 mm, Averages = 3, Slice number = 16. T2 values were extracted using the system's inbuilt software by defining three circular liver ROIs over 3 slices. Statistical analysis was performed to compare the *in vitro* MRI results of different groups using a t-test. In addition, longitudinal repeated measures analyses, under the general framework of mixed-effects models will be conducted for in vivo MRI data. We will correlate T cell counts in histological stainings of tissues to MR signal attenuation using the Kendall Tau method.

Results: Overnight labeling with 10 µl CD4 microbeads/million T cells exhibited the strongest T2 signal decay and showed positive intracellular Prussian Blue staining, indicating successful uptake of CD4 microbeads (Fig. 1A) without viability impairment (94% viable cells, $p<0.01$ compared to unlabeled controls). Unlabeled controls did not exhibit positive Prussian Blue staining. Electron microscopy experiments confirmed intracellular localization of numerous CD4 microbeads, specifically in lysosome-like structures (black beads, Fig. 1B). CD4 microbead-labeled T cells in agarose gels displayed significant T2-weighted MR signal decay compared to unlabeled cells and agarose controls (data not shown), consistent with adequate labeling with a paramagnetic iron oxide. Systemically injected CD4 microbead-labeled T cells exhibited decreased T2 signal as early as 24 hours post-injection (Fig. 1C). The signal intensity remained stable until the 72 hour imaging timepoint, indicating that the T cells that home to the liver remain there for that time (Fig. 1D). Histology analyses are underway to correlate T cell counts to MR signals.

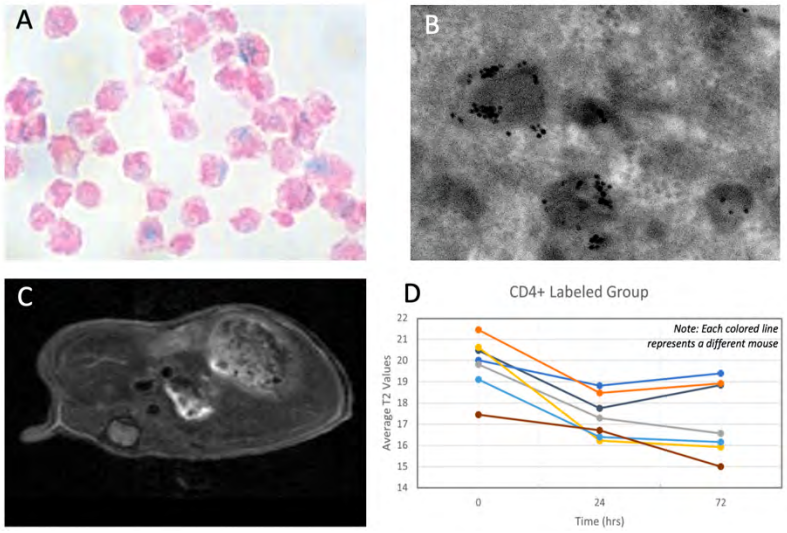

Figure 1. CD4 microbead internalization and *in vivo* T2 signal decay quantification. Prussian blue stain (**A**, blue) and electron microscopy (**B**, black dots) images of CD4 microbead-labeled T cells confirms intracellular localization of the contrast agent. Mice receiving CD4 microbead-labeled T cells systemically exhibit significant T2 shortening in liver tissues (**C**) at 24 and 72 hours post-infusion (**D**).

Discussion and conclusion: In our study, we observed that CD4 microbeads can be internalized into CD4+ T cells through specific binding to the CD4 receptor. Significant T2 signal decay was detected at the smallest concentration of these microbeads. Interestingly, the effect levelled off beyond a certain concentration, suggesting a maximum loading capacity through this approach. Nonetheless, this study demonstrates a pioneering approach in the field of organ transplantation, providing a novel clinically relevant strategy for non-invasive longitudinal tracking of T cells or Tregs using MRI. Looking forward, we aim to track Treg homing in skin transplant models to correlate Treg infiltration with transplanted organ outcomes.

References: (1) Feng, S. *Liver Transpl* 2017. (2) Juneja, T. *Front Immunol* 2022. (3) Khurana, A. *Sci Rep* 2022.

The physico-chemical characterization of [Mn(OPMMA)] complex containing malonate pendant

Abraham Estifanos Debretsion,[1] Szilvia Bunda,[1] Norbert Lihi,[2] Zoltán Garda,[1,3] Dóra Bakos,[1] Emese Kun,[1] Tibor Csupász,[1] Gyula Tircsó,[1] Éva Jakab-Tóth[3] and Ferenc Krisztián Kálmán[1]

[1] Department of Physical Chemistry, Faculty of Science and Technology, University of Debrecen, H-4032 Debrecen, Hungary; [2] ELKH-DE Mechanisms of Complex Homogeneous and Heterogeneous Chemical Reactions Research Group, Department of Inorganic and Analytical Chemistry, Faculty of Science and Technology, University of Debrecen, H-4032 Debrecen, Hungary; [3] Centre de Biophysique Moléculaire, CNRS UPR 4301, Université d'Orléans, Rue Charles Sadron, F-45071, Orléans 2, France

Introduction: Nowadays, the MRI (magnetic resonance imaging) contrast agents (CAs) used in clinical practice are the complexes of paramagnetic Gd(III) ion formed with polyamino-polycarboxylate ligands.[1] The *in vivo* application of the toxic Gd(III) (LD_{50} = 0.1-0.3 mmol/kg) ion was facilitated by the formation of thermodynamically stable and inert complexes, which were considered to be safe for years until the appearance of the nephrogenic systemic fibroses (NSF) in the late 90s.[2] This potentially lethal disease was mostly reported for patients having sever renal failure, when the urine excretion is slower or stopped, thus the *in vivo* life-time of the CAs increases significantly, which can lead to the liberation of the Gd(III) from the agents.[3,4] Due to the "NSF-problem", concerns have been raised over the safety of contrasted MRI investigations, which prompted researchers to find alternatives for the compromised CAs. The replacement of the Gd(III) with the essential Mn(II) ion seems to be an obvious solution, however Mn(II) also displays toxicity in elevated concentrations. Furthermore, the thermodynamic stability and inertness of the Mn(II) complexes are orders of magnitudes lower than those of the Gd(III) chelates due to its d^5 electron configuration, which requires careful ligand design.[5] In this work, we present the result of the physico-chemical characterization of an O-pyclen based Mn(II) complex containing malonate pendant arm (OPMMA, Figure 1.).

Methods: The equilibrium properties of the OPMMA and its Mn(II) complex were studied by pH-potentiometric technique, while spectrophotometric methode was used to characterize the inertness of the chelate. ^{1}H relaxometry, ^{17}O NMR and NMRD experiments were carried out to gain information about the relaxation properties of the complex, furthermore EPR measurements and DFT calculations were performed for describing its structure in solution.

Results and Discussion: The stability constant (log K_{MnL}) of the [Mn(OPMMA)] was found to be relatively low 10.07(5), orders of magnitudes lower than those were obtained for the OPC2A and PC2A complexes. For the better comparison, the pMn values (-log$[Mn(II)]_{free}$, c_{lig}=$c_{Mn(II)}$=0.01 mM, pH=7.4) of the Mn(II) chelates were calculated and those are 6.27, 8.69 and 8.64 for the [Mn(OPMMA)], [Mn(OPC2A)] and [Mn(PC2A)], respectively. The values show that the complex formation in the system of OPC2A and PC2A is practically 100% under these conditions, while circa 5% of the Mn(II) remains free, when OPMMA is the chelator. The inertness of the complexes was studied by means of metal exchange reactions occurring between the Mn(II) complex and Cu(II) applied as a scavenger for the ligand. Unfortunately, the preliminary experiments carried out in the pH range 3.9 - 5.1, have shown that the decomplexation is too fast to be investigated by conventional spectrophotometry, therefore stopped-flow technique was used. Based on the kinetic parameters obtained (k_1 = 1.4±0.1×10^5 M^{-1}s^{-1} and K_H = 4.7±0.6×10^4 M^{-1}) the half-life ($t_{1/2}$) of the dissociation is only 2 minutes at physiological pH, which is not suitable for *in vivo* applications.

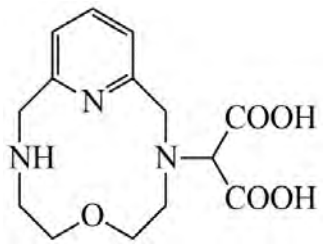

Figure 1. Structure of the OPMMA

The longitudinal relaxivity (r_{1p}) of [Mn(OPMMA)] (3.48 mM^{-1}s^{-1}) at 20 MHz is somewhat higher than that was determined for the OPC2A complex (3.13 mM^{-1}s^{-1}) indicating the presence of a q = 1 complex in solution. The r_{1p} values of [Mn(OPMMA)] decrease with increasing temperature at different magnetic fields, suggesting that it is controlled by the fast rotation of the complex, which is typical for low molecular weight Mn(II) complexes. The complex possesses fast water exchange (k_{ex}^{298} = 220.7±0.1×10^6 s^{-1}), circa 4 times higer than that was gained for the [Mn(OPC2A)], which can be explained by the structural differences.

References: 1. L. Helm, A. E. Merbach, É. Tóth, The Chemistry of Contrast Agents in Medical Magnetic Resonance Imaging, Second edition, 2013; **2.** H. Weinmann et al., Am. J. Roentgenol., 1984, 142, 619; **3.** T. Grobner, Nephrol. Dial. Transplant., 2006, 21, 1104; **4.** C. L. Bennett et al., Clin. Kidney J., 2012, 5, 82; **5.** C. Henoumont et al., Molecules 2023, 28, 7275

Brain State Dynamics

Elaine L. Bearer, Harry B. Gray, Taylor W. Uselman, SonJong Hwang, Andres Collazo, Russell E. Jacobs
University of New Mexico, California Institute of Technology and University of Southern California

Brain networks are dynamic, continuously adapting to a changing environment. At any one time, the relative levels of activity among the nodes of a network may be defined conceptually as a “brain state”, the fundamental framework of whole-brain activity during that experience. Each brain state is defined as a particular pattern of brain activity or functional coupling that emerges from, and has consequences for, physiology. Yet generalizable protocols to detect and analyze brain states in preclinical studies, where pharmaceutical testing would accelerate treatments for neuropsychiatric disorders, are lacking.

Mn(II) is a paramagnetic transition metal ion that increase the relaxation rate of adjacent water protons in T_1-weighted MR imaging yielding a robust RF signal. Mn(II) also has the unique biological attribute of selectively entering neurons through voltage-gated calcium channels labelling active neurons, and of delineating neuronal projections through its transport by endogenous axonal transport machinery. Mn(II), a trace mineral essential to the body in small amounts, has a dose-dependent toxicity at high doses in humans, while at the low doses used for manganese-enhanced MRI (MEMRI), Mn(II) is safe, with few detectable side effects by electrophysiology, histopathology, or behavior as multiple investigators have reported. Because of its very low toxicity and rapid clearance, $MnCl_2$ can be delivered repeatedly or even continuously with very few side effects. Mn(II) is administered in two ways: 1) by systemic infusion, to report on brain-wide neural activity in awake, freely moving animals; and 2) by localized intra-cerebral injection, to map neuronal projections. Mn(II) robust signal allows high resolution (100μm isotropic voxels) with short (30-40min) scan times. Mn(II) and accumulation directly reports on neurophysiology and functional projection anatomy.

Despite its potential, MEMRI has not been widely adopted, in part due to concerns about its toxicity, competition from the established, but more toxic, MR contrast agent, Gd, high cost and technical challenges of preclinical MRI, together with a lack of generalized protocols for harmonization of image capture on different scanners, standardization of image processing and easy to use tools for image analysis. Computational analysis of MR images, often statistically based, has broken open our understanding of the human brain. From anatomical images we can measure changes in regional volumes, from diffusion-tensor images we understand the anatomy of connections, and from BOLD imaging we identify synchronous activity predictive of networks and connections. Without computational techniques, information gleaned from human MRI would be minimal. Yet computational analysis of MEMRI in preclinical brain imaging has lagged far behind.

We are developing standardization procedures for MEMRI imaging to transcend differences in scanner hardware with strategies for SNR and CNR optimization, standardized power analyses procedures for sample size determination, generalization of image processing, and a novel toolbox for computational analysis that takes into consideration the unique properties of manganese-enhanced images. We validate these procedures using imaging data collected on 5 different scanners from three different vendors, at 1T, 7T, and 11.7T (Bruker, MR solutions and Scintica). We are finalizing our digital annotated *InVivoAtlas* that segments 120 mouse brain regions at 80μm isotropic voxel resolution by fitting our 3D atlas to the Allen Institute for Brain Science “common coordinate space”. Ultimately, this atlas will provide a framework to enable comparisons between data collected by different scanners and even by other imaging or physiological techniques, including whole-brain light-sheet microscopy, focused ultrasound (FUS) imaging or neuropixel electrophysiological tracings. We have successfully applied our longitudinal imaging procedure for the study of brain states during normal motility, during acute threat, in an anxiety-like behavior and after early life stress. Staining active nuclei for immediate early genes validates activity patterns detected by MEMRI. We also use MEMRI to track neuronal projections, including from CA3 of the hippocampus and regions of the prefrontal cortex (PFC). We find that afferent projections from the PFC are precisely arranged and locations even 1 mm apart project to significantly different deeper destinations. MEMRI tracing is validated by microscopy of serial sections after a co-injected histological tracer. Whether projections go to active regions is confirmed by cross-validations with seed-based analysis of FUS images, systemic MEMRI data and/or the literature.

Structural equation modeling (SEM) based on our validated MEMRI data assures us that coactivation coefficients are applicable to MEMRI datasets, where variance between individuals rather than between timepoints in the same individual (as in fMRI) provides valid coactivation information for detection of networks in known circuits. Once validated, co-activation matrices are produced to evaluate MEMRI data for network information from preclinical animals under different conditions and after pharmacological manipulations.

Our latest imaging protocols will be presented and we will share concepts for our original custom software.

Quantitative concentration measurements of positive T_1 agents in clinical imaging protocols

Audrey Lavielle, Noël Pinaud, Yannick Crémillieux

Institut des Sciences Moléculaires, CNRS, Université de Bordeaux, Bordeaux, France

Introduction: The use of T_1 contrast agents is ubiquitous in the diagnosis and prognosis of pathologies, and in therapy monitoring. For certain key applications, such as dynamic contrast-enhanced perfusion imaging (1), or in the case of smart contrast agents or theranostic agents, it is necessary to quantify their impact on T_1 values and to assess their concentration in the tissue of interest (2,3). Numerous MRI sequences are available to obtain quantitative T_1 maps in patients. However, in clinical practice, these MRI sequences are rarely incorporated into clinical protocols. In this study, we present alternative approaches, based on the use of T_1-weighted acquisitions included in standard clinical protocols, for obtaining quantitative T_1 maps and concentration measurements of Gd- or USPIO-based T_1 agents.

Methods: MRI acquisitions were performed on tumor-bearing patients at 3 Tesla using conventional T_1-weighted imaging sequences, namely MPRAGE and T_1-weighted TSE for patients with brain metastases or glioblastoma, and the VIBE sequence for patients with lung tumors. Analytical expression of MR signal intensity in MPRAGE and VIBE acquisitions was used to plot the T_1 values as a function of the image signal intensity (Fig. 1A and 1B). For T_1-weighted TSE acquisitions, a phantom (Fig. 1C) consisting of 144 tubes filled with solutions of paramagnetic ions (Mn^{2+}, Cu^{2+}, Ni^{2+}) with known T_1 values was imaged to generate a plot of T_1 values as a function of image intensity. Power regression was used to establish the analytical relationship between the T_1 values and the signal intensity (Fig 1D). For each patient, T_1-weighted images were acquired before and after intravenous injection of Gd-based nanoparticles. T_1 maps were generated from the patient's T_1-weighted images as described above. The concentration maps of the T_1 agent were computed using the equation $\frac{1}{T_{1,post}} = \frac{1}{T_{1,pre}} + r_1 C$ where r_1 is the longitudinal relaxivity of the T_1 agent and C its concentration.

Results: An example of T_1 map obtained in a patient prior to T_1 agent injection is shown in Fig. 2A. The mean T_1 values (21 patients in total) measured in white matter and gray matter regions were found to be within the range of values reported in the literature. Concentration maps of Gd^{3+} ions were obtained in patients with brain metastases (Fig. 2B) with mean values equal to 47 μM of Gd^{3+} in brain metastases (N=153 metastases). In glioblastoma patients (Fig. 2C), the mean Gd^{3+} concentration was equal to 85 μM (N = 6 patients). In lung tumor patients (N=4 patients), the mean Gd^{3+} concentration measured was 96 μM (Fig. 2D).

Discussion and conclusion: The proposed approaches have been successfully validated in animals, phantoms and in patients (4). Our results demonstrate that it is possible to use T_1-weighted acquisitions, which are widely employed in clinical practice, to generate parametric T_1 maps and to image the distribution and the concentration of T_1 agents administered as part of a standard clinical protocol.

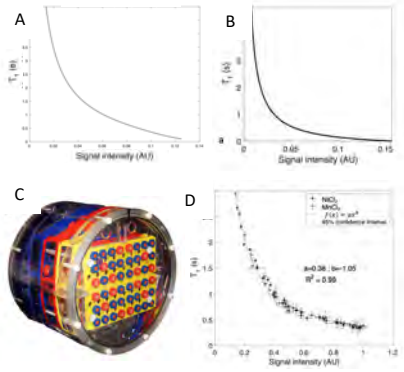

Figure 1 (left): T_1 value plotted as a function of computed signal intensity for MPRAGE (A) and VIBE (B) sequences. Phantom composed of 144 tubes containing paramagnetic solutions with known T_1 values (C). T_1 value as a function of signal intensity in the T_1-weighted TSE image measured in the phantom tubes. The red curve corresponds to the power regression T_1=0.38 $SI^{-1.05}$.

Figure 2 (below): T_1-weighted TSE image acquired from a patient and the T_1 map derived from the TSE image (A). Whole-brain visualization of Gd^{3+} concentration in metastases obtained from 3D TSE T_1-weighted MRI acquisitions in a patient (B). Gd^{3+} concentration map obtained from an MPRAGE acquisition in a patient with glioblastoma (C). T_1 maps derived from VIBE acquisitions in a patient with lung tumor (contoured in white), before and after injection of Gd-based nanoparticles (D).

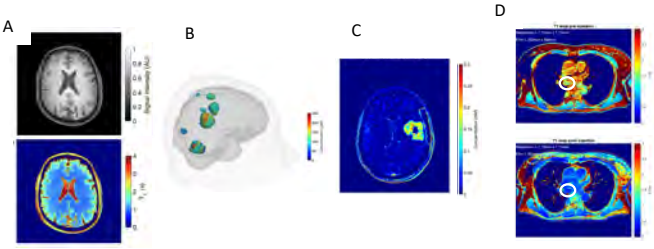

Acknowledgments: A.L. acknowledges a PhD financial support from ANRT and NH TherAguix. The authors thank NH THerAguix and DFCI for providing images of patients.

References: 1. Conte GM et al.: Comparison of T_1 mapping and fixed T_1 method for dynamic contrast-enhanced MRI perfusion in brain gliomas. Eur Radiol 2019. **2**. Mura S, Couvreur P: Nanotheranostics for personalized medicine. Adv Drug Deliv Rev 2012. **3.** Verry C et al.: Targeting brain metastases with ultrasmall theranostic nanoparticles, a first-in-human trial from an MRI perspective. Sci Adv 2020. **4.** Lavielle A et al.: T1 Mapping From MPRAGE Acquisitions: Application to the Measurement of the Concentration of Nanoparticles in Tumors for Theranostic Use. J Magn Reson Imaging 2023.

Temporal In-Vivo Characterization of Diet-Induced Alcoholic and Non-Alcoholic Fatty Liver Diseases: A Molecular Imaging Perspective at 6 Month

Kimia Samadikhah[1], Marta Vuozzo[1,2], Bernd J. Pichler[1,2], Andreas M. Schmid[1,2]

1) Werner Siemens Imaging Center, Department of Preclinical Imaging and Radiopharmacy, Eberhard Karls University Tübingen, Tübingen 72076, Germany
2) Cluster of Excellence iFIT (EXC 2180) "Image-Guided and Functionally Instructed Tumor Therapies", University of Tübingen, Tübingen 72076, Germany

Introduction: Non-alcoholic fatty liver disease and alcoholic fatty liver disease pose significant global health challenges, potentially advancing via non-alcoholic steatohepatitis, alcoholic steatohepatitis to hepatocellular carcinoma. Precise diagnosis is vital for prognosis and personalized treatment. For characterizing liver disease development, this study employs multiparametric MRI to examine T1/T2* tissue properties, fat quantification and composition and immune cell response (utilizing PFC). These techniques allow non-invasive staging of liver disease. Our measurements involved normal chow as control, high-fat choline-deficient (HFCD), and Western diet (WD) with glucose (Glc) in drinking water, generating diverse liver models. To explore the alcohol-diet interaction, we added ethanol (Alc) to Glc-enriched drinking water. This thorough methodology provides insights into the nuanced impacts of diverse diets on various parameters, facilitating a comprehensive understanding of liver condition progression over the study period.

Methods: In this 6-month study, 30 male C57BL/6 mice underwent dietary variations, including a standard diet with water, HFCD with 5% Glc, HFCD with 5% Alc and 5% Glc, WD with 5% Glc, and WD with 5% Alc and 5% Glc, administered ad libitum. Mouse weights were systematically compared weekly, and measurements were taken after 6 months. Liver volumes were compared using T2-weighted 3D MRI images. T1 and fat fraction maps were generated based on FLASH acquisitions with a field-of-view of 50x23x28 and a matrix size of 10x46x28. For T1 maps, we used different flip-angles (FA), and 3 echo times (TE: 2.9, 3.4 and 3.9 ms) for the fat fraction map. T2* maps were acquired with MGE (TR: 1012 ms, TE: 4, 9, 14, 19, 24, 29, 34 ms and 39 ms, FA:50). For perfluorocarbon (PFC) measurements, mice received a 500 µL PFC injection. The [^{19}F] signal was detected 24 hours later using a [^{19}F] coil in 7T-MRI. Liver regions of interest (ROIs) were outlined on the MRI reference image and transferred to the images. Whole liver ROIs were established and normalized to a phantom with 100 µL PFC for PFC analysis. In addition to analyzing the whole liver, voxel-wise analysis was performed for all the parameters using homemade software based on MATLAB.

Results: In this molecular imaging study, after 6 months, liver volumes were as follows: Control=1392±104 mm³, HFCD=1892±514 mm³, Alc+HFCD=2169±620 mm³, WD=4058±974 mm³, Alc+WD=4440±941 mm³. Given the significant difference in liver volumes, a total of [^{19}F] uptake was calculated. After 6 months, [^{19}F] signal intensity in arbitrary units was as follows: Control=16408±4166 a.u., HFCD=22475±10913 a.u., Alc+HFCD=22751±7896 a.u., WD=26682±7236 a.u., Alc+WD=31084±7020 a.u.. In comparison to the control group, mice subjected to the HFCD diet demonstrated an elevation of 6.1 % in liver fat fraction, while those exposed to Alc+HFCD manifested an increment of 8.4 %. The WD-fed cohort displayed the most pronounced increase in liver fat fraction, with a rise of 21.8 % compared to controls, while the Alc+WD group exhibited a marginally lower increase of 19.8 %. Compared to the control group, mice fed HFCD exhibited a decrease in T1 relaxation times of 197 ms, while those on Alc+HFCD showed a decrease of 244 ms. WD-fed mice displayed the highest T1 relaxation times, with an increase of 399 ms compared to controls, whereas Alc+WD mice exhibited a slightly lower increase of 644ms. Regarding T2* values, HFCD-fed mice experienced a decrease of 0.4 ms compared to controls, while Alc+HFCD mice showed a reduction of 0.5ms. The WD-fed cohort exhibited T2* values comparable to controls, with a decrease of 0.2 ms, whereas the Alc+WD group displayed a slightly higher decrease of 1.2 ms. Due to the heterogeneity of the liver, voxel-based analysis were performed and showed different distributions in total [^{19}F] uptake, fat fraction, T1 and T2* parameters for different diets. These results provide detailed insights into the molecular changes induced by diverse diets, emphasizing their impact on liver volumes, total [^{19}F] uptake, fat fraction, T1 and T2* over the 6-month study period.

Conclusion: In this study, dietary variations induced significant changes in liver parameters over the 6 month study period. Notably, WD-fed mice exhibited substantial liver volume expansion compared to controls, with the most pronounced increase observed among WD groups. Total [^{19}F] uptake, liver fat fraction, and T1 and T2* values varied notably across different dietary groups, reflecting distinct molecular changes induced by diverse diets. Voxel-based analysis further demonstrated the heterogeneity of liver responses to dietary interventions. These findings underscore the importance of diet in modulating liver health, and highlight the utility of multiparametric MRI and PFC imaging in comprehensively assessing liver disease progression.

High Chemical-Shift Exchangeable Protons for CEST-Sensitive Reporter Proteins with High Specificity

David E. Korenchan[†], Nicolas Scalzitti[‡], Michael T. McMahon[§], Assaf A. Gilad[‡], and Christian T. Farrar[†]

[†]Athinoula A. Martinos Center for Biomedical Imaging, Massachusetts General Hospital, Charlestown, MA
[‡]Department of Chemical Engineering and Materials Science, Michigan State University, East Lansing, MI
[§]F.M. Kirby Research Center for Functional Brain Imaging, Kennedy Krieger Institute, Baltimore, MD

Introduction: Chemical exchange saturation transfer (**CEST**) leverages proton exchange to obtain highly amplified molecular contrast. A higher chemical shift dispersion between the water and solute protons can accommodate a higher proton exchange rate, which increases the CEST effect magnitude and facilitates contrast generation on lower-field MRI scanners. Additionally, a CEST peak at a high chemical shift would improve the selectivity of reporter gene protein products for *in vivo* applications, such as viral gene delivery or oncolytic virotherapy, especially if greater than 3.5 ppm downfield of water, where the largest endogenous CEST pool caused by amide proton exchange resides. In this work, we explored exchangeable protons with high downfield chemical shifts generated by π-bonding in amino acid sidechains.

Methods: Each peptide or protein was suspended in 1x phosphate-buffered saline (**PBS**) and titrated to pH 7.3. Ultrafast z-spectroscopy[1] at 37 °C was performed in a 14 T spectrometer. Custom MATLAB scripts were used to fit CEST z-spectral peaks with pseudo-Voigt curves, then to fit the fitted peak amplitudes *vs.* saturation amplitude using QUantification of Exchange rate using varying Saturation Power (**QUESP**)[2,3]. Water was referenced to 0 ppm.

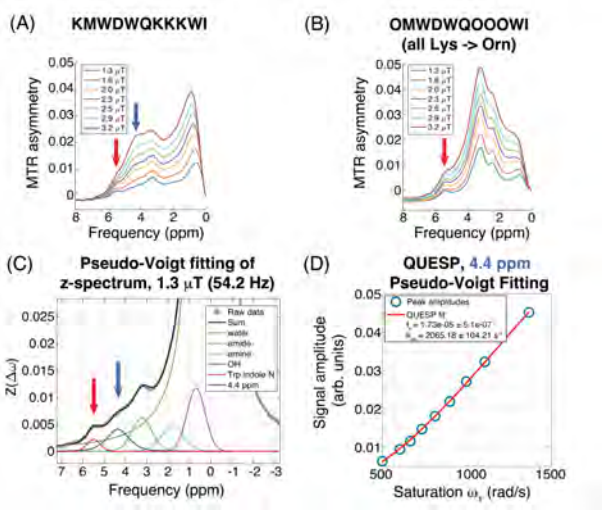

Figure 1. CEST investigation of cation-π shifted protons in Trp-containing peptides. (A) MTR_{asym} *vs.* saturation amplitude showing a 4.4 ppm peak. (B) Orn substitution abolishes the 4.4 ppm peak. (C) Representative z-spectrum with peak fits. (D) QUESP fitting to measure proton exchange rate.

Results: We discovered a tryptophan (**Trp**)-containing peptide which, in addition to having a typical magnetization transfer ratio asymmetry ($\mathbf{MTR_{asym}}$) peak at 5.3 ppm from exchanging protons on the indole nitrogen[4], showed a large resonance at 4.4 ppm (**Fig. 1A**). This resonance probably arises from a lysine (**Lys**) sidechain amine interacting with a nearby Trp indole via a cation-π interaction[5], since substituting ornithine for all Lys in this peptide sequence abolished the 4.4 ppm signal (**Fig. 1B**). Substituting 5-hydroxyTrp for the Trp at position 3 had the same effect (data not shown). We measured the 4.4 ppm proton exchange rate to be 1770 s^{-1} (**Fig. 1D**). Because the protein glucoamylase contains a unique cation-π interacting complex between a Lys, two Trp, and two tyrosines (**Tyr**)[5] (**Fig. 2B**), we also measured its CEST z-spectrum and discovered two highly-shifted, CEST-detectable protons at 7.3 and 9.8 ppm (**Fig 2A**), in agreement with a previous conventional NMR study[6]. Both protons exchange at ≥6000 s^{-1} (data not shown).

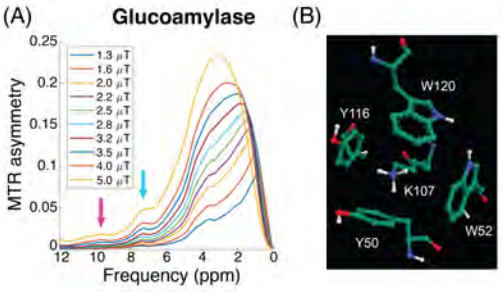

Figure 2. (A) MTR_{asym} profile of glucoamylase. (B) Amino acid sidechains in glucoamylase demonstrating cation-π interactions, likely causing the MTR_{asym} peaks indicated with arrows (image from Mol* on rcsb.org, PDB ID: 1GAI).

Discussion: Endogenous Trp and Tyr residues give CEST contrast at chemical shifts over 4 ppm downfield from water[4,7], but the contrast is relatively weak due to very fast chemical exchange and/or water access to the exchanging moiety. We show that by exploiting interactions between aromatic amino acid sidechains and other groups, we generate large, highly shifted CEST peaks. We believe the aromatic sidechains induce higher deshielding and may also slow down proton exchange to increase the degree of saturation. While protein CEST signals further downfield than those for glucoamylase have been reported at pH 5.5[8], the glucoamylase CEST signals are robust at physiological temperature and pH.

Conclusion: We demonstrate strong CEST contrast arising from highly downshifted exchangeable protons. The resonances can be introduced into proteins endogenously, making them useful for reporter gene protein design. In future work, we will engineer these resonances into a stable reporter gene product, develop imaging sequences that maximize reporter protein detectability and selectivity, and test it with *in vivo* imaging to evaluate viral therapeutic efficacy.

References:

[1]Xu, X., Lee, J.-S. & Jerschow, A. *Angew Chem Int Ed* **52**, 8281–8284 (2013). [2]McMahon, M. T. *et al. Magn Reson Med* **55**, 836–847 (2006). [3]Zaiss, M. *et al. Magn Reson Med* **79**, 1708–1721 (2018). [4]Kawata, Y. *et al. Biochemistry* **27**, 346–350 (1988). [5]Gallivan, J. P. & Dougherty, D. A. *Proc Nat Acad Sci* **96**, 9459–9464 (1999). [6]Firsov, L. M. *et al. Eur J Biochem* **223**, 293–302 (1994). [7]Liepinsh, E., Otting, G. & Wüthrich, K. *J Biomol NMR* **2**, 447–465 (1992). [8]Lauzon, C. B., Van Zijl, P. & Stivers, J. T. *J Biomol NMR* **50**, 299–314 (2011).

Water-Soluble, Fluorinated Manganese Porphyrin Complexes for Redox Detection

Daniela S. S. Teixeira[1,2], Zoltan Garda[2], Agnés Pallier[2], Sara M. A. Pinto[1], Mariette M. Pereira[1] and Éva Tóth[2].

[1]Coimbra Chemistry Centre, University of Coimbra, Portugal; [2]Centre de Biophysique Moléculaire, CNRS, UPR 4301 Université d'Orléans, Orléans, France.

Introduction: *In vivo* assessment of the tissue redox state with imaging techniques is desirable in various pathologies, including cardiovascular diseases[1,2] and cancer.[3] In the past, we reported three redox MRI probes based on fluorinated Mn(III/II) porphyrins[4,5] which undergo reduction in the presence of ascorbic acid followed by a reversible reoxidation with O_2, providing ^{1}H and ^{19}F relaxivity responses to redox changes. Despite these promising features, solubility of these compounds in biological media remains an important issue. Here, we present the synthesis of a novel and more water-soluble fluorinated manganese porphyrin complex and its evaluation as potential redox-responsive ^{19}F MRI contrast agent.

Methods: The synthesis of the porphyrin and the corresponding manganese(III) complex was carried out by adapting previously published methods. The complex and its redox behavior was investigated by UV-Vis spectrophotometry and ^{1}H and ^{19}F NMR. ^{1}H NMRD profiles of both the oxidized and reduced manganese complexes were obtained in the 0.01-80 MHz range. ^{19}F MRI phantom imaging was carried out at 7 T.

Results and Discussion: Mn(III) reduction to Mn(II) was followed through UV-Visible spectroscopy analysis in different solvent mixtures (10%DMSO/90%water or PBS) using ascorbic acid as reducing agent. Under these conditions, reduction was not observed, probably due to aggregation and/or to a coordination effect between PBS salts and Mn(III). Aggregation was indeed evidenced by Dynamic Light Scattering in both solvent mixtures. In contrast to PBS buffer, total reduction was obtained in HEPES (50% DMSO and 50% HEPES) in the presence of 5 equivalents of ascorbic acid. The reduction could be also followed by ^{19}F NMR, via the disappearance of the ^{19}F peak of the Mn(III) complex and the concomitant appearance of a detectable signal corresponding to the reduced Mn(II) form. The NMRD study showed that the Mn(II) complex has higher relaxivity at low fields, while the Mn(III) analogue has a characteristic relaxation peak at high fields between 10-100 MHz. Finally, ^{19}F NMR phantom images were also acquired for the oxidized and reduced forms. Due to the shorter relaxation times, the NMR signal intensity decreased significantly for the reduced sample, resulting in a decrease in the signal-to-noise ratio. Ongoing efforts involve the development of a new porphyrins with enhanced solubility in biological environments.

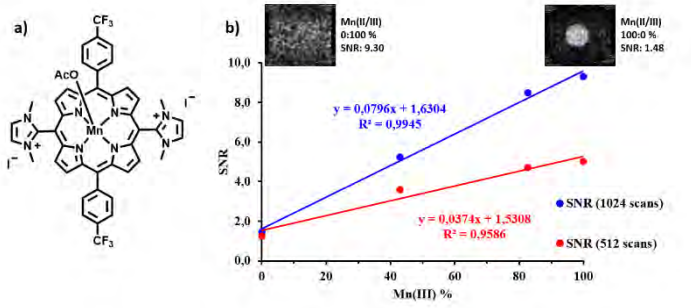

Figure 1: a) Chemical structure of the fluorinated Mn-porphyrin; b) ^{19}F MRI phantom images to monitor reoxidation by air oxygen: signal to noise ratio as a function of the oxidized Mn(III)-porphyrin content (%).

References: 1. Bom, M. J. et al. Circ. Cardiovasc. Imaging, 10, e005973 (2017); 2. Yun, J. W. et al. Pathophysiology,23, 265-274 (2016); 3. Milosevic, M. et al. Technol Health Care, 26, 729-759 (2018); 4. Pinto, S. M. et al. Dalton Trans. 48, 3249-3262 (2019); 5. Pinto, S. M., et al. Chem. - Eur. J. 29, e202301442 (2023).

Development of modular inserts for dynamic studies of biological cells

C. Boutin, F. Nghiem, C. Coutelier, K. Chighine, P. Berthault
NIMBE, CEA, CNRS, Université de Paris Saclay, CEA Saclay, 91191 Gif-sur-Yvette, France

Introduction: MRI is an imaging technique acclaimed for its safety, and is the subject of numerous pre-clinical studies, an essential prerequisite for future medical applications. However, one of the three legislative strands of the regulations associated with European animal experimentation requires these experiments to be replaced as far as possible by experiments on *in vitro* models. It is therefore essential to have high-performance tools enabling the most comprehensive studies possible on complex biological samples. To this end, we are developing high-performance in situ devices for NMR analysis of living biological cells based on previous work.[1,2] These devices have also been coupled with complementary techniques such as hyperpolarization or fluorescence spectroscopy to enrich the information obtained.

Methods: the inserts dedicated to the study of biological samples are designed by CAD and then 3D printed using biocompatible resins. Depending on the type of biological cells to be studied (cells in suspension or adherent cells) and the type of measurements to be carried out, different insert geometries have been produced. Three examples have been chosen here to illustrate the different modularities of these inserts: (a) an insert adapting to high-resolution NMR probes based on inductive coupling. Dedicated to cells in suspension, it stirs the sample using a bubble pump. This also enables hyperpolarized gases such as xenon-129 to be delivered, (b) an insert which plugs onto a micro-imaging probe base (Bruker micro-5), enabling larger volume samples to be analyzed. This insert has been designed to be coupled to fluorescence spectroscopy. A multicore optical fiber illuminates the cells grown in the insert and collects the fluorescence signal emitted. And finally (c) a larger insert dedicated to studying the diffusion of hyperpolarized xenon through biological barriers.

Results and Discussion: Proof-of-concept studies have been carried out on the various types of insert. For the sake of clarity, only the methodology associated with insert (c) is detailed in this abstract. The insert is placed in a 7 T super wide bore spectrometer associated with a $^{1}H/^{129}Xe$ probe. We studied the passage of hyperpolarized xenon through this barrier. In order to study the passage of hyperpolarized xenon through the blood brain barrier (BBB) a permeable cell culture membrane on which BBB cells have been grown[3] is placed in the pre-printed insert. The device thus consists of two biological media separated by the biological membrane: the apical media representing the blood compartment and the basal media representing the brain compartment. After hyperpolarization by spin exchange optical pumping setup, hyperpolarized xenon is injected into the device using a programmable syringe pump. It is dissolved in the culture medium by passing through a bundle of gas exchange membranes. Z-profiles acquired over time show the evolution of the xenon signal density on either side of the biological membrane.

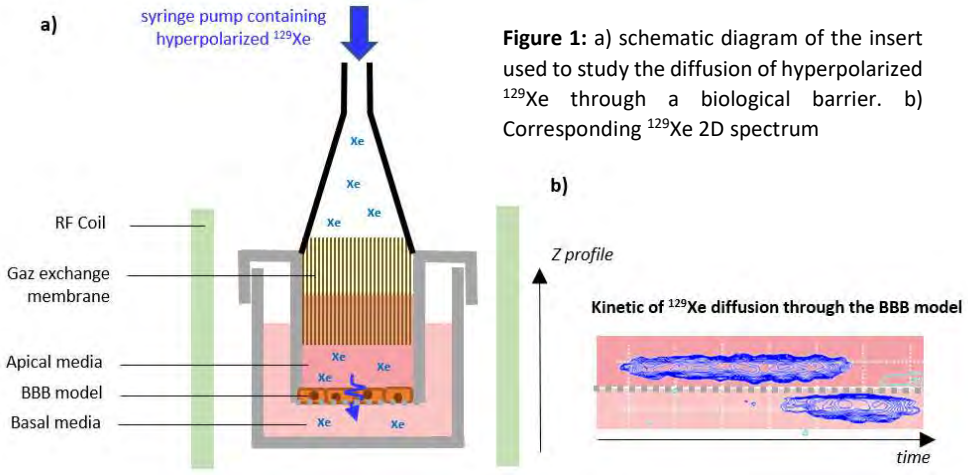

Figure 1: a) schematic diagram of the insert used to study the diffusion of hyperpolarized ^{129}Xe through a biological barrier. b) Corresponding ^{129}Xe 2D spectrum

Conclusion: The various inserts developed in the laboratory are powerful tools, both in terms of the biological questions they address, and in the development of new NMR methodologies for future *in vivo* experiments.

References: 1) Causier A, et al. 3D-printed system optimizing dissolution of hyperpolarized gaseous species for micro-sized NMR. Lab Chip. 2015;15(9):2049-2054. **2)** Carret G, et al. Inductive Coupling and Flow for Increased NMR Sensitivity. Anal Chem. 2018;90(19):11169-11173. **3)** Lacombe O, et al. In vitro primary human and animal cell-based blood-brain barrier models as a screening tool in drug discovery. Mol Pharm. 2011;8(3):651-663.

A non-covalent approach to increasing the relaxivity of Eu^{II}-containing contrast agents for magnetic resonance imaging.

Kailyn K. Fields and Matthew J. Allen
Department of Chemistry, Wayne State University, Detroit, MI, United States of America

Introduction

Recent studies demonstrated methods of kinetically stabilizing the Eu^{II} ion from oxidation to Eu^{III} with relevancy to responsive contrast agents for magnetic resonance imaging.[1,2] One of those studies demonstrated that a phosphonate-containing complex resists oxidation in oxygenated solutions, which is an important step toward the goal of systemic delivery of oxygen-responsive contrast agents.[1] We hypothesize that if the relaxivity of that agent is increased, then the observable persistence time will also increase because the number of observable half-lives will increase as a function of relaxivity. To test this hypothesis, we are increasing the size of the molecule via non-covalent electrostatic interactions with macromolecules to decrease the overall tumbling rate of the contrast agent and, therefore, increase signal intensity. We will present our current results focusing on the combination of the phosphonate-containing probe with protamine sulfate, a cationic polyaminoacid that is approved by the US Food and Drug Administration for heparin overdose treatment. The phosphonate-containing probe carries a negative charge under physiological conditions and is expected to engage in attractive electrostatic interactions with positively charged protamine sulfate. These electrostatic interactions promote the formation of a bulky, slowly tumbling, contrast agent.

Methods

All materials were purchased from commercial sources and used as received. Water was purified (ELGA PURELAB Ultra Mk2) and degassed before transfer into a wet glovebox (water allowed but no molecular oxygen) where all reactions were performed. Phosphate-buffered saline was degassed, transferred into a wet glovebox, and then diluted from commercial 10× phosphate-buffered saline to a tenth of its original concentration using degassed water. Metalation with Eu^{II} was performed following a reported method.[1] Samples were prepared in a wet glovebox before transfer into NMR tubes that were subsequently sealed with paraffin wax. T_1 measurements were acquired using a Minispec (60 MHz, 37 °C, 1.41 T, Bruker).

Results and Discussion

We expect the relaxivity of the phosphonate-containing complex to increase with the addition of protamine sulfate due to increases in molecular weight, similar to recent studies.[3–5] We will present our current results.

References

(1) Rashid, M. M.; Corbin, B. A.; Jella, P.; Ortiz, C. J.; Hassan Samee, Md. A.; Pautler, R. G.; Allen, M. J. Systemic Delivery of Divalent Europium from Ligand Screening with Implications to Direct Imaging of Hypoxia. *J. Am. Chem. Soc.* **2022**, *144*, 23053–23060. https://doi.org/10.1021/jacs.2c10373.

(2) Lutter, J. C.; Batchev, A. L.; Ortiz, C. J.; Sertage, A. G.; Romero, J.; Subasinghe, S. A. A. S.; Pedersen, S. E.; Samee, M. A. H.; Pautler, R. G.; Allen, M. J. Outersphere Approach to Increasing the Persistance of Oxygen-Sensitive Europium(II)-Containing Contrast Agents for Magnetic Resonance Imaging with Perfluorocarbon Nanoemulsions toward Imaging of Hypoxia. *Adv. Healthc. Mater.* **2023**, *12*. https://doi.org/10.1002/adhm.202203209.

(3) Stefania, R.; Palagi, L.; Di Gregorio, E.; Ferrauto, G.; Dinatale, V.; Aime, S.; Gianolio, E. Seeking for Innovation with Magnetic Resonance Imaging Paramagnetic Contrast Agents: Relaxation Enhancement via Weak and Dynamic Electrostatic Interactions with Positively Charged Groups on Endogenous Macromolecules. *J. Am. Chem. Soc.* **2024**, *146*, 134–144. https://doi.org/10.1021/jacs.3c06275.

(4) Boros, E.; Polasek, M.; Zhang, Z.; Caravan, P. Gd(DOTAla): A Single Amino Acid Gd-Complex as a Modular Tool for High Relaxivity MR Contrast Agent Development. *J. Am. Chem. Soc.* **2012**, *134*, 19858–19868. https://doi.org/10.1021/ja309187m.

(5) Rudovsky, J.; Botta, M.; Hermann, P.; Hardcastle, K. I.; Lukeš, I.; Aime, S. PAMAM Dendrimeric Conjugates with a Gd-DOTA Phosphinate Derivative and Their Adducts with Polyaminoacids: The Interplay of Global Motion, Internal Rotation, and Fast Water Exchange. *Bioconjug. Chem.* **2006**, *17*, 975–987. https://doi.org/10.1021/bc060149l.

Zinc finger peptides as a bioinspired scaffold for the design of Zn^{2+} responsive MRI contrast agents

Luke A. Marchetti[1], Patrick Malikidogo[2], Kate Lefroy,[2] Tom Di Santo,[2] Agnès Pallier[1], Manon Isaac[1,2], Olivier Sénèque[2], Célia S. Bonnet[1]

[1]Centre de Biophysique Moléculaire, UPR CNRS 4301, Université d'Orléans, F-45071 Orléans, France

[2]Univ. Grenoble Alpes, CNRS, CEA, BIG, LCBM (UMR 5249), F-38000, Grenoble, France

Introduction: Zinc is the second most abundant metal ion in the body and plays crucial roles in homeostasis and the immune system.[1] Zn^{2+} concentration is tightly regulated and disruption of its concentration has been implicated in neurodegenerative diseases and various cancers.[2] Thus, it is essential to have the ability to detect and monitor Zn^{2+} *in vivo* for the early detection of such diseases and to aid in the understanding of zinc's role in such pathologies. Magnetic resonance imaging (MRI) has proved to be a powerful tool in this field due to its ability to obtain anatomical images with high spatial and temporal resolution, unlimited tissue depth imaging, and its non-invasive nature. Indeed, the utilisation of Gd^{3+}-based MRI contrast agents for the detection of Zn^{2+} *in vivo* has made great strides in recent years.[3] The main approach used by our group and others is to design small molecular complexes and play with the difference of affinity for a given protein in the absence and in the presence of Zn^{2+},[4] or the Gd^{3+} hydration number.[5] Herein, we will present a bioinspired approach for Zn^{2+} detection using a zinc-finger peptide conjugated to a Gd^{3+} chelate, displaying high affinity and selectivity, alongside inherent biocompatibility.

Methods: Solid-phase peptide synthesis was employed to synthesise various zinc-finger peptides, differing by their zinc-binding domains, which were subsequently conjugated to a DO3A-type Gd^{3+}-chelate. Circular dichroism (CD) was performed to investigate the Zn^{2+} binding properties of the peptide. NMRD profiles were generated between 0.01 – 400 MHz to asses ^1H relaxivity of the probe in response to Zn^{2+}, and also in the presence of Human Serum Albumin (HSA). The data was collectively analysed and fitted using Solomon-Bloembergen-Morgan (SBM) theory to determine various microscopic parameters of the system.

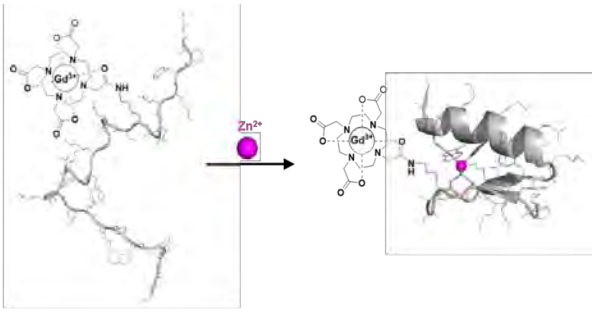

Fig 1. Folding of the peptide into a ββα-fold upon Zn^{2+} binding

Results and Discussion: CD analysis revealed that the peptide adopts a ββα-fold upon Zn^{2+}-binding, which is typical of such zinc-finger peptides (Figure 1).[6] The parent peptide bearing two Histidine and two cysteines interstingly shows a difference of regime depending on the binding of Zn to the probe: rotation (τ_R) limits r_1 in the Zn-free form whereas water exchange (k_{ex}) limits in the Zn-bound form. This non-classical behaviour contributes to the enhancement of the Zn-response at 37 °C. The replacement of the two cysteines by histidines, while more adapted to the physiological environment, decreases the affinity for Zn^{2+}, resulting in a loss of this switch-regime. To rationalize and optimize the Zn^{2+} response, we have modified the Gd chelate, the length of the linker between the Gd chelate and the zinc-finger peptide, as well the positions of the hgistidines and of the Gd complex within the peptide. Finally, the interaction with HSA was also studied for the best systems in the absence and in the presence of Zn^{2+}.

Conclusion: In conclusion, we have presented Zn^{2+}-responsive MRI contrast agents by taking a bio-inspired approach, incorporating a zinc-finger peptide into a Gd^{3+}-based probe. Zn^{2+}-binding causes the peptide to form a ββα-fold, subsequently increasing the MRI efficacy of the probe due to an increase in global rotational correlation time. We are currently rationalizing the structural variation of the probe on the Zn^{2+} response to optimize the system for further in vivo applications.

References: 1. Chasapis, C. T.; Loutsidou, A. C.; Spiliopoulou, C. A.; Stefanidou, M. E., Arch. Toxicol. **2012**, 86 (4), 521-534; 2. Szewczyk, B., Front. Aging Neurosci. **2013**, 5, 33; 3. Malikidogo, K. P.; Martin, H.; Bonnet, C. S., Pharmaceuticals. **2020**, 13 (12); 4. Martins, A. F.; Clavijo Jordan, V.; Bochner, F.; Chirayil, S.; Paranawithana, N.; Zhang, S.; Lo, S.-T.; Wen, X.; Zhao, P.; Neeman, M.; Sherry, A. D., J. Am. Chem. Soc. **2018**, 140 (50), 17456-17464; 5. Wang, G.; Martin, H.; Amézqueta, S.; Ràfols, C.; Bonnet, C. S.; Angelovski, G., Inorg. Chem. **2022**, 61 (41), 16256-16265 ; 6. Isaac, M.; Pallier, A.; Szeremeta, F.; Bayle, P.-A.; Barantin, L.; Bonnet, C. S.; Sénèque, O., Chem. Comm. 2018, 54 (53), 7350-7353.

PiB-derivative metal complexes for selective imaging of amyloid peptides

Simon Hery[1], Saida Majdoub[1], Inga Relich[2], Adèle Brison[2], Sara Lacerda[1], Jean-François Morfin[1], Christelle Hureau[2] and Eva Toth[1]

[1]*Centre de Biophysique Moléculaire, CNRS, Orléans, France*
[2]*Coordination Chemistry Laboratory, CNRS, Toulouse, France*

Introduction: Aggregation of misfolded peptides is a hallmark of increasingly prevalent diseases, including type 2 diabetes mellitus (T2DM) and Alzheimer's disease (AD), implying amyloid forms of amylin and Abeta, respectively.[1] The AD brain is characterized by neuronal loss leading to brain atrophy and by the presence of amyloid plaques and neurofibrillary tangles. On the other hand, the accumulation of amylin (islet amyloid polypeptide, IAPP) that is co-secreted with insulin and deposited in the Langerhans Islets, is observed in >90% of T2DM patients and contributes to cell toxicity.[2,3]

Increasing evidence suggests a link between T2DM and AD, likely mediated by fibril "cross-seeding" processes when one amyloid protein promotes aggregation of another. In this context, selective visualisation of amylin- and Aβ-amyloids becomes important.[4,5] Despite the high number of imaging probes reported for amyloid detection, so far none has shown selectivity for amylin- vs. Aβ-amyloids.[6,7] Here we report the development and initial characterisation of new imaging probes for the selective detection of amylin.[8]

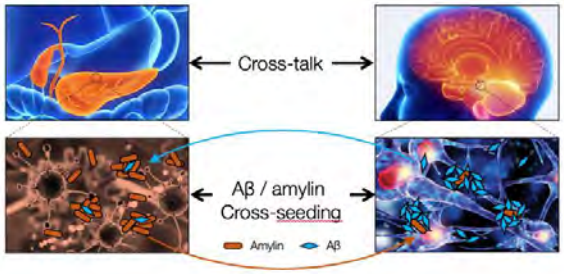

Figure 1: Cross-seeding mechanisms underlying the link between AD and T2DM.

Methods: Imaging probes were synthesised starting from cyclen as starting material. All the intermediate compounds were successfully characterised by High Resolution Mass Spectroscopy (HRMS) and NMR spectroscopy. Affinity constants were determined by surface plasmon resonance (SPR). This technique was used for real time studies to assess the binding of the Gd^{3+} complexes to peptide fibrils immobilized on the sensor chips. In vitro peptide aggregation was monitored with ThT competition assays in the presence of the imaging agents.

Results and Discussion: After multi-step synthesis of different imaging probe candidates, we have recently identified two chelates, bearing two PiB units in *cis* (GdLcis) or *trans* position on a cyclen (GdLtrans), with selectivity for amylin- vs. Aβ–fibrils. Dissociation constants (K_d) measured by SPR are 2-3 orders of magnitude higher for amylin- than for Aβ-fibrils. Likewise, when *in vitro* peptide aggregation is monitored with ThT competition assays, the effect of the compounds is different for Aβ and amylin: GdLcis and GdLtrans readily replace ThT from preformed amylin-fibrils (more than control complexes bearing one PiB unit), but not from Aβ-fibrils.

Conclusions: These complexes are the first examples with several orders of magnitude higher affinity for amylin fibrils than for Aβ–fibrils. The reasons for this selectivity are not yet identified. Novel complexes are currently investigated in order to gain insight into the structural parameters and charge effects that might be responsible for selectivity.

References:

1.Zhang, Y. *et al*, *Chin. J. Chem. Eng.*, *30*, 225–235, (2021). **2.** Villemagne, V. L. *et al*, *Lancet Neurol.*, *12* (4), 357–367, (2013). **3.** Milardi, D. *et al*, *Chem. Rev.*, *121* (3), 1845–1893, (2021). **4.** Oskarsson, M. E. *et al*, *Am. J. Pathol.*, *185* (3), 834–846, (2015). **5.** Fawver, J. *et al*, *Curr. Alzheimer Res.*, *11* (10), 928–940, (2014). **6.** Saito, K. *et al*, *Nucl. Med. Biol.*, *106–107*, 72–79 ,(2022). **7.** Yoshimura, M. et al, *Bioconjug. Chem.*, *27* (6), 1532–1539, (2016). **8.** Saida Majdoub, *PhD Thesis, University of Orléans.*

Improving the physicochemical properties of potential Mn(II)-based liver specific MRI probes

Alexis Cabahug Achacoso[a,b], Sajtos Gergő Zoltán[a,b], Váradi Balázs[a,b], Garda Zoltán[a,c], Tircsó Gyula[a],
[a] *Department of Physical Chemistry, Faculty of Science and Technology University of Debrecen, Hungary,* [b]*Doctoral School of Chemistry University of Debrecen, Hungary and* [c] *Center of Molecular Biophysics, CNRS, University of Orléans, France*

Introduction: Molecular probes capable of targeting specific organs or tissues, such as the liver, spleen, or lymph nodes can be of particular interest for the non-invasive detection of diseases, metabolic disorders etc. The use of hepatobiliary-specific agents in liver imaging can improve the detection of lesions in the liver, allowing for the differentiation of hepatocellular and nonhepatocellular lesions, and provide specific characterization of some hepatocellular lesions, such as focal nodular hyperplasia.[1] Therefore, liver-specific probes can provide relevant information which in turn may be used to evaluate the anatomy and function of the biliary tree and liver. Recently, it was reported that 3,6-PC2A-9-EOB is a potential liver-specific probe.[2] The given probe was shown to accumulate in the liver, but its inertness is questionable. Therefore, in the present work, we investigated the possibility of improving the physicochemical properties (stability, inertness and relaxivity response) of the Mn(II)-based liver-specific probe by applying 3,9-PC2A ligand platform during the ligand design, which has been identified as one of the best candidates for chelating Mn(II).[3]

Methods: The ligand was synthesized using standard chemical synthetic techniques, while the metal complex was isolated and characterized by high-pressure liquid chromatography (HPLC), mass spectrometry (MS), and ^{1}H relaxometry. The thermodynamic stability of the Mn(II) complex was determined by the combination of pH-potentiometric and ^{1}H relaxometric techniques, while solvent exchange kinetics was studied via variable temperature ^{17}O NMR method. Dissociation kinetics of the complexes were accessed by studying metal exchange reactions with essential metal ions (Cu(II) and Zn(II)) and their serum stability was also evaluated by using commercially available human blood serum.

Results: The 3,9-PC2A-9-EOB ligand forms a less thermodynamically stable Mn(II) complex (logK_{MnL}=15.42, pMn=8.35) than that observed for the parent macrocycle (logK_{MnL}=17.09, pMn=8.64) which is the consequence of the electron withdrawing effect of the EOB moiety attached to the parent ligand platform. Kinetic studies showed that the inertness of the [Mn(3,9-PC2A-6-EOB)] complex improved significantly as compared to its isomeric form, [Mn(3,6-PC2A-9-EOB)] ($t_{1/2}$=2.93 h at pH=6.0 vs. 0.13 h at pH=7.0, 25 eq. Zn(II) ion at 37 °C), and this was also true for the relaxivity data (r_{1p}/r_{2p}=3.50/7.37 vs. 2.83/5.37 at 37 °C, 1.41 T). Furthermore, the inertness of the [Mn(3,9-PC2A-6-EOB)] complex and relaxivity data (r_{1p}/r_{2p}=4.70/10.37 at 25 °C, 1.41 T) were significantly improved as compared to the values observed for the parent [Mn(3,9-PC2A)] chelate ($t_{1/2}$=0.35 h at pH=6.0, r_{1p}/r_{2p}=2.43/5.38 at 25 °C, 1.41 T).

Discussion: The use of an ethoxybenzyl (EOB) sidearm attached to the pyclen macrocycle (3,9-PC2A) slightly decreased the thermodynamic stability of the Mn(II)-based liver-specific probe, but it has notably improved the relaxation and dissociation kinetics parameters. In addition, the attachment of the EOB moiety at the N^6 position of the macrocycle made the Mn(II) complex of the 3,9-PC2A-6-EOB significantly better candidate in terms of relaxation and kinetic parameters than the isomeric 3,6-PC2A-9-EOB ligand reported previously.

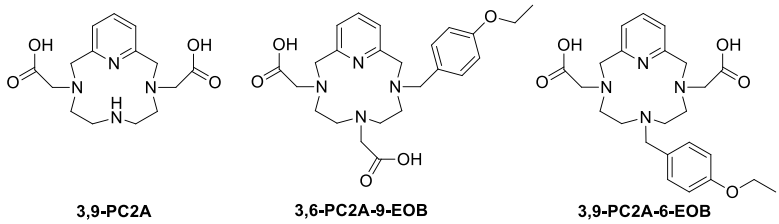

Figure 1. Formulae of the *3,9*-PC2A, *3,6*-PC2A-*9*-EOB and *3,9*-PC2A-*6*-EOB ligands.

Conclusion: The relaxivity response and inertness of the potential Mn(II)-based liver imaging probes can be tuned by the proper selection and arrangement of the metal binding pendant arms attached to the macrocyclic platform (i.e. ligand topology) of the ligand.

References: [1] J. Fidler and D. Hough, *Hepatology*, **2011**, *53(2)*, 678–682; [2] R. C. Hall, J. Qin, V. Laney, N. Ayat, and Z. R. Lu, *ACS Appl Bio Mater*, **2022**, *5(2)*, 451–458; [3] Z. Garda et al., *Inorg Chem*, **2021**, 60(2), 1133–1148.

Acknowledgement: The research was funded by the Hungarian National Research, Development and Innovation Office (NKFIH K-134694 and PD-138064 projects). The scientific research was supported by the Gedeon Richter's Talentum Foundation established by Gedeon Richter Plc (Gedeon Richter Ph.D. Fellowship). The research was prepared with the professional support of the Doctoral Student Scholarship Program of the Cooperative Doctoral Program of the Ministry of Innovation and Technology financed by the NKFIH and the Stipendium Hungaricum Scholarship Program of the Tempus Public Foundation.

Synthesis and evaluation of multimeric nanoparticle-based MRI agents

O. Tyurina [a], J. D. E. T. Wilton-Ely [b], A. Phinikaridou [a] and G. J. Stasiuk [a]

a. *School of Biomedical Engineering and Imaging Sciences, St Thomas' Hospital, Westminster Bridge Road, SE1 7EH, London, UK*

b. *Department of Chemistry, Imperial College London, Molecular Sciences Research Hub, White City Campus, W12 0BZ, London, UK*

Introduction: Gadolinium-based magnetic resonance imaging (MRI) agents have been widely used in the clinic since the popularisation of the technique in 1980s. Over the past 30+ years there have been many developments in the field, however the clinically used agents are still non-specific and require large quantities to achieve sufficient signal enhancement.[1] Improved contrast can be achieved through enhancing relaxivity of the system by modifying the chelators and attaching those to nanoparticle platforms to slow down rotational correlation time of the individual complexes.[2]

Methods: Gold nanospheres ($AuNP_1$, $AuNP_2$ and $AuNP_3$ – 6, 16 and 34 nm in diameter respectively) were synthesised through modified Turkevich reduction method and functionalised with DO3A-based gadolinium units.[3] These were then characterisation using TEM, UV, DLS and relaxivities of the systems were evaluated through NMRD and MRI.

Results and Discussion: The restricted motion of the gadolinium complexes on the surface of the nanoparticles results in superior relaxivities of the resultant systems, calculated per Gd(III) unit, when compared to both the unbound gadolinium complex (Gd.L) and the common clinical contrast agent, Dotarem™, at various field strengths. The larger nanoparticles, with a higher number of associated gadolinium units, were found to display a greater enhancement per Gd(III) unit, (up to 45 mM^{-1} s^{-1} for larger systems compared to 4 and 3 mM^{-1} s^{-1} for unbound Gd.L complex and Dotarem™ at 23.4 MHz).

Conclusion: The larger nanoparticles, with a higher number of associated gadolinium units, were found to display a greater enhancement per Gd(III) unit, up to 12 times higher at 23.4 MHz. In addition, the larger assemblies concentrate a higher number of gadolinium units, up to 150 per particle, into the same region in space. These properties should therefore lead to an enhanced MRI signal and a higher quality image when used to target biological systems *in vivo*.

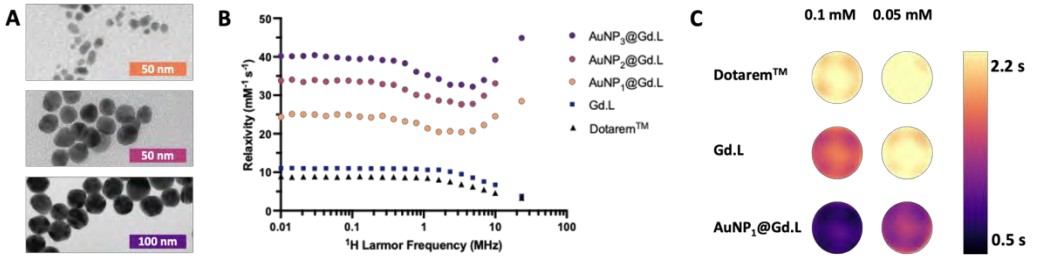

A) TEM images of gold nanospheres; B) NMRD profiles of Gd.L and gold nanospheres, $AuNP_1$, $AuNP_2$ and $AuNP_3$ with multiple Gd(III) units at 37°C; C) T_1 maps of $AuNP_1$@Gd.L compared to Gd.L complex and Dotarem™ measured at 3 T (128 MHz) using a 5(3)3 MOLLI sequence.

References:

[1] B. Brito; *et al. Organomet. Chem.;* **2020**; 43; 83-110.
[2] H. L. Perry; *et al. Chem. Commun.;* **2020**; 56; 4037-4046.
[3] C. J. Eling; *et al. ChemPlusChem.;* **2017**; 82; 674-680; N.G. Bastus; *et al. Langmuir*; **2011**; 27; 17; 11098-11105; T.O. Lilius; *et al. Journal of Controlled Release*; **2023**; 355; 135-148; N. G. Chabloz; *et al. Chem. Eur. J.;* **2019**; 25; 10895-10906.

Oxygen-responsive fluorinated Eu(II)-containing contrast agents for imaging hypoxia via MRI

List of Authors and Affiliations: Batchev, A. L.;[1] Subasinghe, S. A. A. S.;[1] Allen, M. J.[1]
[1] Department of Chemistry, Wayne State University, Detroit, Michigan 48202, United States

Introduction: The $Eu^{II/III}$ redox couple is a promising tool for distinguishing areas of hypoxia in vivo via multiple modalities of magnetic resonance imaging (MRI). The biggest challenge toward using $Eu^{II/III}$-based O_2-responsive contrast agents for a wide-variety of hypoxia imaging applications is that Eu^{II} is rapidly and irreversibly oxidized to Eu^{III} in areas of physiologically normal levels of pO_2. Consequently, these probes require direct injection into sites of suspected hypoxia. To stabilize Eu-containing contrast agents in the Eu^{II} oxidation state long enough to reach regions of hypoxia before oxidizing to Eu^{III}, the Allen lab has investigated kinetic routes of slowing the oxidation of Eu^{II} to Eu^{III}. One such approach uses a perfluorinated Eu^{II}-containing complex converted to a nanoemulsion and perfused with an inert gas to kinetically slow the approach of oxygen to the dispersed Eu^{II}. This approach showed a detectable persistence of Eu^{II} of over 30 minutes in vivo compared to a persistence of less than 5 minutes for a comparable complex outside a perfluorocarbon nanoemulsion as seen by changes in ^{19}F-MRI. This system could be improved by increasing the difference in signal intensity between before and after oxidation to increase the sensitivity of the probes to different oxygen concentrations. Toward addressing this goal, we hypothesized that changing the number of fluorines on ligand arms could affect ^{19}F signal intensity by changing the concentration of Eu^{II} in the perfluorocarbon nanoemulsion. To test that hypothesis, four ligands were synthesized that contained either 24, 28, 44, or 60 fluorine atoms.

Methods: A Eu^{II} complex of a 44-fluorine-containing cyclen derivative was synthesized, characterized, and converted into a perfluorocarbon nanoemulsion (~4.5×10^{-3} M) consisting of a 20% weight/weight of perfluoroctylalcohol in perfluoroctylbromide, phosphate-buffered saline, and lecithin of 199 ± 3 nm. The Eu^{II}-containing perfluorocarbon nanoemulsion was the injected into the thigh muscle of mice, and ^{19}F signal changes were monitored by ^{19}F-MRI to monitor the oxidation of Eu^{II} to Eu^{III}. Three more perfluorinated complexes varying in the number of fluorinated carbons containing 24 F, 28 F, and 60 F were synthesized, and the change in ^{19}F signal of Eu^{II} after oxidation to Eu^{III} was measured using NMR spectroscopy.

Results: Eu^{II} in the first complex persisted for over 30 minutes in vivo compared to less than 5 minutes for a comparable complex outside a perfluorocarbon nanoemulsion as seen by changes in ^{19}F-MRI. Additionally, the difference in ^{19}F signal intensity of the synthesized complexes demonstrated signal changes spanning from 27% to nearly 50% before and after oxidation of Eu^{II}.

Discussion: The perfluorinated nanoemulsion kinetically hinders the approach of O_2 into the outersphere of dispersed Eu^{II} through interfaces created by the nanoemulsion as well as by a pressure gradient caused by the insertion of inert gas that resists the diffusion of O_2. Further, the ligand modifications of the fluorinated pendent arms of the synthesized complexes of Eu^{II} affect ^{19}F signal in response to Eu^{II} oxidation to Eu^{III} possibly due to differences in solubility of the complexes or due to distance of Eu^{II} from F atoms producing signal.

Conclusion: These results are a promising step toward increasing Eu^{II} persistence in vivo to enable systemic delivery and ratiometric imaging of hypoxia in a wide variety of hypoxic environments by kinetically controlling the outersphere environment of Eu^{II}.

References: Lutter, J. C.; Batchev, A. L.; Ortiz, C. J.; Sertage, A. G.; Romero, J.; Subasinghe, S. A. A. S.; Pedersen, S. E.; Samee, M. A. H.; Pautler, R. G.; Allen, M. J., *Adv. Healthc. Mater.* **2023**, 2203209

Analysis of a novel boron drug delivery system and visualization attempts of the boron distribution by ^{11}B MRI

Yu Kimura[1], Hiroki Yokoyama[1], Tomoya Adachi[1], Risako Miura[1], Hisatsugu Yamada[2], Hirohiko Imai[3], Yasuhiro Aoyama[1], Shuichi Furuya[4], Teruyuki Kondo[1]

[1]Graduate School of Engineering, Kyoto University, Kyoto, Japan; [2]Graduate School of Technology, Industrial & Social Science, Tokushima University, Tokushima, Japan; [3]Graduate School of Informatics, Kyoto University, Kyoto Japan; [4]Nagoya University, Nagoya, Japan.

Introduction: Boron Neutron Capture Therapy (BNCT) is an effective method of cancer treatment that destroys only tumor cells without damages for normal cells, by generating α rays through neutron irradiation to cells containing ^{10}B.[1] And the development of novel boron drugs that can be selectively incorporated into tumor cells would be essential for the treatment of cancer by BNCT. Recently, Furuya *et al.* demonstrated that mixture complex of A_6K, an amphiphilic self-assembling peptide consisting of alanine (A) and lysine (K) residues, with sodium mercaptododecaborate (BSH) were delivered selectively through the blood-brain barrier to malignant brain tumors.[2] However, the structural analysis of the A_6K / BSH complexes, their shape change, and the detailed their function for the Drug Delivery System have not been clarified. In this study, we focused on relationship between the structures and the selective accumulation of BSH in tumor tissue. In addition, optimization for pharmacokinetics visualization of the boron agents directly through ^{11}B MRI was examined.

Methods: An A_6K nanotube[3] and A_6K/BSH complexes were prepared with various concentrations and characterized by DLS, ELS, TEM and STEM-EDS. The relaxation time of the ^{11}B nuclei of BSH was measured with bovine serum albumin. ^{11}B Phantom MRI of BSH with tumor extracts and *ex vivo* ^{11}B MRI of the tumors after topical injection of BSH was performed by use of the 3D UTE method.

Results: TEM observation of A_6K/BSH complex revealed that the A_6K nanotubes were aggregated and changed into fibrous secondary aggregates with the same direction. In addition, the complex was changed to the spherical forms under the low concentration conditions. Then, T_2 of the ^{11}B nuclei on BSH was extremely shortened in BSA solution. Phantom ^{11}B MRI showed that the spatial resolution of images was 1.875 mm (Gradient Echo method) and 0.9375 mm (UTE method). Concentration range estimation of ^{11}B MRI with tumor extracts indicated that the limit of detection was 0.2 mM (20.7 ppm in ^{11}B concentration) with S/N = 3.1. Finally, *ex vivo* ^{11}B MRI with transplanted U87 MG tumors revealed that three-dimensional ^{11}B MRI images of BSH were obtained in tumor tissue with a high spatial resolution of less than 1 mm as in the phantom after 76 minutes of measurement. And ICP-OES measurement indicated that the total amount of ^{11}B in tumor tissue was 0.16 mg.

Discussion: The characterization results indicated that the negative charge of the BSH mitigated the electrostatic repulsion between the positive charges on the surface of the A_6K nanotubes and the mixed complex consequently formed the aggregates. On the other hand, the aggregated form was changed to spherical under lower concentration condition below critical aggregation concentration of A_6K (0.2 mM). Such dynamic dilution also could occur *in vivo* and the morphology of the complexes could be changed with a size suitable for retention in the blood and for accumulation in tumors. Also shortening T_2 of ^{11}B on BSH in BSA solution means early loss of transverse magnetization, signal acquisition parameters should be changed in ^{11}B MRI. Finally, we succeeded in obtaining ^{11}B MRI images with high spatial resolution and reliable sensitivity for BNCT treatments by using UTE method.

Conclusion: A6K / BSH complexes could be delivered effectively to tumor tissue with the spherical form. And the UTE method, which provided images with better resolution, was useful for direct imaging boron distribution *in vivo* with high spatial resolution.

References: 1. Miyatake, S. I. *et al. J Neuro-Oncology* 149 (1), 1–11(2020); **2.** Michiue, H.; Furuya, S. *et al*. *J Control Release* 330, 788-796(2021); **3.** Von Maltzahn, G. *et al. Langmuir* 19 (10), 4332–4337(2003).

Size control of gadolinium oxide nanoparticles aggregation for MRI contrast enhancement and the effect for proton relaxation

Yu Kimura[1], Keisuke Kinda[1], Nanase Yoshida[1], Risako Miura[1], Hirohiko Imai[2], Teruyuki Kondo[1]

[1]Graduate School of Engineering, Kyoto University, Kyoto, Japan; [2]Graduate School of Informatics, Kyoto University, Kyoto Japan

Introduction: Nanoparticulate MRI contrast agents is known that the effect for signal enhancement on MRI correlates to the size of nanoparticles, because water coordination to gadolinium would be correlated to the surface area of nanoparticles directly indicated the site of coordination.[1] Consequently, shortening effect of transverse relaxation time (T_2) would be much obvious on smaller nanoparticles than the larger one. We previously succeeded the synthesis of gadolinium oxide nanoparticles modified with acidic gelatin for dual photoacoustic and magnetic resonance imaging.[2] In this study, we prepared gelatin-coated gadolinium oxide nanoparticles with the controlled sizes and performed ^{17}O NMR to analyze the interaction between nanoparticles and water molecules.

Methods: Gadolinium oxide nanoparticles were synthesized by a polyol method using gadolinium nitrate hexahydrate as a starting material, washed with acetone, dispersed in water at room temperature, and after various time lapses, gelatin-coated gadolinium oxide nanoparticles were obtained by adding gelatin derived from pig skin (molecular weight: 2,000). Water suspensions of gelatin-coated gadolinium oxide nanoparticles with three different particle sizes were used for phantom imaging using a 7 T MRI, and ^{17}O NMR (400 MHz) was performed in the presence of 5 v/v% $H_2{}^{17}O$ at varying temperatures.

Results: The size of NPs were controlled by changing the time for incubation before gelatin modification, the consequent average size of NPs were 30, 65, and 198 nm respectively. We tried to evaluate the stability of NPs size under various temperature conditions. From the result, all NPs were stable under every temperature conditions (4 - 60ºC) for 5 days. As a result of calculating the longitudinal and transverse relaxivity from the phantom image, the results showed that relaxivities of nanoparticles suspension phantom were all higher than that of Gd-DTPA. Moreover, the relaxivities of gelatin-coated gadolinium oxide nanoparticles was increased, following to increase the particle size. From ^{17}O NMR measurements of nanoparticle suspensions with three types of concentrations, it was revealed that the bulk water peaks shifted to the high magnetic field and sharpened with increasing concentration and temperature. The temperature dependence of the transverse relaxation rate of the bulk water indicated that the transverse relaxation rate of the nanoparticle suspensions was simply decreased with increasing temperature.

Discussion: The concentration and particle size dependence for chemical shift of bulk waters in ^{17}O NMR indicated that the surface area effect was similar to that of ordinary nanoparticulate Gd-MRI contrast agents. The water exchange rate of gelatin-coated gadolinium oxide nanoparticles suspension seemed to be faster than that of Gd-DTPA and even the transverse relaxation rate of them. Recently, there are several reports about effects for gadolinium-water interactions, by hydrophilic modification on nanoparticles[3] and Gd-DTPA.[4] Although gelatin was used for making protective colloids to stabilize the aggregation in our system, it could also have some effects for water coordination on the nanoparticles.

Conclusion: Gelatin-coated gadolinium oxide nanoparticles with various sizes were successfully synthesized by varying the elapsed time from water dispersion to gelatin addition. Much precise evaluations should be needed to clarify the proton relaxation mechanism of them with other analysis methods.

References: 1. Anishur Rahman, A. T. M. *et al. Contrast Media Mol Imaging* 8(1), 92–5(2013); **2.** Kimura, Y. *et al. Adv Healthcare Mat* 1(5), 657-60(2012); **3.** Miao, X. *et al. RSC Adv* 8(6), 3189–97(2018); **4.** De Sarno, F. *et al. Theranostics* 9(6), 1809–24(2019).

Zn^{2+}-Responsive bimodal MR probes for Monitoring Glucose Stimulated Zinc Release in mouse pancreas.

Angelina Prytula-Kurkunova[1,2], Jan Kretschmer[1,2], Remy Chiaffarelli[1,2], Yasmin Al-moufleh[1], André F. Martins[1,2,3]

[1]Werner Siemens Imaging Center, Department of Preclinical Imaging and Radiopharmacy, Eberhard Karls University, Röntgenweg 13, 72076, Tübingen, Germany, [2]Cluster of Excellence iFIT (EXC 2180) "Image Guided and Functionally Instructed Tumor Therapies", Röntgenweg 11, 72076, Tübingen, Germany, [3]German Cancer Consortium (DKTK), partner site Tübingen, German Cancer Research Center (DKFZ), Im Neuenheimer Feld 280, 69120, Heidelberg, Germany

Introduction: Imbalances of zinc levels in tissues have been linked to various diseases, including Alzheimer's disease, diabetes, transient neonatal zinc deficiency, and prostate cancer. In diabetes, β-cells, located in the pancreatic islets[1], play a crucial role in insulin release, during which zinc is co-released with glucose in high concentrations when required[2]. In this preliminary study, we designed a new generation of lanthanide-based agents with varying MR response. Interestingly, we found that agents with slower water exchange kinetics demonstrated superior T_1/T_2 MR imaging of insulin release by the pancreas. These findings hold significant promise for detecting and monitoring the glucose-stimulated zinc release by the pancreas.

Methods: We have performed the synthesis of a new Zn(II) responsive contrast agent with procedures previously described[3]. The two series of macrocyclic contrast agents possess DOTA and DOTMA motifs for higher kinetic inertness *in vivo*. Moreover, we introduced a substituted fluoro-pyridine-containing pendant arm for subsequent bimodal applications (Fig.1). Subsequently, the relaxivity of these complexes was evaluated both in vitro and in vivo using a 7T Bruker MRI scanner. *In vitro* relaxivity measurements (r_1 and r_2) were conducted by preparing solutions of Ln**1**, Ln**2** (Ln = lanthanide) along with their binary complexes with Zn^{2+} and their ternary complexes with both Zn^{2+} and human serum albumin (HSA), all in 100mM Tris buffer at 37°C. T_1w DCE images and T_1 maps (VFA method) of healthy C57BL/6 mice were acquired before and after injecting 0.1 mmol/Kg of Gd**1**, and an i.v. challenge of 2,2 mmol/Kg of glucose. Control animals received a dose of saline solution instead of glucose.

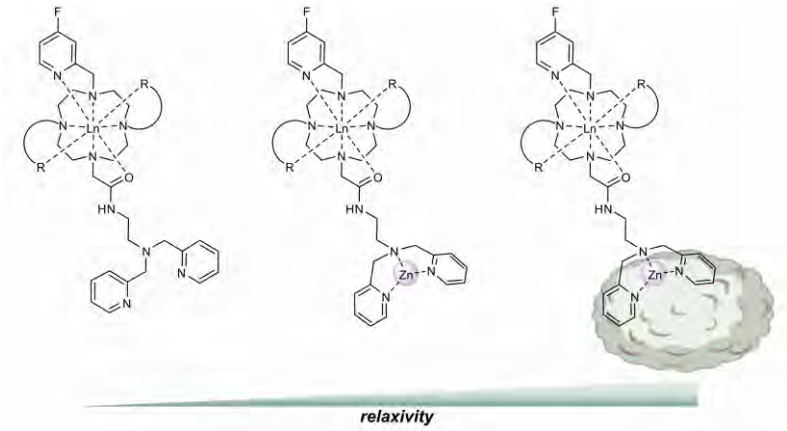

Fig. 1. Schematic illustration of the Lnx (x = 1,2) interaction with Zn2+ and HSA to form a ternary complex

Results and Discussion: We observed that the DOTMA-type enantiomerically pure complexes Gd**2** created a more rigid environment around the lanthanide atom, resulting in an increased relaxivity compared to the DOTA-type Gd1 complex. Specifically, Gd**1** and Gd**2** showed improved r_1 relaxivity values from 2.2 $s^{-1}mM^{-1}$ to 3.79 $s^{-1}mM^{-1}$, respectively. In the absence of Zn^{2+}, the newly synthesized zinc sensors showed little to no affinity for human serum albumin (HSA), but after binding to 1 equivalent of Zn^{2+}, the resulting complexes then bind strongly to HSA, resulting in a remarkable increase in r_1 relaxivity. This is particularly evident for Gd**2**, which showed an r_1 increase ~110% at 7T. We have observed that while the T_1 contrast at 7T is sufficient for accurately detecting Zn^{2+}, the T_2 contribution was even more pronounced under the same conditions[3]. For instance Gd**1** alone showed r_2 3.86 $s^{-1}mM^{-1}$, and the ternary complex with zinc and HSA a r_2 of16.31 $s^{-1}mM^{-1}$. This observation prompted us to prepare Dy**1** complexes, as the high magnetic moment of Dy^{3+} induces larger pseudo-contact shifts, leading to a pronounced change in transverse relaxation time (T_2), creating a negative contrast[4]. Indeed, we observed a selective r_2 increase of 140% for Dy**1** in the presence of Zn^{2+} and HSA, while the longitudinal relaxation values were almost zero for all the conditions. *In vivo* studies with Gd**1** showed a rapid clearance of Gd**1** through renal elimination and a marginal enhancement in the pancreas when no D-glucose was co-injected with the agents. When glucose was co-injected with Gd**1**, the pancreas showed superior T_1 contrast compared to controls. Data suggested that Gd**1** is uniquely sensitive to zinc co-released with insulin from β-cells in response to glucose-stimulated insulin secretion.

References: 1. Cabrera, O. *et al. PNAS* 103, 2334–2339 (2006); **2**. Kim, B. J. *et al. Diabetes* 49, 367–372 (2000); **3**. Martins, A. F. *et al. J. Am. Chem. Soc.* 140, 17456–17464 (2018); **4**. Vander Elst, L. *et al. Magnetic Resonance in Medicine* 47, 1121–1130 (2002).

Gene-reporter-engineered tricistronic cell tracker for non-invasive metal-free PET, MRI, and optical imaging.

Qiuchen Cai[1], Lucas Freidel[1], Azam Salimi[1,2], Laura Kübler[1], Oliver Hihn[1], Dr. Max Zimmermann[1], Ramona Stremme[1], Dr. Andreas Maurer[1], Dr. Gregory Bowden[1], Arnab Mukherjee[3] and André F. Martins[1,2]

[1]Werner Siemens Imaging Center, Department for Preclinical Imaging and Radiopharmacy, Eberhard Karls University Tübingen

[2]Cluster of Excellence iFIT (EXC 2180) «Image-Guided and Functionally Instructed Tumor Therapies,» University of Tübingen

[3] Dept. of Chemical Engineering, Univ. of California, Santa Barbara, CA 93106

Background: Cell engineering plays a key role in oncology as it helps visualize and understand tumor biology at cellular and molecular levels. For instance, optical gene reporters such as UV/NIR fluorescent proteins have tremendously impacted modern molecular biology and imaging. These methods have limitations regarding providing detailed information about biological processes deep within living tissues. Motivated by recent reports on gene-encoded biscistronic strategies, we developed a unique metal-free triscistronic cell engineering approach for hybrid PET/MRI and Optical imaging applications.

Methods: The gene reporter system (AQP1-mCherry-CLIP) was subcloned into lentiviral vectors and is used as a tri-cistronic construct for non-invasive multimodal functional imaging in vitro and in vivo. Tumor cell lines were transduced with the construct expressing AQP1, mCherry, and CLIP proteins. Then, expression levels of the reporter proteins were validated by flow cytometry, western blot, microscopy, and multimodal imaging modalities *in vitro*. Non-invasive multimodal diffusion-weighted, optical, and ^{18}F-O_6-benzylcytosine PET have been performed in a home-built 7T Brucker PET/MRI system and an IVIS system with excitation and emission wavelength at 570 nm and 620 nm, respectively.

Results and discussions: We successfully transduced the AQP1-mCherry-CLIP reporter system into the CHO, Jurkat, MC38, 4T1, and PyMT cells and validated the expression levels of AQP1, mCherry, and CLIP proteins by FACS, microscopy, and WB. A significant increase in ADC values in cells expressing AQP1 was observed in diffusion-weighted MRI, indicating enhanced water diffusion in the transduced cells, and thus validating the functional activity of AQP1 ($p < 0.001$). In addition, results showed that the mCherry reporter could be detected in the same transduced cell lines by optical imaging with a significant increase in the fluorescence signal vs the controls ($p < 0.001$). Moreover, we found higher standard uptake values (SUV) of the ^{18}F-O_6-benzylcytosine tracer compared to the controls ($p < 0.001$, Figure 1). Our results indicated a successful implementation of a unified tri-cistronic PET/MRI/Optical gene reporter system in several cell lines.

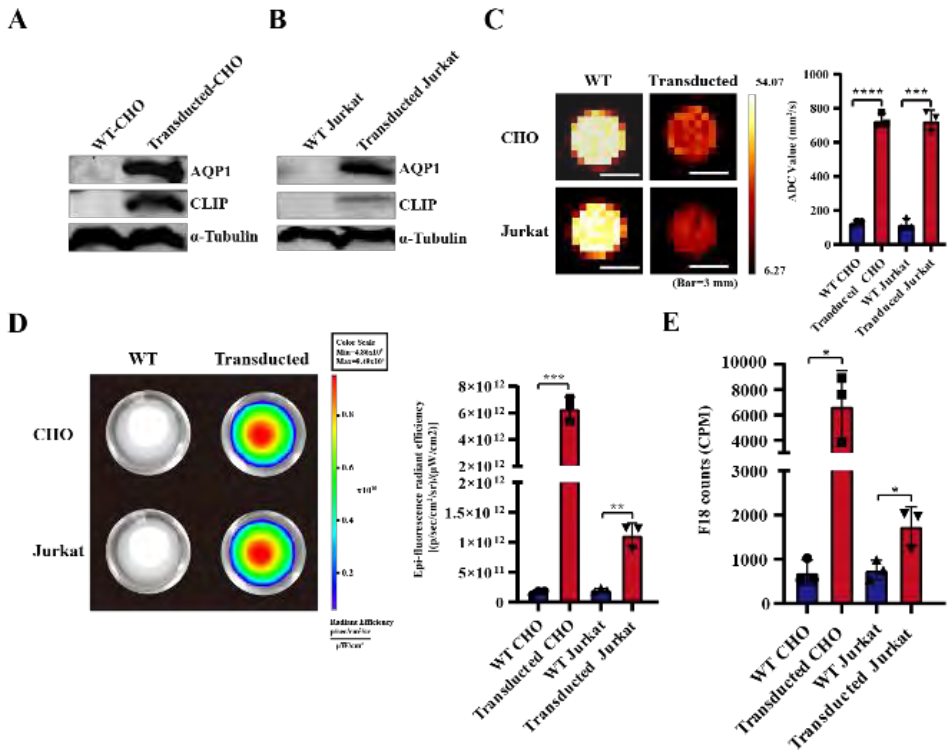

Conclusion: This innovative tricistronic cell tracker shows great promise in advancing cellular imaging by allowing simultaneous, multimodal imaging of various engineered cell lines. The engineered AQP1-mCherry-CLIP reporter system facilitates the visualization of cells across MRI, optical microscopy, and PET imaging platforms and paves the way for further cellular dynamics and interaction studies through a singular and integrated reporter gene system.

Novelty: This integrated reporter gene system offers a unified approach for non-invasive, free-metal, in-depth monitoring of cellular dynamics.

Impact: This study opens new venues for deep-tissue, whole-body studies of cellular dynamics non-invasively, potentially serving as a theragnostic tool.

Figure 1. DWI, Optical imaging, and Gamma counter measurements of transduced CHO and Jurkat cells after AQP 1-mCherry-CLIP reporter lentivirus transduction. A-B) Expression of AQP1 and CLIP in CHO and Jurkat cells after transduction. C) DWI of transduced CHO and Jurkat cells after transduction. D) Optical imaging of transduced CHO and Jurkat cells after reporter lentivirus transduction. E) Gamma counter measurements of transduced CHO and Jurkat cells after reporter lentivirus transduction. *$p < 0.05$, **$p < 0.01$, ***$p < 0.001$, ****$p < 0.0001$, error bars represent SEM. One-way ANOWA with Tukey method for multiple *t*-test; n = 3.

Radiosensitizing Magnetic Nanoparticles as a Targeted Theragnostic Agent for Cancer Therapy

V. Lecomte[1] & I. Ternad[1], D. Stanicki[1], T. Vangijzegem[1], S. Penninckx[3], S. Boutry[2], R.N. Muller[1,2], S. Lucas[4], S. Laurent[1,2]

[1]*General, Organic and Biomedical Chemistry Unit, NMR and Molecular Imaging Laboratory, University of Mons (UMONS)*
[2]*Center for Microscopy and Molecular Imaging (CMMI)*
[3]*Medical Physics Department, Jules Bordet Institute, Free University of Brussels, Brussels, Belgium*
[4]*Research Center for the Physics of Matter and Radiation (PMR-LARN), Namur Research Institute for Life sciences (NARILIS), University of Namur*

Introduction: Since 2004, High-Z nanoparticles (NPs) have been studied as radiosensitizing agents. Reports suggest that these nanoparticles can enhance the effectiveness of radiation therapy by increasing the rate of tumour cell death in response to radiation. However, the mechanisms responsible for the radiosensitization effect of such nanoparticles are not well understood. Most researches to date has focused on physical impacts. However, recent research indicates that certain metabolic processes are crucial to the observed radiosensitizing effect. (1) Specifically, the magnitude of the radiosensitizing effect and the inhibition of an enzyme that acts as a metabolic hub (thioredoxin reductase (TrxR)) in NP-treated cells were found to be significantly correlated.(2) Regarding these considerations, our laboratory has previously shown that similar enzymatic behaviour is observed in cells exposed to iron oxide nanoparticles (IONPs ; Figure A), which appear as a promising theragnostic nanoplatform due to their biocompatibility and magnetic properties (3). To further improve our previously described nanoplatform, we evaluated *in vitro* the biological impact of a vectorisation strategy for the IONPs using the H1299.3 peptide (4).

Methods: To achieve this objective, IONPs were synthetised by coprecipitation in alkaline polyol media and functionalised with PEG and a targeting peptide. We therefore compared the levels of internalization of IONPs in two cellular models: a lung cancer-derived cell line (A549) and a non-cancerous lung-derived cell line (NL20) using a colorimetric assay that involves the Prussian Blue reaction. The activity of TrxR inhibited by IONPs was measured using a commercial kit. The cell lines were incubated with various formulations at a concentration of 50 µg Fe/mL for determined incubation times. Radiosensitizing potential of the different IONPs platform were assessed by clonogenic assays after irradiation of cells. Cells were irradiated with 225kV X-rays at a rate of 2 Gy/min (X-Rad 225 XL, PXi Precision x-ray, USA). MR images of mice were captured using a Biospec 9.4T (Bruker, Germany) after the intravenous injection of the IONPs to CD1 mice at a rate of 250 µmoles Fe/100 g. Cytotoxicity of the different platforms were assessed by MTT assay.

Results and discussion: The current results show that the employed synthesis method resulted in stable and monodispersed in size IONPs. Also, the *in vitro* internalisation of vectorised particles is greater than that observed for non-vectorised particles (Figure B). Additionally, the vectorisation strategy does not compromise the inhibition of TrxR activity. Consequently, the employed vectorisation strategy is encouraging for the development of a specific theragnostic platform for cancer cells. This platform still needs to be evaluated *in vivo* through a comparative study of the biodistribution of vectorised particles and non-vectorised particles.

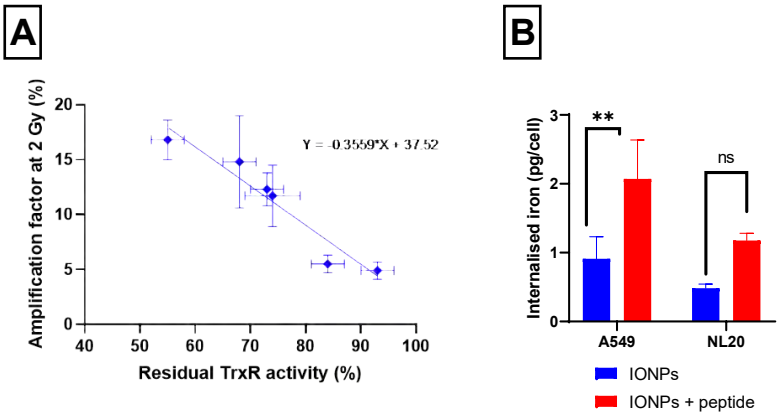

Figure A: Linear regression of the amplification factor at 2 Gy as a function of the activity of TrxR (A549 cells); Figure B: Comparison between the Internalisation of vectorised IONPs and non-vectorised IONPs (24 hours of exposition, n = 3)

References: (1) S. Penninckx, A.-C. Heuskin, C. Michiels, S. Lucas, Cancers. 12 (2020). (2) S. Penninckx, A.-C. Heuskin, C. Michiels, S. Lucas, Nanomaterials. 9, 295 (2019). (3) I. Ternad et al., Nanomaterials. 13, 201 (2023). (4) B. J. Umlauf, J. S. Mercedes, C.-Y. Chung, K. C. Brown, Bioconjug. Chem. 25, 1829–1837 (2014).

Novel peptide-based MRI probe targeting Netrin-1 : early detection of metastatic breast cancer

Clémentine Moreau,[1] Tea Lukačević,[1] Agnès Pallier,[1] Julien Sobilo,[2] Samia Aci-Sèche,[3] Norbert Garnier,[1] Sandra Même,[1] Éva Tóth,[1] Sara Lacerda[1]

1) Centre de Biophysique Moléculaire, CNRS UPR4301, 45071 Orléans Cedex 2, France ; 2) TAAM-In vivo Imaging Centre, MO2VING, CNRS UAR44, 45071 Orléans 2, France ; 3) ICOA, UMR7311, Université d'Orléans, 45067 Orléans Cedex 2 France

Introduction: Despite significant progress in cancer imaging and treatment, early diagnosis and metastasis detection remain a challenge. Molecular magnetic resonance imaging (MRI) is well adapted to fulfil this need, but requires novel contrast agents targeting specific tumor biomarkers. Netrin-1 is an extracellular protein overexpressed in metastatic breast cancer, implicated in tumor progression and appearance of metastasis[1]. While antibody Netrin-1 targeting has been recently explored for SPECT[2] and ultrasound imaging[3], we provide the first example of MR imaging of tumors using a Netrin-1-specific probe, which also holds multimodal potential.

Methods: The targeting peptide sequence of ***K*** was designed based on x-ray structure of complexes of Netrin-1 with other proteins[4], it was costume-synthesized by Peptide Synthetics and later conjugated to a DOTA-like unit. Molecular docking studies were done for validation of the structure (Fig.1a). Eu-***K*** luminescence-based in vitro binding studies were performed with Netrin-1, HSA, Collagen I and Laminin. *Ex vivo* biodistribution was done in murine models of triple negative breast cancer, overexpressing (metastatic 4T1) or non-expressing (MDA-MB-231) Netrin-1, using the ^{111}In- ***K*** analogue. 4T1 tumor-bearing mice were imaged at 9.4T, at different stages of tumor evolution using Gd-***K*** complex (intravenous 0.2mmol/kg). The clinically available Dotarem® was also used as a reference.

Results/Discussion: Molecular docking and *in vitro* binding studies revealed submicromolar Netrin-1 affinity of the probe, certainly due to the chelate unit; but of similar order than other MRI peptide-based probes.[5] At clinically relevant magnetic field 1.5T, the relaxivity of Gd-***K*** is 2.3-fold higher than Dotarem®, the MRI gold standard contrast agent. *Ex vivo* biodistribution showed that for small tumors (vol≈50mm^3), at 4h post injection the difference in the tumor uptake is higher for 4T1 and significantly different between the two models (p=0.0102; Fig.1b). MRI studies were performed at different 4T1 tumor evolution stages. Mice intravenously injected with Gd-***K*** displayed higher signal enhancement than Dotarem® for small 0-50 mm^3 tumor range, up to 1h post injection (Fig.1c); enabling early-stage tumor detection.

Conclusion: We studied a peptide-based MRI probe specific for the emerging metastatic breast cancer biomarker Netrin-1. Gd-***K*** has good relaxivity and µM *in vitro* affinity for Netrin-1. *In vivo* studies indicate promising tumor uptake, with a significative difference for overexpressing *vs*. non-expressing Netrin-1 tumors. In early-stage small tumors, Gd-***K*** provides 3-fold higher MRI signal enhancement than the gold standard Dotarem®.

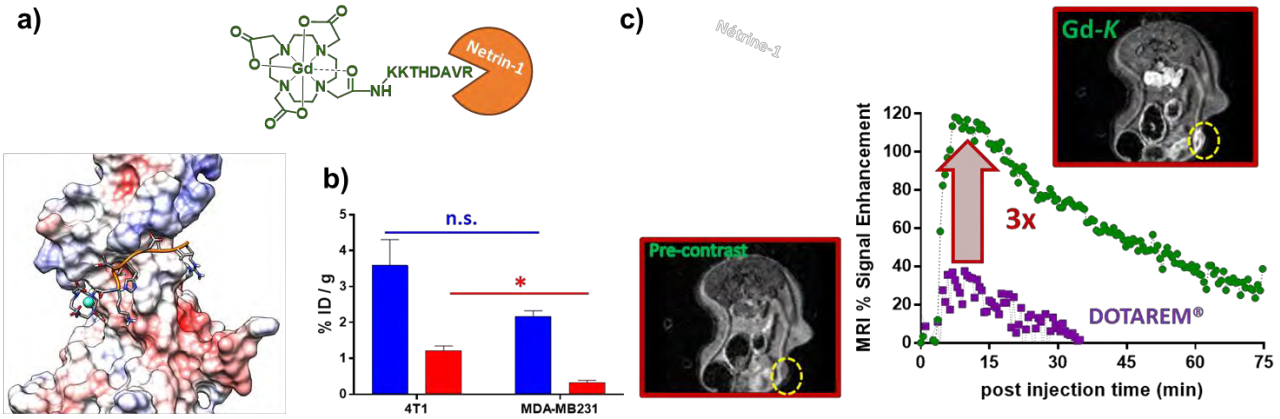

Figure 1: a) Molecular modeling and structure of the studied probe ***K***; **b)** *Ex vivo* tumor uptake in overexpressing (4T1) or non-expressing (MDA-MB-231) Netrin-1 tumor bearing mice, 15min and 4h post injection of ^{111}In-***K***; **c)** MRI signal enhancement: Gd-K and Dotarem in 0-50 mm^3 4T1 tumors.

Aknowledgements: La Ligue Contre le Cancer & Cancéropôle Grand Ouest for funding. SL thanks M. Le Mee, S. Retif and R. Clémençon; MRI & TAAM-In vivo Imaging sub-platforms, MO2VING (Orléans, France); Dr B. Gibert for kindly providing the 4T1 cells.

References: 1. (a) Mehlen P. & Guenebeaud C. "Netrin-1 and its dependence receptors as original targets for cancer therapy" *Curr. Opin. Oncol.* **2010**, 22, 46; (b) Fitamant J. et al. "Netrin-1 expression confers a selective advantage for tumor cell survival in metastatic breast cancer" *PNAS* **2008**, *105*, 4850. **2.** Kryza D. et al. "From netrin-1-targeted SPECT/CT to internal radiotherapy for management of advanced solid tumors" *EMBO Mol. Med.* **2023**, e16732. **3.** Wischhusen J. et al. "Ultrasound molecular imaging as a non-invasive companion diagnostic for netrin-1 interference therapy in breast cancer" *Theranostics* **2018**, *8*, 5126. **4.** Finci L.I. et al. "The crystal structure of netrin-1 in complex with DCC reveals the bifunctionality of netrin-1 as a guidance cue" *Neuron* **2014**, 83, 839. **5.** (a) Lacerda S. "Targeted Contrast Agents for Molecular MRI" *Inorganics* **2018**, *6*, 129.

Pt(II)-Phenanthroline-Ln(III)-DOTA *d-f* hybrids as small-molecule theranostics

Beatriz Brito,[a,b,c] Thomas W. Price,[a] Manuel Bañobre-López,[b] Juan Gallo,[b] Graeme J. Stasiuk*[a]

[a]School of Biomedical Engineering and Imaging Sciences, King's College London, St Thomas' Hospital, SE1 7EH London, UK, E-mail: graeme.stasiuk@kcl.ac.uk

[b]Advanced Magnetic Theranostic Nanostructures Lab, International Iberian Nanotechnology Laboratory, Av. Mestre José Veiga, 4715-330 Braga, Portugal

[c]School of Life Sciences, Faculty of Health Sciences, University of Hull, Cottingham Road, HU6 7RX Hull, UK

Introduction: The combination of therapeutic and diagnostic functionalities into a single agent allows for monitoring and evaluation of drug delivery and efficacy, with application in patient care management.[1] *d-f* hybrids combine metals from the *d*-block with metals from the *f*-block; these different metals can be exploited to produce systems with multiple, distinct properties.[2] In this study, bimetallic *d-f* hybrids were prepared by combining 1,10-phenanthroline and 1,4,7,10-tetraazacyclododecane-1,4,7,10-tetraacetic acid (DOTA) moieties and sequential complexation. These complexes act as theranostic agents to simultaneously achieve both imaging and therapeutic effects.

Methods: The chelator, **4**, was prepared by conjugating 1,10-phenanthrolin-5-amine to a DOTA scaffold. The Ln(III) complexes, **Ln.4**, were prepared in aqueous conditions at pH 5.5. The phenanthroline unit was coordinated to Pt(II) by addition of K_2PtCl_4 at pH 6.5. Fluorescence properties of **Ln.4** and **Pt.Ln.4** were analysed using an Edinburgh Instruments FS5 spectrometer, and magnetic properties investigated using a Bruker 400 MHz NMR. Toxicity studies were performed by incubating A549 cells (seeded at $5x10^3$ cells/well) with varying concentrations of the analytes for 48 h, and then with Resazurine for 4 h. The resultant emission was measured using a Biotek Synergy H1 Microtiter plate reader (λ_{ex} = 535 nm, λ_{em} = 590 nm) and IC_{50} values determined by fitting the obtained data to a sigmoidal dose-response curve using GraphPad Prism (v 6.05). DNA binding studies with **Pt.Eu.4** were undertaken *via* fluorescence.

Results: **Eu.4** and **Gd.4** were prepared and their identities confirmed with high-resolution mass spectrometry (HRMS). Through fluorescence lifetime studies in H_2O and D_2O the hydration state of **Eu.4** was confirmed to be q = 1 at pH 7.4. The fluorescence emission of **Eu.4** was demonstrated to be pH dependent in an off/on/off manner, with the emission intensity being at its greatest between pH 6 and 7.5. Two pK_a values were determined for the **Eu.4** system; $pK_{a,1} = 4.7 \pm 0.1$, and $pK_{a,2} = 8.5 \pm 0.1$. **Gd.4** was shown to be an efficient T_1 contrast agent, with $r_1 = 5.15 \pm 0.05$ mM^{-1} s^{-1} (9.4 T, 298 K, pH = 7.4). The *d-f* hybrids **Pt.Eu.4** and **Pt.Gd.4** were prepared, HRMS identified **Eu.Pt.4** with the expected isotopic splitting. **Pt.Eu.4** displayed quenched emission in comparison to **Eu.4**, and a shift in excitation maxima following Pt(II) complexation. **Pt.Gd.4** had an increased relaxivity of 7.53 ± 0.69 mM^{-1} s^{-1}. In A549 human non-small cell lung carcinoma cells, **Pt.Gd.4** (IC_{50} = 24.9 µM) had a higher toxicity than cisplatin (IC_{50} = 31.6 µM), and the non-platinated **Gd.4** and **4** displayed a very low toxicity (IC_{50} >1 mM). The interaction of **Pt.Eu.4** and DNA was evaluated through fluorescence binding studies; upon addition of DNA the **Pt.Eu.4** system could be more efficiently excited *via* the DNA base pairs (λ_{ex} = 265 nm) with no change when excited either directly (λ_{ex} = 395 nm) or *via* the phenanthroline unit (λ_{ex} = 320 nm).

Discussion: These results demonstrate the potential of *d-f* hybrid systems, and particularly those based upon phenanthroline-DOTA conjugates. The complexation of two different metals by the chelator endows the system with both therapeutic and diagnostic properties. In the absence of Pt(II), **Eu.4** has a potent off/on/off fluorescent switch that may find application in biological imaging. When complexed to Pt(II), **Pt.Eu.4** allowed for the confirmation of the mechanism of toxicity for this *d-f* hybrid system to be through DNA binding by the Pt(II) motif as the emission due to excitation of Eu(III) or the phenanthroline unit was unaffected by DNA binding whereas the emission *via* the DNA base pairs was promoted. **Pt.Gd.4** has promising MR properties, with a high r_1 compared to most small molecule, q = 1, contrast agents. This system also has potent cytotoxicity, slightly greater than cisplatin. This may be due to the Ln-DOTA motif allowing for an alternate uptake pathway, or due to a degree of phenanthroline intercalation.

Conclusion: This *d-f* hybrid system represents a flexible, versatile, system that can have multiple applications including fluorescence, MR imaging, and therapy. This system can also be further developed by substituting the individual metals to produce a plethora of *d-f* hybrids with optimised properties.

References: [1] A. O'Shea, A. Iravani, B. Saboury, *et al.*, Integrating Theranostics Into Patient Care Pathways: AJR Expert Panel Narrative Review, American Journal of Roentgenology, 2023, 220, 619–629. [2] S.P. Vaidya, S. Gadre, R.T. Kamisetti, M. Patra, Challenges and opportunities in the development of metal-based anticancer theranostic agents, Biosci Rep, 2022, 42 (5) BSR20212160

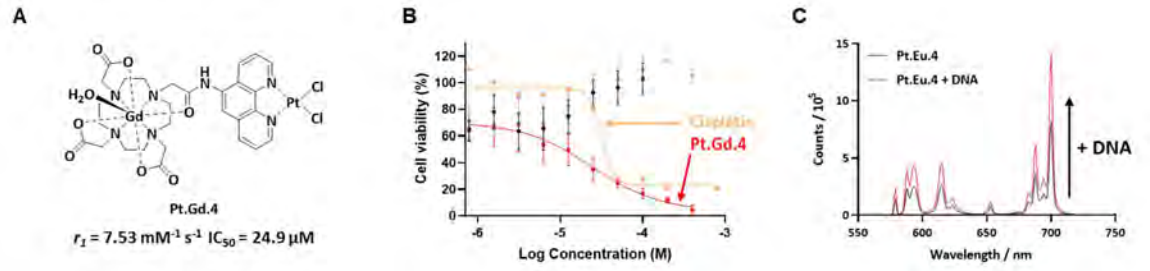

Figure 1: A: Structure of **Pt.Gd.4** B: Cytotoxicity in A549 vells after 48 h. C: Fluorescent monitoring of DNA binding of **Pt.Eu.4** (λ_{ex} = 265 nm, I = PB, pH = 7.4, T = 298 K).

A Switchable MRI Reporter to Address Collagen IV – Interpretation of Initial HyperCEST Signatures of Functionalized Xe

Patrick Werner[1], Jabadurai Jayapaul[1], Leif Schröder[1,2,3]

[1]German Cancer Research Center (DKFZ) Heidelberg, Translational Molecular Imaging, Germany
[2] German Cancer Consortium (DKTK), Partner Site Heidelberg, Germany
[3] Department of Physics and Astronomy, Ruprecht-Karls University, Heidelberg, Germany

Introduction: Conventional contrast agents require relatively high concentrations to influence the relaxivity of surrounding water magnetization. This limits their ability to monitor subtle biochemical changes such as degradation in the extracellular matrix (ECM). While many of these processes are understood, visualizing them with MRI remains challenging. It is thus necessary to develop new biosensors and related detection techniques for visualizing such biochemical processes. This study aims to develop an NMR reporter for visualizing structural changes in ECM composition, specifically those induced by metalloproteinases (MMPs). MMPs cause alterations in collagen distribution, which these sensors aim to unveil. The reporter concept is based on the HyperCEST technique[1], utilizing reversible bound hyperpolarized ^{129}Xe nuclei to detect compounds at nanomolar concentrations. This method selectively saturates reporter-associated nuclei, reducing the bulk pool's magnetization and enabling detection at relatively low reporter concentrations. The primary focus of this abstract is to validate the functionality of synthesized biosensors carrying the CrA molecule with a functionalization for non-fibrillar collagen VI.

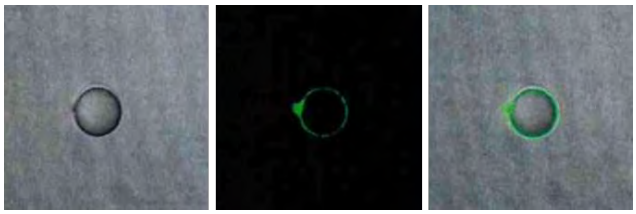

Figure 1: Fluorescence microscopy of the bound sensors on collagen beads.

Methods: Synthesis of constructs targeting collagen IV involved attaching linkers, a fluorophore, and CrA-ma to the peptide binding sequence ("KLWVLPK") specific to collagen IV[2]. All measurements were conducted on a 9.4 T NMR system. A 1 ml aqueous solution sample was exposed to a gas mixture of Xe, N_2, and He for 10 seconds at a flow rate of 100 ml/min. The saturation pulse power was varied, ranging from A) 10 mW to B) 20 mW for the solution containing collagen coated beads. For the NMR and microscopy measurements, collagen beads were incubated overnight in a biosensor containing solution.

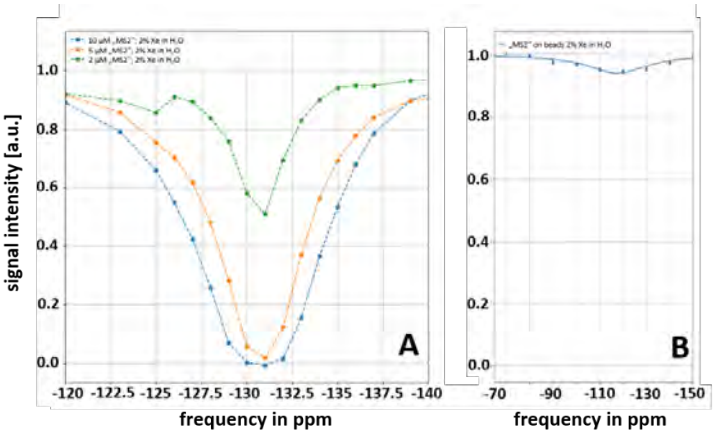

Figure 2: Z-spectra of A) collagen IV targeting bio-sensors with different concentrations (10, 5 and 2 µM) B) CEST response of the bound sensors on collagen beads.

Results: In Figure 2A, z-spectra are presented, illustrating the Chemical Exchange Saturation Transfer (CEST) response of the collagen IV biosensor in solution at varying concentrations (10, 5, and 2 µM). Upon matching the resonance frequency of reversibly bound xenon (Xe) at -131 ppm, signal loss in the bulk pool occurs. Notably, a distinct peak is visible even at the lowest concentration, negating any substantial hindrance of Xe access to the CrA cavity, as previously reported for certain CrA-peptide conjugates. Figure 2B shows the CEST response from collagen beads in solution after incubation with the biosensor (Fig. 1). The CEST response exhibits a broader profile (~70 ppm in (B) compared to ~4 ppm in (A)), indicate a potentially diminished tumbling of the CrA units upon binding of the targeting peptide to the larger beads. Additionally, a noticeable shift in the CrA signal is evident in (B) at -119 ppm.

Discussion and Conclusion: Based on these preliminary findings, our research aims to understand the complexity of the interactions of xenon biosensors with ECM structures. Researching optimal CEST conditions is an iterative process regarding the sensor design and its detection. The changes in z-spectra foster further investigation regarding the feasibility of caged Xe in the ECM environment. The ultimate goal is to transform these xenon biosensors from promising prototypes into essential tools for early disease detection.

(1) Schröder, L. (2013). Xenon for NMR biosensing–inert but alert. *Physica Medica*, *29*(1), 3-16.
(2) Wahyudi, H., Reynolds, A. A., Li, Y., Owen, S. C., & Yu, S. M. (2016). Targeting collagen for diagnostic imaging and therapeutic delivery. *Journal of Controlled Release*, *240*, 323-331.

High relaxivity MRI molecular contrast agent to target Gb3 expressing cancer cells

Stéphanie Deville-Foillard[1,4]; Anne Billet[1,5]; Rose-Marie Dubuisson[3]; Philippe Durand[4]; Ludger Johannes[1]; Frédéric Schmidt[1] et Andreas Volk[2,3*]

[1] Institut Curie CNRS UMR3666 - INSERM U1143 - 26, rue d'Ulm - PARIS FRANCE
[2] Institut Curie CNRS UMR9187 - INSERM U1196 - Rue Henri Becquerel - ORSAY FRANCE
[3] IR4M Université Paris Sud – CNRS UMR8081 – 114, rue Edouard Vaillant - VILLEJUIF FRANCE
[4] Institut de Chimie des Substances Naturelles - CNRS UPR2301 - 1, av. de la Terrasse – GIF-SUR-YVETTE FRANCE
[5] Université Paris Descartes - 12 Rue de l'École de Médecine - PARIS FRANCE
stephanie.deville-foillard@cnrs.fr

Vectorized contrast agents are promising tools for molecular magnetic resonance imaging (MRI) and early cancer diagnosis. We have developed and optimized MRI probes for targeting tumor cells overexpressing the glycosphingolipid Gb3 on their surface. We built it from a cyclic peptide scaffold functionalized by 6 to 9 monoamide derivatives of DOTA[Gd^{3+}] and vectorized by a natural ligand of Gb3, the Shiga toxin B subunit (STxB). The molecular scaffold with nine complexes of Gd^{3+} showed interesting relaxivity at 1.5 and 9.4 Tesla and was conjugated to STxB. The specific internalization and cellular distribution of this vectorized contrast agent were demonstrated by immunofluorescence microscopy, and its accumulation was quantified by dosage of Gd^{3+}using ICP-MS.

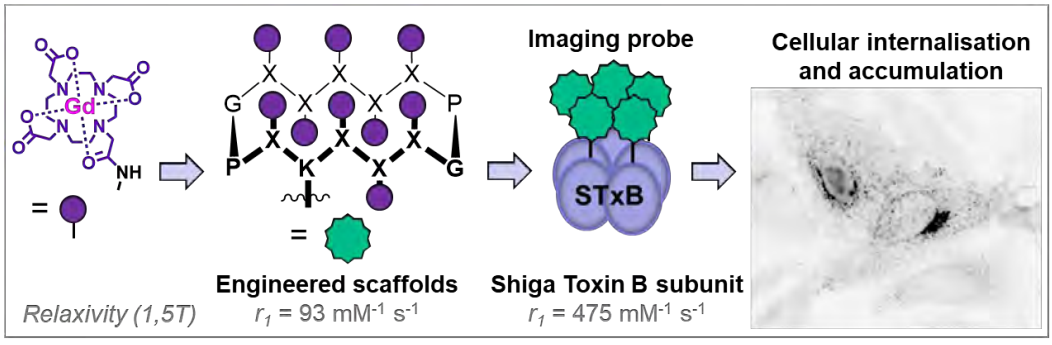

Deville-Foillard, S.*; Billet, A.; Dubuisson, R.-M.; Johannes, L.; Durand, P.; Schmidt, F.; Volk, A.* High relaxivity molecular MRI contrast agent to target Gb3 expressing cancer cells. *Bioconjug Chem* **2022**, *33*, 180–193.

[Gd(HB-DO3A)]: Equilibrium, Dissociation Kinetic and Structural Differences in a Simple Homolog of [Gd(HP-DO3A)] (Prohance®)

Silvia Versolatto,[a] Mariangela Boccalon,[b] Nicol Guidolin,[b] Fabio Travagin,[c] Enzo Alessio,[a] Silvio Aime,[d] Gabriele Balducci,[a] Giovanni B. Giovenzana,[c] Zsolt Baranyai[b]

[a] *Dipartimento di Scienze Chimiche e Farmaceutiche, Università di Trieste, Piazzale Europa 1, 34127 Trieste (TS), Italy*
[b] *Bracco Imaging Spa, CRB Trieste, AREA Science Park, 34149 Basovizza (TS), Italy*
[c] *Dipartimento di Scienze del Farmaco, Università del Piemonte Orientale, Largo Donegani 2/3, 28100 Novara (NO), Italy*
[d] *IRCCS SDN Research Institute Diagnostics and Nuclear SynLab, Via E. Gianturco, 113, 80143 Napoli (NA), Italy*

Introduction: Magnetic Resonance Imaging (MRI) contrast agents (CAs) are used to increase the contrast between, for example, two different tissues in the same anatomical regions or between a lesion and a healthy tissue. Currently used MRI CAs are represented by gadolinium-based CAs (GBCAs), accounting for about 30 million administrations per year, corresponding approximately to 40% of MRI scans acquired at clinical settings worldwide.[1] In the last decade, reports concerning the deposition of tiny amounts of gadolinium compounds in several organs[2] and tissues of patients have prompted new studies in the field of GBCAs. Thermodynamic stability and kinetic inertness do not appear to be involved for macrocyclic GBCAs present dissociation half-lives in physiological conditions that exceeds 10^3 years, while usually after 48 h more than 98% of the GBCAs has been eliminated from the organism.[3] Recent works have demonstrated intraclass differences for the three clinically approved macrocyclic GBCAs, with a different behaviour in terms of gadolinium retention in patients upon *i.v.* administration (retention order: gadobutrol > gadoterate > gadoteridol).[4] Our previous studies for the interaction of the macrocyclic GBCAs with collagen (one of the most abundant proteins in the body) reveals that the retention of macrocyclic GBCAs involves a complex interplay of electrostatic interactions, hydrogen bonds and hydrophilic/lipophilic balance. Moreover, gadoteridol analogue (*i.e.*: [Gd(**HB-DO3A**)], Figure 1) designed to display a slightly increased lipophilicity showed an interaction with collagen significantly lower than the macrocyclic GBCAs.[5] For these reasons, a thorough physico-chemical characterization of [Gd(**HB-DO3A**)] was performed in order to determine its solution and solid-state structure, its thermodynamic and kinetic stability, and its relaxometric properties.

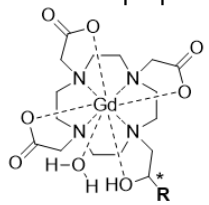

R = -CH_3: [Gd(**HP-DO3A)] gadoteridol**; **R** = -CH_2-CH_3: [Gd(**HB-DO3A)]**

Figure 1. Structure of [Gd(HB-DO3A)] and [Gd(HP-DO3A)] complexes ((*) stereocenter)

Methods: The equilibrium properties of the [Gd(**HP-DO3A**)] complex have been investigated by pH-potentiometry and ^{1}H NMR relaxometry (21 MHz, 0.15 M NaCl, 25°C). The kinetic inertness of the [Gd(**HP-DO3A**)] have been determined by monitoring the dissociation of the Gd(III) complex with ^{1}H NMR relaxometry in 0.01 – 1.0 M HCl solution (21 MHz, 25°C). The relaxation and proton exchange properties of [Gd(**HP-DO3A**)] have been studied by ^{1}H NMR relaxometry in the presence and absence of piperazine and 1,4-dimethylpiperazine buffers ([piperazine]=[1,4-dimethylpiperazine]=50.0 mM, 21 MHz, 25°C, 0.15 M NaCl). In order to acquire deeper insight into the solution and solid state structure, variable temperature and pH, multinuclear 1D and 2D NMR studies of [Gd(**HP-DO3A**)] and single crystal X-ray diffraction studies of $(C(NH_2)_3)_2${[Gd(**HB-DO3A**)$_2$](CO_3)} have been performed.

Results: The slightly higher inductive effect of an additional methylene group directly reflects in the variation of the protonation constant of the coordinating alkoxide group, leading to a minor influence on thermodynamic and kinetic stabilities. The somewhat higher steric bulk of an ethyl *vs* methyl substituent in the coordinating side arm appears to induce a minor shift in the diastereomeric ratio to favour the more expanded TSAP structure formed by [Eu(**HB-DO3A**)]. On the other hand, the analysis of the high-resolution NMR data obtained for [Eu(**HB-DO3A**)] actually reveals that the TSAP structure is entropy-favoured in the interconversion process with the SAP isomer.

Conclusions: Entropy-favoured interconversion process of TSAP structure with the SAP isomer appears of general interest as it brings new insights on the dynamic processes involving the interconversion of conformational and coordination isomers, traced back to a different solvation of the transition state of this specific process, which might influence their *in vivo* retention.

References: [1] J. Wahsner et al., *Chem. Rev.* **2019**, *119*, 957–1057, [2] N. Murata et al., *Invest. Radiol.* **2016**, *51*, 447–453, [3] Z. Baranyai, Z. Pálinkás et al., *Chem. Eur. J.* **2012**, *18*, 16426–16435, [4] A. L. Stanescu et al., *Pediatr Radiol* **2020**, *50*, 388–396, [5] N. Guidolin et al., *Dalton Trans.* **2020**, *49*, 14863–14870.

Cell surface Mannose Expression as a Diagnostic Biomarker for Molecular MRI of Glioblastoma Aggressiveness

Behnaz Ghaemi[1,2], Shreyas Kuddannaya[1], Hernando Lopez-Bertoni[3,4], John J. Laterra[3,4], Guanshu Liu[1,5], Jeff W.M. Bulte[1-4]

[1]Russell H. Morgan Department of Radiology and Radiological Science, Division of MR Research, [2]Cellular Imaging Section and Vascular Biology Program, Institute for Cell Engineering, [3]Department of Oncology, [4]Department of Neurology, the Johns Hopkins University School of Medicine, Baltimore, Maryland, USA. [5]F.M. Kirby Research Center for Functional Brain Imaging, Kennedy Krieger Inc., Baltimore, Maryland, USA.

Introduction: Glioblastoma (GBM) is the most aggressive cancer known to men. Non-invasive assessment of aggressiveness is crucial for treatment planning, but current MRI protocols lack specificity. Amide proton transfer CEST MRI can grade diffuse gliomas, but not GBM aggression levels. GBM invasiveness arises from a shift from a pro-neural to mesenchymal phenotype. Leveraging a report on mannose-weighted (MANw) CEST MRI for detection of unlabeled mesenchymal stem cells overexpressing mannose [1], we investigated if mesenchymal CSCs (MCSCs) could be detected "label-free" in a similar fashion.

Method: Low aggressive GBM1a and highly aggressive M1123 cells were used. Mannose expression was assessed using fluorescein-labeled galanthus nivalis lectin (GNL) staining of 2D cells and 3D spheres. In vitro MANw CEST MRI was conducted using a Bruker 11.7T vertical bore spectrometer. Z-spectral data were collected using a CW RF pulse of B_1=2.4 μT, and T_{sat}=3 s. For in vivo tumor models, 2×10^5 M1123 and GBM1a spheres were injected into the right and left striatum of NSG mice brain. In vivo T2-w and MANw CEST MRI was performed 1, 8 and 16 days after injection using an 11.7 T Bruker Biospin horizontal bore scanner. CEST MRI was performed with a saturation pulse B_1=2.4 μT and T_{sat}=3 s, with the saturation frequency step between ±5 ppm. Tumor and brain ROIs were manually drawn based on T2-w images.

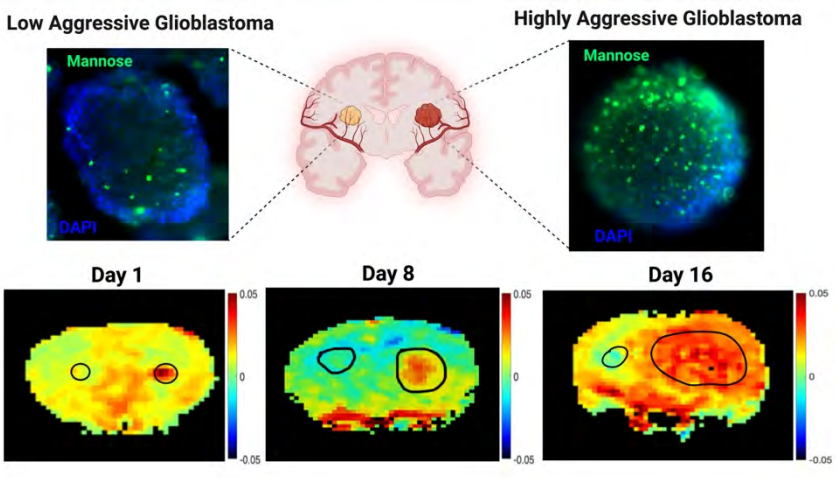

Figure 1. In vitro mannose N-linked glycan expression (green) of GBM1a and M1123 3D tumor sphere cultures. MANw CEST MRI of GBM1a and M1123 tumor spheres xenografted in immunodeficient NSG mice at 1-, 8- and 16-day post implantation. Color bar in (B) represents data acquired at 1.2 ppm.

Results and Discussion: GNL staining indicated low mannose expression for both 2D cell cultures, but M1123 3D sphere cultures contained more mannose (MCSCs) compared to GBM1a. In vitro MANw CEST MRI showed the highest CEST signal for the M1123 3D spheres. After transplantation of 3D tumor spheres in mouse brain. T2-w MRI showed M1123 cells growing much faster than GBM1a invading across the entire hemisphere on day 16, with pronounced hypointense regions due to necrosis and hemorrhage. For the MANw CEST MRI on day 1, a distinct signal was observed for M1123, whereas GBM1a signal levels were not distinguishable from normal brain tissue background. Eight and 16-day post-injection follow-up revealed a continuous pronounced MANw CEST signal only for the highly aggressive tumor. The difference in MANw CEST signal of M1123 was significantly higher (>1.8-fold) than GBM1a and host brain for all three time points.

Conclusion: Our findings suggest that MAN-w CEST MRI is able to discern highly aggressive from low aggressive GBM, potentially allowing a label-free, non-invasive differentiation of GBM aggressiveness. This advancement may be used to decrease the time interval between diagnosis and treatment, increasing patient survival. Since brain tumor patients already undergo routine MRI, our approach can be added to existing MRI protocols without further regulatory approval.

References

[1] Yuan, Y., et al., In vivo tracking of unlabeled mesenchymal stromal cells by mannose-weighted chemical exchange saturation transfer MRI. Nature Biomedical Engineering, 2022. 6(5): p. 658-666.

Non-invasive molecular MR imaging of fibrosis and treatment response in the deep vein thrombosis

Ling Gao[1], Nadia Chaher[1], Joana C. Serralha[2], Carlos Velasco[1], Gastão Cruz[1,3], Claudia Prieto [1,4], René M. Botnar[1, 5, 6], Alberto Smith[2,5], Prakash Saha[5], Alkystis Phinikaridou[1, 5]

[1] King's College London, School of Biomedical Engineering & Imaging Sciences, London, UK
[2] King's College London, School of Cardiovascular and Metabolic Medicine & Science, London, UK
[3] University of Michigan, Department of Radiology, Michigan, USA
[4] Pontificia Universidad Católica de Chile, Escuela de Ingeniería, Santiago, Chile
[5] King's College London, BHF Centre of Research Excellence, London, UK
[6] Pontificia Universidad Católica de Chile, Instituto de Ingeniería Biológica y Médica, Santiago, Chile

Introduction: Deep Vein Thrombosis (DVT) is a significant cause of morbidity and mortality worldwide[1]. DVT resolves naturally through a fibrotic process that involves the replacement of fibrin with collagen (fibrosis)[2]. The extent of fibrosis in DVT can determine the response to treatment[3]. But current diagnostic methods are not informative of the collagen content of DVT and cannot monitor the response to treatment. Here, we investigated whether molecular MRI using a collagen I targeting probe can be used to stage fibrosis and monitor the effects of statins in a murine model of DVT.

Methods: Venous thrombus was induced in the inferior vena cava (IVC) of mice by combining stenosis and endothelial injury **(Fig. 1A)**. Sham-operated mice were used as controls. A subgroup of mice with DVT was treated orally with pravastatin (40mg/kg/day) up to 3 weeks post-DVT. Mice were imaged using a clinical 3T MRI scanner pre and post injection of collagen I targeting agent (EP-3533; i.v; 10 µmol/kg). Mice were imaged at weeks 1, 2, and 3 post-surgery. Statin-treated mice were imaged at week 3 post-DVT. 2D MR venography (MRV) was used to calculate thrombus volume. 3D inversion recovery images, pre and post injection, were used to analyse the Contrast-to-Noise Ratio (CNR) and Signal-to-Noise Ratio (SNR). 3D T1 maps were used to measure the R1 relaxation rate. Fold change of CNR, SNR, and R1 were calculated.

Results: Pre-contrast images showed signal in the thrombus and low T1 values due to methaemoglobin **(Fig. 1B, C)** at weeks 1 and 2. Administration of the probe resulted in further signal enhancement in the thrombus at weeks 1, 2 and 3 that became stronger at week 3 as seen on late gadolinium enhancement (LGE) images **(Fig. 1B)**. Additionally, there was a strong reduction of T1 values at week 3 post injection of the collagen I agent **(Fig. 1C)**. The fold change of CNR, SNR and R1 was higher at week 3 compared with weeks 1 and 2 indicating higher uptake of the probe because of increased fibrosis **(Fig. 1D)**. Mice treated with statin, had similar thrombus volume as untreated mice **(Fig. 1E)**. However, post-contrast LGE images and T1 maps showed less enhancement and longer T1 values in statin-treated mice **(Fig. 1B, C)** leading to a lower fold change in CNR, SNR and R1 suggesting that statin treatment reduces fibrosis in DVT **(Fig. 1E)**.

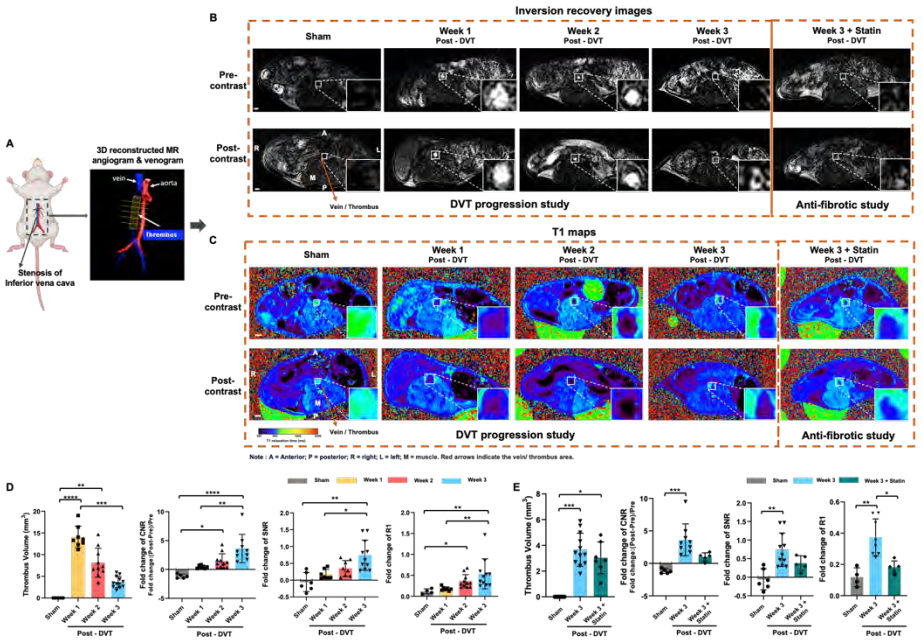

Fig.1: **A.** Schematic of the murine model of DVT and fusion of MR angiogram and venogram. **B-C**. Representative pre- and post-contrast LGE images and T1 maps in sham animals, at weeks 1, 2, 3 and statins-treated mice post-DVT. **D.** Quantification of the thrombus volume and the fold change of CNR, SNR and R1 in sham mice and at weeks 1, 2, 3 post-DVT. **E.** Quantification of the thrombus volume and the fold change in CNR, SNR and R1 in sham mice, at week 3 in untreated and statin-treated mice post-DVT. (Scale bar =1mm). *P < 0.05, **P < 0.01, ***P < 0.001, ****P < 0.0001

Discussion: Collagen I can be detected in vivo using molecular MRI at a clinical field, enabling selective detection and quantification of fibrosis in a venous thrombus. This approach enabled detection and staging of fibrosis during the organisation and resolution of DVT and monitored the antifibrotic effects of statins.

Conclusion: We show for the first time that molecular MR imaging using a collagen I probe can detect fibrotic venous clot and monitor treatment response.

Reference:

[1] White RH. Circulation. 2003 Jun 17;107(23 Suppl 1): I4-8.
[2] Mukhopadhyay S, Johnson TA, Duru N, Buzza MS, Pawar NR, Sarkar R, Antalis TM. Front Immunol. 2019 Jun 14;10:1348.
[3] Nicklas JM, Gordon AE, Henke PK. Int J Mol Sci. 2020 Mar 18;21(6):2080.

Improving the inertness of oxygen-containing macrocyclic Mn(II) complexes via careful ligand design: synthesis, characterization and *in vivo* studies

Tibor Csupász[1], István Kapus[1,2], Enikő Silyéné Madarasi[1,2], Ferenc Krisztián Kálmán[1], Imre Tóth[1], Gyula Tircsó[1]

[1]*University of Debrecen, Department of Physical Chemistry (H-4032 Debrecen, Egyetem tér 1., Hungary)*
[2]*University of Debrecen, Doctoral School of Chemistry (H-4032 Debrecen, Egyetem tér 1., Hungary)*

Introduction: One of the biggest challenge of using Mn(II) complexes as contrast agents (CAs) is to maintain the appropriate inertness. One possible solution to this problem is building in various structural motifs into the ligand structure, which improves the resistance of Mn(II) complexes towards acid assisted dissociation as well as to transmetalation or transchelation reactions. The rigid 4-oxo-1,7-diaza-2,6-piridinophane (O-pyclen) macrocycle and its derivates were found to be promising candidates.[1] Mn(II) complex of **3,9-OPC2A** ligand has an acceptable thermodynamic, dissociation and solvent exchange kinetics, but the successful human application as a contrast agent require further improvement of dissociation kinetic parameters. The extension of the new family of O-pyclen ligands was planned to be achieved by the replacement of acetate pendants by amide moieties. Similar structural changes in Mn(II) complexes of cyclen derivative ligands were found to be beneficial while attempting to improve the kinetic properties of the complexes.[2]

Methods: The protonation and stability constants of the ligands and their metal complexes, as well as the concentrations of the ligand solutions, were determined by pH-potentiometric method using a Metrohm 785 DMP Titrino automatic titrator. The protonation and stability constants of the ligands and complexes were evaluated by PSEQUAD program. The inertness of the Mn(II) complexes was investigated by T_2 relaxometry using the conditions suggested by P. Caravan et. al. and these studies were carried out using a Bruker Minispec MQ60 relaxometer (proton Larmor frequency of 60 MHz) at 25 °C and 37 °C. Bruker Minispec MQ20 (B_0 = 0.49 T) and MQ60 (B_0 = 1.41 T) relaxometers were used for the determination of the ^{1}H relaxivity of Mn(II) complexes at 25.0 and 37.0 (±0.2) °C. The longitudinal ($1/T_1$) and transverse ($1/T_2$) relaxation rates and number of coordinated water molecules of the complexes were determined by ^{17}O-NMR using Bruker Avance I 400 MHz (9.39 T) spectrometer.

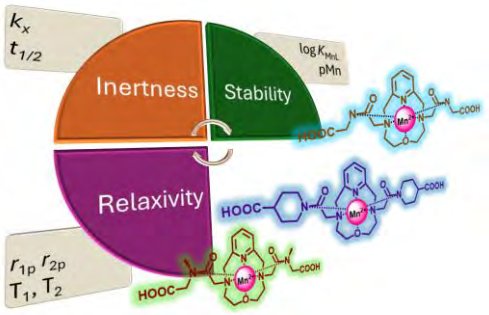

Results and Discussion: The secondary **3,9-OPC2AM^{gly}**, and the tertiary amide side arm-containing **3,9-OPC2AM^{sarc}** and **3,9-OPC2AM^{pipcarb}** ligands were prepared by the alkylation of the secondary amino groups of the O-pyclen macrocycle, followed by saponification of the protecting groups. The Mn(II) complexes formed with the less basic amide derivatives (the decrease in basicity is caused by the electron-withdrawing effect of the amide groups) are 2-3 log unites lower as compared to the [Mn(**3,9-OPC2A**)] complex. However, even the complex with the lowest stability ([Mn(**3,9-OPC2AM^{gly}**)]) keeps the 99.63 % of Mn(II) in complexes form near to physiological pH. The tertiary [Mn(**OPC2AM**)] complexes display half-lives of up to 40-230 h under the conditions applied (37 °C, 0.15 M NaCl, pH = 6.0 in the presence of 25 equivalents of Zn(II)) evidencing an outstanding inertness. Ligand possessing secondary amide pendants (**3,9-OPC2AM^{gly}**) displayed increased tendency to the dissociation owing to the easier involvement of the amide group in the proton transfer process. The relaxivity of the [Mn(**OPC2AM**)] complexes approaches, and in several cases exceeds (e.g., r_{1p} = 5.31 mM^{-1}s^{-1} for [Mn(**3,9-OPC2AM^{pipcarb}**)]) the relaxivities of the commercially available Gd(III) complexes (e.g., r_{1p} = 3.83 mM^{-1}s^{-1} for [Gd(**DOTA**)]$^-$), which allows for lowering the dose of the agent during the application. The improved relaxivity of our Mn(II) complexes can be interpreted in part by their increased molecular weight of the chelates, which increases the rotation-correlation time of the complexes in solution. On the other hand, the lower k_{ex}^{298} water exchange rate observed for the Mn(II) complexes of tertiary amide derivatives (as verified by temperature-dependent ^{17}O-NMR measurements) also improves the relaxation properties of the Mn(II) complexes. The results of the *in vivo* mouse experiments performed with [Mn(**3,9-OPC2AM^{pipcarb}**)]) complex confirms the applicability of the given chelate as CAs, so there is a good chance that our complexes can be used as real imaging agents in the future.

References: [**1**] T. Csupász, et. al. – *Molecules*, **2022**, *27*, 371; [**2**] A. Forgács, et. al. - *Eur. J. Inorg. Chem.*, **2016**, *8*, 1165-1174

Acknowledgement: The research was funded by the Hungarian National Research, Development and Innovation Office (NKFIH K-134694, FK-134551 and PD-138064 projects) and implemented with the support of the University of Debrecen's Publication Support Programme.